

**ENG 350**

ENG 350-(EQC 2006/516)

**Assessment of material strain limits for defining different forms  
of plastic hinge region in concrete structures**

*Rajesh P Dhakal, Richard Fenwick, Adam Walker, University of  
Canterbury*

# EQC Project 06/516

Assessment of material strain limits for  
defining different forms of plastic regions in  
concrete structures

Prepared for EQC

Principal Investigator: Adam Walker

07

**Assessment of Material Strain Limits for Defining Different  
Forms of Plastic Hinge Region in Concrete Structures.**

A Thesis submitted in partial fulfilment of the requirements for the degree of  
Master of Engineering  
at the University of Canterbury by

**Adam Walker**

University of Canterbury  
Christchurch, New Zealand  
2007

## TABLE OF CONTENTS

Abstract	xiv
Acknowledgements	xv
1. Introduction	
1.1 Introduction of problem	1
1.2 Scope of thesis	
1.2.1 Research objectives	2
1.2.2 Organisation of thesis	3
1.2.3 Research outcomes	3
2. Background and Literature Review	4
2.1 Code specifications	
2.1.1 Loadings standard (NZS 4203:1992 and NZS 1170.5:2004)	4
2.1.2 Concrete material design code (NZS 3101:1995 & 2006)	8
2.2 Motivation	11
2.3 Uni-directional plastic hinges	16
2.4 Strain penetration	18
3. Experimental Details	
3.1 Objective	20
3.2 Test arrangement	20
3.3 Section design	
3.3.1 Section geometry	21
3.3.2 Material properties	21
3.3.3 Yield penetration	23
3.4 Specimen construction	25
3.5 Instrumentation	27
3.6 Test procedure	29



4. Experimental Results	30
4.1 Material properties	
4.1.1 Concrete properties	30
4.1.2 Steel properties	31
4.2 Observed test behaviour	
4.2.1 Unit A	
4.2.1.1 General details	33
4.2.1.2 Test A1	33
4.2.1.3 Test A2	41
4.2.2 Unit B	
4.2.2.1 General details	47
4.2.2.2 Test B1	47
4.2.2.3 Test B2	54
4.2.3 Unit C	
4.2.3.1 General details	60
4.2.3.2 Test C1	60
4.2.3.3 Test C2	67
4.2.4 Unit D	
4.2.4.1 General details	72
4.2.4.2 Test D1	72
4.2.4.3 Test D2	79
5. Analytical Investigation	
5.1 Introduction	86
5.2 Analytical model	90
5.3 Analysis results	
5.3.1 Unit A	92
5.3.2 Unit B	101
5.3.3 Unit C	107
5.3.4 Unit D	112
5.4 Elongation	116

5.5 Further investigation	121
6. Discussion	127
6.1 Material strain limits	127
6.2 Plastic hinge lengths	133
6.3 Shear behaviour	145
6.4 Member stiffness	151
6.5 Buckling behaviour	157
6.6 Elongation	161
7. Recommendations on Limiting Material Strains for all Plastic Regions	164
7.1 Beams	164
7.2 Columns	165
7.3 Walls	166
7.4 Recommendations for material strain limits	168
8. Conclusions and Recommendations	
8.1 Conclusions	170
8.2 Recommended further research	172
9. References	173
10. Appendices	
A. Materials tests	
A.1 Concrete cylinder tests	178
A.2 Steel testing	179
B. Flexural and shear displacement calculation	183
C. Neutral axis depth calculation	184
D. Photos of buckled reinforcing bars	185
E. CD contents	186

## TABLE OF FIGURES

Figure 1.1-Effect of foundation rigidity on displacement ductility (Fenwick and Dhakal, 2007 a) .....	1
Figure 2.1-Calculating plastic rotation for reversing plastic hinges (NZS 1170.5:2004)... 6	
Figure 2.2-Calculating plastic rotation for uni-directional plastic hinges (NZS 1170.5:2004) .....	7
Figure 2.3-Strain distribution in hinge region (NZS 3101:2006) .....	9
Figure 2.4-Calculation of plastic hinge rotations (Fenwick and Dhakal, 2007 a) .....	12
Figure 2.5-Effective plastic hinge lengths for reversing and unidirectional plastic hinges (Fenwick and Dhakal, 2007 b).....	16
Figure 3.1-General test arrangement.....	20
Figure 3.2-Loading actuator arrangement and loading plate .....	21
Figure 3.3-Orientation and termination of round bars welded to longitudinal reinforcing bars within support block.....	24
Figure 3.4-Formwork construction .....	26
Figure 3.5-Stud welded to reinforcing bar with surrounding void .....	26
Figure 3.6-Pouring of concrete .....	27
Figure 3.7-Dimensions of linear potentiometer grid.....	28
Figure 3.8-Linear potentiometer grid in place .....	28
Figure 3.9-Layout of all potentiometers .....	29
Figure 3.10-Illustrative loading protocol for: (a) reversing plastic hinge and (b) uni-directional hinge.....	29
Figure 4.1-Typical steel stress-strain curves.....	31
Figure 4.2-Crack pattern after first complete cycle at 0.5% drift (A1).....	33
Figure 4.3-Cracks after two cycles to 1.0% drift (A1) .....	34
Figure 4.4-Cracking of support block after first cycle of 1.0% drift (A1).....	34
Figure 4.5-Cracking in hinge region at 2.0% drift (A1) .....	35
Figure 4.6-Transverse reinforcement visible through diagonal tension crack at 3.0% drift (A1).....	35
Figure 4.7-Extensive spalling and reinforcement buckling visible at 3.5% drift (A1).....	36



Figure 4.8-End of test after removing spalled concrete showing deformation of reinforcement (A1).....	36
Figure 4.9-Load displacement response of specimen A1 as to 4.0% drift .....	37
Figure 4.10-Contribution of shear and flexure to the total displacement at the peaks of the loading cycle for beam A1 .....	38
Figure 4.11-Flexural displacement versus force curve of beam A1 to 3.0% drift.....	39
Figure 4.12-Shear force-shear displacement relationship of beam A1 to 3.0% drift .....	40
Figure 4.13-Beam elongation (A1) .....	41
Figure 4.14-Reduced spacing of flexural cracks of test A2 at 2 <sup>nd</sup> cycle at 0.5% drift.....	42
Figure 4.15-Flexural and diagonal tension cracking within plastic region of beam A2 at 1.0% drift .....	43
Figure 4.16-Spalled concrete exposing reinforcing after 4.5% drift (A2).....	43
Figure 4.17-End of test after removing spalled concrete showing deformation of reinforcement (A2).....	44
Figure 4.18- Load displacement response of specimen A2 .....	44
Figure 4.19-Contribution of shear and flexure to the total displacement at the peaks of the loading cycles for beam A2 .....	45
Figure 4.20-Flexural displacement versus force curve of beam A2 to 4.0% drift.....	46
Figure 4.21-Shear force versus shear displacement response of beam A2 to 4.0% drift .	46
Figure 4.22-Beam elongation (A2).....	47
Figure 4.23-Flexural cracks after one complete cycle to 0.5% drift (B1) .....	48
Figure 4.24-Inclination of cracks at 1.0% displacement (B1) .....	48
Figure 4.25-Spalling of concrete at 2.0% drift (B1) .....	49
Figure 4.26-Buckled bars exposed by spalling after 2.0% drift (B1) .....	49
Figure 4.27-Ruptured bars after one cycle to 3.5% drift (B1) .....	50
Figure 4.28-Crack pattern at end of test (B1) .....	50
Figure 4.29-Load displacement response of specimen B1 .....	51
Figure 4.30-Contribution of shear and flexure to the total displacement at peak loading cycles for beam B1.....	52
Figure 4.31-Shear displacement versus shear force (B1) .....	52
Figure 4.32-Flexural displacement versus force relationship (B1).....	53



Figure 4.33-Beam elongation (B1) .....	54
Figure 4.34-Crack pattern after two complete cycles at 1.0% drift (B2).....	55
Figure 4.35-Extent of crushed concrete at 4.0% drift (B2).....	55
Figure 4.36-Buckled and ruptured bars after two complete cycles at 6.0% drift (B2).....	56
Figure 4.37-Crack pattern at the end of test (B2) .....	56
Figure 4.38-Load displacement response of beam B2.....	57
Figure 4.39-Contribution of shear and flexure to the total displacement at the peaks of the loading cycles beam B2 .....	58
Figure 4.40-Flexural displacement versus applied force (B2).....	58
Figure 4.41-Shear displacement versus applied load (B2) .....	59
Figure 4.42-Beam elongation (B2) .....	60
Figure 4.43-Crack pattern after two cycles at 0.5% drift (C1) .....	61
Figure 4.44-Crushing of concrete during positive cycle to 1.0% drift (C1).....	61
Figure 4.45-First evidence of buckling at 2.5% drift (C1) .....	62
Figure 4.46-Pronounced buckling at 3.0% drift (C1) .....	62
Figure 4.47-Crack pattern at the end of test (C1) .....	63
Figure 4.48-Load displacement response for specimen C1 .....	63
Figure 4.49-Contribution of shear and flexure to the total displacement at the peaks of the loading cycles for beam C1.....	64
Figure 4.50-Shear displacement versus applied load (C1) .....	65
Figure 4.51-Flexural displacement versus applied load (C1).....	66
Figure 4.52-Beam elongation (C1) .....	66
Figure 4.53-Flexural cracking at 2.0% drift (C2) .....	67
Figure 4.54-Buckling of bottom bars at 5.0% drift (C2) .....	68
Figure 4.55-Crack pattern at the end of test (C2) .....	68
Figure 4.56-Load displacement response of specimen C2 .....	68
Figure 4.57-Contribution of shear and flexure to the total displacement at the peaks of the loading cycles for beam C2.....	70
Figure 4.58-Shear displacement versus applied load (C2) .....	70
Figure 4.59-Flexural displacement versus applied load (C2).....	71
Figure 4.60-Beam elongation (C2) .....	72

Figure 4.61-Crack pattern after two complete cycles at 1.0% drift (D1) .....	73
Figure 4.62-Crack pattern after two complete cycles to 2.5% drift (D1) .....	73
Figure 4.63-Displacement of concrete at top of beam indicating buckling at 3.0% drift (D1) .....	74
Figure 4.64-Buckled top bars at 4.5% drift (D1) .....	74
Figure 4.65-Ruptured bar and deformed stirrup at the end of test (D1) .....	75
Figure 4.66-Condition of beam at the end of test (D1) .....	75
Figure 4.67-Load displacement response of specimen D1 .....	76
Figure 4.68-Contribution of shear and flexure to the total displacement at the peaks of the loading cycles for beam D1 .....	77
Figure 4.69-Shear displacement versus applied load (D1) .....	77
Figure 4.70-Flexural displacement versus applied load (D1) .....	78
Figure 4.71-Beam elongation (D1) .....	78
Figure 4.72-Crack pattern after two complete cycles at 1.0% drift (D2) .....	79
Figure 4.73-Open cracks at 2.5% drift (D2) .....	79
Figure 4.74-Concrete crushing and positive shear crack at 3.0% drift level (D2) .....	80
Figure 4.75-Crack pattern after 3.5% drift (D2) .....	80
Figure 4.76-Ruptured bar and deformed stirrup at the end of test (D2) .....	81
Figure 4.77-Beam condition at the end of test (D2) .....	81
Figure 4.78-Load displacement response of specimen D2 .....	82
Figure 4.79-Contribution of shear and flexure to the total displacement at the peaks of the loading cycles for beam D2 .....	83
Figure 4.80-Shear displacement versus applied load (D2) .....	83
Figure 4.81-Flexural displacement versus applied load (D2) .....	84
Figure 4.82-Beam elongation (D2) .....	85
Figure 5.1-Bond affected zone in reinforced concrete elements (UC-win) .....	88
Figure 5.2-Effect of varying tension softening factor on concrete stress strain behaviour .....	89
Figure 5.3-Mesh layout for numerical model of Test A1 .....	90
Figure 5.4-Numerical and experimental comparison (A1) .....	92



Figure 5.5-Comparison of experimental flexural displacement and the total numerical displacement (A1).....	93
Figure 5.6-Comparison of initial stiffness (A1).....	94
Figure 5.7-Failure and damage regions (Shear failure) (A1).....	95
Figure 5.8-Crack pattern from analysis (A1).....	95
Figure 5.9-Crack pattern from test (A1) .....	95
Figure 5.10-Analytical stress results (A1) .....	96
Figure 5.11-Analytical yield results (A1) .....	96
Figure 5.12-Comparison of numerical model with and without joint model (A1).....	97
Figure 5.13-Numerical and experimental comparison (A2) .....	98
Figure 5.14-Failure and damage regions (Shear failure) (A2).....	98
Figure 5.15-Analytical crack pattern (A2).....	99
Figure 5.16-Experimental crack pattern (A2).....	99
Figure 5.17-Analytical stress result (A2).....	99
Figure 5.18-Analytical yield result (A2).....	99
Figure 5.19-Numerical comparison for Tests A1 and A2.....	100
Figure 5.20-Experimental comparison for Tests A1 and A2.....	101
Figure 5.21-Numerical and experimental comparison (B1) .....	102
Figure 5.22-Failure and damage regions (Compression failure) (B1).....	102
Figure 5.23-Analytical crack pattern (B1) .....	103
Figure 5.24-Experimental crack pattern (B1) .....	103
Figure 5.25-Analytical stress result (B1) .....	103
Figure 5.26-Analytical yield result (B1).....	104
Figure 5.27-Numerical and experimental comparison (B2) .....	104
Figure 5.28-Failure and damage regions (Compression failure) (B2).....	105
Figure 5.29-Analytical crack pattern (B2) .....	105
Figure 5.30-Experimental crack pattern (B2).....	105
Figure 5.31-Analytical stress result (B2) .....	106
Figure 5.32-Analytical yield result (B2).....	106
Figure 5.33-Numerical and experimental comparison (C1) .....	107
Figure 5.34-Failure and damage regions (Tension failure) (C1) .....	108

Figure 5.35-Analytical crack pattern (C1).....	108
Figure 5.36-Experimental crack pattern (C1).....	108
Figure 5.37-Analytical stress result (C1).....	109
Figure 5.38-Analytical yield result (C1).....	109
Figure 5.39-Numerical and experimental comparison (C2).....	110
Figure 5.40-Failure and damage regions (Shear failure) (C2).....	110
Figure 5.41-Analytical crack pattern (C2).....	110
Figure 5.42-Experimental crack pattern (C2).....	111
Figure 5.43-Analytical stress result (C2).....	111
Figure 5.44-Analytical yield result (C2).....	111
Figure 5.45-Numerical and experimental comparison (D1).....	112
Figure 5.46-Failure and damage regions (Tension failure) (D1).....	113
Figure 5.47-Analytical crack pattern (D1).....	113
Figure 5.48-Experimental crack pattern (D1).....	113
Figure 5.49-Analytical stress result (D1).....	113
Figure 5.50-Analytical yield result (D1).....	114
Figure 5.51-Numerical and experimental comparison (D2).....	114
Figure 5.52-Failure and damage regions (Tension) (D2).....	115
Figure 5.53-Analytical crack pattern (D2).....	115
Figure 5.54-Experimental crack pattern (D2).....	115
Figure 5.55-Analytical stress result (D2).....	116
Figure 5.56-Analytical yield result (D2).....	116
Figure 5.57-Comparison of elongation between the experiment result and the numerical model (A1).....	117
Figure 5.58- Comparison of elongation between the experiment result and the numerical model (A2).....	118
Figure 5.59- Comparison of elongation between the experiment result and the numerical model (B1).....	118
Figure 5.60- Comparison of elongation between the experiment result and the numerical model (C1).....	119



Figure 5.61- Comparison of elongation between the experiment result and the numerical model (D1).....	120
Figure 5.62- Comparison of elongation between the experiment result and the numerical model (D2).....	120
Figure 5.63-Mesh layout for length to depth ratio of 2.....	121
Figure 5.64-Effect of increasing length of restrained beam .....	122
Figure 5.65-Effect of increasing length of unrestrained beam .....	122
Figure 5.66-Effect of increasing transverse steel content for restrained beam, $L/d=1$ ...	123
Figure 5.67-Effect of increasing transverse steel content for restrained beam, $L/d=2$ ...	123
Figure 5.68-Effect of restraining horizontal degree of freedom .....	124
Figure 5.69-Deflection and crack pattern for $L/d=1$ with a) Unrestrained horizontal displacement and b) Restrained horizontal displacement.....	124
Figure 5.70-Effect of increasing transverse steel content of unrestrained beam .....	125
Figure 6.1-Calculating allowable curvature from strain limits.....	127
Figure 6.2-Obtaining experimental curvature.....	128
Figure 6.3-Crack widths and estimation of yielding length (A1).....	134
Figure 6.4-Strains obtained from longitudinal potentiometers (A1) .....	135
Figure 6.5-Crack widths and estimation of yielding length (A2).....	135
Figure 6.6-Strains obtained from longitudinal potentiometers (A2) .....	136
Figure 6.7-Crack widths and estimation of yielding length (B1) .....	136
Figure 6.8-Strains obtained from longitudinal potentiometers (B1).....	137
Figure 6.9-Crack width and estimation of yielding length (B2).....	138
Figure 6.10-Strains obtained from longitudinal potentiometers (B2).....	138
Figure 6.11-Crack width and estimation of yielding length (C1).....	139
Figure 6.12-Strains obtained from longitudinal potentiometers (C1).....	139
Figure 6.13-Crack width and estimation of yielding length (C2).....	140
Figure 6.14-Strains obtained from longitudinal potentiometers (C2).....	140
Figure 6.15-Crack widths and estimation of yielding length (D1) .....	141
Figure 6.16-Strains obtained from longitudinal potentiometers (D1) .....	141
Figure 6.17-Crack widths and estimation of yielding length (D2) .....	142
Figure 6.18-Strains obtained from longitudinal potentiometers (D2) .....	142

Figure 6.19-Triangular approximation of strain profile and corresponding effective hinge length.....	144
Figure 6.20-Diagonal tension cracks at 3.0% drift (A1).....	147
Figure 6.21-Diagonal tension cracks at 3.5% drift (A2).....	147
Figure 6.22-Diagonal tension cracks at 2.0% drift (B1).....	148
Figure 6.23-Diagonal tension cracks at 2.0% drift (B2).....	148
Figure 6.24-Diagonal tension cracks at 1.5% drift (C1).....	149
Figure 6.25-Diagonal tension cracks at 1.5% drift (C2).....	149
Figure 6.26-Diagonal tension cracks at 3.0% drift (D1).....	149
Figure 6.27-Diagonal tension cracks at 4.0% drift (D2).....	150
Figure 6.28-Calculating initial stiffness.....	151
Figure 6.29-Calculating secant stiffness.....	152
Figure 6.30-Normalised secant stiffness versus drift level.....	153
Figure 6.31-Calculating tangential stiffness.....	154
Figure 6.32-Normalised tangent stiffness versus drift level.....	155
Figure 6.33-Buckling mechanism #1.....	157
Figure 6.34-Buckling mechanism #2.....	157
Figure 6.35-Layout of reinforcing for beam A1 to determine $n_b$ , $n_l$ and $l_e$ .....	158
Figure 6.36-Assumed clear span for stirrup bending.....	159
Figure 7.1-Ultimate curvatures sustained in beam tests versus normalised shear stress	165
Figure 7.2-Ultimate curvatures sustained in column tests versus normalised axial stress	166
Figure 7.3-Ultimate curvatures sustained in singly reinforced walls versus normalised stress.....	167



## TABLE OF TABLES

Table 3.1-Test beam properties.....	22
Table 3.2-Minimum tensile strengths for test welds (NZS 1554.3:2007, draft).....	25
Table 4.1-Average concrete strengths on day of test.....	30
Table 4.2-Steel properties .....	32
Table 5.1-Comparison of experimental and numerical initial stiffness of all beams .....	94
Table 6.1-Comparison of curvature limits and experimental curvatures using nominal material properties .....	130
Table 6.2-Comparison of curvature limits and experimental curvatures using measured material properties .....	131
Table 6.3-Ultimate curvature as a factor of nominal first yield.....	132
Table 6.4-Comparison of experimental and code hinge lengths.....	143
Table 6.5-Transverse reinforcement details.....	145
Table 6.6-Concrete shear capacity .....	146
Table 6.7-Initial Stiffness's.....	151
Table 6.8-Drifts at which failure occurred using strength, secant stiffness and tangent stiffness criteria.....	156
Table 6.9-Values of $k_{eq}$ for stable buckling modes (Dhakal and Maekawa, 2002) .....	158
Table 6.10-Results of buckling mode calculation.....	159
Table 6.11-Maximum elongation from experiment and numerical analysis .....	163
Table 7.1-Summary of ultimate curvatures from test results.....	168
Table 7.2-Recommended $K_d$ values for determining curvature limits for reversing plastic regions.....	169

## ABSTRACT

The New Zealand Structural Loading Standard, until its latest revision, was using the structural displacement ductility factor as a measure of the deformation demand of all potential plastic hinges in a structure. In the revised version of New Zealand Structural Loading Standard for Earthquake Actions (NZS 1170.5:2004) the detailing of potential plastic regions is determined according to the local inelastic deformation demand in these regions. The change has been prompted by evidence that the structural ductility factor gives a poor indication of the demand on individual plastic regions. This is a major paradigm shift in international design codes. This new approach has been adopted by the New Zealand Concrete Structures Standard (NZS 3101:2006) which classifies potential plastic regions into three categories (namely ductile, limited ductile and nominally ductile) based upon their inelastic deformation demand which has been specified in terms of material strain limits in the form of curvatures or shear deformations. The values of material strain limits currently used in New Zealand Concrete Standard (NZS 3101:2006) to categorise the plastic regions are based on limited evidence and need a closer revision. This research attempts to obtain more justifiable values of material strain limits through experimental data existing in literature. Moreover, experimental testing is also conducted to compensate for a lack of data in the nominally ductile range of detailing. The experimental work explores the effects of transverse reinforcement arrangement, reinforcing steel grade and plastic hinge type. Together the literature review and experimental work provide a sound basis for re-defining the material strain limits for different plastic regions.



## **ACKNOWLEDGEMENTS**

Most importantly I would like to thank my supervisors, Dr Rajesh Dhakal and Associate Professor Richard Fenwick. Their direction, motivation and technical guidance has been absolutely invaluable.

For providing financial support and resources I would like to extend a thank you to the Earthquake Commission, the Cement and Concrete Association of New Zealand and the University of Canterbury, particularly the Department of Civil Engineering.

The laboratory technicians at the university are also to be thanked, particularly Russell McConchie and his colleagues Tim Perigo, Gavin Keats, Norm Pilling, Richard Newton and Peter Coursey.

# 1. INTRODUCTION

## 1.1. INTRODUCTION OF PROBLEM

In the previous version of the New Zealand standard for the design of reinforced concrete structures, NZS 3101:1995; the minimum detailing requirements for potential plastic regions were based on the structural displacement ductility factor,  $\mu$ . This factor has been shown to be a poor indicator of the required level of inelastic deformation on individual plastic regions (Fenwick and Dhakal, 2007 a). This was illustrated with reference to the walls shown in Figure 1.1. In the first case the wall is constructed with a stiff foundation while in the second the foundation is flexible. The effect of the flexible foundation is to increase the displacement to first yield, which is taken as the ductility one displacement. Thus when the structure is displaced to higher levels of displacement ductility, the actual displacement required to reach this level is increased for the flexible foundation case. As this plastic displacement arises due to deformation in the plastic region of the wall, it can be seen that the second wall has a greater demand on its plastic region and that the structural ductility factor does not provide the same demand in these two cases.

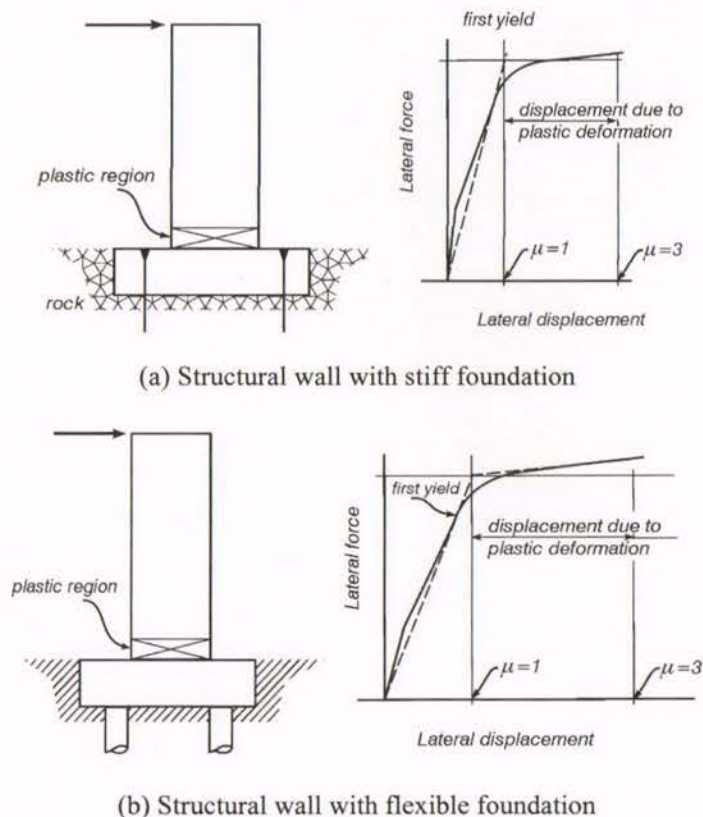


Figure 1.1-Effect of foundation rigidity on displacement ductility (Fenwick and Dhakal, 2007 a)

The latest revision of the New Zealand Loading Code for Earthquake actions (NZS 1170.5:2004) has recognised this inadequacy and requires that the detailing of potential plastic regions be based on the expected inelastic deformation in individual plastic regions. The demand is specified as material strains in the hinge region. For columns, beams and walls in flexure the material strains are in the form of a curvature, while for shear links in eccentrically braced frames or reinforced concrete coupling beams the material strains are shear deformations. Axial tensile or compressive strains can also be considered, however, no allowance has been made for these in NZS 3101:2006.

The New Zealand Design Code for Reinforced Concrete Structures has adopted the approach prescribed by the loadings standard in its latest revision, NZS 3101:2006. The concrete code divides potential plastic regions into three categories based on the expected material strain they would sustain in a limit state design basis earthquake. The three categories are ductile, limited ductile and nominally ductile. The limiting material strains are specified in terms of a curvature or shear deformation with no consideration given for axial strains.

In order to enable safe and efficient structural design, it is desirable that the material strain limits be based on significant experimental information. At the time of publication of the design code an in-depth investigation into appropriate material strain limits had not been conducted. Following publication of the code, Fenwick and Dhakal (2007 b) have submitted proposed amendments to the material strain limits for ductile and limited ductile plastic regions based on experimental results found in the literature. No satisfactory test results could be found for reinforced concrete members with nominally ductile detailing.

## **1.2. SCOPE OF THESIS**

### **1.2.1. Research Objectives**

The plan behind this project is to gather a wider range of data on tests published in the literature to enable material strain limits to be assessed for different levels of detailing. There are three principle objectives for the research project.

- Conduct cyclic tests on nominally ductile beams designed according to detailing provisions in NZS3101:2006.
- Review test results, existing and proposed, to examine the material strain limits for plastic regions in members with different levels of detailing.



- Review, and propose revisions if appropriate, to the material strain limits for different levels of detailing in plastic regions given in the New Zealand Structural Concrete Standard, NZS3101:2006.

These values are of key importance in the seismic design process established in the Earthquake Loadings Standard NZS1170.5-2004 and the Structural Concrete Standard, NZS3101:2006.

### **1.2.2. Organisation of Thesis**

Following this introductory section, Chapter 2 of this thesis contains a review of relevant literature, which highlights experimental work of previous researchers that can be used to reinforce the work already carried out by Fenwick and Dhakal.

Chapter 3 details the experimental setup used for testing nominally ductile beams. Chapter 4 contains the results of the tests. An analysis and discussion of the test results is detailed in Chapter 5 and the material strain limit recommendations given in Chapter 6.

The Appendices include:

- Full detailed drawings of the test setup.
- Results of steel tests including welded bar tests.
- Complete details of beam test results not described in-depth in the main text.

### **1.2.3. Research Outcomes**

The outcomes of the project are recommendations for the material strain limits for nominally ductile, limited ductile and ductile plastic regions for reinforced concrete members. The outcome may be used to either confirm or amend the limiting values given in the Structural Concrete Standard (NZS3101:2006). This research can be expected to improve the economy of construction, the seismic performance of concrete structures and the level of confidence with which the new provisions of the Earthquake Loadings Standard (NZS 1170.5:2004) and the revision of the concrete Standard (NZS 3101:2006) can be applied in structural design.



## **2. BACKGROUND AND LITERATURE REVIEW**

This chapter contains a review of literature related to material strains. Of specific importance are recent changes to New Zealand Standards relating to detailing requirements in reinforced concrete structures, namely, NZS 4203:1992, NZS 1170.5, NZS 3101:1995 and NZS 3101:2006. Two papers by Fenwick and Dhakal (2007 a & b) that provide the main motivation behind this project are reviewed in depth in this section. The first of the papers examines material strains and their use in seismic design in a general sense while the second paper looks at the adoption of material strain limits for use in the concrete design code. Other aspects reviewed are uni-directional plastic hinges and strain penetration.

### **2.1. CODE SPECIFICATIONS**

#### **2.1.1. Loadings standard (NZS 4203:1992 and NZS 1170.5:2004)**

The previous loading standard, NZS 4203:1992, defined the loads and forces to be used in the design of structures for dead, live, wind, snow and seismic loading. The seismic section detailed how to calculate the seismic actions to be used in design and the methodology for finding the deflection profile. The requirements for detailing of potential plastic regions were left to the appropriate materials standard. The reinforced concrete standard (NZS 3101:1995) used the structural displacement ductility factor to determine the minimum detailing requirements.

Analyses have showed that the structural ductility factor is a poor indicator of local deformation demand in plastic hinges (see Chapter 1). Thus, the latest revision of the loading standard, NZS 1170.5:2004 requires the level of detailing to be based upon the local inelastic deformation in the form of expected material strain. This change uncouples the structural ductility factor and the level of detailing. This is the first time this has been implemented in a national design code.

The new loading standard (NZS 1170.5:2004) uses the structural ductility factor to classify structures into four categories, ductile, limited ductile, nominally ductile and brittle structures. As in the previous loadings standard (NZS 4203:1992), the structural ductility

factor is used to determine the seismic forces and modify the deflection profile. The classification of structures is as follows:

- Ductile structures:  $1.25 < \mu < 6.0$
- Limited ductile structures:  $1.25 < \mu < 3.0$
- Nominally ductile structures:  $1.0 < \mu < 1.25$
- Brittle structures:  $\mu = 1.0$

Limited ductile structures are a subset of ductile structures which are assumed to have either low inelastic deformation demand or low inelastic deformation capacity. They are designed to resist higher seismic forces derived with the use of a lower force reduction factor ( $\mu$ ). The structures classified as nominally ductile are not expected to develop significant inelastic deformation.

The level of detailing dictates the level of deformation the individual plastic regions can sustain. In any design, the designer needs to check the material strain demand in individual plastic regions and detail accordingly or reduce the structural ductility factor so that the deformation demand is reduced to an acceptable level. There are maximum values for curvature sustained by different types of hinges, and if these values are exceeded the designer should review the entire structure geometry and redesign.

Appendix C of NZS 1170.5 describes the recommended methodology for calculating the expected material strains (curvatures) in individual potential plastic regions. The first step is the calculation of the expected deflections using an approved method as described in the standard.

The type of potential plastic region (i.e. reversing or uni-directional) alters the methodology for calculating the expected curvature. A review of the different forms of plastic regions follows in Section 2.3. For reversing plastic regions, as illustrated in Figure 2.1, the plastic rotation in the hinge can be obtained from the inter-story displacement by:

$$\theta_p = \frac{\delta_p L}{hL'} \quad \text{Equation 1}$$

Where:  $\delta_p$  is plastic component of the inter-story displacement

$h$  is inter-story height

$L$  is distance between column centrelines



$L'$  is distance between centres of the hinges

Designers can conservatively neglect the elastic deformation, assuming the entire inter-story displacement is due to plastic rotation. Then the curvature is found by dividing the plastic rotation by the effective hinge length, as found in the appropriate material code. For nominally ductile structures the assumption of the total displacement being equal to the plastic displacement is conservative due to the relatively high ratio of elastic to plastic displacements. This will make it difficult for designers to satisfy the material strain limits when using this assumption.

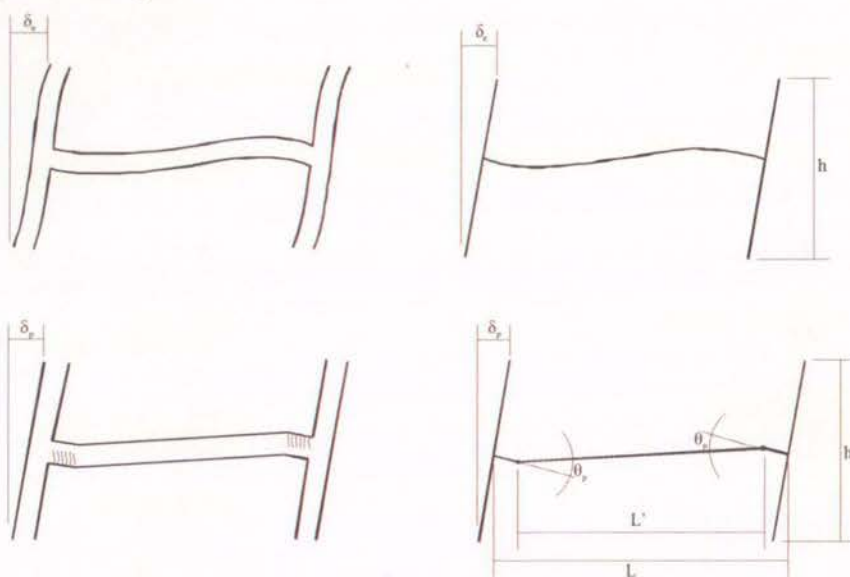


Figure 2.1-Calculating plastic rotation for reversing plastic hinges (NZS 1170.5:2004)

With uni-directional plastic hinges the inelastic rotation imposed is significantly greater than that of a reversing hinge due to the accumulation of rotation in one direction during a seismic event. However the rotation that a uni-directional plastic hinge can sustain is also substantially greater than a reversing hinge (Fenwick and Davidson, 1987). To determine the plastic rotation, the plastic hinges are assumed (incorrectly) to be located on the column centrelines while the columns are inclined at an angle,  $\alpha = \frac{\delta_e + \delta_p}{h}$ . This is indicated in

Figure 2.2. The plastic rotation is then obtained by multiplying alpha by the appropriate factor below depending on the magnitude of the structural ductility factor.

$$1.0 + 0.63(\mu - 1) \quad \text{for } \mu \leq 2.0$$

$$1.63\sqrt{(\mu - 1)} \quad \text{for } \mu > 2.0$$

It is important to note that the calculated rotation from this method is only an indicative rotation for design purposes. Again, the reliability of this method for calculating the plastic



rotation for nominally ductile structures is very conservative. The expected curvature follows using the same method as for the reversing plastic regions.

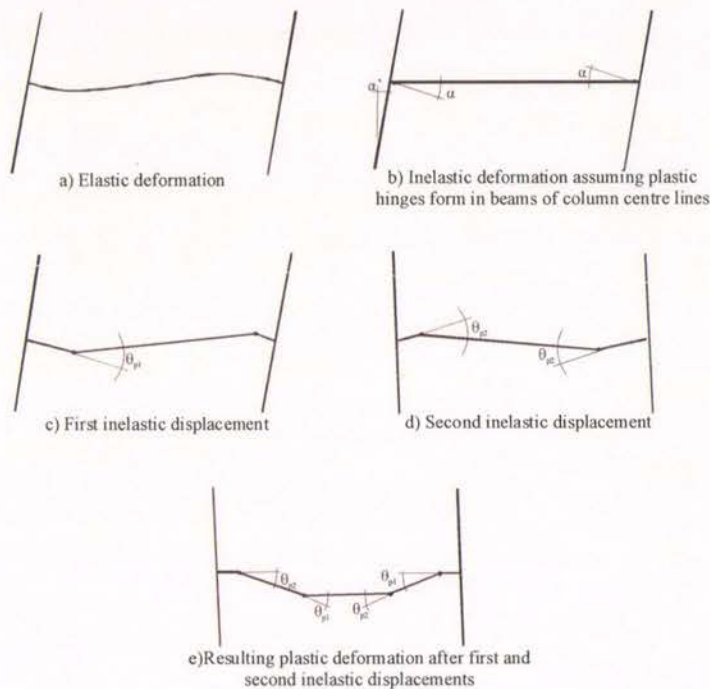


Figure 2.2-Calculating plastic rotation for uni-directional plastic hinges (NZS 1170.5:2004)

Note that the plastic hinges forming away from the column face form over a longer length than reversing hinges or hinges located at the column faces because yield can extend in both directions from the critical section.

For structural walls the curvature is determined from the displacement at the ultimate limit state at the top of the wall. The rotation is given by:

$$\theta_p = \frac{(\mu - 1)}{\mu} \frac{\delta}{h'} \quad \text{Equation 2}$$

Where:  $\delta$  is the displacement at the top of the wall

$h'$  is the distance between top of wall and centre of hinge region

$\mu$  is the structural ductility factor.

The ratio  $(\mu - 1)/\mu$  converts the total wall displacement to the plastic component. Again the curvature is found by dividing the rotation by the effective hinge length as defined in the appropriate material code.

### **2.1.2. Concrete material design code (NZS 3101:1995 & 2006)**

The previous edition of the New Zealand Concrete Structures Standard, NZS 3101:1995 followed the objectives and guidelines set out in NZS 4203:1992. The Concrete Standard classified three different forms of concrete structure; fully ductile, limited ductile and elastically responding, based upon the structural ductility factor.

NZS 3101:1995 specified the minimum detailing for potential plastic regions based on the structural ductility factor. The detailing requirements were specified in general for all structural types including elastic responding structures. Additional requirements for ductile structures were then specified under “additional requirements for earthquake effects” at the end of each force related design section. A separate chapter was included in the code for the detailing of members in limited ductile structures. Elastic responding structures were expected to form an admissible mechanism when loads exceed those expected during design and the code exempted such structures from the additional seismic requirements.

In 2006 a new edition of concrete design standard, NZS 3101:2006, was released. This edition adopted the approach specified by the loading standard (NZS 1170.5:2004) for the detailing of potential plastic regions based upon the expected material strains. This revision of the concrete code is the first material standard in New Zealand to meet the requirements of the new loading standard. For the purposes of detailing, individual potential plastic regions are classified as nominally ductile plastic regions (NDPR), limited ductile plastic regions (LDPR) and ductile plastic regions (DPR) based on the expected material strain in terms of a section curvature or shear deformation.

This latest revision of the concrete structures standard classifies structures as specified by NZS1170.5 but does not give provisions for the design of brittle structures. The code suggests that nominally ductile structures ( $1.0 < \mu < 1.25$ ) are likely to contain NDPRs' and LDPRs'. Similarly limited ductile structures ( $1.25 < \mu < 3.0$ ) will likely contain LDPRs' and DPRs'. Ductile structures ( $3.0 < \mu < 6.0$ ) should only contain ductile plastic regions as the accuracy with which deformation demand can be predicted decreases with increasing structural ductility factor.

The expected material strains are to be obtained from the deflected profiles found following the method specified in NZS 1170.5:2004. The method requires the use of an effective hinge length to calculate the hinge curvature from the plastic rotation. NZS 3101:2006 specifies the hinge lengths to be used as:

- For reversing hinges of walls and beams and uni-directional hinges constrained on one side, the smaller of, half the effective depth or  $0.2M^*/V^*$  but not less than one quarter of the effective depth.
- For uni-directional hinges unconstrained on either side the length is the effective depth.
- For shear deformation in a diagonally reinforced coupling beam, the clear span.

The effective plastic hinge length is an assumed length for the purposes of calculating the material strains. There are assumptions of plane sections remaining plane and uniform curvature over the length which are not valid, making the calculated material strain indicative rather than realistic. The reinforcing bars actually yield over a longer length, generally more than twice the effective length as seen in Figure 2.3. The provided detailing should extend past this length.

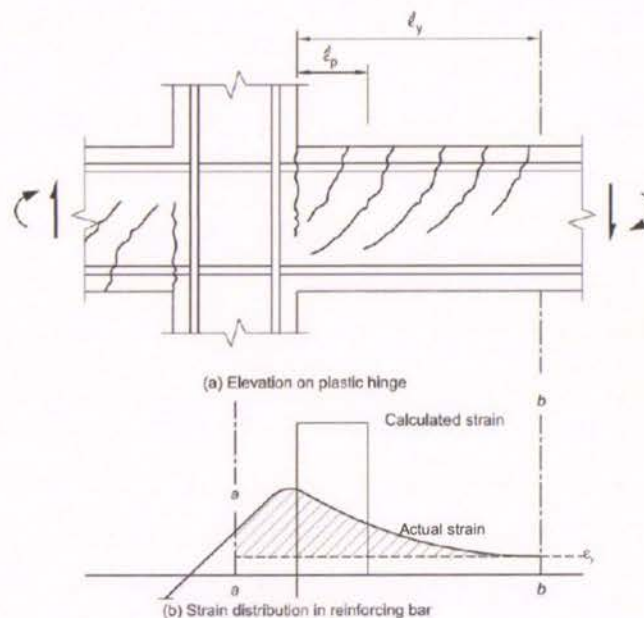


Figure 2.3-Strain distribution in hinge region (NZS 3101:2006)

For uni-directional plastic regions in nominally ductile beams and walls limiting material strains are given as the smaller of:  $\frac{0.004}{c}$  or  $\frac{0.018}{(d-c)}$ , where 0.004 is a limiting compression



strain in concrete and 0.018 is a limiting tensile strain in the longitudinal reinforcement. For reversing nominally ductile plastic regions the values are taken as 60% of the above. The material strain limits for nominally ductile columns are the same as those for limited ductile columns. Table C2.2 is included in the appendix of NZS3101:2006, which provides limits in terms of the first yield for nominally ductile uni-directional plastic hinges in beams.

Limiting curvatures for limited ductile and ductile plastic regions are provided in Table 2.4 of the concrete code. The curvatures limits for these hinge regions are given in terms of the nominal curvature corresponding to first yield of the reinforcing bars:  $\varphi_y = \frac{\varepsilon_y}{(d-c)}$ . As the curvature at first yield increases with the yield stress of reinforcement it is necessary to multiply the limiting values by a yield strength factor,  $\alpha_{fy}$ , to prevent excessive concrete strains for higher reinforcing grades, where  $\alpha_{fy} = \frac{400}{f_y}$ . This provision ensures that the ultimate curvature does not increase for  $f_y > 400\text{MPa}$ ; a phenomenon observed in tests.

Detailing specifications are given for all member types in the main text of each component based chapter in the material standard. An additional part of each chapter modifies the detailing requirements for beams designed for ductility greater than nominally ductile plastic region. Both ductile and limited ductile specifications are included within this additional section. The same principle applies for columns, walls and beam-column joints. The limits that determine the detailing on beam column joints is the type of members framing into the joint. If limited ductile or ductile members frame into a joint then the additional requirements for seismic effects must be met. Tables summarising the different design requirements are provided in the commentary of the standard. For nominally ductile structures where the likely mechanism that will form if the design forces are exceeded is not permissible by the code, any nominally ductile plastic regions within the structure are not exempt from the additional seismic requirements.

Common areas that differentiate between the different detailing classifications are:

- Restrictions on reinforcement ratio
- Anti-buckling transverse reinforcement
- Maximum stirrup spacing

## 2.2. MOTIVATION

### Material strains and their relevance to seismic design (Fenwick and Dhakal, 2007 a)

Fenwick and Dhakal reviewed the standing of the New Zealand design standards relating to reinforced concrete members. The emphasis of the review focussed around the requirement for detailing based upon the expected material strains in individual plastic regions introduced into the loadings standard (NZS 1170.5:2004) and its incorporation in the latest revision of the concrete standard (NZS 3101:2006). Comments over and above what has already been covered in the previous section include; the magnitude of deformation without strength degradation is dependent on the detailing (confinement, anti-buckling and portion of shear resisted by transverse steel). Other factors are the hinge type and the loading history. This new approach is incorporated because of the inadequacies of the structural ductility factor to indicate the deformations of individual plastic regions. Fenwick and Dhakal illustrate this inadequacy using the two walls previously described in Figure 1.1.

Having reviewed the code standing; Fenwick and Dhakal provide a recommended method for calculating the plastic rotations, similar to that used in NZS 1170.5:2004, but without allowing for the additional calculations needed to calculate the rotations of uni-directional plastic hinges. The ultimate inter-storey displacements are obtained from time history analysis results or the appropriately scaled elastic analysis predictions. This total displacement consists of elastic and plastic components, where the elastic component can be conservatively taken from a first mode or equivalent static analysis. Alternatively, a less conservative value for the elastic component is found by scaling the elastic value in the above analysis by the ratio of average design flexural strength of the primary plastic regions in the story under consideration to the corresponding average value of seismic design moments. The plastic component is simply the difference between the total displacement and the elastic component. The rotation of the columns can then be taken as:

$$\theta_c = 0.5 \left( \frac{\delta_{i,p}}{h_i} + \frac{\delta_{i-1,p}}{h_{i-1}} \right) \quad \text{Equation 3}$$

Where:  $\theta_c$  is the column rotation,

$\delta_{i,p}$  is the inter-storey deflection of the storey if interest,

$\delta_{i-1,p}$  is the inter-storey deflection of the storey below

$h_i$  is the inter-storey height and  $h_{i-1}$  is the inter-storey height of the storey below



Then the plastic rotation ( $\theta_p$ ) is:

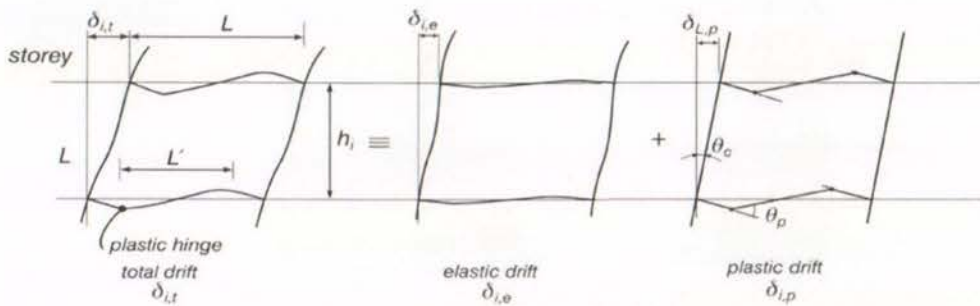
$$\theta_p = \frac{\theta_c L}{L'}$$

Equation 4

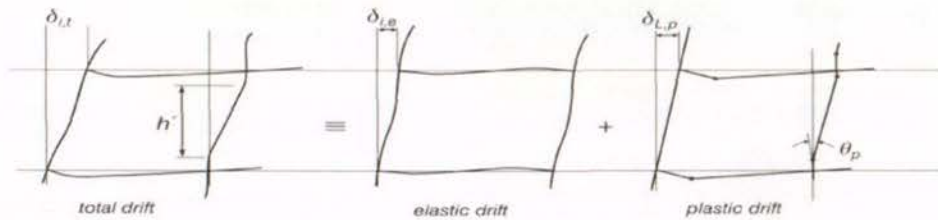
Where:  $L$  is the distance between column centrelines

$L'$  is the distance between the centres of the effective hinge lengths

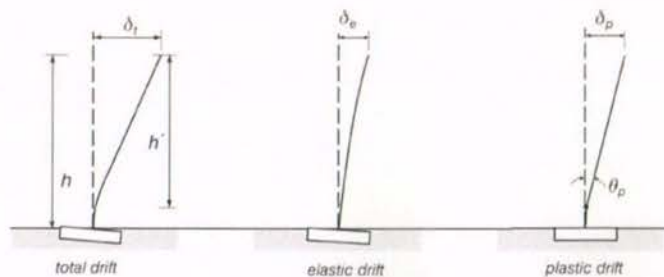
For walls the plastic rotation simply the plastic displacement at the top of the wall divided by the distance between the centre of the hinge and the top of the wall. The methods used for calculating the rotations in beams, columns and walls are further illustrated in Figure 2.4.



(a) Plastic hinge rotation in beams



(b) Plastic hinge rotation in a column



(c) Plastic hinge rotation in a wall

Figure 2.4-Calculation of plastic hinge rotations (Fenwick and Dhakal, 2007 a)



The ultimate curvature ( $\phi_{ult}$ ) is then found by dividing the plastic rotation by the effective plastic hinge length ( $L_{eff}$ ) and adding the curvature associated with the first significant yield in the plastic region ( $\phi_y$ ).

$$\phi_{ult} = \frac{\theta_p}{L_{eff}} + \phi_y \quad \text{Equation 5}$$

The curvatures calculated by this process are only indicative curvatures used to ensure that the maximum values for given detailing levels are not exceeded. As such Fenwick and Dhakal suggest some conservative short cuts available to designers to simplify the process.

- Checking curvatures only for beams in the storey with the highest inter-storey drift and applying the detailing across a range of storeys.
- Assuming the column rotation due to plastic deformation is equal to the drift in the storey with the maximum inter-storey drift.
- Assuming the elastic drift component is negligible.

As mentioned earlier, some of these assumptions can be very conservative, especially for nominally ductile structures, possibly making meeting of curvature limits difficult using this simplified method.

#### **Material strain limits for seismic design of concrete structures (Fenwick and Dhakal, 2007 b)**

The second paper by Fenwick and Dhakal makes recommendations on the material strain limits to be included in the concrete design code, NZS 3101:2006. Because it is difficult to calculate realistic strains in reinforced concrete hinges under cyclic loading, curvatures are used to define the detailing limits. The maximum curvatures were found from 37 beams, 25 columns and 36 walls with different detailing. The curvature corresponded to the maximum displacement sustained when the lateral force dropped to 80% of the theoretical strength. The limits are intended to satisfy the ultimate limit state and the maximum credible event design levels. Usually the displacements of a maximum credible earthquake are approximately 1.8 times the displacements of the ultimate limit state event.

A process for determining the plastic curvatures from the test results is described in the paper. The process uses an assumption that all the inelastic deformation arises from curvature in the effective hinge length.

1. The detailing category of the plastic region was assessed (i.e. nominally ductile, limited ductile or ductile), some members did not qualify for any category.
2. Extrapolating from the displacement at 75% of the theoretical strength to the theoretical member strength gives the ductility one displacement,  $\delta_e$
3. The average of the maximum positive and negative displacements before failure occurred is calculated.
4. Many tests used set displacement cycles, meaning larger displacements could have been sustained before failure. Thus the average maximum displacement was multiplied by the factor  $1.05^{(n-1)}$  where  $n$  is the number of times the positive and negative peaks were sustained in the displacement cycles being considered before the load dropped below 80% of the theoretical value.
5. The plastic curvature is then calculated from:

$$\varphi_p = \frac{(0.5(\delta_{max}^+ - \delta_{max}^-)^{n-1}) - \delta_e}{\left(\frac{M}{V} - L_{eff}\right)L_{eff}} \quad \text{Equation 6}$$

Where:  $\varphi_p$  is the plastic curvature,

$\delta_{max}^+$  is the maximum positive displacement sustained,

$\delta_{min}^+$  is the minimum negative displacement sustained,

$\delta_e$  is the elastic component of displacement,

$M$  is the moment at the column face,

$V$  is the shear demand,

$L_{eff}$  is the effective plastic hinge length.

Strain limits are proposed by Fenwick and Dhakal for nominally ductile plastic regions. These correspond to a maximum compressive strain of 0.004 in concrete and a maximum tensile strain of 0.016 in reinforcing bars. Because uni-directional plastic hinges can sustain greater deformation than reversing plastic hinges (Fenwick and Davidson, 1987) these strain values are reduced to 60% for reversing plastic hinges.

For limited ductile and ductile plastic regions the material strain limits are specified in terms of the curvature corresponding to the initiation of significant inelastic deformation. As suggested by Priestley and Kowalsky (2000), this indicative elastic curvature limit is estimated as the product of a factor and the yield strain divided by the member depth. The



factor varies depending on type of member but is approximately 2 such that  $\phi_y = \frac{2\varepsilon_y}{h}$ .

Because the reinforcing grade changes the curvature at yield but does not significantly change the maximum curvature achieved, an additional factor ( $K_y$ ) is applied.  $K_y$  is unity below 425 MPa and  $= \frac{425}{f_y}$  for yield stress above 425 MPa. The results of the investigation

and the recommended material strain limits are described in Chapter 7.

As mentioned earlier, the limiting material strains are intended to meet the ultimate limit state with a high margin of safety and the maximum credible event with an adequate margin of safety. Fenwick and Dhakal give two key reasons for the ability of the material strain limits to meet the demands of a maximum credible event. The first is that the limits are based on consecutive positive and negative displacements of nearly the same value; however, in an earthquake the peak displacement is only sustained in one direction. The second reason is that in practice a drop in strength of a single hinge region results in a redistribution of forces to other plastic regions. Thus it is the average strength and deformation capacities of the hinges that control the structural resistance.

These two papers highlight several inadequacies with the material strain limits currently in the New Zealand standards. There is a complete absence of experimental data for beams falling into the nominally ductile detailing category. It is this point that this project centres around. Other deficiencies highlighted are the lack of limited ductile beam data and that there are very few tests on uni-directional plastic regions. As with any recommendations based upon experimental data, the greater the data range the greater the confidence in the recommendations and these papers indicate that a much greater level of confidence could still be achieved with the inclusion of more experimental results.



### 2.3. UNI-DIRECTIONAL PLASTIC HINGES

The formation of a plastic hinge has a significant impact on the material strain (curvature) demand and the hinges capacity to sustain that demand. Two different forms of plastic hinge have been identified (Fenwick and Davidson, 1987), namely, uni-directional and reversing plastic hinges. The form of hinge is dependent on the ratio of the gravity induced moments to the seismic induced moments in the span of interest.

When the gravity moments are small compared to the seismic moments, reversing plastic hinges form at the column faces. These hinges sustain both positive and negative inelastic rotations. The maximum rotation sustained by the plastic hinge is related to the maximum rotation of the columns during the earthquake.

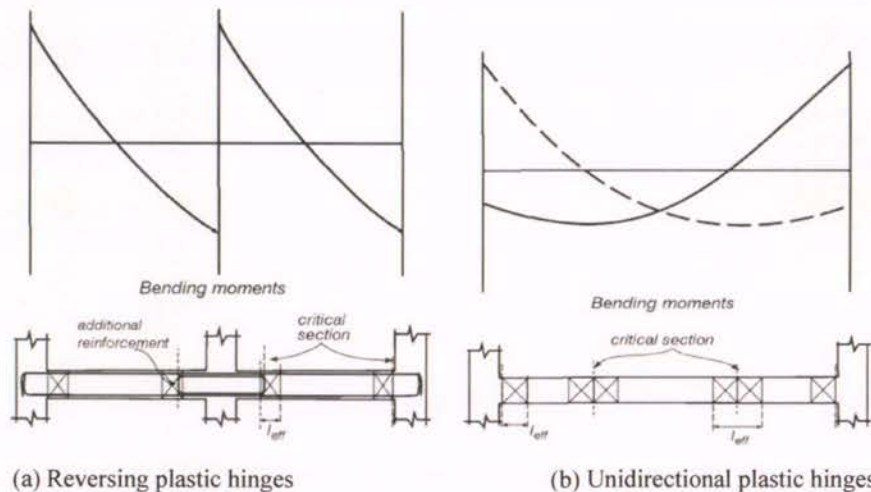


Figure 2.5-Effective plastic hinge lengths for reversing and unidirectional plastic hinges (Fenwick and Dhakal, 2007 b)

When the gravity induced moments exceed a critical level in relation to the seismic moments (or due to different reinforcement distributions) hinges will form in the span away from the column faces which sustain only positive inelastic rotations. Hinges still form at the column faces but these only sustain negative inelastic rotations. In these uni-directional hinges the total rotation sustained depends on the sum of the inelastic rotations arising from each inelastic displacement during the seismic event. This means that the hinge rotations accumulate and the vertical beam deflection will increase during the earthquake. No decrease of these deflections is possible (Fenwick, Dely an Davidson, 1999). The rotations sustained are not related to the structural displacement ductility, instead they are related to the energy required to be dissipated during the seismic event by yielding of the reinforcement.

Megget and Fenwick (1989) constructed a reinforced concrete portal frame to study the response of multi-storey buildings to cyclic lateral loading. The frame was loaded in the span with two constant point loads to represent the gravity loads and proportioned such that uni-directional hinges would form. Key observations to come from the test of the portal frame were:

- Sagging of the beam

- Elongation of the beam

- Redistribution of moments due to hinge formation

A series of time history analyses was undertaken by Fenwick, Dely and Davidson (1999) to assess the magnitude of the inelastic rotation sustained by both reversing and uni-directional plastic hinges. The positive moment plastic hinges form at locations of low shear, and as a result spread over a relatively long length. Their analyses indicated that the strains in the longitudinal reinforcement within the beam hinges are one third to one fifth of those sustained in the column face hinges carrying the same rotation. Other important results to come out of the analyses were that the rotation sustained by uni-directional plastic hinges was 2.5 to 4.0 times that of a similar reversing plastic hinge.

The mechanism that causes uni-directional hinges to form is well understood. Although it is not as well researched as reversing plastic hinges, the expected rotational demand has been examined. However the level of rotation that a uni-directional plastic hinge can sustain has not been well quantified, although it is anticipated that an increase in capacity will be seen compared with reversing plastic hinges (Fenwick and Davidson, 1987).



## 2.4. STRAIN PENETRATION

The pullout of longitudinal reinforcing bars at the interface between a structural member and its supporting element has a significant effect on the total deformation sustained by the member. Strain penetration results from the gradual transfer of longitudinal bar forces into the surrounding concrete. The loaded end of the bar experiences slip at the interface due to an accumulative strain difference between the bar and the concrete. This causes a crack to form at the interface and an overall member rotation that can contribute up to 35% of displacement in flexural members (Zhao and Sritharan, 2007).

The magnitude of the slip is dependent on several parameters, concrete strength, transverse reinforcement, bar diameter, bar surface properties, the bond length and the member geometries. When yielding of the reinforcement entering the support element occurs, the number of parameters influencing the magnitude of slip increases to include the yield stress, the length of the yield plateau and the strain hardening behaviour (Bonacci, 1994). Analyses made by Bonacci found that a slip of 1mm at the support interface related to approximately 0.2% drift, with the total slip accounting for approximately 10% of the total displacement for a given structural arrangement.

A series of experiments carried out by Saatcioglu et al. (1992) on columns under axial load found that the effect of yield penetration was significant. The bond slip contributed to 50% of the total displacement of the columns at yield. The slip continued to increase during the inelastic range, contributing between 30 and 40 percent of the total deflection. The yield of reinforcement in the supporting element in compression had negligible influence on the total displacement.

These tests show the significant contribution that bond slip can have on the total member deformation. Attempts have been made to model the effects of bond slip under cyclic loading. These range from establishing the local bond stress versus slip relationship to quantifying the bond slip effects at the member level. Many of these methods are very computationally expensive and difficult to implement (Sritharan, Priestley and Seible, 2007).

In the tests conducted in this project, adequate anchorage length is provided so anchorage failure is not expected. However, these specimens are still likely to induce significant slip due



to strain and yield penetration into the support block. This will result in an overestimation of the material strains (curvatures) if strain penetration is not considered when calculating limits following the methodology described in Section 2.2. The difficulty and expense involved in implementing strain penetration modelling in seismic analyses means that this effect will often be absent from the deflection results calculated by designers. The overall effect is inflated material strain limits that are being satisfied by underestimated analysis results. In order to conservatively limit the effect of strain and yield penetration it was decided to weld additional reinforcing to the longitudinal bars within the support block, as described in Chapter 3.

### 3. EXPERIMENTAL DETAILS

#### 3.1. OBJECTIVE

There is a lack of information in the literature on the performance of beams with nominally ductile detailing subjected to inelastic seismic loading. To enable design criteria to be established for nominally ductile plastic regions a series of beams detailed to fall into the nominally ductile category according to NZS 3101:2006 were built and tested. Details of the testing program are given in the remainder of this section.

#### 3.2. TEST ARRANGEMENT

The beams were supported as cantilevers and subjected to quasi-static loading via a single reversing hydraulic jack at the end of the beam. The general arrangement of the tests is shown in Figure 3.1.

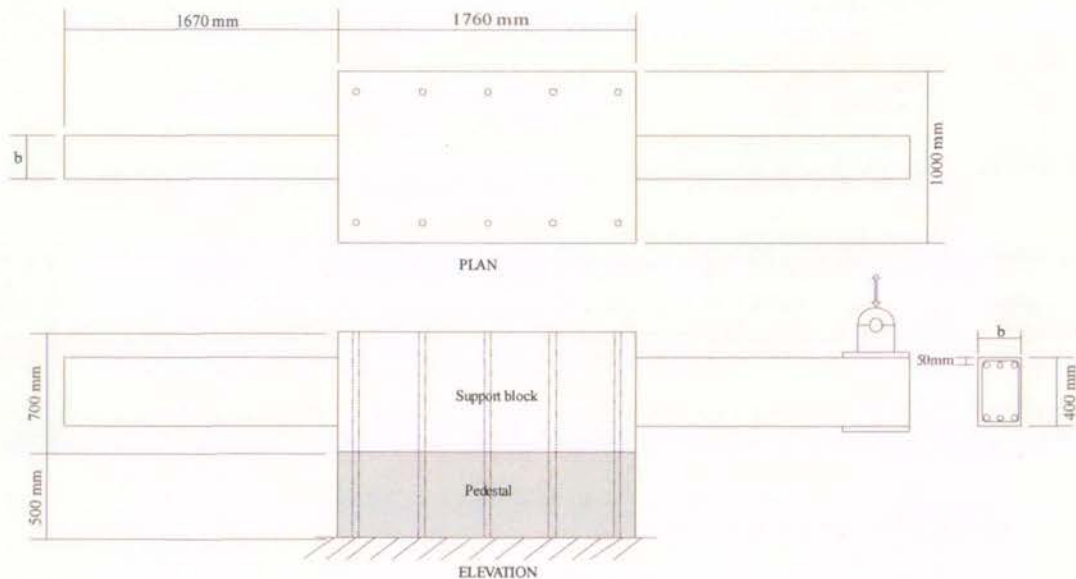


Figure 3.1-General test arrangement

Altogether, four test units were constructed. Each unit had a central support block (1760mm x 1020mm x 700mm) in the middle and two test beams of 1600mm length. The unit was mounted on a 500mm pedestal which provided clearance for the beam deflection and a suitable working height for testing. Each unit was secured by two rows of five 38mm diameter bolts passing through PVC ducting through the pedestal into the strong floor. The spacing of these bolts is 380 mm.

The test displacement was applied to the end of the beam by a reversing hydraulic jack mounted on a reaction frame above the beam. The jack was secured to the beam and frame by a one way pin connection as shown in Figure 3.2.

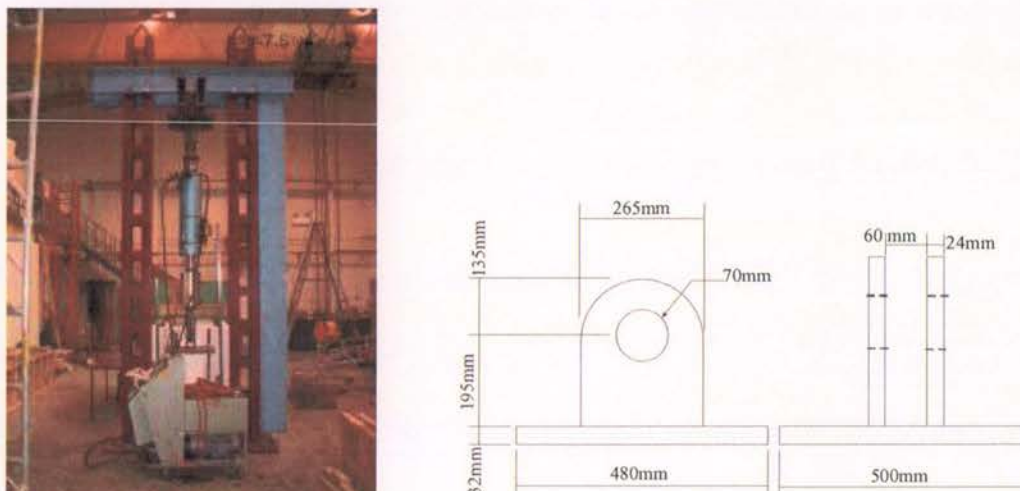


Figure 3.2-Loading actuator arrangement and loading plate

### 3.3. SECTION DESIGN

#### 3.3.1. Section Geometry

The beams were designed to meet the requirements of the design standard, NZS 3101:2006 for nominally ductile detailing. Each test was designed to examine the effect of varying one of the parameters which determine the detailing level. The cross section of six of the beams was 400mm deep by 250mm wide. For the seventh and eighth beams the width was extended to 410mm to accommodate a change in stirrup arrangement.

#### 3.3.2. Material Properties

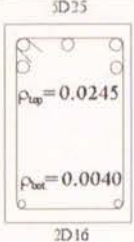
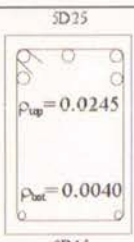
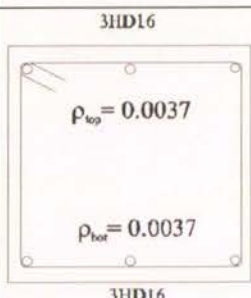
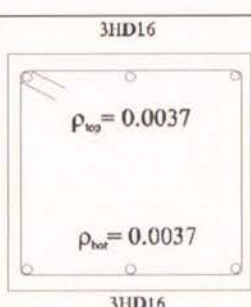
Only two grades of reinforcing steel are available in New Zealand, Grade 300 and Grade 500 steel. As the grade of reinforcement was expected to influence the ductility of reinforced concrete members, beams were constructed using both grades of reinforcement. With the high grade reinforcement the bar size was chosen to give a comparable strength to the beams with the lower grade reinforcement.



The grade of transverse reinforcement was expected to have little influence on the member ductility. Therefore, 500 Grade steel was used for the transverse reinforcement throughout all beams. Using the higher grade steel for transverse reinforcement also allowed for using larger stirrup spacing without compromising the shear strength. To allow comparable results between tests, a constant design concrete compressive strength of 30MPa was used. Table 3.1 summarises the design parameters of each test.

Table 3.1-Test beam properties

Beam	$f_y$ (MPa)	B (mm)	Transverse Reinforcement	Test type	Cross section
A1	300	250	2 legs HR10 @ 175mm C/C $\rho = 0.0036$	Reversing	
A2	300	250	2 legs HR10 @ 100mm C/C $\rho = 0.0063$	Reversing	
B1	500	250	2 legs HR10 @ 135mm C/C $\rho = 0.0047$	Reversing	
B2	500	250	2 legs HR10 @ 135mm C/C $\rho = 0.0047$	Uni-directional	

C1	300	250	2 legs HR10 @ 130mm C/C $\rho_l = 0.0048$	Reversing	
C2	300	250	2 legs HR10 @ 130mm C/C $\rho_l = 0.0048$	Uni-directional	
D1	500	400	2 legs HR10 @ 175mm C/C $\rho_l = 0.0036$	Reversing	
D2	500	400	2 legs HR10 @ 175mm C/C $\rho_l = 0.0036$	Uni-directional	

### 3.3.3. Yield Penetration

Because the longitudinal reinforcing bars from the beams runs into the central support block, yield of the longitudinal bars is likely to penetrate into the support block. Yield penetration occurs in all plastic hinges forming at a column face in real structures. However the level of the penetration varies depending on the geometric and mechanical properties of the beam and column as discussed in 2.4.

In this series of tests the objective is to obtain (conservative) limits for material strains. Yield penetration into the support or column increases the rotation and deflection of the beam. To

maintain the conservative nature of the results it was desirable to minimise yield penetration in this series of tests. The approach used was to weld two additional ten millimetre diameter round bars to all the longitudinal reinforcing bars as they passed through the support block.

The positioning and orientation of the additional bars is important. If the bars are positioned as shown in Figure 3.3, a large change in bending stiffness occurs at the interface creating excessively high bending stresses in the longitudinal bars. High deformation demand is placed on the longitudinal bars if the additional round bars terminate at the beam springing. To minimise this effect, the 10mm bars were terminated 50mm short of the beam springing and they were welded on the sides of the beam bars.

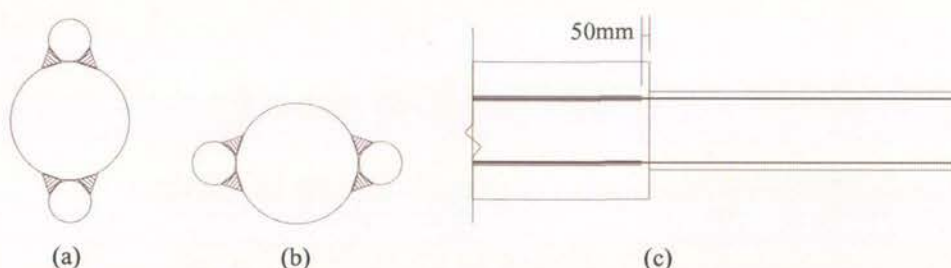


Figure 3.3-Orientation and termination of round bars welded to longitudinal reinforcing bars within support block

There is significant concern that welding of reinforcing bars detrimentally alters their performance, especially for Grade 500 reinforcing bars. The New Zealand standard for welding contains a section relating to the welding of reinforcing bars, NZS 1554.3. Section 4.11.6 relates to preheating of reinforcing and inter-run temperatures. For a given reinforcing grade, bar diameter, weld type (i.e. butt weld or other) and arc energy the minimum preheat temperature is given. For the parameters of this experimental program, a preheat temperature of approximately 50 degrees Celsius was indicated.

Section 8.3 of NZS 1554.3 specifies the requirements to be met when conducting tensile tests on welded reinforcing bar samples. The code requires that fracture shall occur outside the welded region. If the bar does fracture in the welded region then the minimum tensile strengths of Table 3.2 must be met.



Table 3.2-Minimum tensile strengths for test welds (NZS 1554.3:2007, draft)

AS/NZS Reinforcing Grade	Minimum tensile strength (MPa)
250N	270
300E	345
500L	515
500N	540

No allowance is made for fracture of Grade 500E reinforcing bar within the welded area.

The input of Dr John Smail, a senior lecturer in the mechanical engineering department of the University of Canterbury was sought. Dr Smail has been involved in research relating to the suitability of New Zealand reinforcing bars for welding. His recommendations were as follows:

- Use non or low-hydrogen electrodes.
- Preheat the reinforcing bar to approximately 150 degrees Celsius.
- Maintain the temperature after welding to allow the bar to cool slowly.

Tests were conducted on samples of both grades of reinforcement. Three configurations were used, namely, un-welded bar, bar with a length of round bar welded to it and bar with a stud welded to it. The test results showed that the stress-strain curves exhibited no loss of strength or ductility between the three different arrangements. Full results of the testing can be seen in Appendix A.

### 3.4. SPECIMEN CONSTRUCTION

The support block reinforcing was tied first while the additional bars were welded to the longitudinal bars to minimise the yield penetration. Once both were prepared, the longitudinal bars were passed through the support block cage and tied in position. Stirrups were placed on the beam bars, resulting in one complete cage per unit.

Formwork was constructed using 150mm by 50mm and 100mm by 50mm timber and 16mm plywood. The formwork was arranged as shown in Figure 3.4 to enable the unit to be cast in one pour.



Figure 3.4-Formwork construction

A polythene sheet was placed underneath the formwork. Silicone RTV was used to seal around the formwork to provide a water tight joint. Floor bolts were placed in the appropriate bolt holes and encased in PVC conduit. The conduit was secured by washer and nut to prevent any concrete leaks. Before casting the plywood was brushed with oil to reduce bond between timber and concrete. The steel cage was lowered into position into the formwork, with 30mm bar chairs placed below the support block and beam steel. Rubber tubing was placed over the studs welded to the longitudinal reinforcing to create a void and protect the thread. Figure 3.5 illustrates the void formed using the rubber tube around the stud.

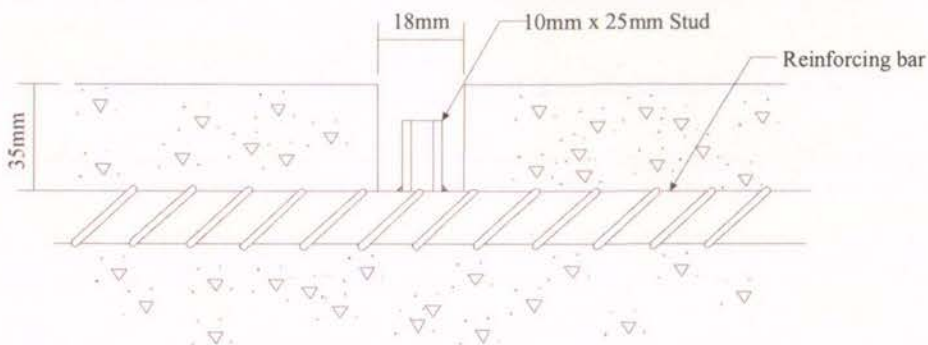


Figure 3.5-Stud welded to reinforcing bar with surrounding void

Two cubic metres of 30MPa concrete with 100mm slump and 13mm maximum aggregate size was ordered from Firth Concrete for each pour. The measured slumps were 100 mm, 180 mm, 160 mm and 160 mm for the four pours respectively. The concrete was placed directly from the truck and using wheel barrows into the formwork and vibrated with a 20mm poker vibrator. The beams were screeded, with final finishing done three to four hours after the pour. Figure 3.6 shows a photo from one of the concrete pours. Four 2.5 ton lifting eyes were placed into the setting concrete in each corner of the top surface of the support block. The



units were covered with dampened hessian mats and then with tarpaulins. The formwork was left on for the first two to three days to aid the curing process. After this the formwork was removed but the coverings were left on the units and test cylinders. After seven days, the first sets of concrete cylinders were tested. Provided these tests met specification, the curing covers were removed. If the cylinders did not meet their targeted strength, the covering was left on for a further week.



Figure 3.6-Pouring of concrete

Twelve concrete cylinders were cast during the pour, six of these being placed in the fog room. The remainder stayed with the specimen so that they had the same curing conditions, these cylinders were used to find the concrete strength on the day of testing.

The unit was lifted and placed on the pedestal. A layer of grout was placed between the pedestal and the support block. This served to eliminate the unlevel surfaces caused by casting directly onto the strong floor. The unit was secured by two rows of five 1.5inch bolts and nuts with washers. The beams were painted white to aid in crack identification. At this point the specimen was ready for the instrumentation to be added.

### 3.5. INSTRUMENTATION

Three main forms of measurement were obtained during the beam tests, namely, deformations of the different segments of the beam, the overall displacement and the applied load. A grid of linear potentiometers was placed across and beyond the potential plastic hinge region to gather detailed information on the deformations within the plastic hinge region. A



diagram and photo of the main potentiometer layout are illustrated in Figure 3.7 and Figure 3.8.

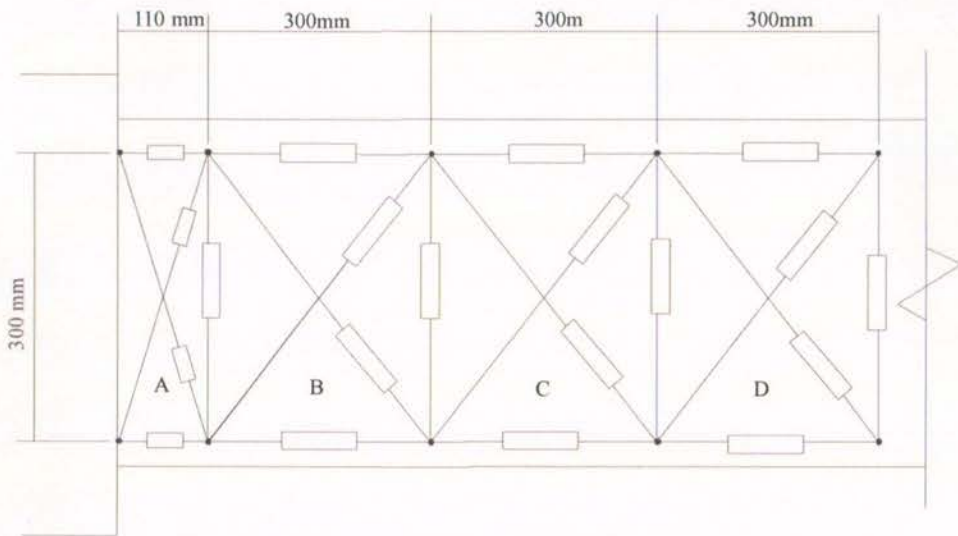


Figure 3.7-Dimensions of linear potentiometer grid



Figure 3.8-Linear potentiometer grid in place

The layout of the linear potentiometers was designed to allow the shear, flexure and elongation in each block to be measured. These potentiometers were attached to the studs welded to the main reinforcing steel via threaded rod and steel plate. Aluminium angles attached to threaded bar epoxied into the concrete were used to secure the potentiometers at the beam to support block interface.

Linear potentiometers were placed across the interface between the unit and the pedestal and between the pedestal and the strong floor, to enable the rotation (rocking) across these surfaces to be measured. One more linear potentiometer was placed at the far end of the unit to help in assessing the overall rigid rotation. The vertical displacement was measured by rotary potentiometers, one at mid-span and another in line with the loading ram. This second potentiometer also served as the hydraulic jack controller. One potentiometer was used to

measure the displacement of the jack. The placement of these potentiometers is shown in Figure 3.9.

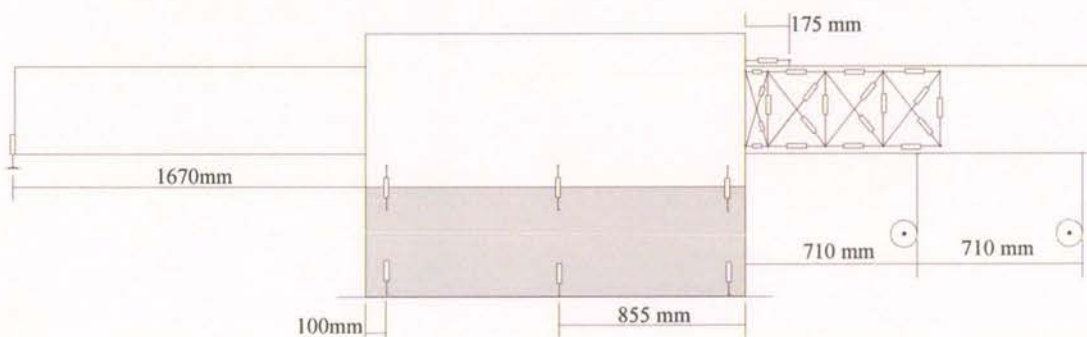


Figure 3.9-Layout of all potentiometers

The load was measured by a load cell with a 1000kN capacity. The load cell was calibrated prior to testing using an Avery test machine.

### 3.6. TEST PROCEDURE

The test consisted of two phases. Initially the beams were loaded to 75% of their theoretical yield load to assess the stiffness of the member and to check the instrumentation. Two full cycles were applied at this load and this phase was repeated two or three times if instrumentation needed altering. During the second phase the beams were loaded under deflection control. The chosen load protocol was to increase the end displacement by 0.5% of the beam length (drift) every two cycles. For the reversing plastic hinge tests, the drift was increased in both directions. While for the uni-directional hinge tests the drift was increased in one direction and returned to the displacement corresponding to 75% of yield force in the other direction. An illustration of the load protocol for both test types is shown in Figure 3.10.

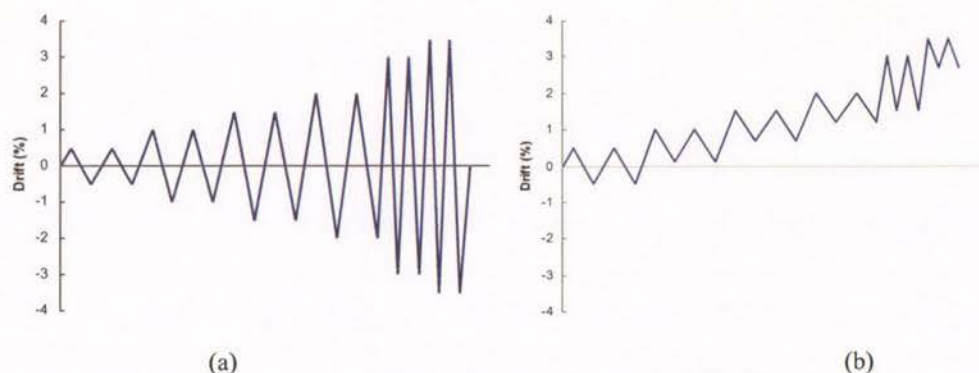


Figure 3.10-Illustrative loading protocol for: (a) reversing plastic hinge and (b) uni-directional hinge

## 4. EXPERIMENTAL RESULTS

This chapter describes the experimental results of the eight tested units. The results include propagation of cracks, load displacement behaviour, contributions of flexure and shear deformation and beam elongation. In addition, it also presents the results of standard materials (concrete cylinders and rebar) tests.

### 4.1. MATERIAL PROPERTIES

#### 4.1.1. Concrete Properties

For each concrete pour, twelve test cylinders were cast. Six of these were stored in the fog room and the remainder with the test units. The cylinders stored in the fog room were used for 7 day and 28 day compression tests while the cylinders kept with the test units were used to determine the strength on day of testing. Full results of the compression tests are included in Appendix A while Table 4.1 provides the average concrete strength of the cylinders tested on the day of the test.

Table 4.1-Average concrete strengths on day of test

Unit	Test	Concrete Strength (MPa)
A	1	41.5
	2	42.2
B	1	20.7
	2	21.8
C	1	27.4
	2	27.4
D	1	25.2
	2	26.0

Although the specimens were designed assuming a concrete strength of 30MPa, and 30 MPa concrete was ordered for all pours, the actual strength of the concrete delivered varied between 21MPa (Unit B) and 42MPa (Unit A). Note that the concrete strength will influence the behaviour of the specimens and this variation in concrete strength needs to be considered while comparing different specimens.



#### 4.1.2. Steel Properties

Tension tests were performed on pieces of bar cut from the longitudinal and transverse steel of all units. One specimen was tested for each set of bars. The tests were carried out in the Avery testing machine using an extensometer clipped onto the test sample. Figure 4.1 shows a typical stress strain curve with the yield stress, maximum stress, strain at onset of strain hardening and strain at maximum stress indicated. These values are listed in Table 4.2. Curves of each individual test are included in Appendix A. The extensometer was removed when the load decreased to 99% of the peak value to prevent damage as the bars failed. Thus the full range of the stress-strain curves was not able to be plotted. The stirrup sample from Unit C gave abnormal results, with the stress-strain curve not showing a clear yield point. The stress-strain curve having a smooth transition without a clear yield point is a unique feature of cold-formed high strength reinforcement. A second sample from a different stirrup of the same set again confirmed the behaviour. It was not anticipated for this to adversely affect behaviour of the tested specimen.

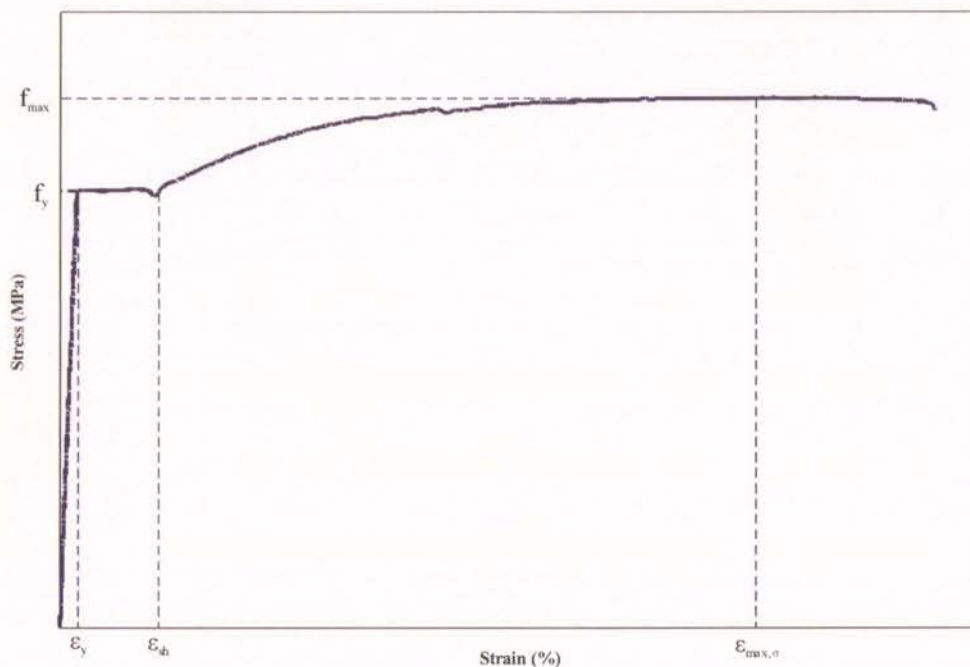


Figure 4.1-Typical steel stress-strain curves

Table 4.2-Steel properties

Unit	Diameter (mm)	Grade	$f_y$ (MPa)	$f_{max}$ (MPa)	$\epsilon_{sh}$ (%)	$\epsilon_{max \sigma}$ (%)
<b>A</b>	25	300	350	525	1.75	13.80
	10	500	445	530	0.82	8.38
<b>B</b>	25	500	605	750	1.74	12.03
	12	500	553	723	1.10	10.46
	10	500	575	706	1.92	11.24
<b>C</b>	25	300	350	520	1.96	18.12
	16	300	303	445	2.39	17.52
	10	500	570	711	N/A	7.51
<b>D</b>	16	500	570	689	1.97	11.97
	10	500	560	694	1.82	12.76

## 4.2. OBSERVED TEST BEHAVIOUR

### 4.2.1. Unit A

#### 4.2.1.1. General details

The cross section of beam A1 and A2 was 250mm wide by 400mm deep. The longitudinal reinforcement consisted of three 25mm diameter Grade 300 bars at the top and bottom. The transverse reinforcement consisted of stirrups with two legs of 10mm Grade 500 bars spaced at 175mm centres for beam A1 and 100mm for A2. This beam was tested under reversed cyclic loading.

#### 4.2.1.2. Test A1

During the first (load controlled) phase of testing flexural cracks formed along the member. The cracks were spaced at approximately 175mm centres, close to the location of the transverse reinforcement. These were hairline cracks and extended from top/bottom to the mid-height of the beam. These cracks did not grow in length during the repeated cycles. During the second (displacement controlled) phase of the test, the beam end displacement was increased in steps equal to 0.5% of the beam length. The first displacement cycle of this phase had an amplitude that resulted in a drift of 0.5%. At this stage no new cracks formed but the flexural cracks extended beyond the mid-depth of the beam. The cracks also started to become inclined, as seen in Figure 4.2.

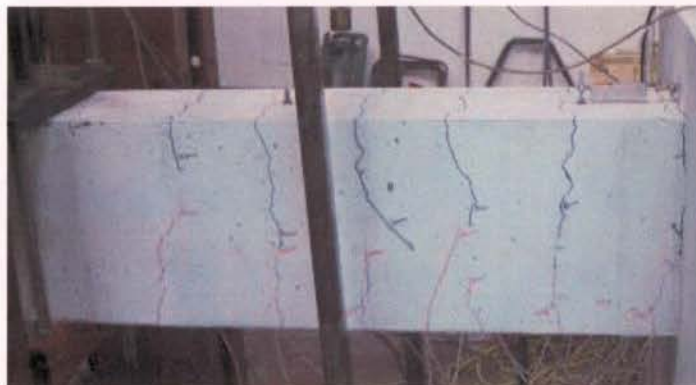


Figure 4.2-Crack pattern after first complete cycle at 0.5% drift (A1)

The load-deflection relationship (shown later in Figure 4.9) shows that the first yield in the positive direction occurred at 0.6% drift (i.e. 8.5mm displacement) in the first 1.0% drift cycle. At this stage two flexural cracks, approximately 1.5mm and 1.0mm in width, had opened at the beam springing and approximately 180mm along the beam respectively. These



cracks remained open to 1.0mm and 0.8mm respectively when the load was removed after two complete cycles of 1.0% drift. At this point, the diagonal tension cracks could easily be distinguished, as shown in Figure 4.3. A single crack was also seen on the top of the support block, as shown in Figure 4.4. This crack grew in length by 10mm and 15mm over the next two displacement cycles, after which it remained stable. Throughout the test, the width of this crack was small, approximately 0.2mm. This crack was a common feature of all tests.

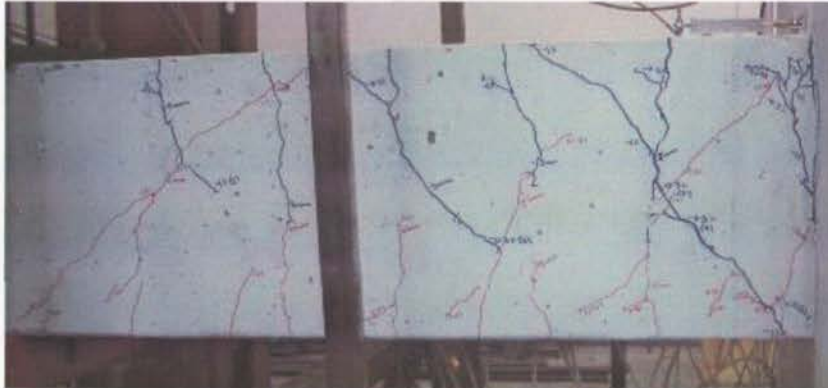


Figure 4.3-Cracks after two cycles to 1.0% drift (A1)



Figure 4.4-Cracking of support block after first cycle of 1.0% drift (A1)

Spalling of concrete first occurred during the 2.0% drift cycles. At this stage of the test the majority of the deformation was concentrated at the intersecting diagonal tension cracks located immediately adjacent to the beam springing and the two flexural cracks previously mentioned. The main diagonal tension crack opened to 5mm and the two flexural cracks at the beam springing and at 180mm away from the springing opened to 2.4mm. These cracks are clearly visible in Figure 4.5.

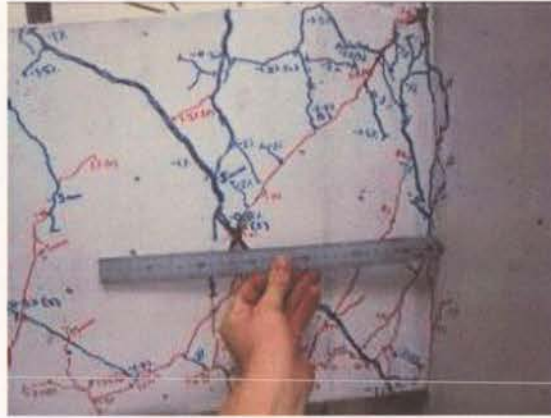


Figure 4.5-Cracking in hinge region at 2.0% drift (A1)

The diagonal tension cracks widened to 9mm after the first 3.0% drift cycle. The width of this crack made the stirrups and longitudinal bars visible, as seen in Figure 4.6. Significant spalling had started to occur from the underside of the beam and pieces of concrete were sitting loosely on the side and top of the beam.

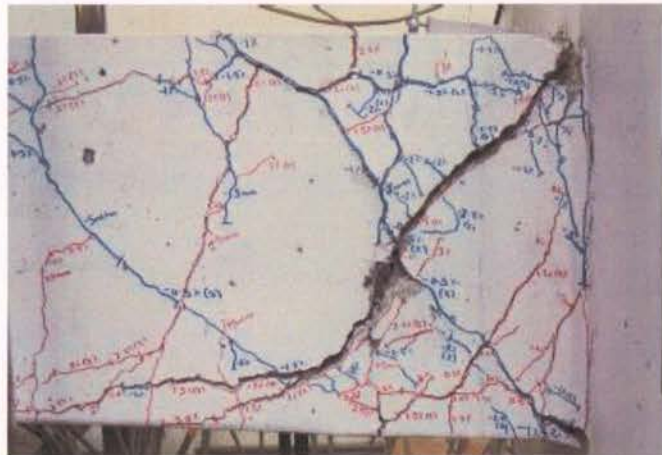


Figure 4.6-Transverse reinforcement visible through diagonal tension crack at 3.0% drift (A1)

During the second 3.5% drift cycle enough spalling had occurred so that the longitudinal reinforcement could be seen to have buckled in compression, as shown in Figure 4.7. The concrete and steel continued to degrade such that the strength of the member rapidly decreased as seen on the load deflection relationship shown in Figure 4.9.



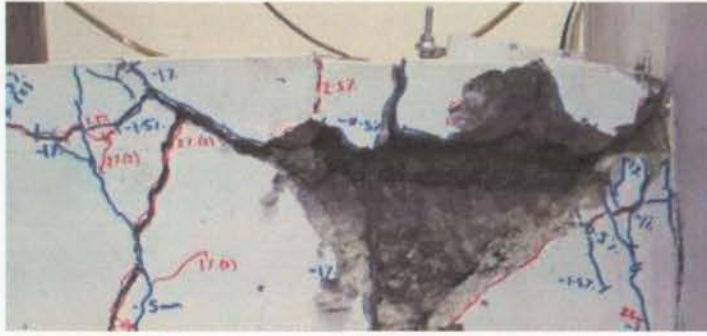


Figure 4.7-Extensive spalling and reinforcement buckling visible at 3.5% drift (A1)

The test was stopped after the second 4.0% drift cycle when the strength had degraded to 30% of the maximum load applied. There was extensive spalling of concrete which was removed to show the extent of the damaged region (see Figure 4.8). The deformation of the longitudinal bars is also visible.



Figure 4.8-End of test after removing spalled concrete showing deformation of reinforcement (A1)

The potentiometers placed along the length of the beam allowed the flexural and shear components of the deflection to be calculated as outlined in Appendix B. The shear deformation, flexural deformation and the combined total deformation versus the applied load curves for Test A1 are presented in Figure 4.9 through Figure 4.12. Also included is a plot showing the contribution of shear and flexure to the total displacement at peak drifts, allowing the measurement error to be estimated. The contribution of the rocking of the entire unit was measured but was found to be negligible so is not shown on the plots. Shear and flexural displacements could not be calculated once appreciable buckling occurred in the longitudinal reinforcement. The total displacement can be shown for the entire test as it was measured directly at the load application point. The dotted straight line in the following figures is due to an error with the instrumentation that resulted in no records over that half



cycle. The displacement cycles have been labelled with lower case letters with a cycle number; e.g. the first cycle at 0.5% drift is “a1”, the second cycle at 2.0% drift is “d2”.

The load deflection curve of beam A1 and the theoretical strength are shown in Figure 4.9. The theoretical strength is calculated using basic ultimate section analysis. The experimental result is in good agreement with the theoretical strength. The initial stiffness can be estimated by connecting the point at 75% of the theoretical strength to the origin. The stiffness of beam A1 was estimated to be 13.2kN/mm. The yielding of reinforcement during the 1.0% drift cycles (as previously mentioned) is clear. A decrease in beam stiffness with an increase in the applied displacement is obvious in the figure. A slight decrease in load capacity occurred in the first 3.0% drift cycle. On the second 3.0% cycle the decrease in load capacity became more significant; this is associated with the buckling of reinforcement mentioned above. The stiffness decreased dramatically by the end of the test at 4.0% drift. The most obvious feature of this hysteresis loop is the large pinching behaviour. This is due to the beam slipping along the diagonal shear cracks during unloading and reloading.

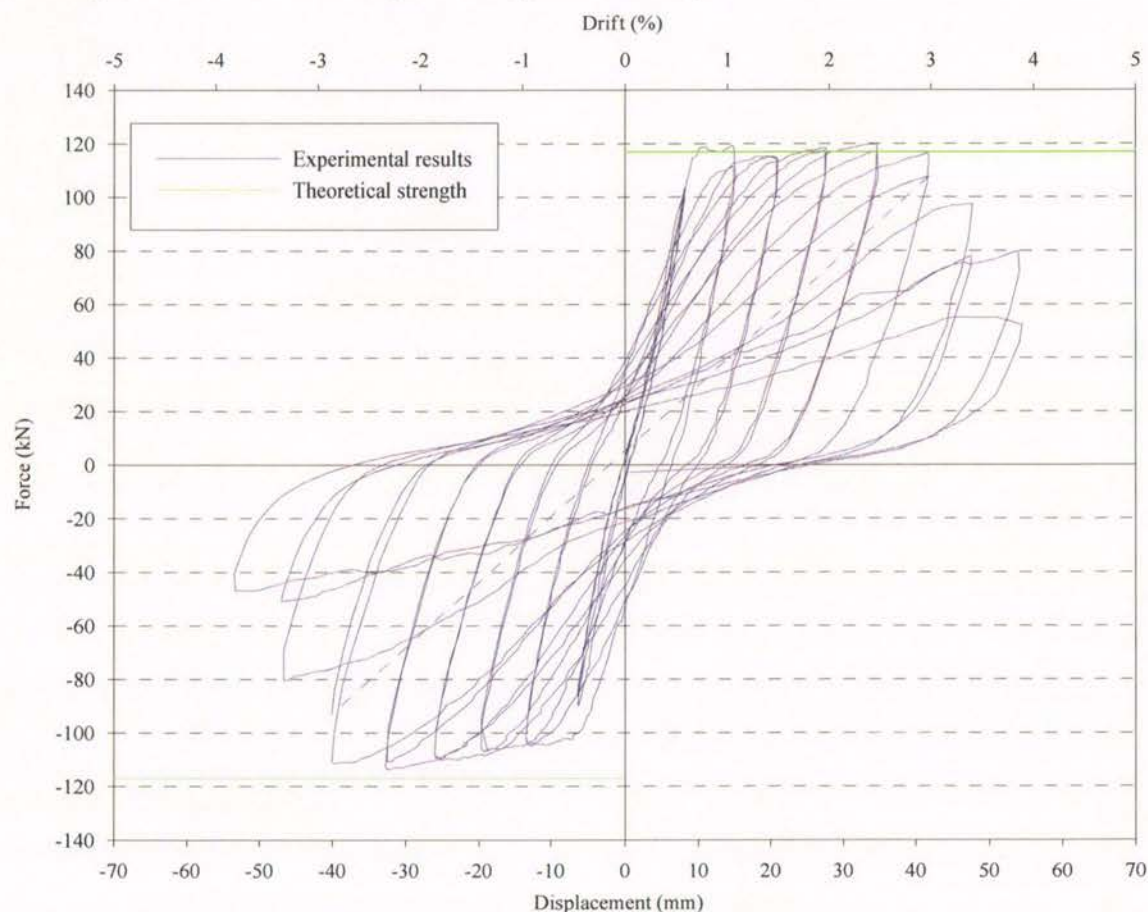


Figure 4.9-Load displacement relationship response of specimen A1 as to 4.0% drift

Figure 4.10 shows the breakdown of the total applied displacement into shear and flexural deformations. The rocking of the entire tests unit is included in the calculation of the total displacement but is very small and thus not shown in the figure. It is obvious from the figure that the total end displacement is dominated by the flexural component. The percentage contribution of shear deformation increases as the applied displacement is increased. In general, there is a decrease in the flexural displacement in the second cycle compared to the first cycle of the same displacement level.

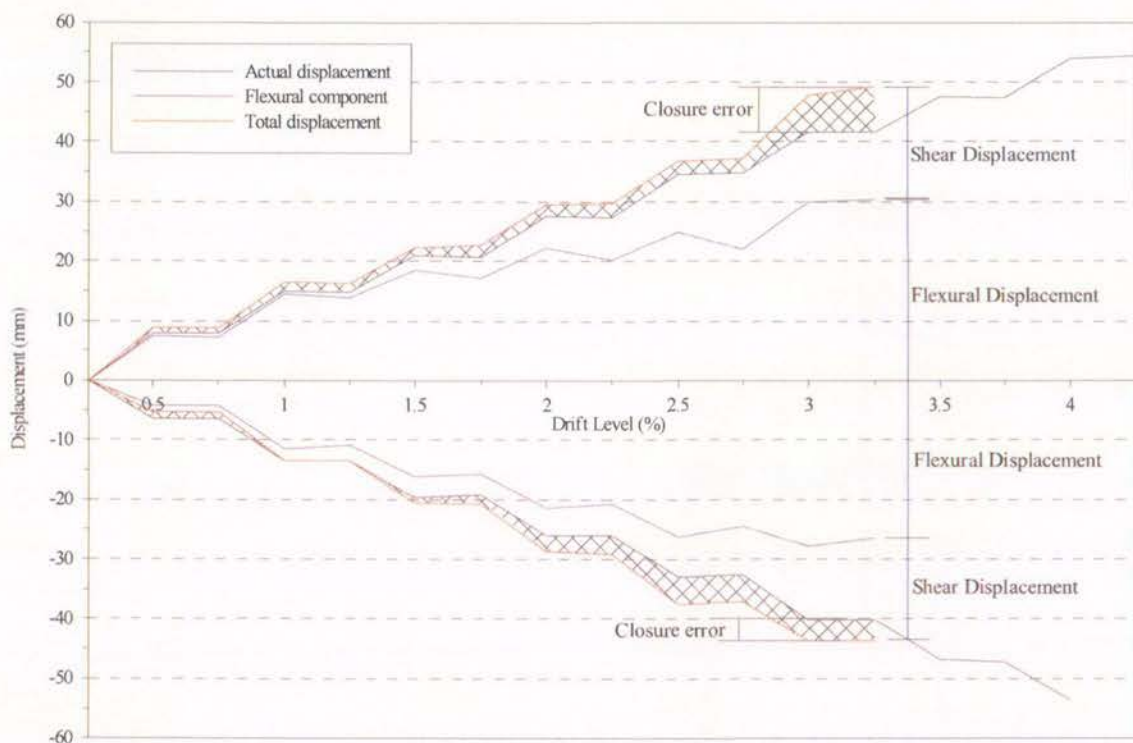


Figure 4.10-Contribution of shear and flexure to the total displacement at the peaks of the loading cycle for beam A1

Figure 4.11 plots the applied force against the flexural component of the total displacement. A slight decrease in flexural displacement in the second cycle at the same displacement level can be seen. A slight pinching to the flexural loops is exhibited, the cause of this behaviour could not be ascertained.

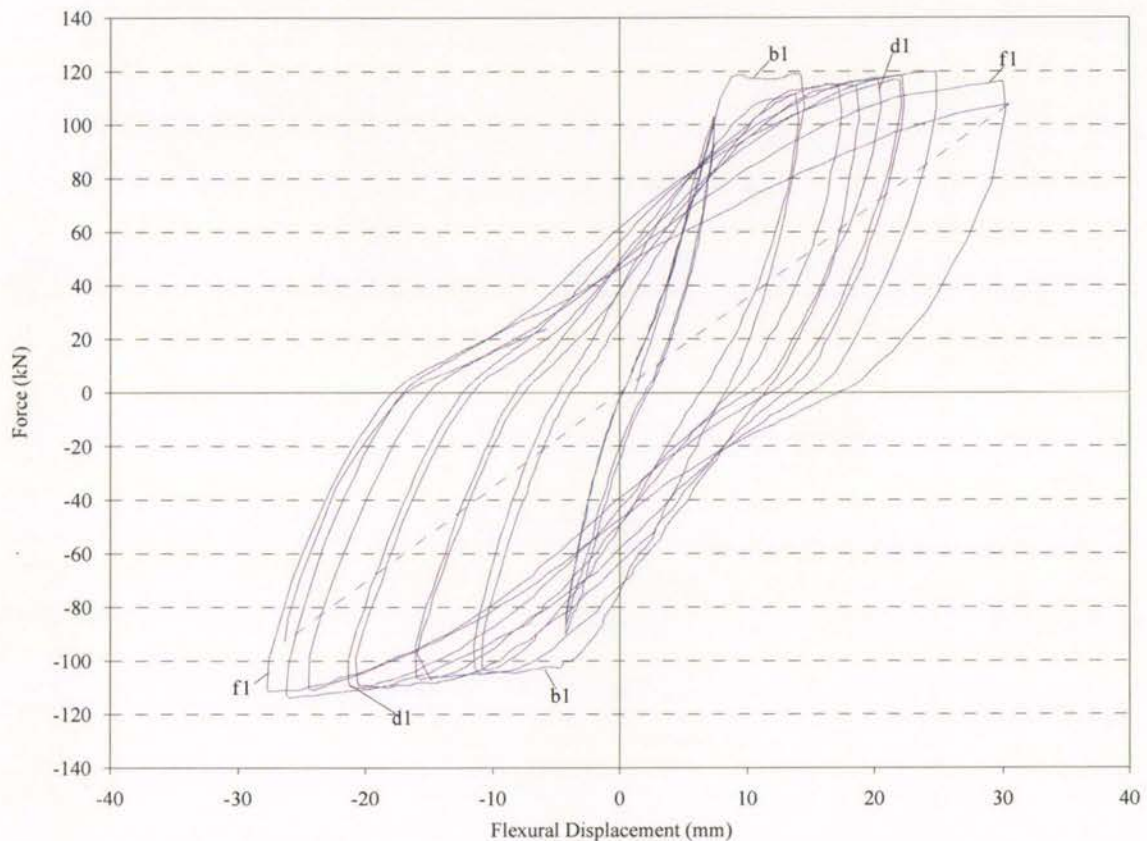


Figure 4.11-Flexural displacement versus force curve of beam A1 to 3.0% drift

Figure 4.12 shows the shear displacement plotted against the applied force. Note the increase in shear deformation in consecutive cycles although the applied displacement was the same (e.g d1, d2). This explains the decrease in flexural component in consecutive cycles shown in Figure 4.10; the total displacement remains constant on each cycle so as the shear displacement increases the flexural displacement must decrease. The curve shows that the shear component causes the pinching behaviour seen in Figure 4.9.



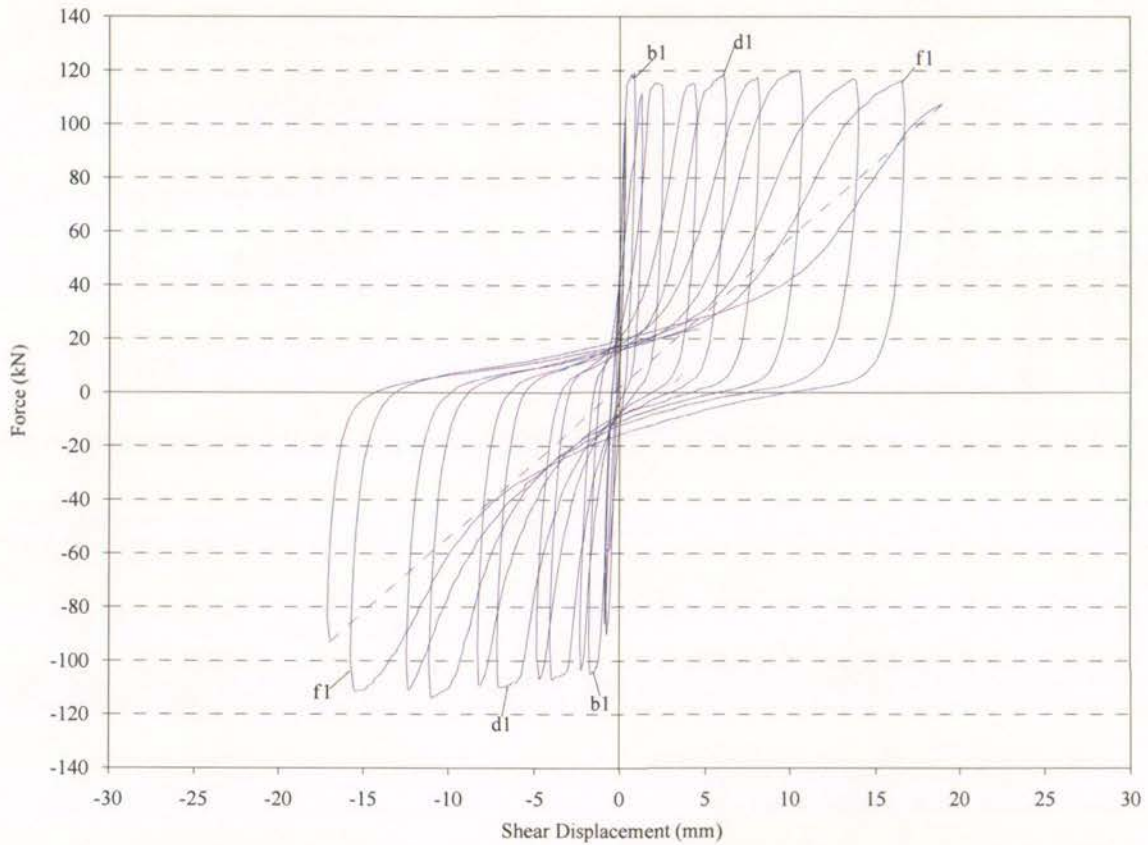


Figure 4.12-Shear force-shear displacement relationship of beam A1 to 3.0% drift

The reinforcing steel experiences a greater tensile strain than compressive strain under cyclic loading. Once cracking occurs the beam begins to elongate and is accelerated when the reinforcement yields (Fenwick and Megget, 1993). Figure 4.13 shows the elongation of beam A1 plotted against the applied drift level. The elongation is found by combining the average elongation of the top and bottom potentiometers of each block of potentiometers. The elongation behaviour is, as expected, increasing as a load is applied and then decreasing slightly as the load is removed. Also observed was the elongation increasing on each consecutive cycle. However, the elongation appears to decrease during 3.0% drift cycles. This is possibly due to the initiation of reinforcement buckling, which caused shortening of the beam.

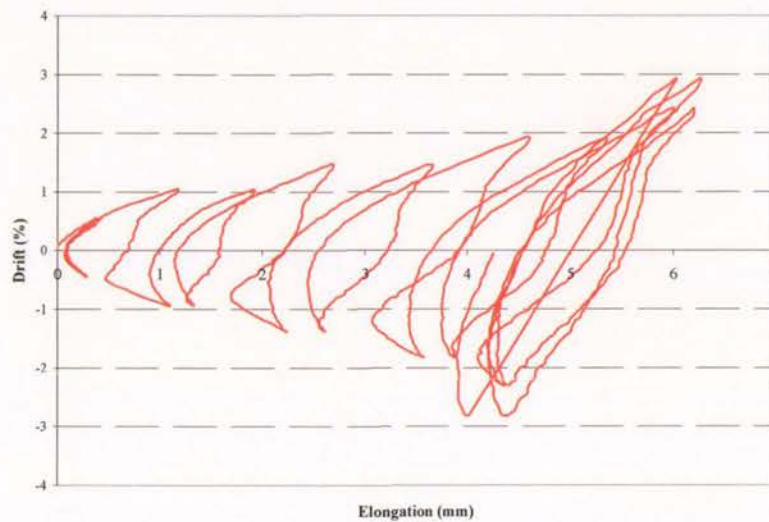


Figure 4.13-Beam elongation (A1)

#### 4.2.1.3. Test A2

The beam A2 was identical to A1 except that the spacing of transverse reinforcement within the ductile detailing length (600 mm) was reduced from 175mm to 100mm. For the design of beam A2 the shear strength of the concrete within the potential plastic region was ignored. The test procedure was the same as that used in A1.

In the first phase of the test, hairline flexural cracks formed in a very similar manner to that observed in Test A1. Elastic behaviour similar to that of A1 was seen in the first cycle of the second phase of the test (i.e. 0.5% drift cycle). However, as seen in Figure 4.14, the flexural cracks initiated near the location of the transverse reinforcement which was spaced at 100mm centres within the ductile detailing length and 175mm centres outside this zone.

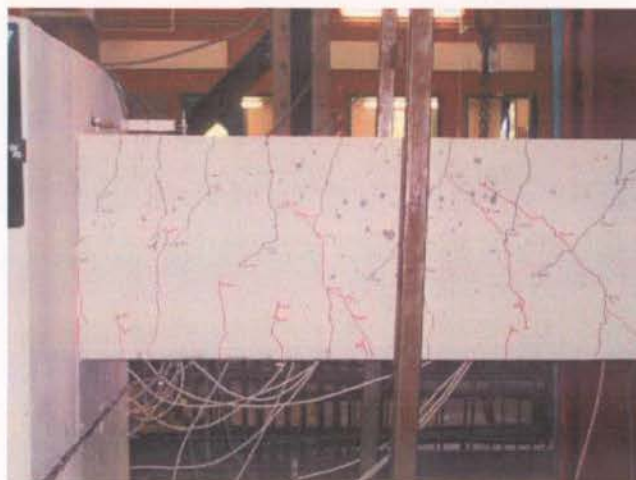


Figure 4.14-Reduced spacing of flexural cracks of test A2 at 2<sup>nd</sup> cycle at 0.5% drift

The load deflection curve (shown later in Figure 4.18) indicates that yielding of the longitudinal reinforcement occurred at 0.67% drift (9.5mm displacement) on the first positive 1.0% drift cycle. The only wide crack was located at the beam springing and it was approximately 1.0mm wide. Yielding of the longitudinal reinforcement in the other side also occurred on the first negative 1.0% drift cycle. At this stage, the beam had two cracks, one with a width of 1.0mm at the springing and a second located 150mm along the beam had a width of 1.2mm. These cracks closed to 0.7mm and 1.0mm respectively when the load was removed. In this load cycle, the crack pattern was similar to that observed in the test of beam A1. As shown in Figure 4.15, diagonal tension cracks started to form, the largest of which opened to 1.0mm during the second positive cycle.

By the second cycle of 2.0% drift, there were pronounced diagonal tension cracks in the plastic region with widths up to 3.0mm. When the load was removed, four flexural cracks remained open over a length of 260mm from the beam springing. These cracks can all be seen in Figure 4.15. The diagonal tension cracks continued to increase in width as the displacement levels were increased. During cycles of 3.0% drift the diagonal tension crack opened to 6mm, enabling the transverse reinforcement to be seen through the crack.



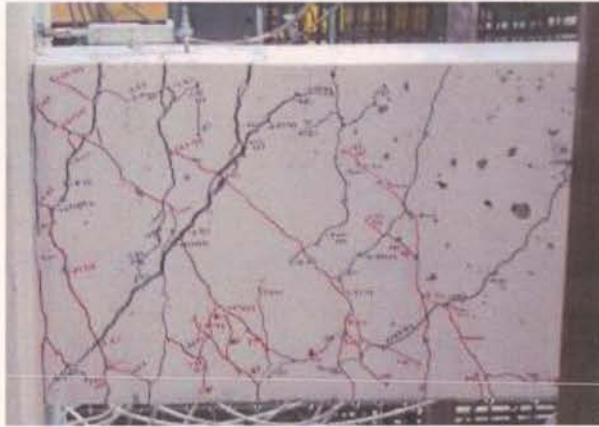


Figure 4.15-Flexural and diagonal tension cracking within plastic region of beam A2 at 1.0% drift

Significant spalling occurred during the first 3.5% drift cycle. This was accompanied by a decrease in stiffness and a loss of strength in the second displacement cycle of this drift. On the second positive cycle to 4.5% drift the load had degraded to below 80% of the maximum applied load and there was extensive spalling, exposing large sections of transverse and longitudinal reinforcement as shown in Figure 4.16.

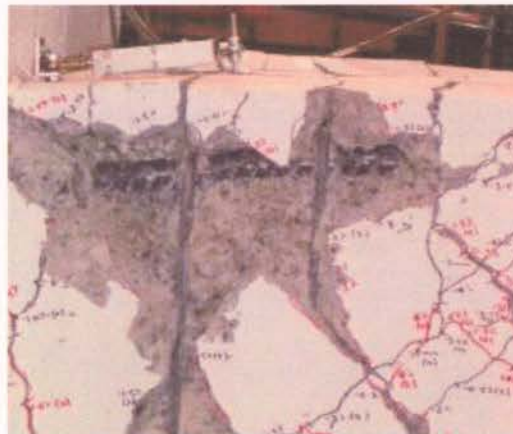


Figure 4.16-Spalled concrete exposing reinforcing after 4.5% drift (A2)

The test was stopped after two cycles of 5.5% drift. The spalled concrete was removed to show the damaged region, as seen in Figure 4.17. The longitudinal bars deformed similar to those in test A1 but the deformation (i.e. buckling) is not as pronounced due to the additional restraint from increased density (smaller spacing) of transverse reinforcement.



Figure 4.17-End of test after removing spalled concrete showing deformation of reinforcement (A2)

Figure 4.18 shows that the load deflection relationship of beam A2 was in many ways similar to that of beam A1. One of the key differences is that buckling induced degradation of strength is delayed to a higher drift level of 4.5% compared with 3.5% drift in beam A1. The rate of the strength degradation is also reduced along with the level of shear pinching. This can all be contributed to the presence of additional stirrups within the hinge region.

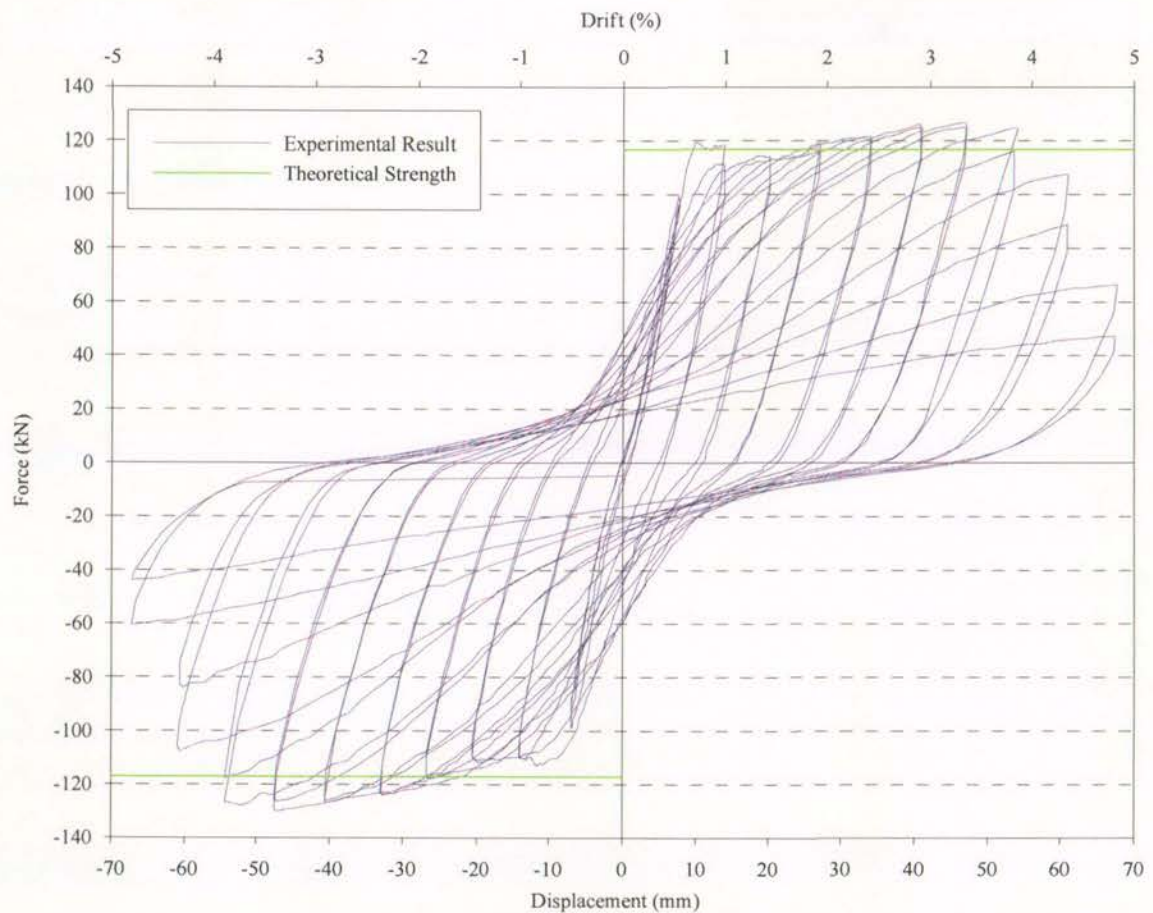


Figure 4.18-Load displacement response of specimen A2

Figure 4.19 shows the contributions of flexure and shear to the total displacement. It shows that the flexural component dominates the displacement as was the case in beam A1. The closure error in the positive direction is small while the error in the negative direction is approximately 13% in the higher displacement levels. The flexural contribution is approximately 65% in the positive direction and 55% in the negative direction.

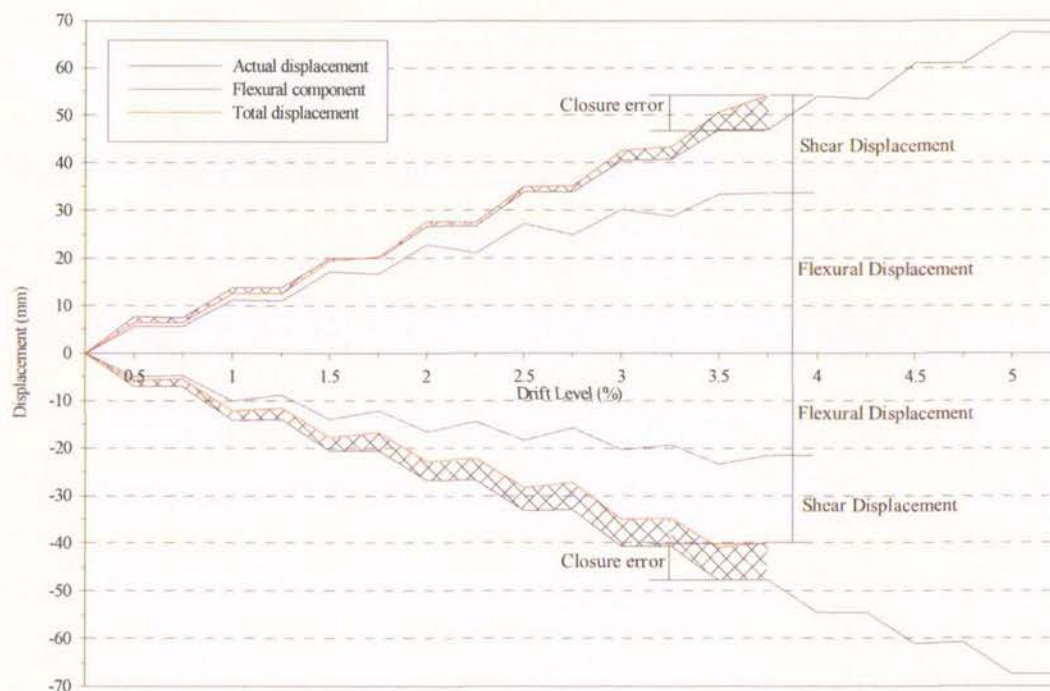


Figure 4.19-Contribution of shear and flexure to the total displacement at the peaks of the loading cycles for beam A2

Figure 4.20 shows the flexural displacement component plotted against the applied shear force. The curve does not exhibit the pinched behaviour of Test A1 until the second 3.5% drift cycle (i.e. g2).



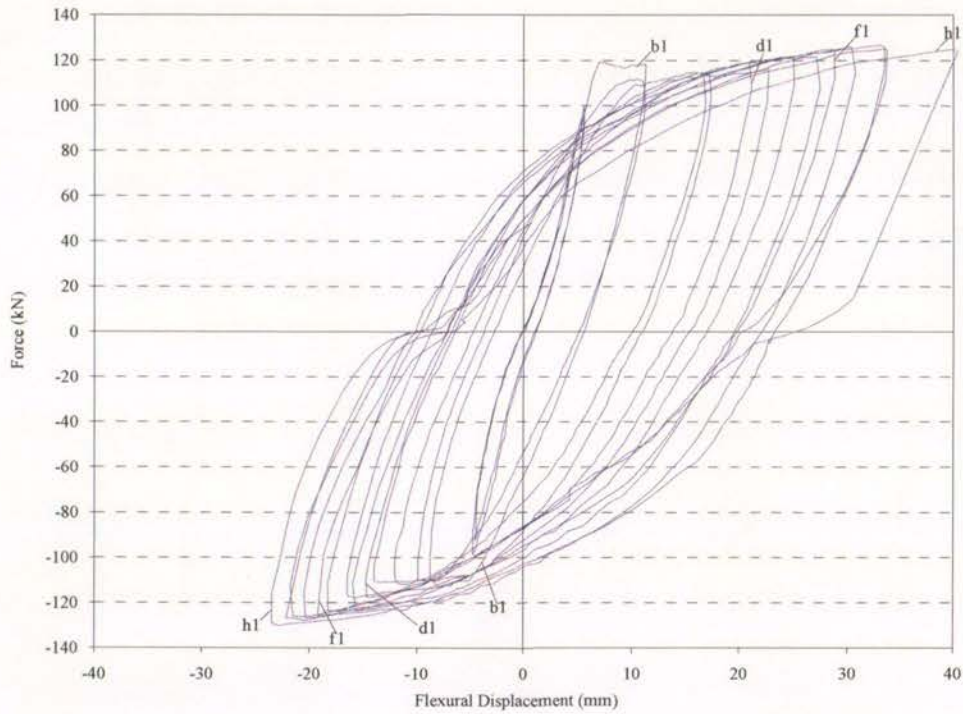


Figure 4.20-Flexural displacement versus force curve of beam A2 to 4.0% drift

Figure 4.21 shows the shear component of displacement plotted against the applied shear force. As in beam A1, the shear displacement increases on each consecutive cycle. The pinched behaviour of the shear loops is similar to that of beam A1.

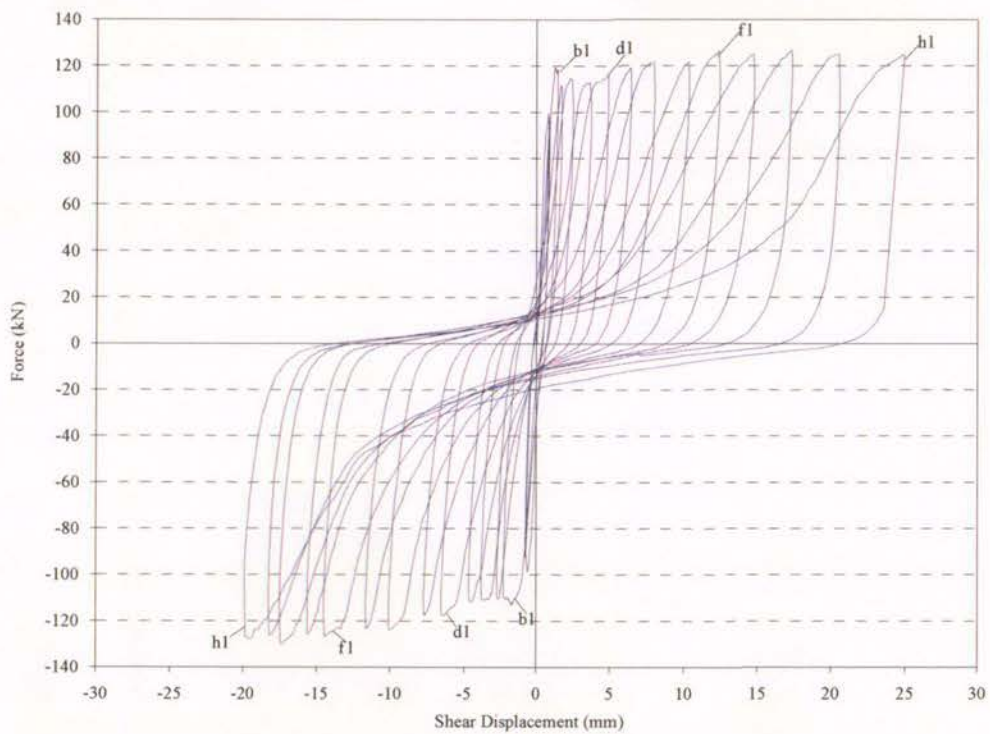


Figure 4.21-Shear force versus shear displacement response of beam A2 to 4.0% drift

The elongation of beam A2 is plotted against the applied drift level in Figure 4.22. The elongation of beam A2 is significantly larger than beam A1. This is partially due to the delay of buckling in beam A2 allowing the beam to continue elongating at the higher drift levels. Another cause is the decreased level of shear displacement, thereby increasing the strain in the flexural reinforcement (at the same applied drift level) and thus the elongation.

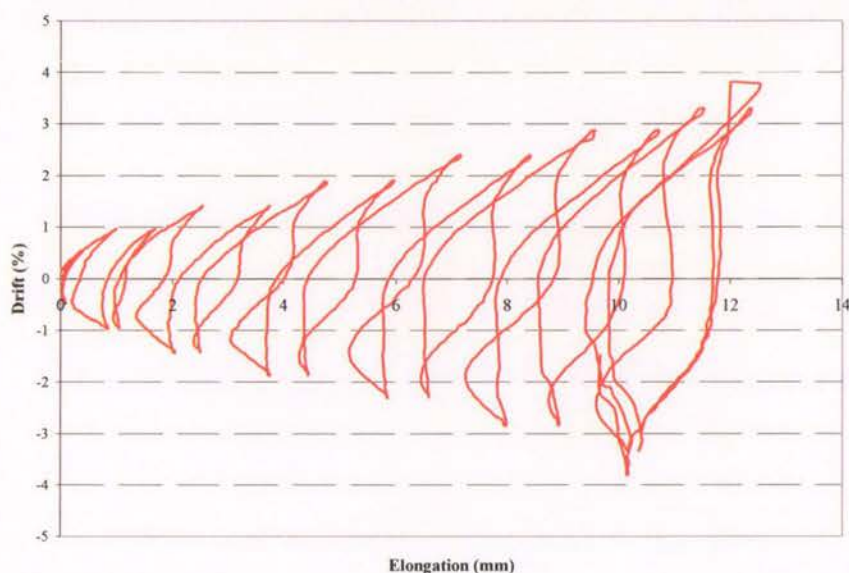


Figure 4.22-Beam elongation (A2)

## 4.2.2. Unit B

### 4.2.2.1. General details

The section dimensions for beams B1 and B2 were the same as beams A1 and A2. The longitudinal steel consisted of three Grade 500 25mm diameter bars at the top and two Grade 500 12mm diameter bars at the bottom. Two-legged 10mm stirrups made from Grade 500 reinforcement were used at 135mm centre to centre. Cylinder tests for Tests B1 and B2 gave an average concrete compressive strength of 21.0MPa, which was below the design strength of 30MPa.

### 4.2.2.2. Test B1

This beam was subjected to reversed cyclic loading following the loading sequence used in beams A1 and A2. Observed initial behaviour was similar to beam A1 with small hairline flexural cracks forming during the load controlled loading phase. The flexural cracks



extended to near the mid depth when the drift was increased to 0.5%, as shown in Figure 4.23.



Figure 4.23-Flexural cracks after one complete cycle to 0.5% drift (B1)

On the first positive cycle to 1.0% drift the load deflection relationship (see Figure 4.29) showed yielding of the bottom reinforcing occurred at 0.64% drift (9.1mm displacement). This was accompanied by the opening of a flexural crack located 180mm along the beam to a width of 1.7mm measured at 1.0% drift. Flexural cracks had started to become slightly inclined at this displacement. The width of this crack when the load was removed was 1.2mm. During the negative cycle to 1.0% drift no obvious yield plateau could be seen on the force-displacement plot, see Figure 4.29. The flexural cracks appeared to close when the load was removed. A residual drift of 0.2% was evident in the force-displacement plot. Diagonal tension cracks were prominent during the negative half cycle at this displacement level, as seen in Figure 4.24.



Figure 4.24-Inclination of cracks at 1.0% displacement (B1)

On the positive cycle to 1.5% displacement the flexural crack located 180mm out from the beam springing continued to widen. This was the only crack that opened appreciably during positive displacement cycles. During the negative cycle at 1.5% drift, crushing of the concrete could be seen at the bottom of the beam springing. It is evident that due to the low concrete strength crushing of concrete in compression occurred before the flexural



reinforcement yielded. On the second positive cycle at this displacement the beam strength decreased by approximately 15kN, as seen on the force displacement relationship in Figure 4.29.

As the load was removed after reaching the peak displacement on the first cycle to 2.0% drift spalling occurred for the first time. This was due to the crushed concrete on the underside of the beam experiencing a relaxation in the compressive force it was sustaining, allowing the crushed concrete to fall. The extent of some the spalling on the underside of the beam can be seen in Figure 4.25.



Figure 4.25-Spalling of concrete at 2.0% drift (B1)

At the peak displacement in the second negative cycle to 2.0% drift a further drop in load capacity was observed in the load displacement curve, see Figure 4.29. This was accompanied by significant spalling as the load was released, exposing the bottom longitudinal reinforcing bars. Inspection of the bottom reinforcement showed that it had buckled between the first and second sets of stirrups, as shown in Figure 4.26. The first cycle to 2.0% drift was the cycle at which the beam reached its maximum load capacity. After this cycle the peak load decreased on each consecutive cycle as seen in Figure 4.29. This is not surprising given the significant damage to the lower portion of the beam with crushed concrete and buckled bars.



Figure 4.26-Buckled bars exposed by spalling after 2.0% drift (B1)

On following cycles spalling of concrete continued and the buckling of the bottom bars became more pronounced. The deformation in the positive direction was still concentrated at the flexural crack located 180mm along the beam, opening to a width of 5mm. The test was stopped when the bottom bars ruptured. This occurred in tension after one cycle to a negative 3.5% drift. This failure was due to low cycle fatigue of the bars, which were bent and straightened during each transition between positive and negative cycles. Figure 4.27 and Figure 4.28 show the damaged beam at the end of the test and the ruptured bottom bars.



Figure 4.27-Ruptured bars after one cycle to 3.5% drift (B1)

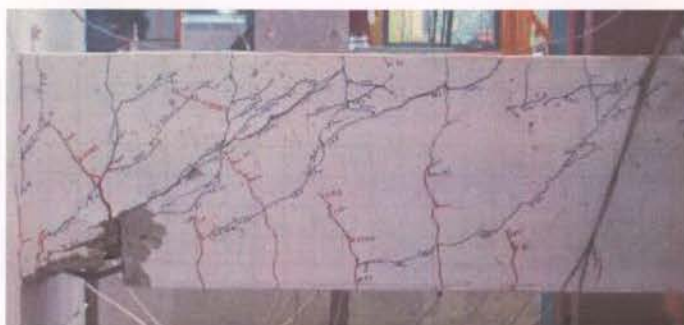


Figure 4.28-Crack pattern at end of test (B1)

Figure 4.29 shows the load deflection relationship for beam B1. It is easy to see that yielding of the bottom flexural reinforcement occurred during the positive cycles while no yielding occurred during negative cycles. The degradation in strength after the first cycle to 2.0% drift is severe due to the significant spalling of concrete and buckling of bottom reinforcement. However, the buckling of the bottom reinforcement only resulted in a slight decrease in the section capacity in the positive direction. This indicates that full tensile strength can be developed by buckled reinforcing bars upon stress reversal. The pinched hysteresis loops, due to a combination of shear deformation and concrete dominating the overall response, is more pronounced in Figure 4.29 than was seen in beams A1 and A2, see Figure 4.9 and Figure



4.18. The initial stiffness in the negative direction is clearly greater than the stiffness in the positive direction. During drift cycles to displacements greater than 2.0% the stiffness of the beam is very low through near zero displacement and increases as the beam reaches its target displacement.

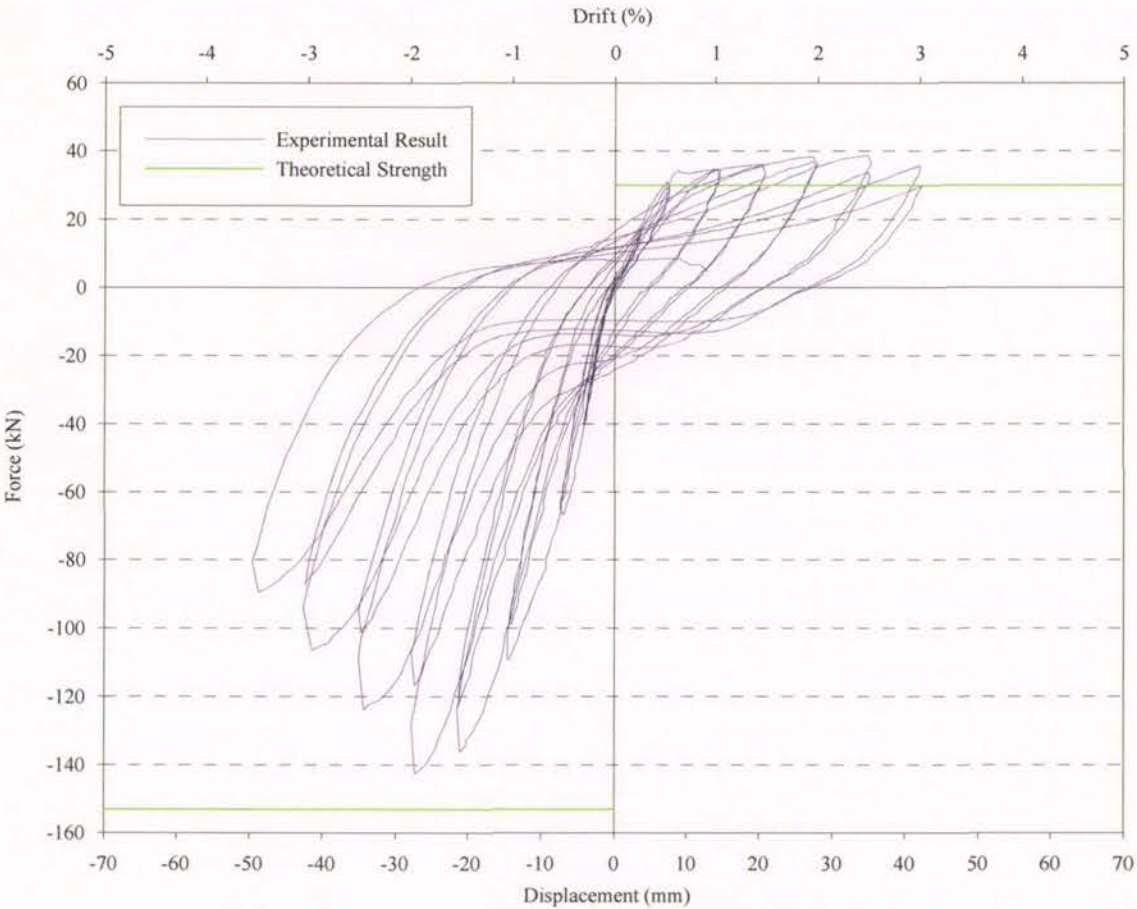


Figure 4.29-Load displacement response of specimen B1

Figure 4.30 shows the contributions of flexure and shear to the total displacement. As seen in Figure 4.30, the flexural component of displacement dominated the total displacement. The decrease in flexural displacement on the second cycle at the same displacement level in this test is not as pronounced as it was in beams A1 and A2 (see Figure 4.10 and Figure 4.19). The closure error is small in the positive direction and still reasonable in the negative direction.



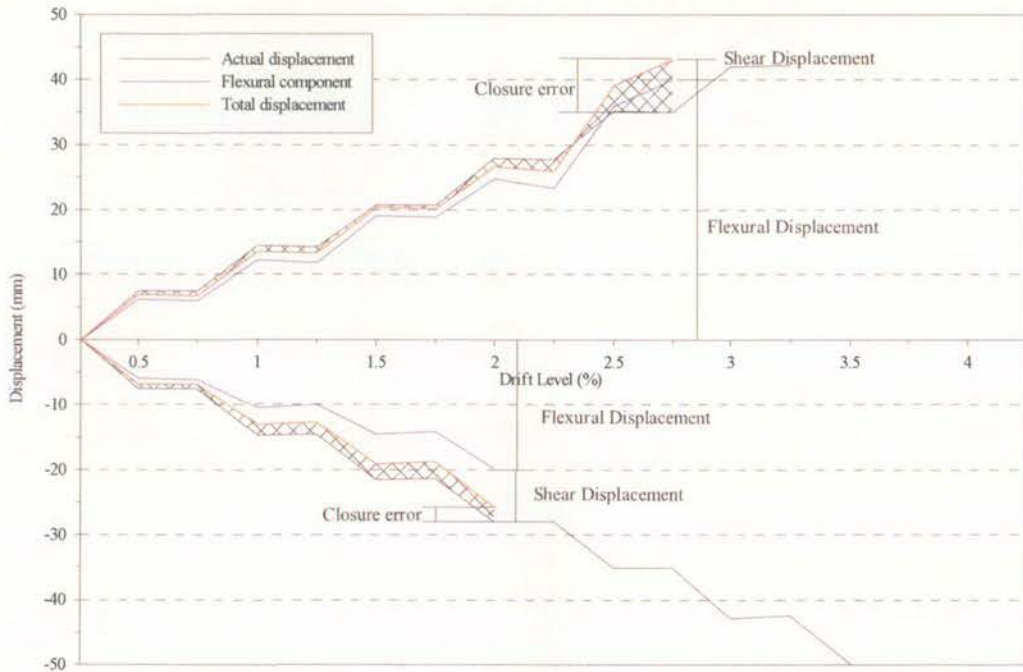


Figure 4.30-Contribution of shear and flexure to the total displacement at the peaks of the loading cycle for beam B1

The shear displacement component is plotted against the applied force in Figure 4.31. As indicated by Figure 4.30, the shear displacement is only a minor contribution to the total end displacement.

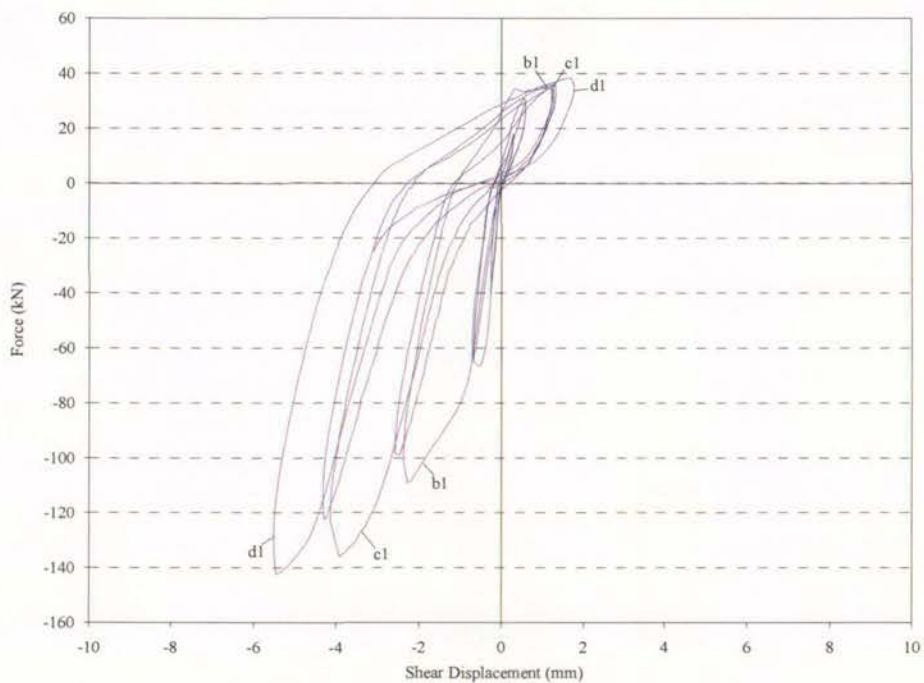


Figure 4.31-Shear displacement versus shear force (B1)

The flexural displacement component shown in Figure 4.32 reflects the shape of the total displacement hysteresis loop shown in Figure 4.29. The absence of yield of the reinforcement in the negative direction is again clear.

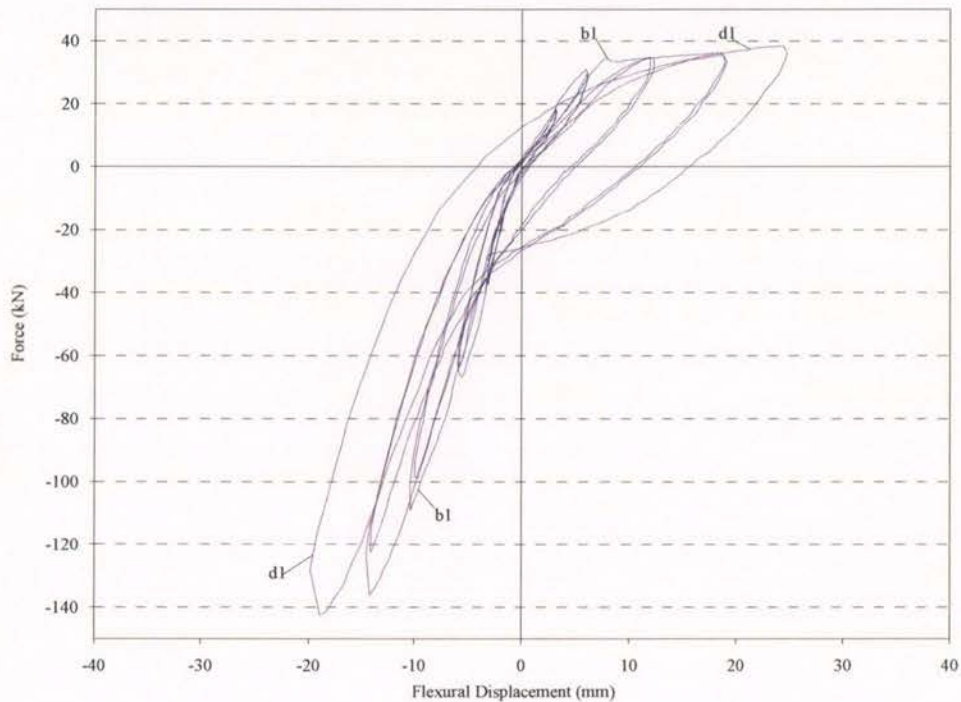


Figure 4.32-Flexural displacement versus force relationship (B1)

The beam elongation of beam B1 shown in Figure 4.33 is not as large as that of beams A1 and A2 (see Figure 4.13 and Figure 4.22). This is understandable as there was no yielding of reinforcement in one direction, the main driver of beam elongation. The lack of yield is reflected in the elongation plot with elongation at peak displacement continuing to grow in the positive direction as the reinforcement yields but the residual elongation when the load was removed was limited by the lack of beam lengthening in the negative direction.

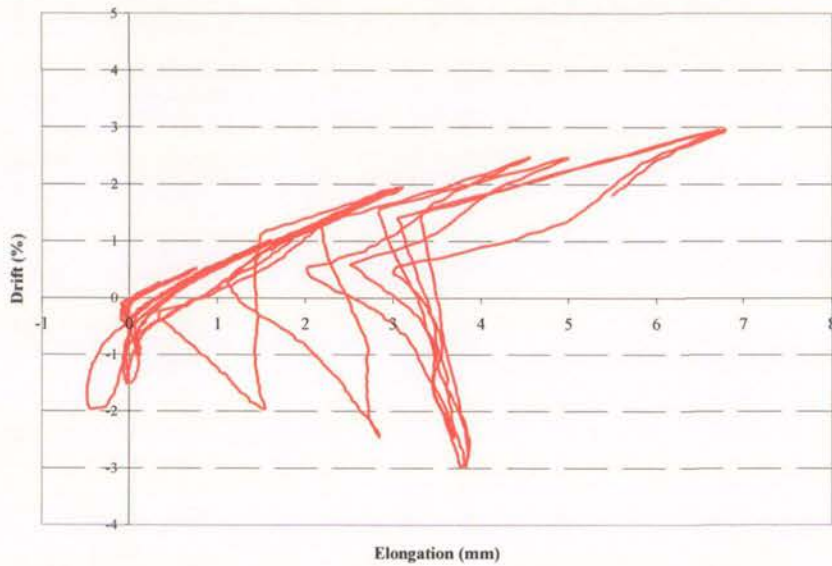


Figure 4.33-Beam elongation (B1)

#### 4.2.2.3. Test B2

The beam of Test B2 was identical to that of Test B1, reinforced with three Grade 500 25mm bars at the top and two Grade 500 12mm bars at the bottom. Transverse reinforcement comprised of two legs of Grade 500 10mm bars at 135mm centres. While B1 was subjected to reverse cyclic displacement with the intention of yielding the section in both directions, B2 was tested as a uni-directional plastic region. This meant continuing the same increasing 0.5% displacements in the negative direction but restricting the displacement in the positive direction such that the load in that direction did not exceed 75% of the theoretical strength.

Behaviour in the first phase of the test and during two full cycles to 0.5% drift was similar to that of beam B1; small flexural cracks formed which then extended during the cycles to 0.5% drift. The negative cycle to 1.0% caused diagonal tension cracks to form similar to those seen in B1. As in beam B1 there was no evidence in the force displacement relationship (see Figure 4.38) of yield occurring at this displacement level. In the positive direction the beam was not allowed to displace to the full 1.0% drift because of the restriction on the load to 75% of theoretical maximum. This dictated the maximum displacement the beam sustained in the positive direction. The crack pattern in the positive moment tension zone shown in Figure 4.34 remained stable for most of the test.



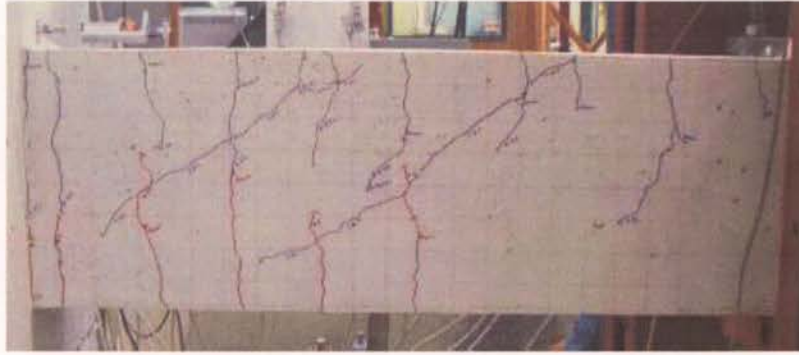


Figure 4.34-Crack pattern at after two complete cycles at 1.0% drift (B2)

At the peak of the second cycle of 1.5% drift crushing of the concrete at the bottom of the beam was first noticed, similar to that in B1. Two diagonal tension cracks initiated at 400mm and 700mm along the beam, and these cracks opened to 1.1mm and 1.6mm, respectively. Spalling first occurred as the load was relaxed after the negative cycle to 2.5% drift. This was followed by significant spalling at after the second cycle to 3.0% drift. After the first cycle to 4.0% drift it became evident that the bottom reinforcing bars had started to buckle between the first and second stirrup sets. This was similar to the behaviour observed in beam B1. The area affected by crushing of the concrete had grown significantly to be approximately 175mm up the height of the beam and 225mm from the beam springing, as shown in Figure 4.35.

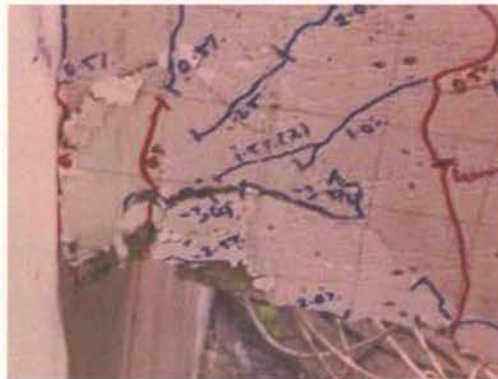


Figure 4.35-Extent of crushed concrete at 4.0% drift (B2)

The degradation of strength was not as pronounced in this uni-directional hinge test as in the reversing test of B1. This is probably due to less spalling of concrete during the positive cycles of the test because the tensile strains were not as large as in beam B1. The compressive steel was also more resistant to buckling as it had not been yielded in tension on previous cycles as it would have in B1. This enabled the test to continue until two full cycles at 6.0% drift were applied. At this displacement level the bottom bars ruptured in tension, again due

to low cycle fatigue. The ruptured bars are shown in Figure 4.36 and the condition of the beam at the end of the test shown in Figure 4.37. Both these tests contained Grade 500 reinforcing with studs welded to the longitudinal reinforcement. There was no evidence that the welding had any adverse effect on the beam behaviour.



Figure 4.36-Buckled and ruptured bars after two complete cycles at 6.0% drift (B2)

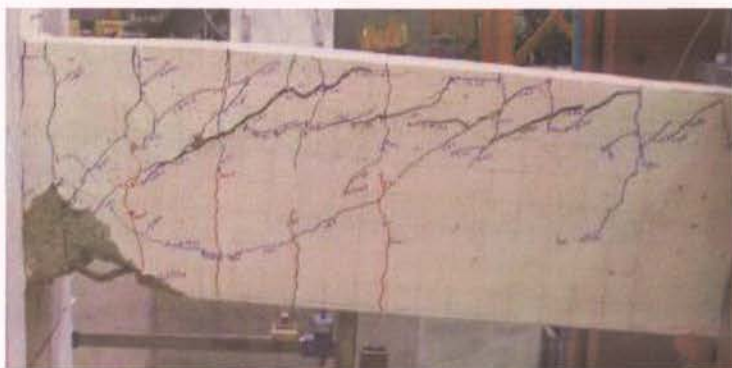


Figure 4.37-Crack pattern at the end of test (B2)

Figure 4.38 shows the load deflection relationship of beam B2. The absence of reinforcement yielding in the negative direction is clear. The beam exhibited a gradual decrease in stiffness at each displacement level until the peak load capacity was reached at 2.0% drift. This behaviour is similar to that seen in beam B1; see Figure 4.29. The uni-directional nature of the test resulted in only a small positive displacement and the beam continually stepping its way down (i.e. negative displacement). The beam loaded and unloaded along approximately the same path during cycles to the same displacement, resulting in narrow loops of low dissipative nature. The shear pinching behaviour seen in the reverse cyclic tests is not observed here. The degradation of strength shown in Figure 4.38 is not as severe as that of Test B1 as damage to the compressive concrete was not as significant due to smaller tensile strains. There is a noticeable decrease in stiffness as the displacement level is increased.



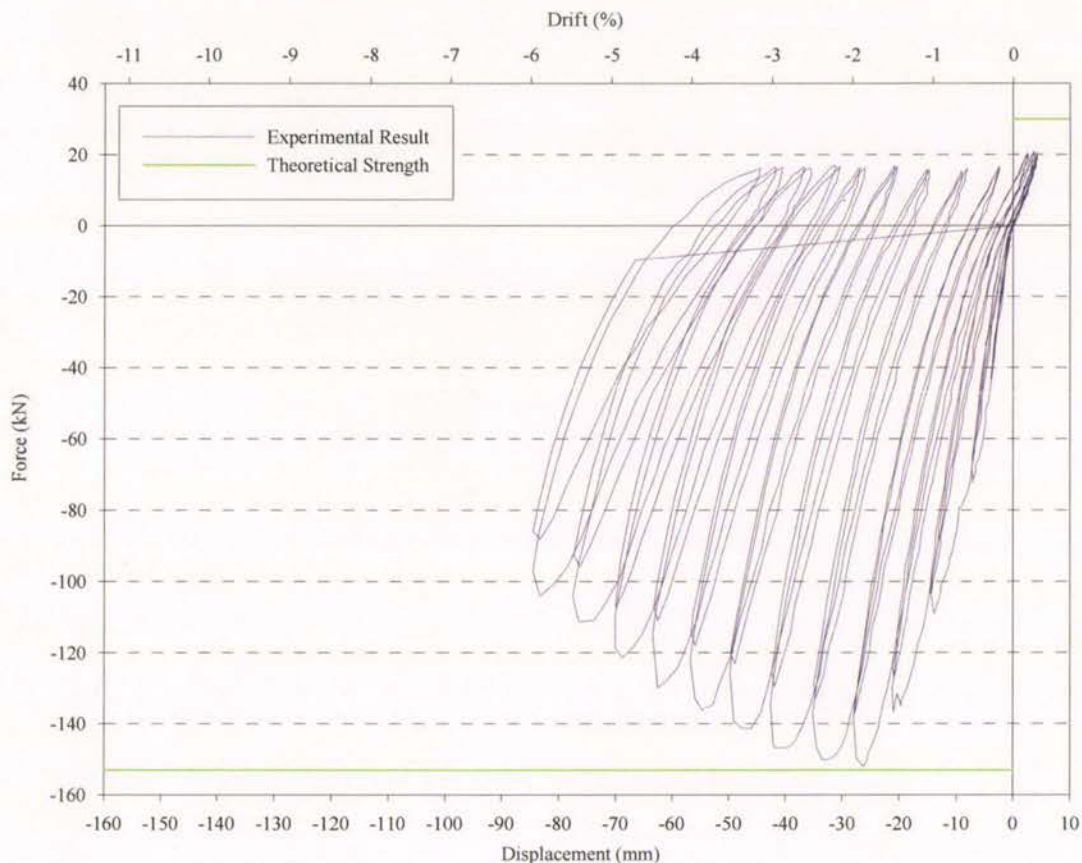


Figure 4.38-Load displacement response of specimen B2

Figure 4.39 shows the contribution of shear and flexure to the total displacement. Only the negative direction is shown as there is little value in showing the positive direction. As in previous tests, the overall behaviour is dominated by the flexural component. The flexural component decreases on consecutive cycles at the same displacement level, similar to the behaviour of beams A1 and A2, see Figure 4.10 and Figure 4.19. However in this case the difference is not taken up by the shear displacement as would be expected. This is probably due to a slight error in the measurements.



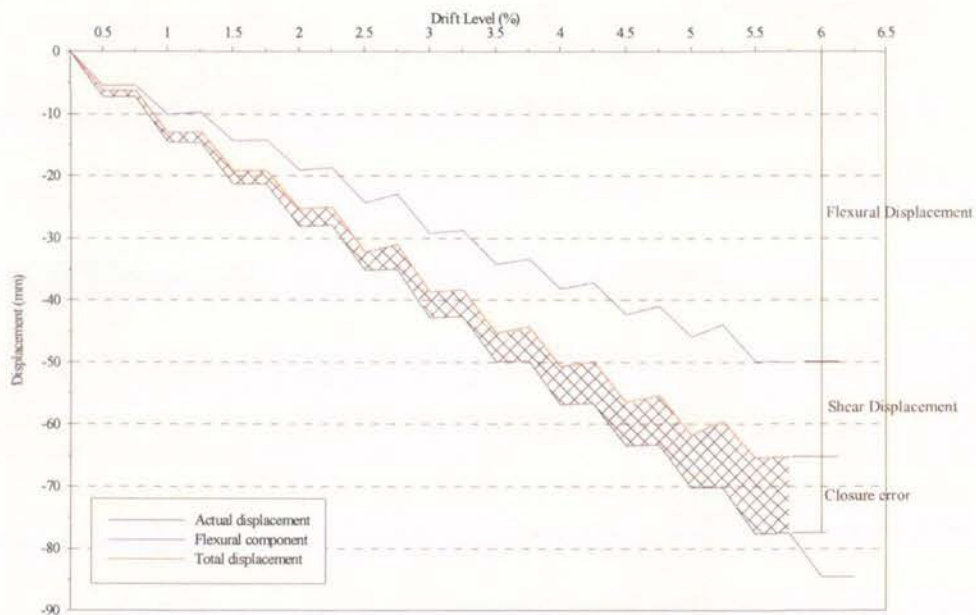


Figure 4.39-Contribution of shear and flexure to the total displacement at the peaks of the loading cycles for beam B2

The flexural component of the total displacement is plotted against the applied force in Figure 4.40. The flexural response is similar to the overall beam behaviour. The hysteresis loops of the flexural component are very narrow while the shear component shown in Figure 4.41 exhibits a more dissipative loop.

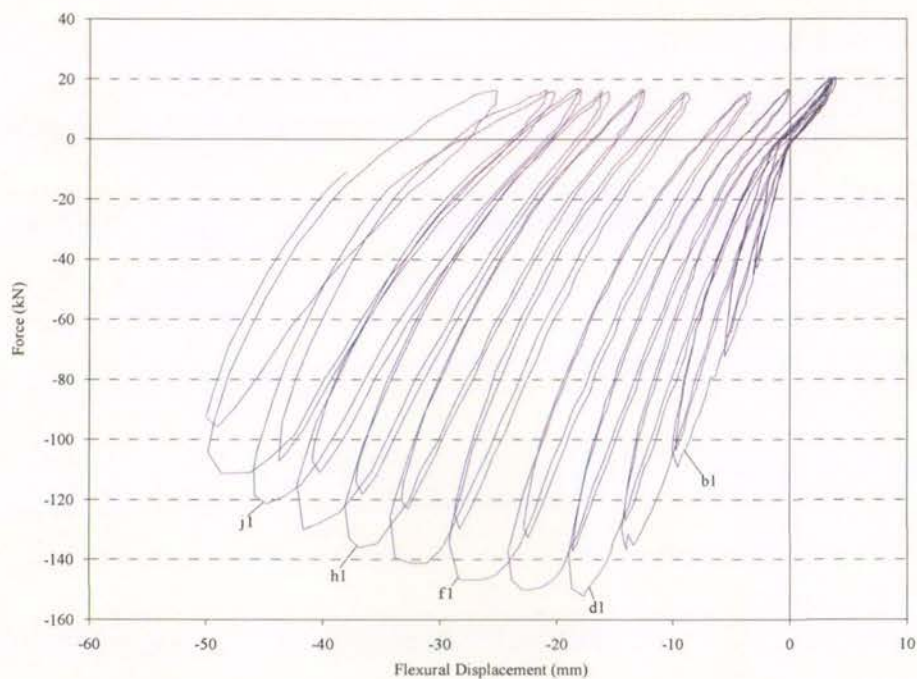


Figure 4.40-Flexural displacement versus applied force (B2)

Figure 4.41 also reinforce the trend observed in Figure 4.39 of no increase in the shear displacement between cycles at the same displacement level, contrary to behaviour of previous tests (see Figure 4.12).

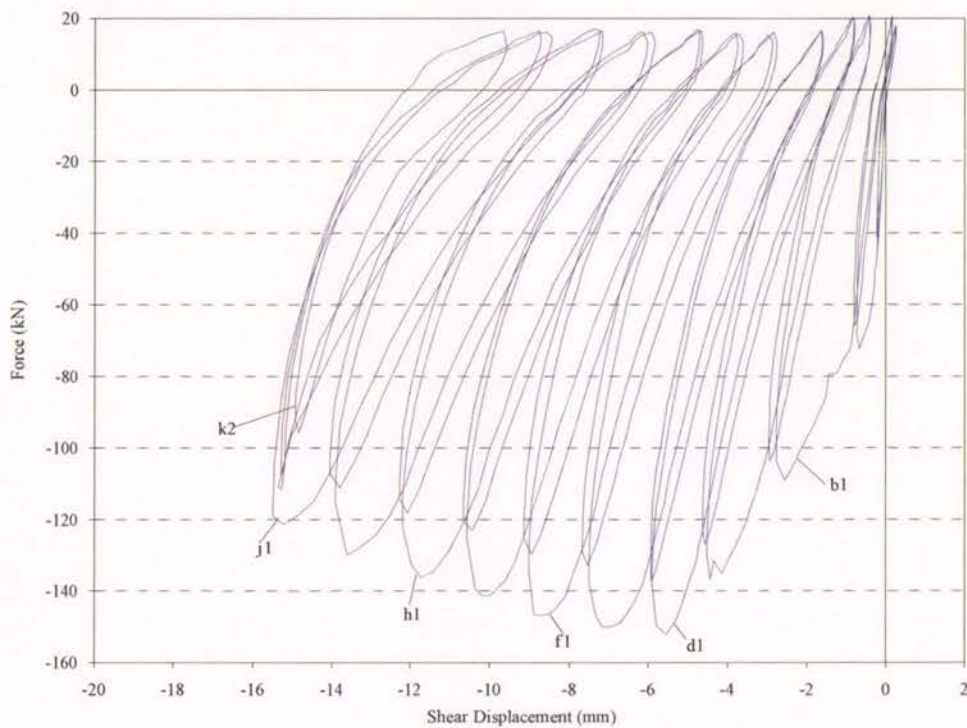


Figure 4.41-Shear displacement versus applied load (B2)

The magnitude of beam elongation seen in Figure 4.42 is comparable to previous tests (see Figure 4.13), despite the flexural reinforcement not yielding in either direction. The plot only shows elongation in one direction of drift, mainly because of the uni-directional nature of the test.

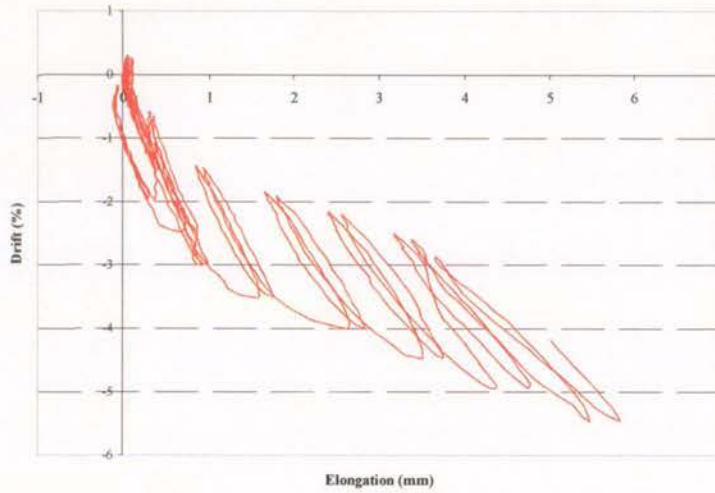


Figure 4.42-Beam elongation (B2)

### 4.2.3. Unit C

#### 4.2.3.1. General details

The section dimensions of beam C1 and C2 were the same as beams A1 and A2. The longitudinal steel consisted of five Grade 300 25mm diameter bars at the top and two Grade 300 16mm diameter bars in the bottom. Two-legged 10mm stirrups made from Grade 500 reinforcement were used at 130mm centres. The first beam (i.e. C1) was subjected to reversed cyclic loading and the second (i.e. C2) was used in a uni-directional hinge test.

#### 4.2.3.2. Test C1

In the first phase of the test very similar behaviour to that of beams A1 and A2 was observed. The behaviour was also similar in the first two complete cycles to 0.5% drift. However many of the cracks that opened during the negative cycles at this displacement were inclined to a greater degree than previously seen, this is shown in Figure 4.43



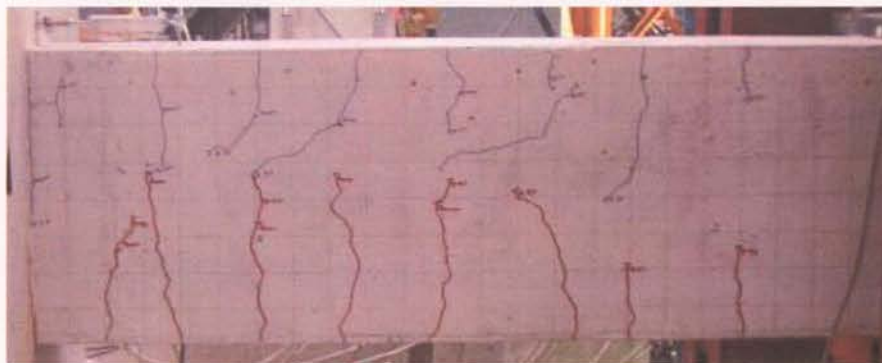


Figure 4.43-Crack pattern after two cycles at 0.5% drift (C1)

The load deflection relationship (see Figure 4.48) showed that yielding of the top flexural reinforcement occurred in the first negative cycle to 1.0% drift at 0.92% drift (13.1mm displacement). A crack at the beam springing opened to a width of 1.0mm and remained open to 0.8mm when the load was removed. Crushing of concrete at the bottom of the beam was noticed, as shown in Figure 4.44, indicating the section neutral axis was near the balanced condition. Several diagonal tension cracks had formed along the beam length. The load deflection curve showed that yielding of the bottom reinforcement occurred in the first positive cycle to 1.0% drift at 0.61% drift (8.7mm displacement). Flexural cracks located at 100mm and 180mm from the beam springing opened to a width of 0.6mm and 0.4mm, respectively.

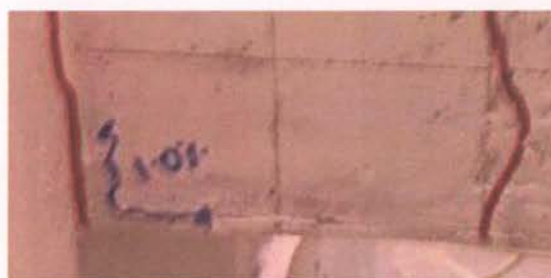


Figure 4.44-Crushing of concrete during positive cycle to 1.0% drift (C1)

At 2.0% drift the load capacity of the beam decreased as shown on the load deflection relationship in Figure 4.48. The decrease in capacity was accompanied by more crushing of concrete at the bottom of the beam during that cycle. The second flexural crack located 180mm along the beam opened to a width of 1.0mm. The crack at the beam springing was open to 2.0mm. These cracks remained open to 0.6mm and 1.5mm respectively when the load was removed. On the positive cycle, three flexural cracks located 100mm, 180mm and

220mm from the springing opened to 1.5mm, 1.0mm and 0.7mm respectively. When the load was removed these cracks remained open to 1.2mm, 0.9mm and 0.5mm.

Spalling first occurred in the first negative cycle to 2.5% drift. This was followed by significant spalling exposing the bottom reinforcing bars on the second cycle at this displacement. The bars appeared to have buckled slightly when examined as shown in Figure 4.45. On the subsequent negative cycle to 3.0% drift the reinforcement buckled further, having lost the restraint of the cover concrete. This can be seen in Figure 4.46. This pronounced buckling was accompanied by a significant drop in load capacity on the load deflection curve (Figure 4.48).



Figure 4.45-First evidence of buckling at 2.5% drift (C1)



Figure 4.46-Pronounced buckling at 3.0% drift (C1)

A further decrease in load capacity was seen on the load displacement curve on cycles to 3.5% and 4.0% drift before rupture of bottom bars in tension occurred after one negative cycle at 4.0% drift. As with tests B1 and B2, the rupture of the bars was caused by low cycle fatigue. The condition of the beam at the end of the test can be seen in Figure 4.47.



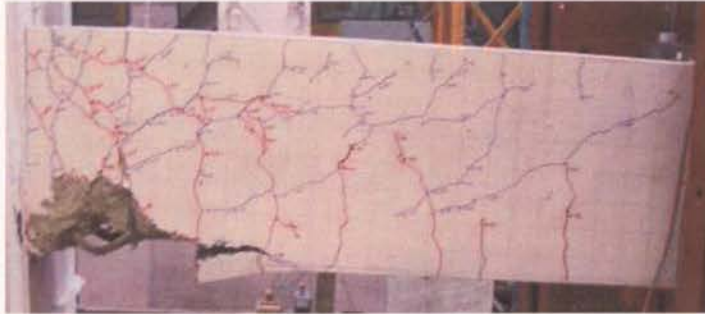


Figure 4.47-Crack pattern at the end of test (C1)

The load deflection curve from beam C1 is shown in Figure 4.48. The load capacity is limited by yielding of the flexural reinforcement in both directions. However, the amount of yielding appears to be smaller in the negative direction. The initial stiffness is different between the two directions, similar to that of beam B1 (see Figure 4.29). A significant drop in load capacity can be seen in the second cycle to 1.5% and 2.0% drift followed by a continued degradation of load capacity in subsequent drift cycles. The pinching behaviour due to shear displacement is evident only when the beam unloaded from the positive direction and loaded in negative direction.

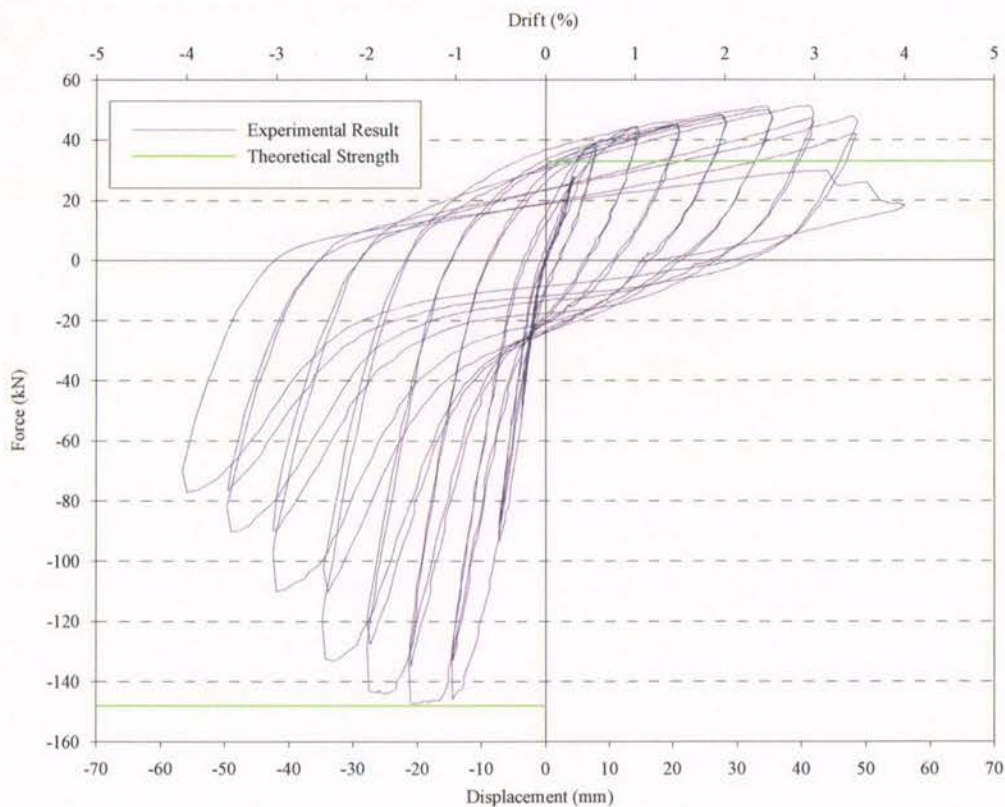


Figure 4.48-Load displacement response of specimen C1



Figure 4.49 shows the contributions of flexure and shear to the total displacement. There is very little closure error in the results from this test. As in previous tests the displacement is dominated by the flexural component and shear deformation accounts for approximately 10-15% of the total displacement.

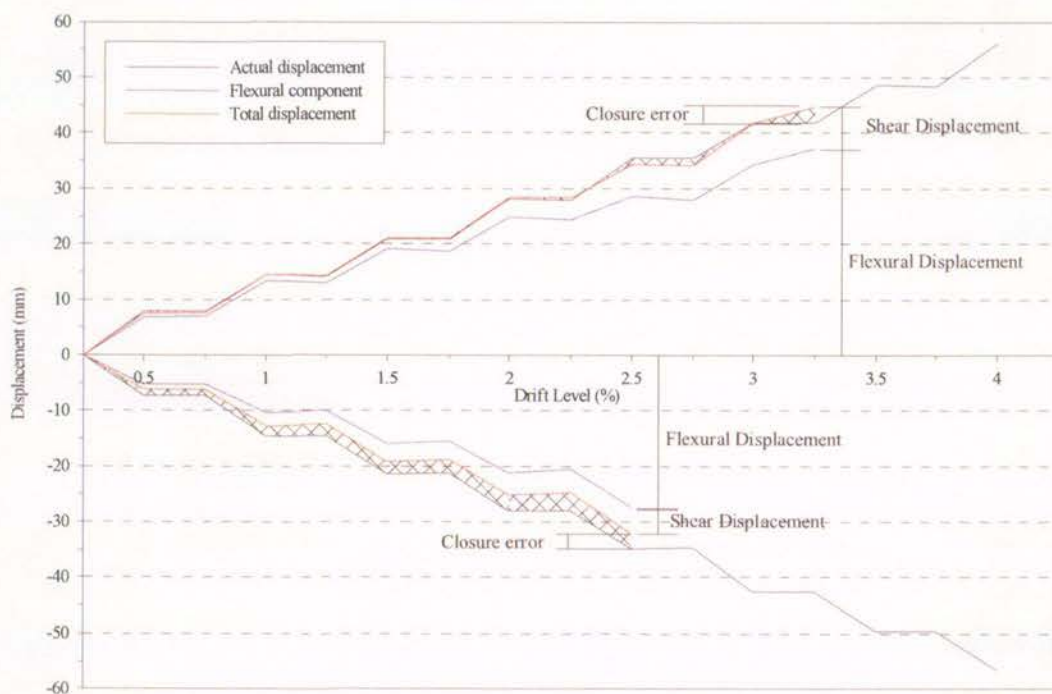


Figure 4.49-Contribution of shear and flexure to the total displacement at the peaks of the loading cycles for beam C1

The pinching behaviour exhibited in Figure 4.48 is also reflected in the shear response shown in Figure 4.50, only during the unloading from the positive to negative drift.

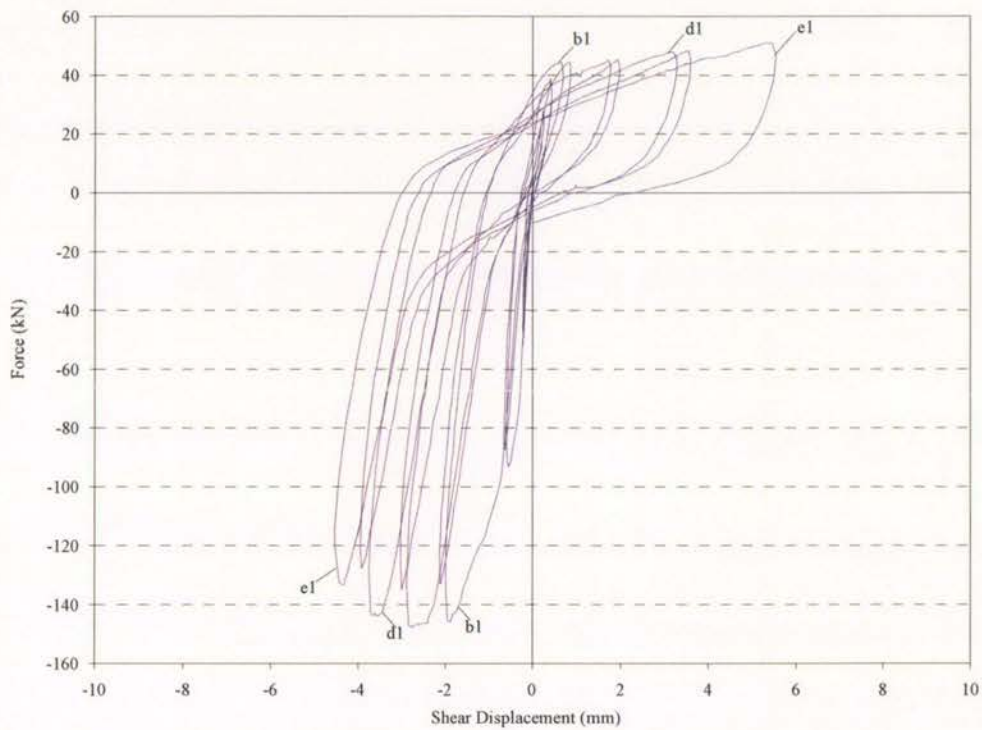


Figure 4.50-Shear displacement versus applied load (C1)

The flexural displacement is plotted against the applied load in Figure 4.51. The flexural hysteresis loops are very full in the positive direction. There is also very little reduction in the flexural displacement in subsequent cycles at the same drift level in the positive direction in comparison to the negative direction.

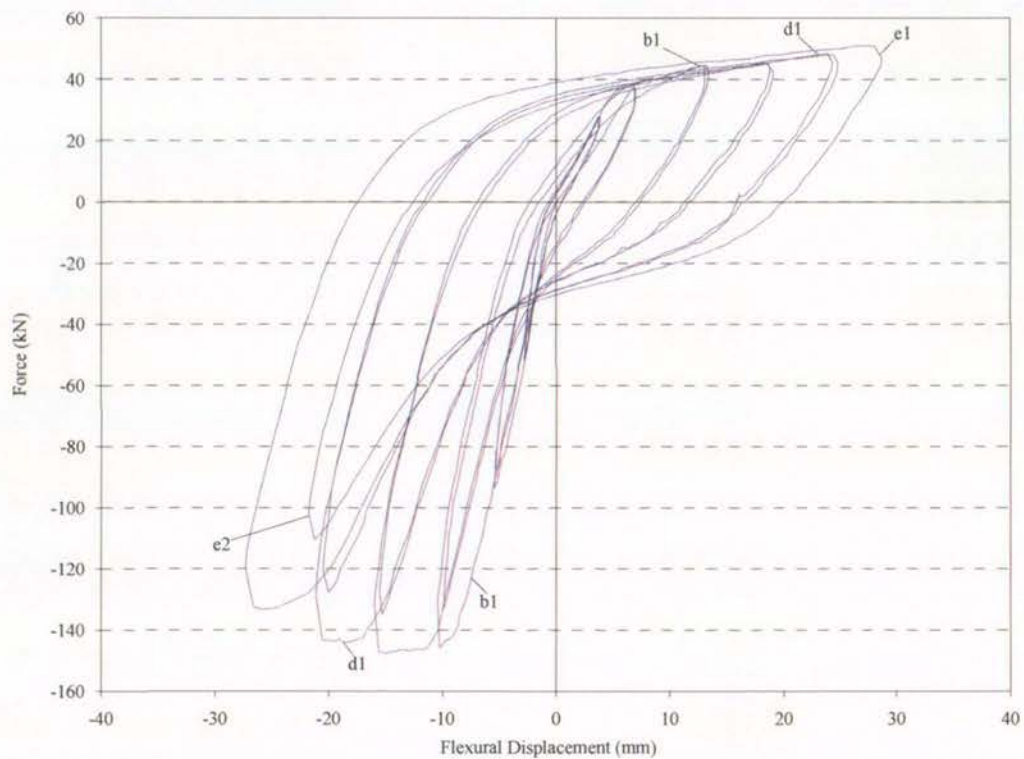


Figure 4.51-Flexural displacement versus applied load (C1)

The elongation of beam C1 shown in Figure 4.52 is very similar to that of A1 (see Figure 4.13). The elongation is limited slightly in the negative displacement direction due to less yielding of the top reinforcement.

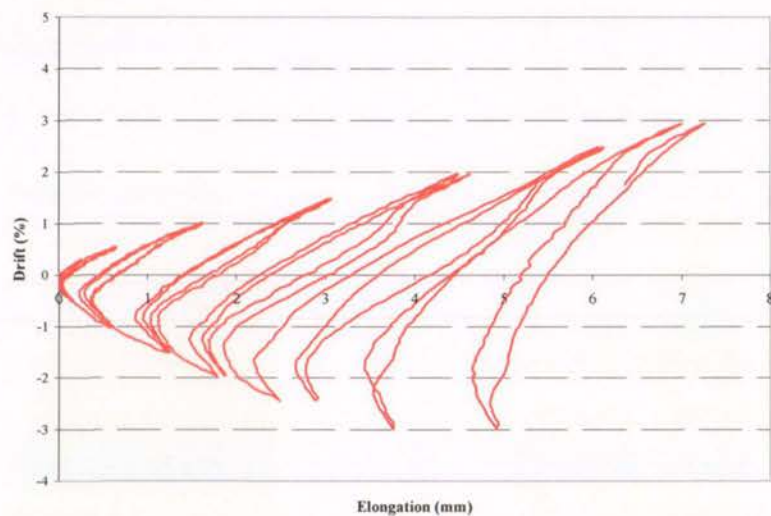


Figure 4.52-Beam elongation (C1)



#### 4.2.3.3. Test C2

The beam of Test C2 was identical to that of C1 except that the loading procedure was that of a uni-directional hinge test. The behaviour of the beam was very similar in the first phase of the test and during the cycles to 0.5% drift.

The load deflection curve (see Figure 4.56) showed that yielding of the reinforcement occurred on the first negative cycle to 1.0% drift at 0.96% drift (13.4mm displacement). At this stage a crack at the beam springing opened to a width of 0.8mm. Several diagonal tension cracks had also formed along the beam.

Crushing of concrete occurred during the first negative cycle to 1.5% drift. The crack at the springing had a width of 1.5mm. The load deflection curve in Figure 4.56 shows that the beam reached its maximum load capacity on this cycle. Crushing of concrete continued as the beam was displaced to 2.0% drift and was accompanied by minor spalling when the load was relaxed. A second flexural crack located 150mm out from the beam springing opened to a width of 1.5mm, while the crack at the springing was open to 3.0mm. These cracks can be seen in Figure 4.53.

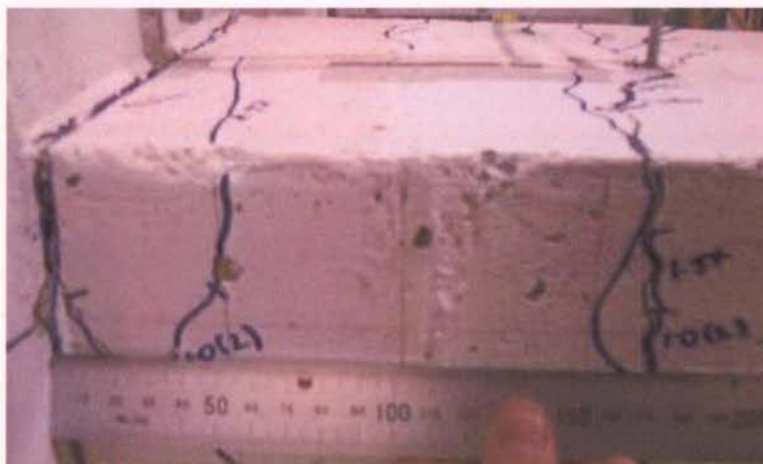


Figure 4.53-Flexural cracking at 2.0% drift (C2)

Significant spalling occurred during cycles to 3.0% drift. During load cycles to 3.5% drift further spalling exposed the transverse and longitudinal reinforcing on the underside of the beam. This was accompanied by a drop of load capacity as can be seen in the load deflection relationship shown in Figure 4.56. During the first cycle to 5.0% drift the bottom longitudinal reinforcement buckled, as shown in Figure 4.54.



Figure 4.54-Buckling of bottom bars at 5.0% drift (C2)

The load deflection curve showed that degradation of load capacity continued during the following cycles. The strength degradation was not as rapid as that seen in the load deflection curves of beams B2 (see Figure 4.38) or C1 (see Figure 4.48). The buckling of the bottom reinforcing bars also became more pronounced. The test was stopped after two complete cycles at 8.5% drift when the load deflection relationship (Figure 4.56) showed the load capacity had dropped below 80% of its peak value. The condition of the beam at the end of the test is shown in Figure 4.55.

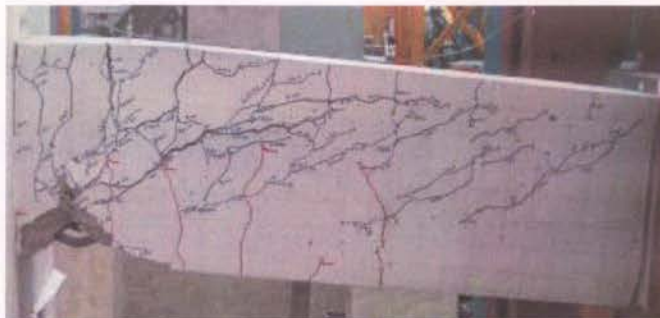


Figure 4.55-Crack pattern at the end of test (C2)

As can be seen in Figure 4.56, the loss of stiffness is not as severe as that exhibited by Test B2. This might be due to less damage to the concrete in the compression zone because of the higher concrete compressive strength.

The displacement of beam C2 in Figure 4.56 shows larger ductility for uni-directional hinges compared with the reverse cyclic test of C1 seen in Figure 4.48. The decay in strength is much slower than in beam C1. The beam also retains its stiffness for much longer than in the reverse cyclic test.



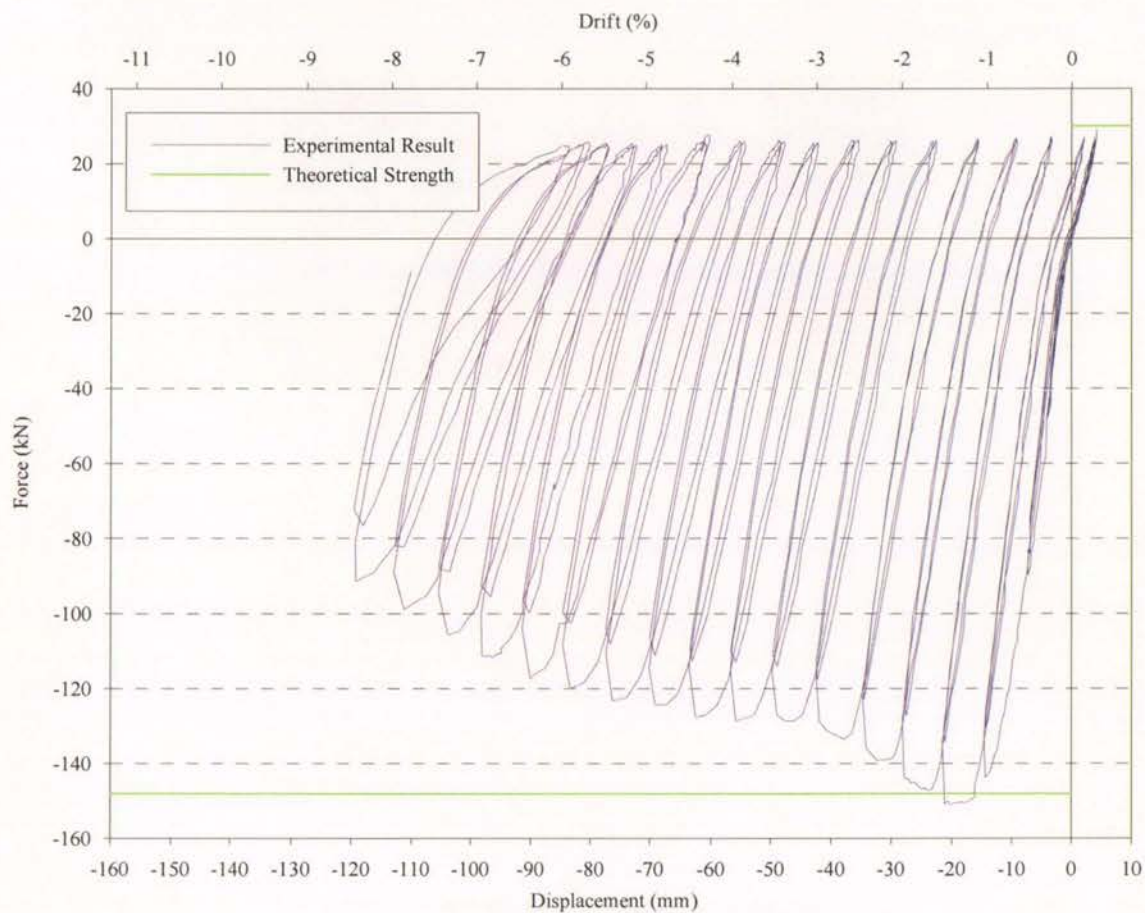


Figure 4.56-Load displacement response of specimen C2

Figure 4.57 shows the contribution of the shear and flexural displacement components to the overall beam displacement. The flexural component dominates the displacement in this test. The closure error is very small. The shear component increases during later cycles, but still the shear deformation is only about 10% of the total displacement. This explains the little pinching and dissipative loops in the hysteresis loops seen in Figure 4.56.



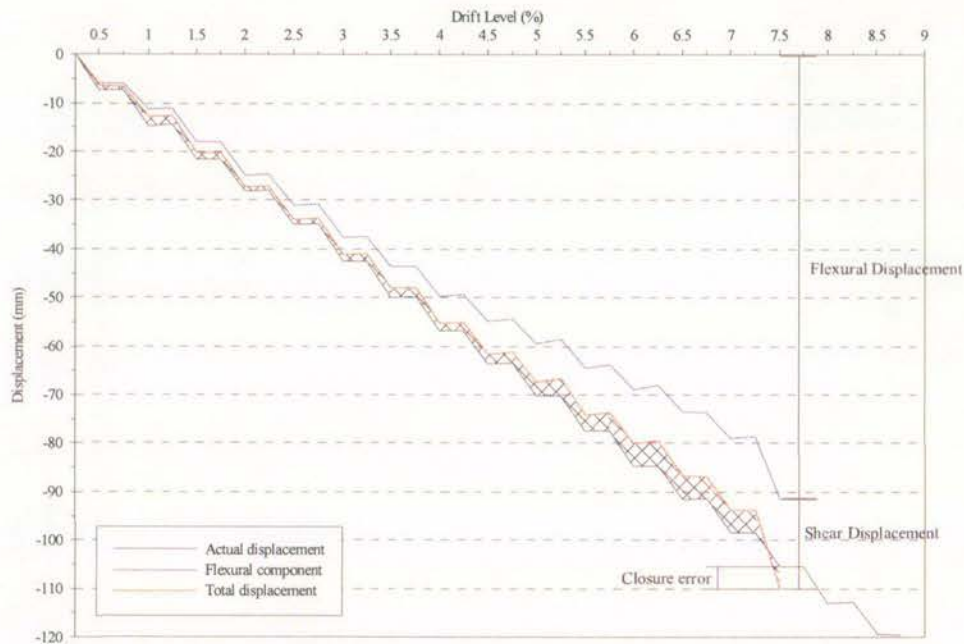


Figure 4.57-Contribution of shear and flexure to the total displacement at the peaks of the loading cycles for beam C2

The shear and flexural responses, shown in Figure 4.58 and Figure 4.59 respectively, reflect the previous observations of flexural dominant behaviour but increased contribution of shear in later cycles.

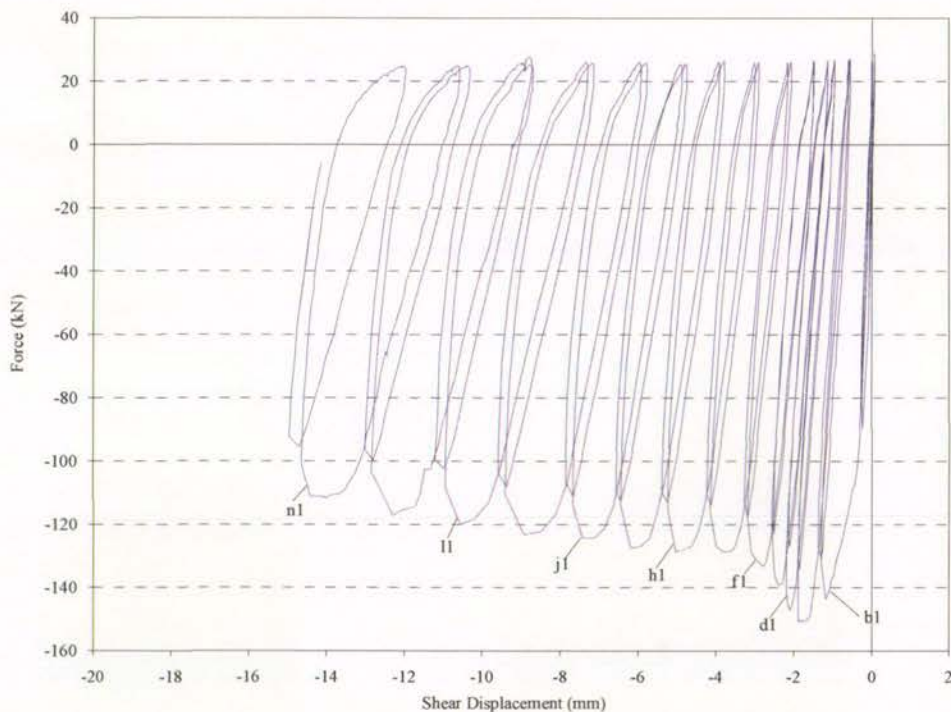


Figure 4.58-Shear displacement versus applied load (C2)

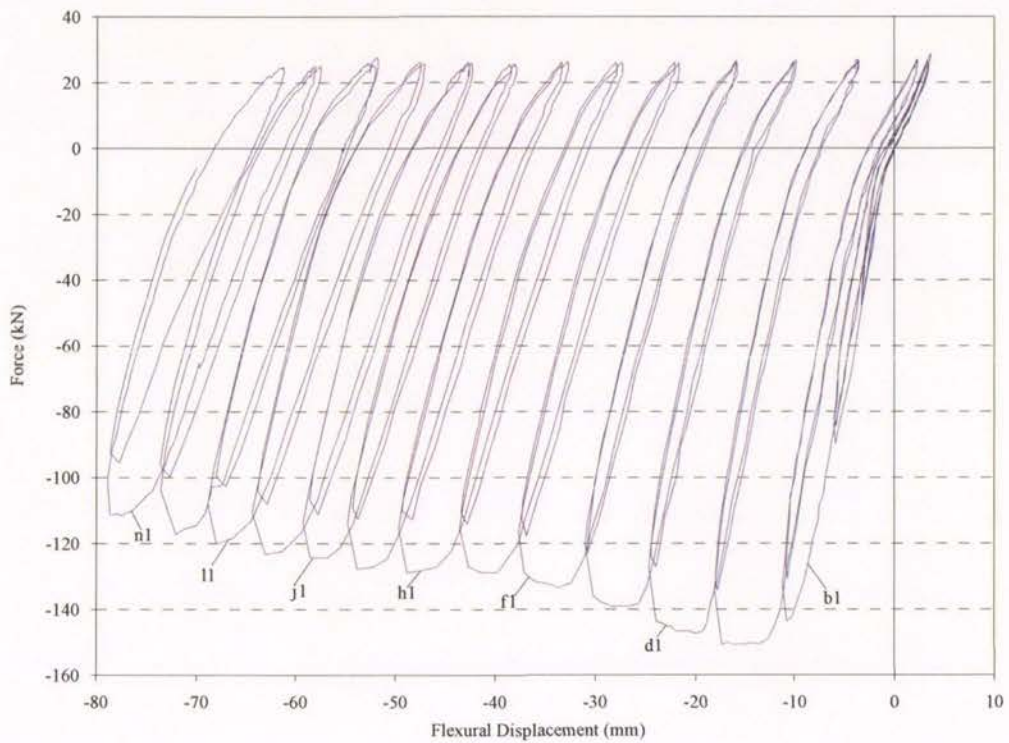


Figure 4.59-Flexural displacement versus applied load (C2)

The elongation data shows unexpected patterns during the early stage of the test, Figure 4.60 shows negative elongation or beam shortening up to 2.0% drift after which the beam lengthens again. It is very unlikely this would have actually been the case and must be due to some instrumentation error. The total amount of elongation is small when compared to the uni-directional test of B2 (see Figure 4.42). This is surprising as yield of reinforcement occurred in beam C2 and not in B2, thus more elongation would be expected in C2. This behaviour also indicates there may have been some instrumentation error.

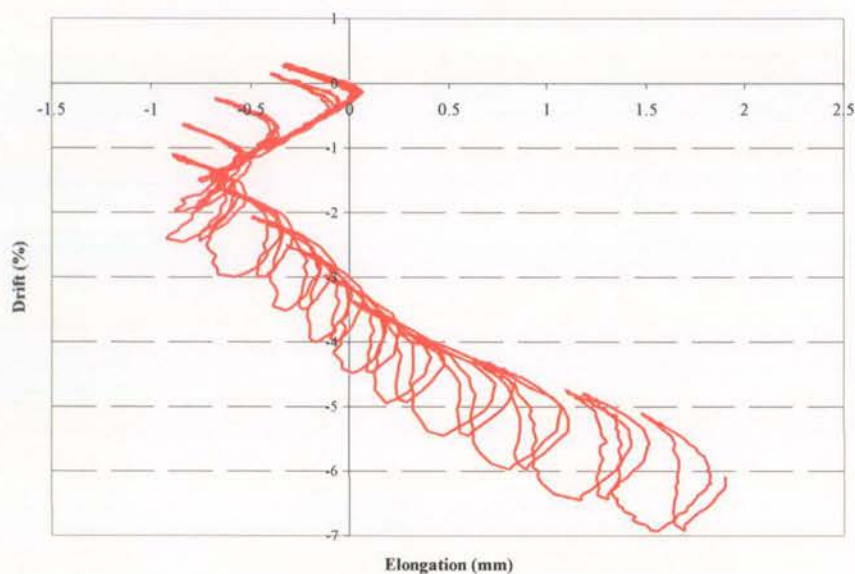


Figure 4.60-Beam elongation (C2)

#### 4.2.4. Unit D

##### 4.2.4.1. General details

The width of beams D1 and D2 was increased to 410mm while keeping the same section depth and beam length as in the previous six tests. The increased width meant the central longitudinal reinforcing bar was at the limit of the horizontal spacing, beyond which a central transverse leg (i.e. an intermediate tie) would be required. The longitudinal steel for these two tests consisted of three 16mm diameter Grade 500 bars top and bottom. Two-legged 10mm stirrups made from Grade 500 reinforcement were used at 175mm centres. The first of these tests was reversing hinge test and the second a uni-directional test.

##### 4.2.4.2. Test D1

Behaviour in the early stages of the test D1 was similar to that of previous tests. Flexural cracks formed at the approximate location of the transverse reinforcement in the first phase. The load deflection relationship (see Figure 4.67) showed that yielding of flexural reinforcement occurred at 0.77% drift (10.9mm displacement) and 0.70% drift (9.9mm displacement) in the negative and positive directions respectively in the first cycle to 1.0% drift. A crack at the beam springing was open to 0.9mm. Unlike in previous tests, there was little inclination to the cracks except for one diagonal tension crack located near the load application as seen in Figure 4.61.



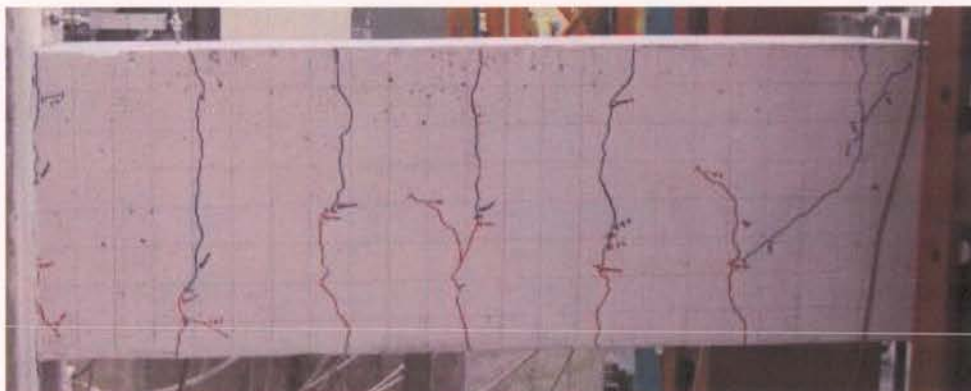


Figure 4.61-Crack pattern after two complete cycles at 1.0% drift (D1)

A crack located 210mm from the springing opened to a width of 0.8mm in the first cycle to 2.0% drift. This crack remained open to a width of 0.5mm when the load was removed. Inclined cracks also formed within the hinge zone that intersected the flexural crack located 210mm out from the springing. The diagonal tension crack had a width of 1.0mm during cycles to 2.5% drift. The crack pattern at 2.5% drift can be seen in Figure 4.62.

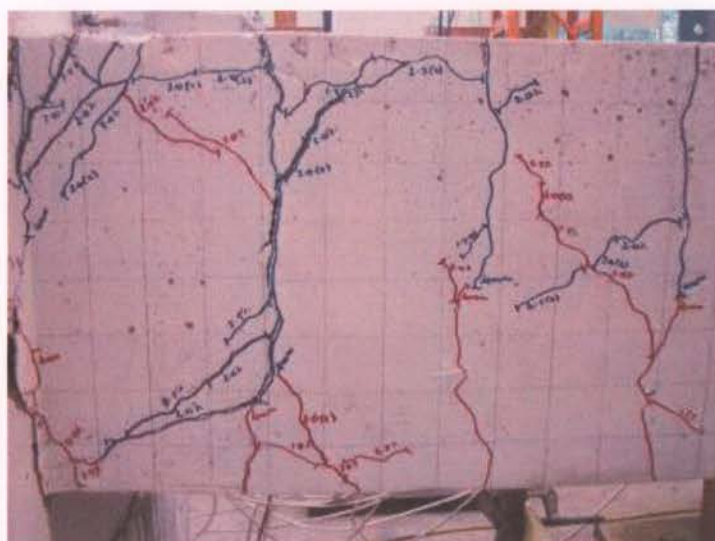


Figure 4.62-Crack pattern after two complete cycles to 2.5% drift (D1)

By the completion of the 3.0% drift cycles the diagonal tension cracks shown in Figure 4.62 were open to a width of 7.0mm. This enabled the transverse reinforcement to be seen through the crack. Upwards displacement of cracked concrete on the top of the beam indicated initiation of buckling of the top steel as shown in Figure 4.63. Similar movement was exhibited on the underside of the beam. This phenomenon was accompanied by a decrease in

load capacity on subsequent displacement levels in the load deflection relationship (see Figure 4.67).



Figure 4.63-Displacement of concrete at top of beam indicating buckling at 3.0% drift (D1)

During the first cycle at 4.0% drift spalling of concrete exposed the buckled reinforcement. The reinforcement had buckled between the first and second stirrup sets as shown in Figure 4.64. This was followed by the exposure of the buckled bottom bars at 4.5% drift.



Figure 4.64-Buckled top bars at 4.5% drift (D1)

The top longitudinal reinforcement ruptured during the first cycle to 5.5% drift. As in beams B1 and C1, the reinforcement ruptured due to flow cycle fatigue. The fractured bar is shown in Figure 4.65. Also visible is the deformed second stirrup caused by the middle bar buckling over a longer length than the outer two bars. Similar behaviour to this was seen in beam A1. The condition of the beam at the end of the test is shown in Figure 4.66.



Figure 4.65-Ruptured bar and deformed stirrup at the end of test (D1)



Figure 4.66-Condition of beam at the end of test (D1)

Figure 4.67 clearly shows that the load capacity of the beam was limited by yielding of the flexural reinforcement in both displacement directions. There is an obvious decrease in stiffness on each consecutive cycle. A drop in load capacity is seen at the 3.5% drift level, this was associated with buckling of reinforcement and spalling of cover concrete.



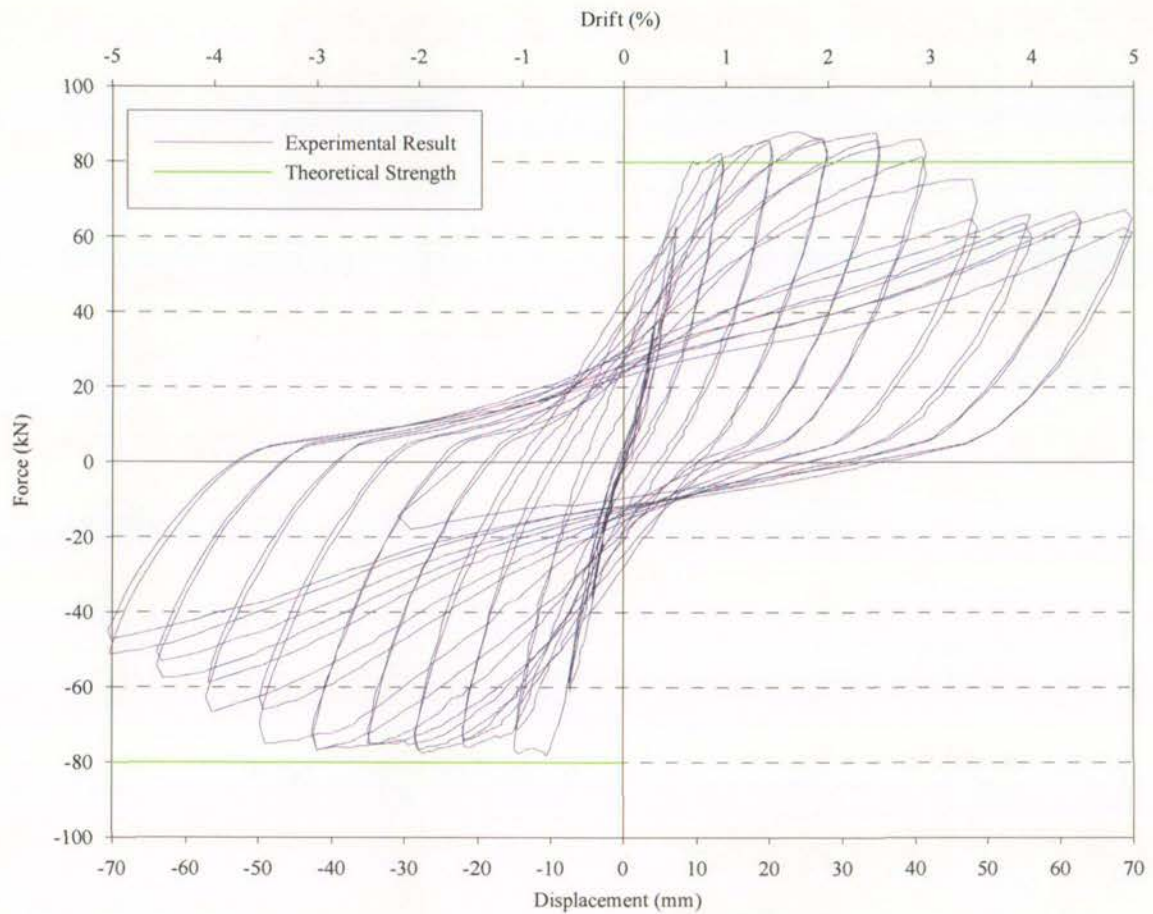


Figure 4.67-Load displacement response of specimen D1

Figure 4.68 indicates there was some instrumentation error during the test of beam D1 which resulted in large closure error throughout the test. This is also indicated by the unusual shape of the shear and flexural force-displacement curves shown in Figure 4.69 and Figure 4.70 respectively.

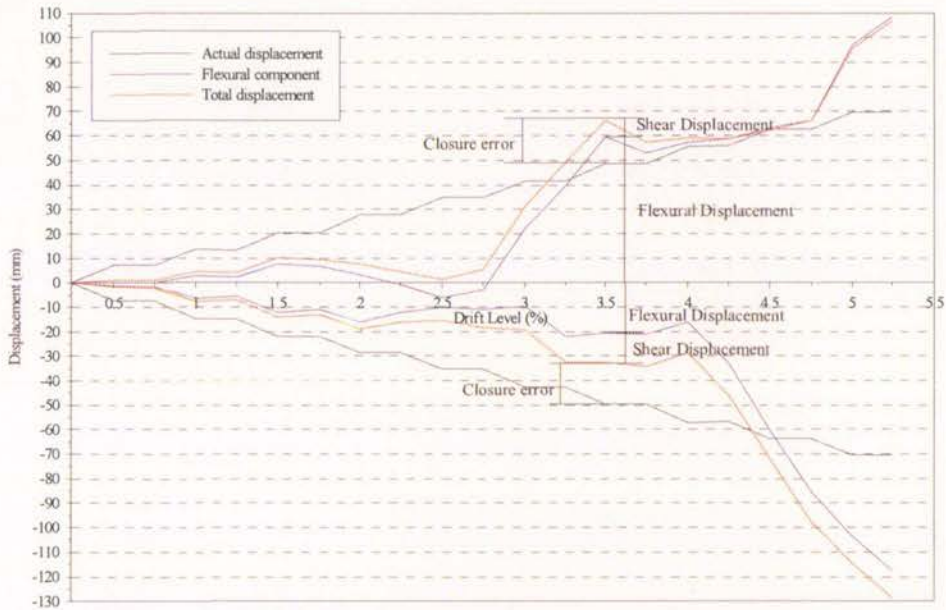


Figure 4.68-Contribution of shear and flexure to the total displacement at the peaks of the loading cycles for beam D1

The shear response shown in Figure 4.69 is reasonable until the shear displacement reaches approximately 12mm. This indicates the bulk of the error seen in Figure 4.68 is due to the flexural component. Figure 4.69 shows that the shear displacement is the source of the pinching behaviour seen in Figure 4.67. Also visible is the increase of shear displacement on each consecutive cycle as exhibited in previous tests.

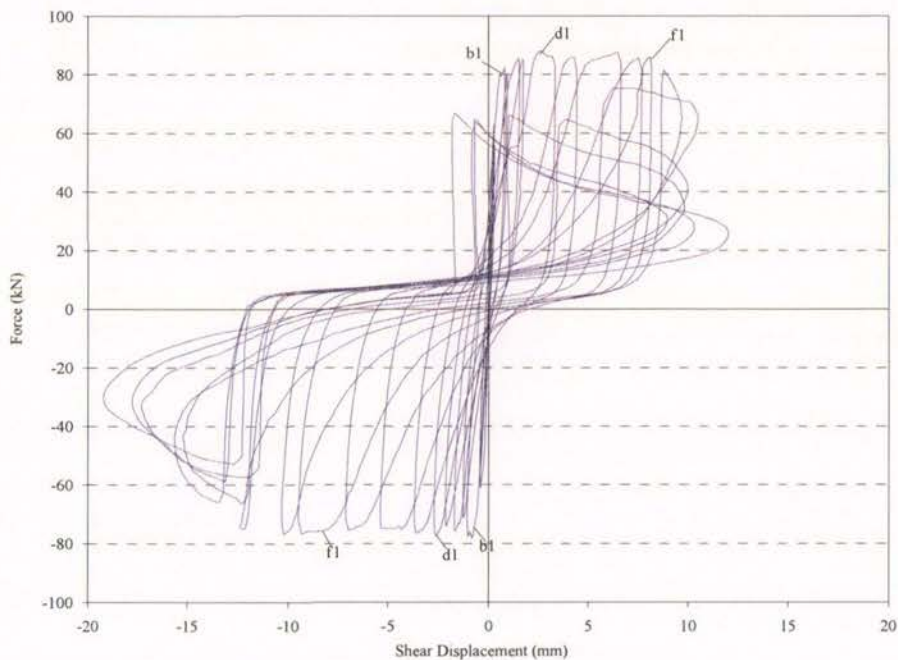


Figure 4.69-Shear displacement versus applied load (D1)

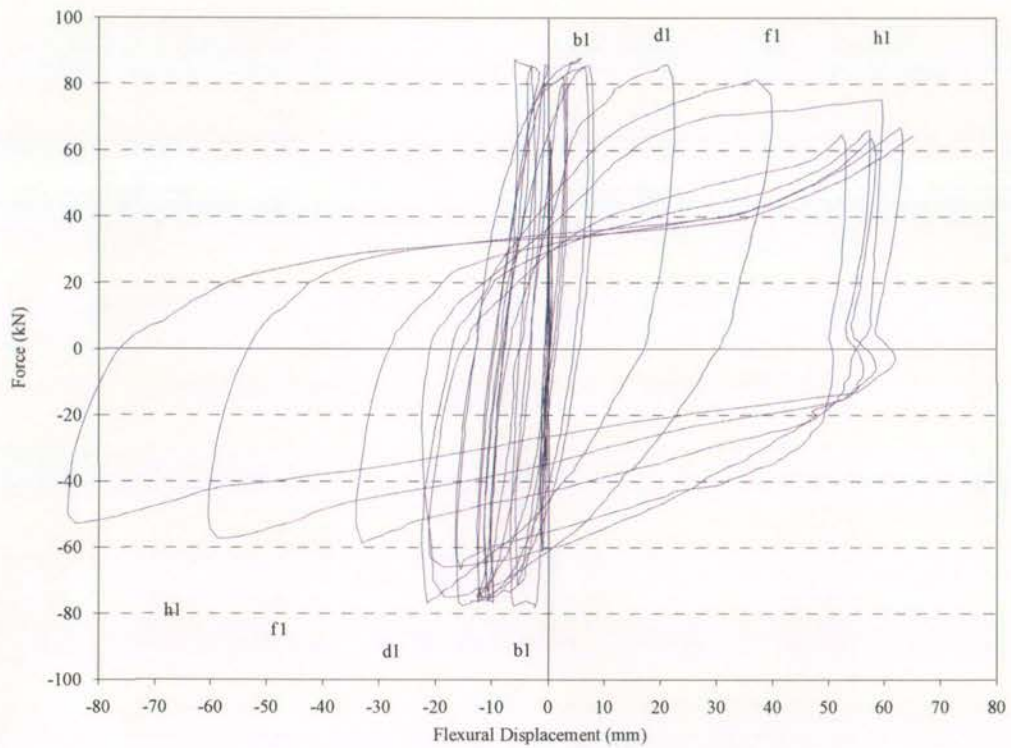


Figure 4.70-Flexural displacement versus applied load (D1)

Because the flexural displacement is unreliable, the elongation data is not expected to be accurate. However Figure 4.71 does show the qualitative behaviour previously seen in beams A1 and A2 (see Figure 4.13 and Figure 4.22).

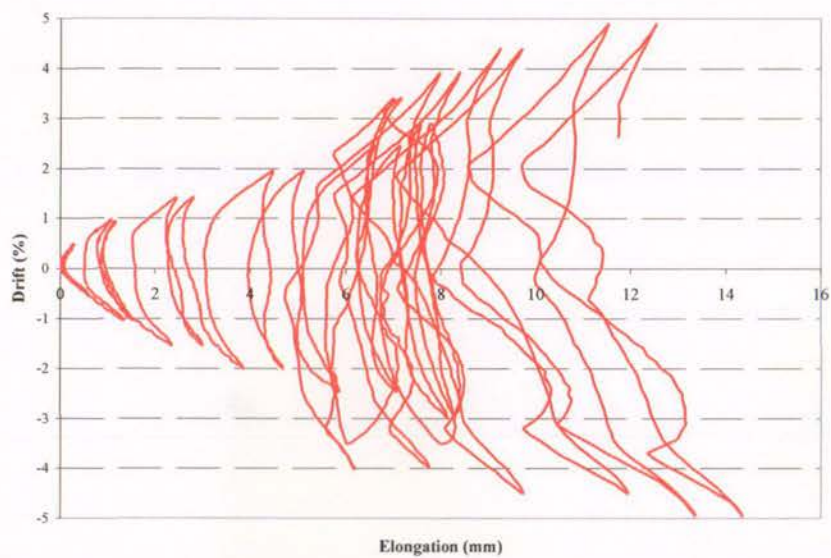


Figure 4.71-Beam elongation (D1)



#### 4.2.4.3. Test D2

Test D2 was the uni-directional hinge test with the same details as beam D1. Behaviour of the beam was similar to that of D1 in the initial stages of the test. The load deflection relationship showed that yield of the flexural reinforcement occurred at 0.68% drift (9.7mm displacement) on the first negative cycle to 1.0% drift. A flexural crack located 70mm out from the springing opened to a width of 1.5mm. The crack pattern at this point is shown in Figure 4.72.

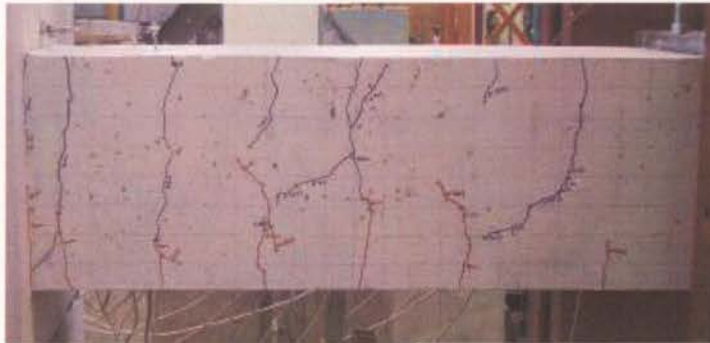


Figure 4.72-Crack pattern after two complete cycles at 1.0% drift (D2)

After two full cycles at 2.5% drift the flexural crack 70mm from the beam springing was open to a width of 4.5mm and the crack at the beam springing was open to a width of 1.5mm as shown in Figure 4.73.



Figure 4.73-Open cracks at 2.5% drift (D2)

During the first cycle to 3.0% drift crushing of concrete at the bottom of the beam was visible. This was followed by a diagonal tension crack forming in the hinge region during the

load controlled cycle to 75% of the theoretical strength. Both crushing and the diagonal tension crack are shown in Figure 4.74.

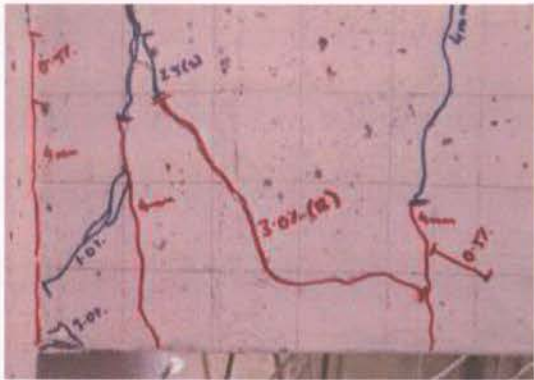


Figure 4.74-Concrete crushing and positive shear crack at 3.0% drift level (D2)

A flexural crack located 250mm out from the springing opened to a width of 1.5mm during the negative cycle to 3.5% drift. Diagonal tension cracks formed along the length of the beam on the negative cycle as seen in Figure 4.75. As the load was released spalled concrete fell from the underside of the beam.

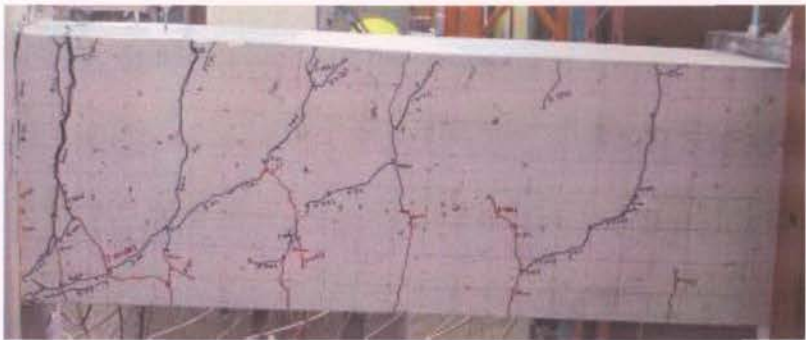


Figure 4.75-Crack pattern after 3.5% drift (D2)

During the cycles to 5.5% drift the flexural crack located 70mm out opened to a width of 7mm exposing the transverse reinforcement. During the positive cycle to 8.0% drift the cracked concrete on the top of the beam displaced upwards indicating possible buckling of the top reinforcing. At this point there was no evidence of the bottom bars having buckled despite being subjected to a higher compressive force. This was due to the reduction of buckling resistance of the top bars when they yielded in tension during previous cycles.

During cycles to 9.0% drift extensive spalling from the underside of the beam exposed slightly bent longitudinal bars. The test was stopped when the top longitudinal reinforcement ruptured during the first cycle to 10.5% drift. Removal of spalled concrete showed that the central top bar had bent the second stirrup upwards in a similar manner to that of beam D1, as shown in Figure 4.76. Figure 4.77 shows the condition of the beam at the end of the test.



Figure 4.76-Ruptured bar and deformed stirrup at the end of test (D2)

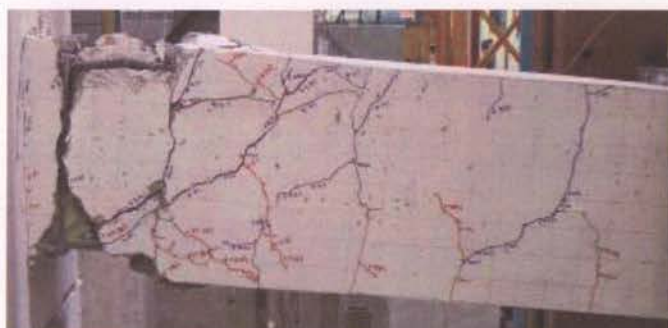


Figure 4.77-Beam condition at the end of test (D2)

Figure 4.78 illustrates the increased ductility of the uni-directional hinge test compared with the reverse cyclic test (see Figure 4.67). During cycles in excess of 8.0% drift there is a significant increase in the energy dissipation and reduction in stiffness of the hysteresis loops, this is probably related to an increased contribution of shear behaviour.



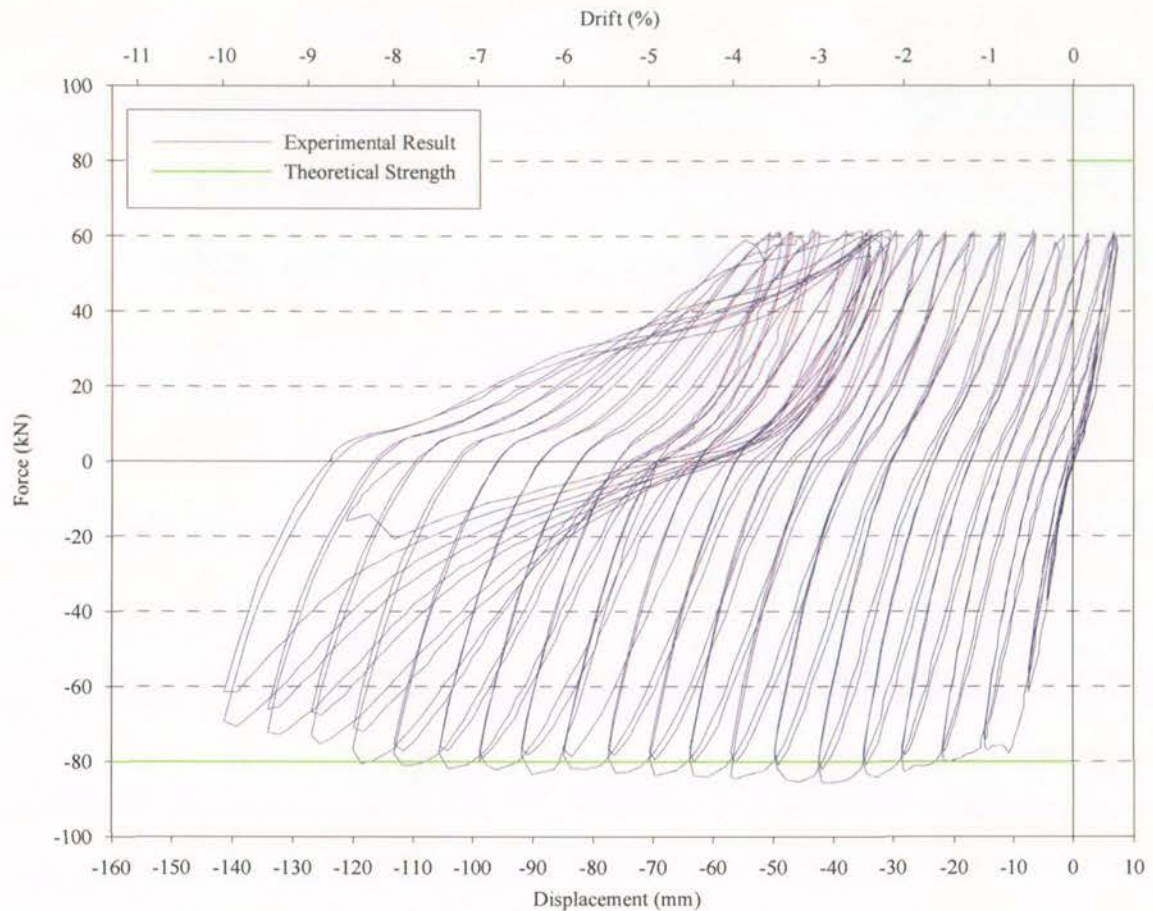


Figure 4.78-Load displacement response of specimen D2

Figure 4.79 shows breakdown of the total beam displacement into shear and flexural components. It illustrates the dominant contribution of flexure to the total displacement. The closure error is small but is of the same order of magnitude as the shear displacement. An increase in shear contribution at higher displacement levels can be seen, however the full extent of this can not be seen due to lack of reliable data at the higher displacement levels due to buckling of the reinforcing.



Figure 4.79-Contribution of shear and flexure to the total displacement at the peaks of the loading cycles for beam D2

Figure 4.80 shows the shear force-displacement response of test D2. Unlike in previous tests, there is not an obvious increase in the shear displacement on each consecutive cycle. This indicates the shear stiffness was not degrading significantly on each cycle. This is possibly linked to the lower shear stress applied to this beam than the first three test units because of the increased shear area and reduced steel content.

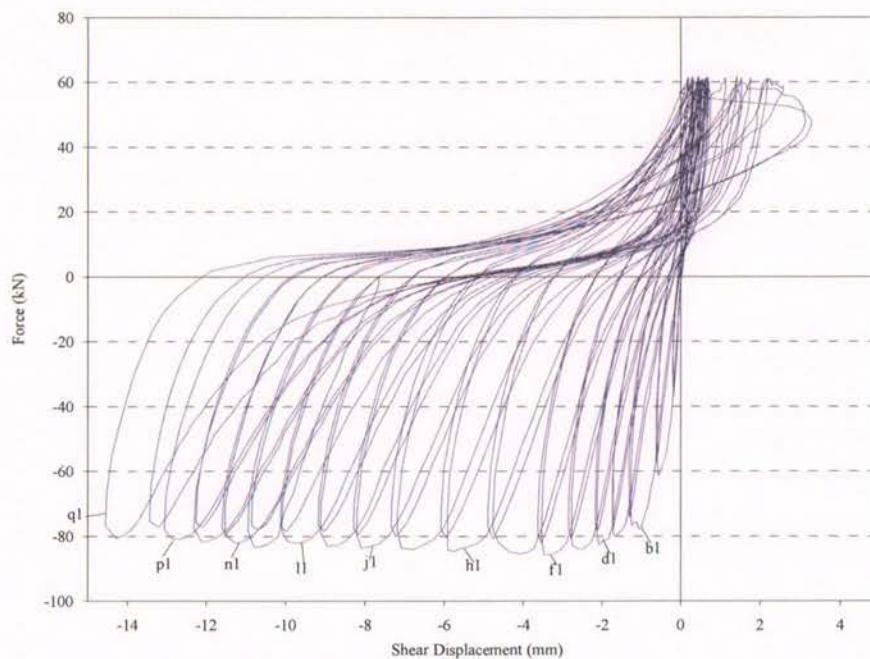


Figure 4.80-Shear displacement versus applied load (D2)

The flexural behaviour shown in Figure 4.81 is similar in many ways to previous uni-directional tests. However, during the last two displacement cycles the hysteresis loops become much fatter and dissipative.

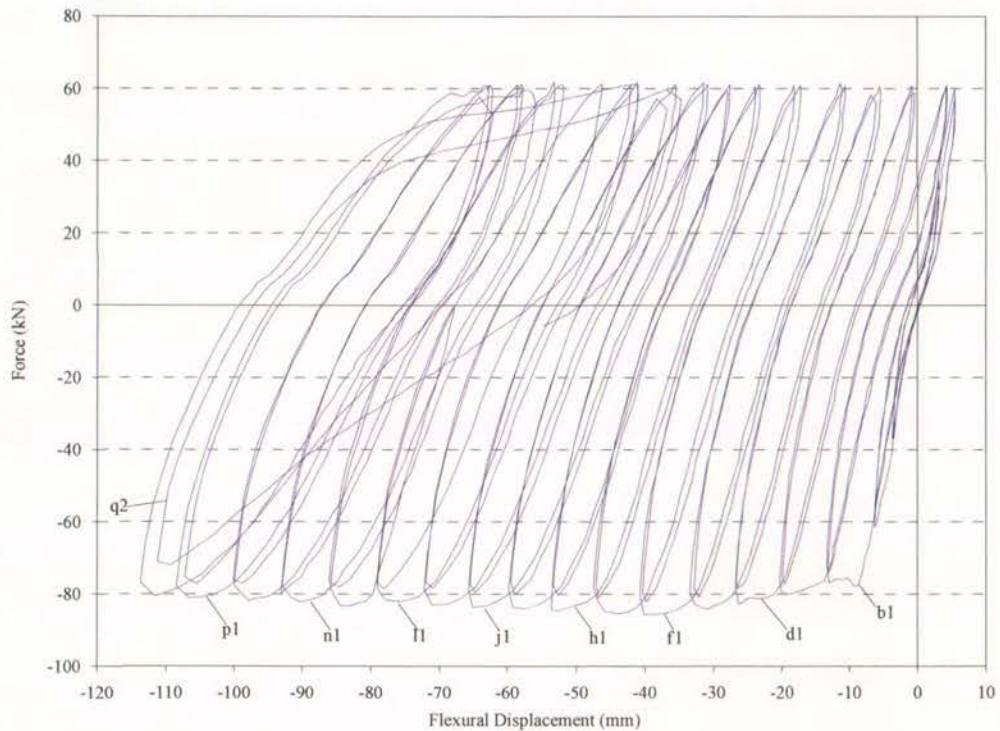


Figure 4.81-Flexural displacement versus applied load (D2)

There was significant elongation of beam D2 as shown in Figure 4.82. There is some unusual behaviour in the cycles to 9.0% drift, but ignoring these, the elongation is still approximately 11mm. There is much more elongation of this beam than in the previous two uni-directional beams, likely due to the increased amount of yielding of the flexural reinforcement.



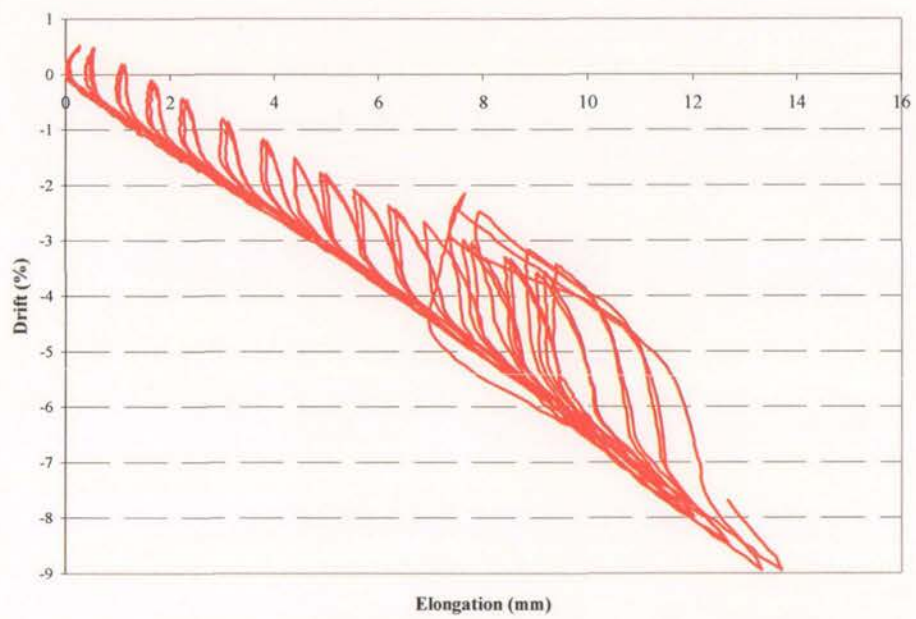


Figure 4.82-Beam elongation (D2)

## **5. ANALYTICAL INVESTIGATION**

### **5.1. INTRODUCTION**

Finite element models of the test beams were analysed to see if the observed behaviour of the beams could be predicted analytically. Comparisons of experimental measurements and the analytical prediction of the total end displacement, shear and flexural contributions and the beam elongation were made.

The analytical tool used was UC-win, a non-linear finite element analysis programme that is based on material models developed by Okamura and Maekawa (1991). The programme consists of two sections; the analysis solver section and the interface section. The analysis engine was developed in the Concrete Laboratory, University of Tokyo. It deals with two-dimensional non-linear dynamic and static analysis of reinforced concrete structures. The interface was developed by FORUM8, a civil engineering design software and marketing company.

The programme itself consists of two user interfaces, UC-win/MESH and UC-win/COMD. In UC-win/MESH, the user is required to set up the mesh, the support conditions and to identify the material properties within each element. The mesh can be transported into UC-win/COMD where the load types are specified and the model is analysed.

Unlike other common finite element analysis programmes, such as SAP2000 or ETABS, UC-win analysis is based on element material properties rather than overall member behaviour. Uni-axial stress-strain relationships of reinforcing bars and biaxial stress-strain relationship of concrete are combined to form generalized constitutive relationships of reinforced concrete elements following smeared crack approach. The non-linear material models used are fully path-dependent and cover all possible loading, unloading and reloading paths.

In the macroscopic smeared crack model, the material properties are expressed as average stress – average strain relationships over the entire element. A finite region containing several cracks and reinforcing bars can be treated as a continuum. This approach is suitable for members with distributed reinforcement in two directions such as frames or walls. On the other hand, for reinforced concrete joints, where the local discontinuity is large, the discrete

crack model may be used to characterize the behaviour, including bond-slip relationship between concrete and reinforcement, interface shear transfer across cracks, and opening and closing of the cracks at the section.

The program can be used to find the peak response, the strain profile and the residual damage. The time history response leading to failure of a reinforced concrete structure can also be tracked. In the analysis, the program has the option of a Basic Mode or an Advanced Mode. In the Advanced Mode, extra input items or property parameters are available in addition to those in the Basic Mode. For example, allowance can be made for effective reinforcement ratio, tension softening, shear dilatancy and peak compressive strain. The recommended values used in Basic Mode are displayed as guidelines for the advanced setting.

In order to account for the bond between the reinforcing bars and the surrounding concrete, the reinforcing bars' local stress-strain relationship is modified to relate the average stress and average strain within the element length. The average stress takes into account the stress carried by the concrete between the cracks. The details of the average constitutive relationships of reinforcing bars and concrete used in UC-win/COMD are given in Okamura and Maekawa (1991).

The concrete in the cross section is divided into two zones namely, a reinforced concrete zone and a plain concrete zone, as illustrated in Figure 5.1. The reinforced concrete zone represents the area of concrete contributing to tension stiffening close to the longitudinal reinforcing bars and the plain concrete zone consists of the area far from the reinforcing bars. In the reinforced concrete zone, the average tensile stress carried by concrete has a significant value in the post-cracking stage, whereas the plain concrete zone abruptly loses its tensile stress carrying capacity after cracking.

The average stress of a 2-D smeared element combines the average stress of concrete and average stress of reinforcing bars. To exclude the bond ineffective plain concrete zone in the post-cracking tensile response, the effective reinforcement ratio is calculated as the area of reinforcement divided by the area of reinforced concrete zone. The reinforced concrete zone is calculated as the area which cracks when the reinforcing bars yield. Assuming the bond



effective zone to be a square of side,  $h$ , surrounding a reinforcing bar of diameter,  $d$ , force equilibrium gives:

$$h^2 \cdot f_t = \frac{\pi \cdot d^2}{4} f_y \quad \text{Equation 7}$$

$$h = \sqrt{\frac{\pi}{4} \frac{f_y}{f_t}} d \text{ (mm)} \quad \text{Equation 8}$$

Where:  $f_y$  = bar yield stress (MPa)  
 $f_t$  = concrete tensile strength (MPa)  
 $d$  = bar diameter (mm)

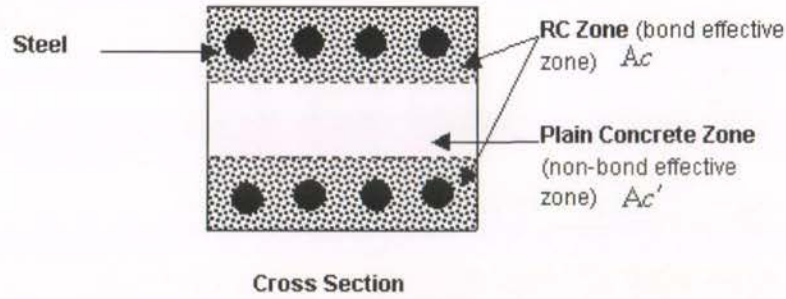


Figure 5.1-Bond affected zone in reinforced concrete elements (UC-win)

The software also allows the post-cracking degradation of tensile stress to be defined by specifying a tension softening factor,  $c$ , which can vary from 0.1 to 2.0. The effect of this parameter on the tensile stress degradation after cracking of the concrete is governed by equation 9:

$$\sigma = f_t \left( \frac{\varepsilon_{cr}}{\varepsilon} \right)^c \quad \text{Equation 9}$$

Where:  $\varepsilon_{cr} = 2 \times \frac{f_t}{E_t}$

$\varepsilon$  is the strain in the concrete,  $f_t$  is the concrete tensile strength and  $E_t$  is the tensile elastic modulus of concrete. The effect of different values of tension softening factor on the stress-strain curve is illustrated in Figure 5.2.

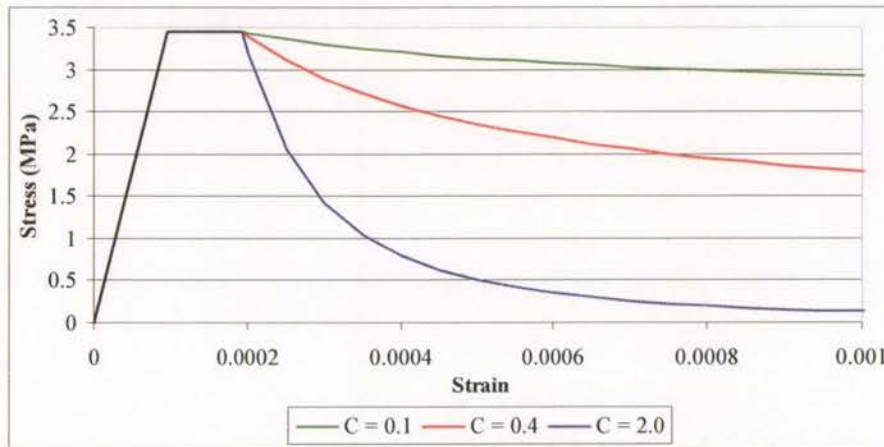


Figure 5.2-Effect of varying tension softening factor on concrete stress strain behaviour

The program uses three different failure criteria, namely the maximum tensile strain normal to a crack, the maximum compressive strain parallel to a crack and the maximum shear strain parallel to a crack. When one of these strain values is reached in any element, the program gives a message of failure and terminates the analysis. The default values for these failure criteria are 3%, 1% and 2% respectively. As these values correspond to localised failure of an element and not necessarily the global failure, in reality (i.e. experiments) a structure can still function beyond such a localised failure. Therefore, the maximum failure strain of 10% was used for all tests in order to capture as much of the experimental cycles as possible.

Other parameters available in the analytical tool are the crack shear dilatancy factor and the crack shear transfer factor. The crack shear dilatancy factor scales the component of shear stress parallel to the crack added to the normal stresses. The two extreme values for the shear dilatancy factor, 0 and 1, were investigated by Peng (2005). They were found to have little effect for beams similar to those tested in this project. The programme suggests a shear dilatancy factor of 0 for normal concrete, and this value was used for the models analysed in this project.

The crack shear transfer factor describes the crack plane geometry, essentially the amount of interlock between two surfaces of a crack. The programme suggests a value of 1.0 for normal strength concrete. This value was used for all models. Note that as smeared crack approach is used in these analyses, the slip of the elements along diagonal shear cracks is not captured. This may have been significant in the tested beams, because they are nominally ductile beams with minimal shear reinforcement.



## 5.2. ANALYTICAL MODEL

Each test beam was modelled separately as illustrated for beam A1 in Figure 5.3. The mesh geometry in each beam was altered to match the spacing of the transverse reinforcement. The nodes along the base of the support block and along the centre line were fixed in the horizontal and vertical directions. The overall dimensions of the model were the same as those of the actual test.

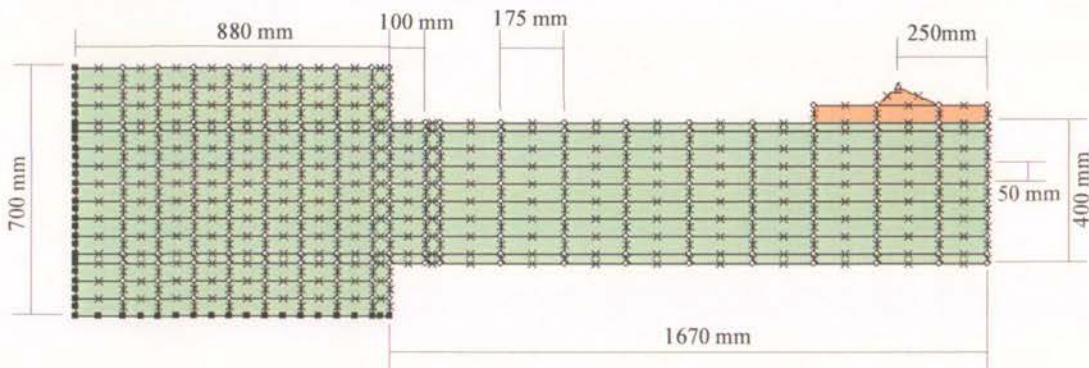


Figure 5.3-Mesh layout for numerical model of Test A1

Reinforced concrete elements were used for all parts of the specimen except for the elastic loading plate, which was modelled using steel plate elements to simulate the loading arrangement used in the tests. The concrete material properties specified were based on the cylinder strengths, which are given in Table 4.1. Each row of reinforcing steel was modelled in a single layer of reinforced concrete elements, while each stirrup set was modelled in a single column of elements. The vertical reinforcement within the support block was not considered in the model.

Different steel properties, based on measured steel yield stress values, given in Table 4.2, were created for each different bar type. As the reinforcement in the experiments did not sustain high strains, little strain hardening would have occurred. This means that any differences between actual bare bar behaviour and the bi-linear stress-strain relationship assumed in UC-win would have little influence on the numerical results.

The loading history used in each test, namely uni-directional or reversing was used in the corresponding analysis of the beam model. The uni-directional load protocol required the displacements recorded during the test to be used as the displacement history in the analysis



as the displacement corresponding to 75% of theoretical yield could not be obtained independently.

An analysis was carried out using a series of discrete joint elements (available in the program) at the beam to rigid block connection. Results of the analysis with joint elements are discussed in section 6.3. Parameters required for the joint are bar diameter, reinforcing ratio, steel yield stress, concrete compressive strength and the joint stiffness,  $K$ , which is given by the formula:

$$K = \frac{1}{100} E_c = \sqrt{2000 \times f'_c} \quad (\text{Peng, 2005}) \quad \text{Equation 10}$$

### 5.3. ANALYSIS RESULTS

#### 5.3.1. Unit A

Comparisons between the force displacement curves, for the load point, obtained from the tests and the numerical models were made for all eight beams. The experimental curves are those previously presented in Chapter 4.

Figure 5.4 shows the numerical and experimental force displacement curves for Test A1. The difference between the two is significant. The yield force has been overestimated by UC-win by approximately 20%, while the theoretical strength obtained from basic stress block calculations matches well with the experimental result.

There is a significant degradation of strength in the experimental result after the onset of buckling during the 3.0% drift cycles. The analytical curve does not exhibit any degradation of strength until the last cycle at 4.5% drift after which failure occurs in shear at the top of the beam (see Figure 5.7) and the analysis stops. The programme does not consider buckling of reinforcement so it is expected that the strength degradation caused by buckling in the experiment would not be captured.

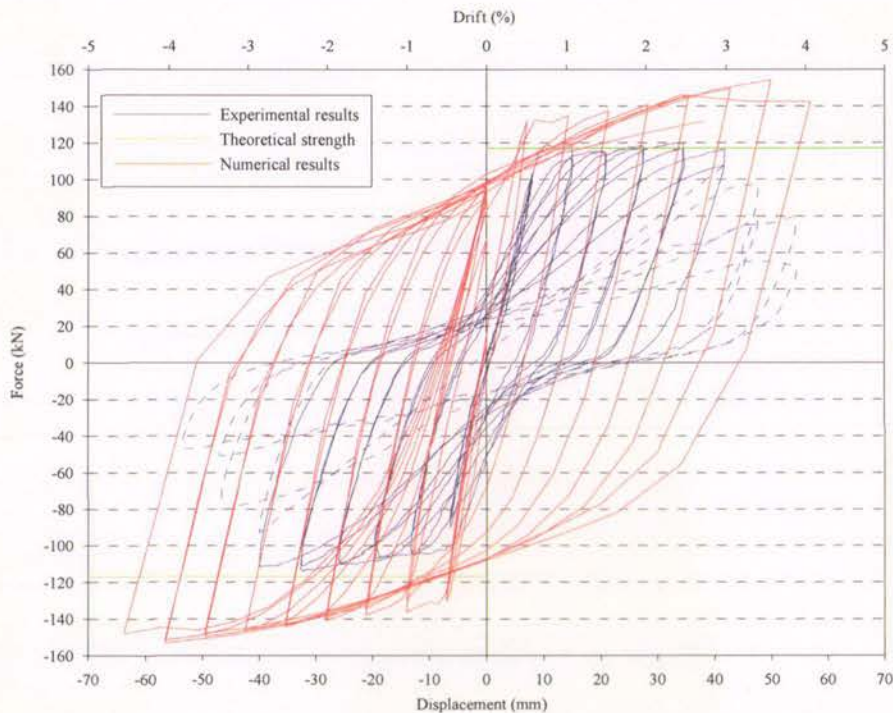


Figure 5.4-Numerical and experimental comparison (A1)

Figure 5.4 shows that the experimental result exhibits significant pinching behaviour which is not captured by the analysis. The total response is the combination of the flexural and shear components of displacement. When the shear component is inelastic and large, pinching of the overall result is more prominent. The analysis does not consider shear slip along cracks as the crack model used is a smeared crack model. The analysis also only considers elastic shear contribution. These two factors explain why there is no pinching behaviour in the analytical results. Figure 5.5 shows the flexural displacement from the experiment and the total displacement from the numerical analysis plotted against the applied force up to a drift level of 2.5%. The dramatic difference between the experimental flexural and numerical displacement at 2.5% highlights the magnitude of the shear component in the experiment. The absence of this shear component in the analysis is clearly one of the causes of the poor correlation between the experiment and numerical results.

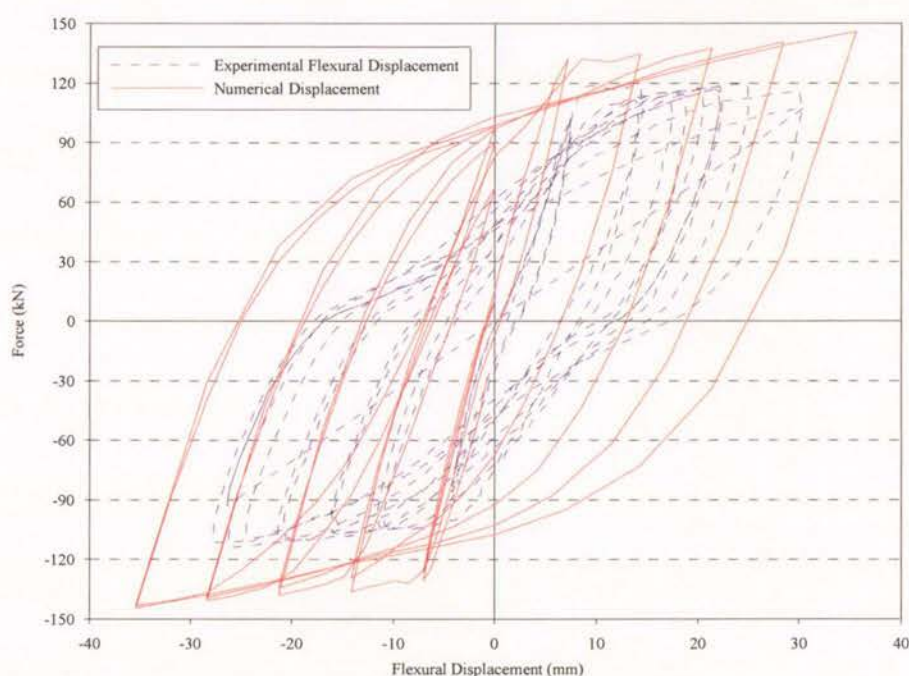


Figure 5.5-Comparison of experimental flexural displacement and the total numerical displacement (A1)

Figure 5.6 compares the initial stiffness in the experimental and analytical results. It is clear that the analysis overestimates the stiffness of the system. This is not surprising as there is invariably some degree of flexibility and slackness in the loading frame and support block. Table 5.1 compares the numerical and experimental initial stiffness of all beams in the both loadings directions. It is clear that the numerical analysis overestimates the initial stiffness of all the tested beams. The variation ranges from 35% to 71%.



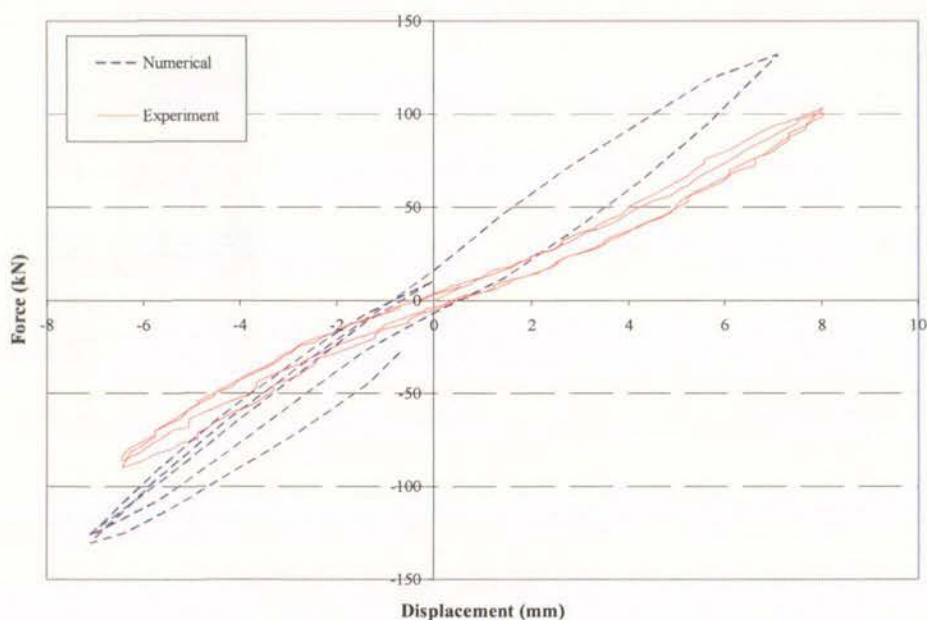


Figure 5.6-Comparison of initial stiffness (A1)

Table 5.1-Comparison of experimental and numerical initial stiffness of all beams

Beam	Negative Stiffness (N/mm)			Positive stiffness (N/mm)		
	Experiment	Numerical	% Difference	Experiment	Numerical	% Difference
A1	12.9	18.4	43	13.4	18.6	39
A2	13.0	18.2	40	12.7	18.4	45
B1	9.5	13.5	42	4.0	5.4	35
B2	9.7	13.5	39	4.4	7.3	66
C1	12.0	19.3	61	4.8	7.0	46
C2	11.4	19.3	69	6.5	11.1	71
D1	8.1	11.9	47	8.2	12.4	51
D2	7.7	11.9	55	8.0	12.4	55

Figure 5.7 shows the damaged regions taken directly from the analysis. Light damage is shown in yellow, considerable damage is shown in purple and failure damage is shown in red. The light and considerable damage relate to average strains (within the element) of 0.1% and 0.38% respectively while the failure damage is as previously specified in Section 5.2. In this case the mode of localised failure was excessive shear strain at the top of the beam in the second row of elements. This column of elements did not contain transverse reinforcement

due to the layout of the mesh; this explains why this column of elements failed before any other in shear.

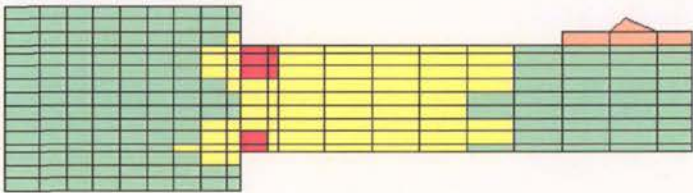


Figure 5.7-Failure and damage regions (Shear failure) (A1)

Figure 5.8 and Figure 5.9 show the crack patterns at 3.0% drift obtained from the analysis and experiment respectively. The displacement shown in Figure 5.8 is in centimetres. Both show extensive cracking in the plastic hinge region. The analytical crack pattern shows several cracked elements within the support block which were not observed during the test. The different deformation patterns between the two tests can be seen in the figures. The analytical deformation appears to be largely rotational at the hinge region, while the experimental deformation is clearly a mixture of a hinge rotation and shear deformation.

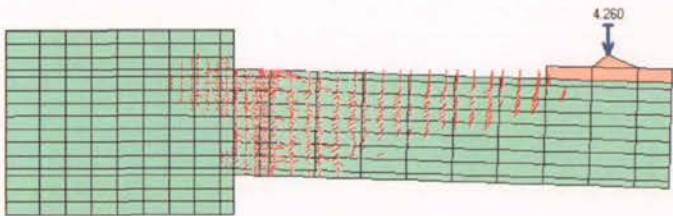


Figure 5.8-Crack pattern from analysis (A1)

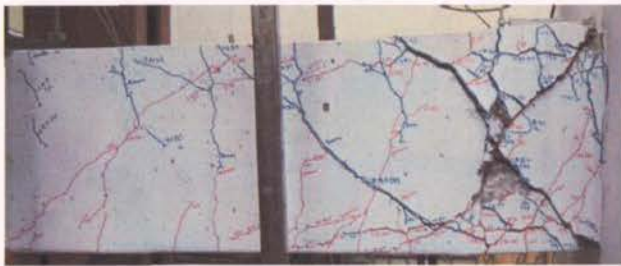


Figure 5.9-Crack pattern from test (A1)

Figure 5.10 shows the stress results taken from the analysis. The stresses displayed are those at 3.0% drift, which also corresponds to the load stage shown in Figure 5.8. In Figure 5.10 tensile stresses are shown in red at the top of the beam while the compressive stresses are shown in blue at the bottom of the beam. The high stress levels are concentrated in the



elements containing longitudinal reinforcement. The stress levels in the support block where additional bars are welded to the longitudinal reinforcement are low.

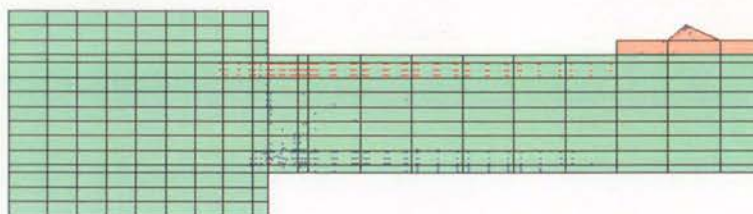


Figure 5.10-Analytical stress results (A1)

Figure 5.11 shows where the analysis has predicted that yielding has occurred in the reinforcement. As expected yield has only penetrated into the support block as far as the additional bars welded to the longitudinal reinforcement. The result shows yield occurring into the fifth column of elements from the beam springing, indicating a yield length of between 530mm and 660mm. The analysis also indicated that transverse reinforcement within the plastic hinge length yielded. This is not surprising as extensive diagonal tension cracking was observed to occur within this zone with a crack width in excess of 5mm being recorded, see Figure 5.9.

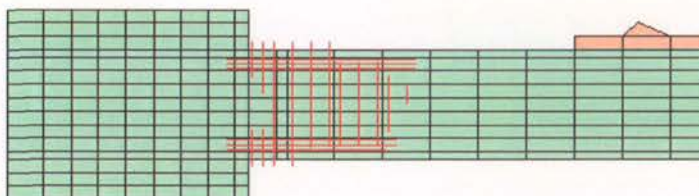


Figure 5.11-Analytical yield results (A1)

An analysis was carried out using a series of joint elements available in the program at the beam springing using the properties as described in section 5.2. Figure 5.12 shows the force displacement curve obtained from this analysis. This shows that the presence of the joint model does not significantly change the analytical prediction in this case. Thus no further analyses using a joint model were carried out.



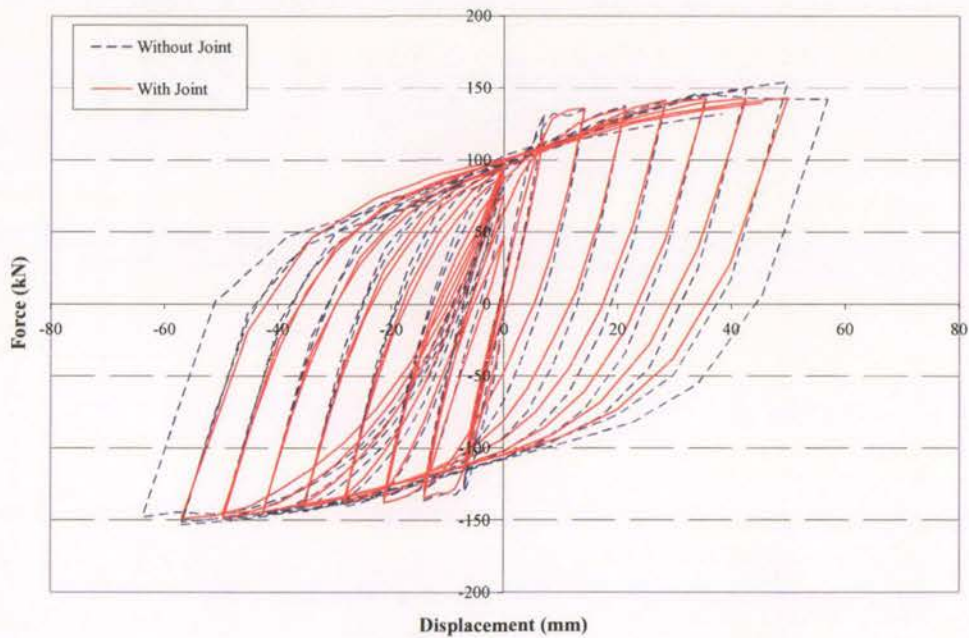


Figure 5.12-Comparison of numerical model with and without joint model (A1)

Figure 5.13 shows the experimental and analytical force displacement curves for beam A2. Similar problems exist with the model of Test A2 as those observed in A1; overestimation of strength, no pinching behaviour and no strength degradation. The difference between the analytical stiffness prediction and experiment at high displacement levels is not as large as in the previous case. This is due to increased shear steel in the plastic hinge zone reducing the effect of shear deformation and delaying buckling induced strength degradation during the experiment rather than any improvement in the analytical prediction.

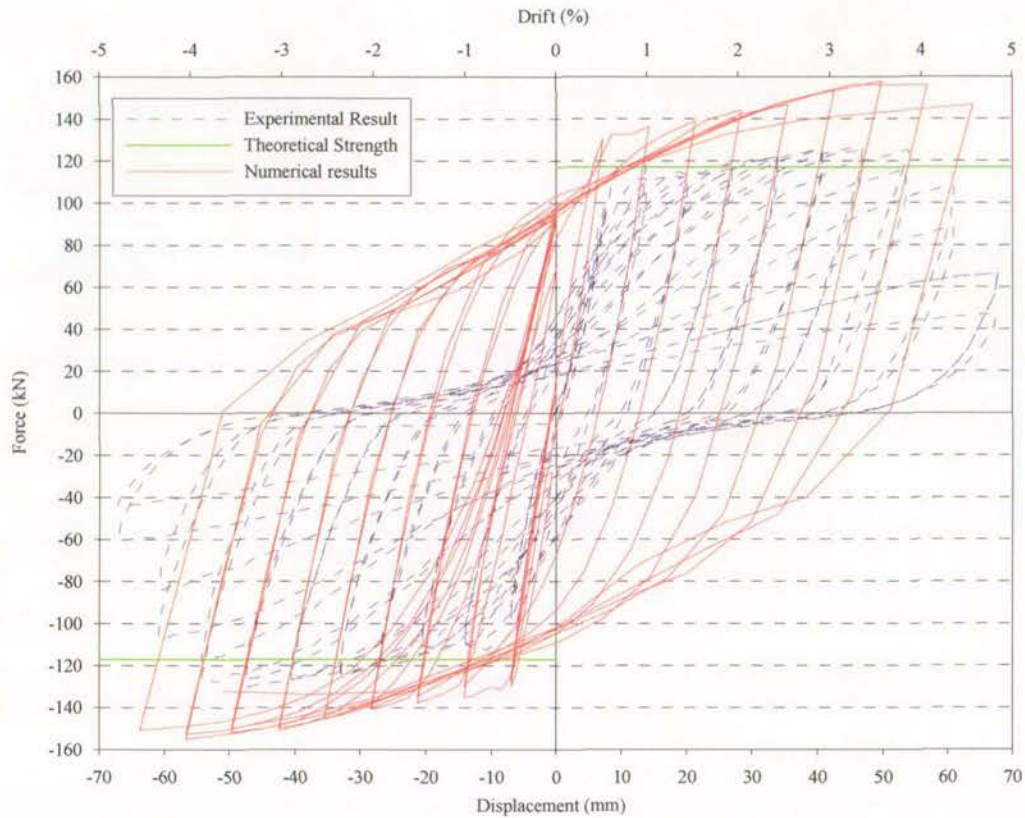


Figure 5.13-Numerical and experimental comparison (A2)

Figure 5.14 shows the damaged elements for beam A2, as defined by the criteria specified earlier. The failure occurred in shear within the support block, adjacent to the beam springing. The reason for this is unknown at this stage and further investigation may be needed.

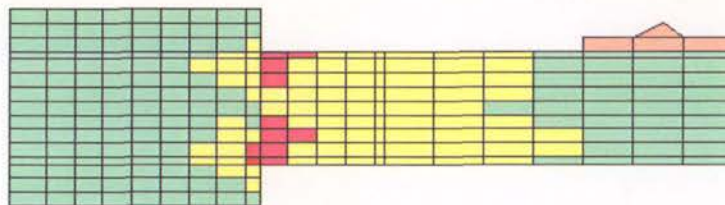


Figure 5.14-Failure and damage regions (Shear failure) (A2)

The analytical and experimental crack patterns at 4.5% drift are shown in Figure 5.15 and Figure 5.16 respectively. There is significant cracking within the support block which was not seen in the experiment, similar to beam A1.

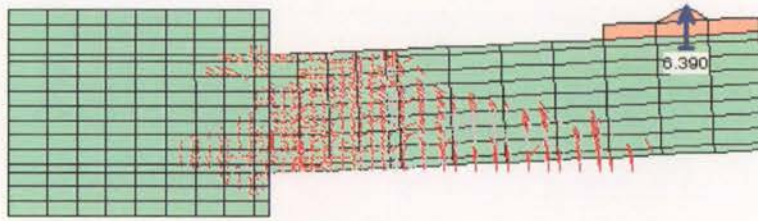


Figure 5.15-Analytical crack pattern (A2)



Figure 5.16-Experimental crack pattern (A2)

Figure 5.17 shows the stress result for beam A2. The stress distribution is in many ways similar to that of beam A1.

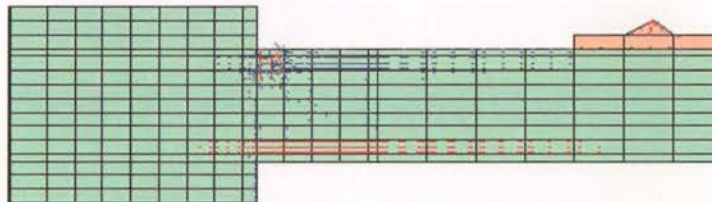


Figure 5.17-Analytical stress result (A2)

Figure 5.18 shows the yield result from beam A2. As in beam A1, the yield is limited by the additional bars welded to the longitudinal reinforcement within the support block. In this case the yield length is between 485mm and 660mm in length.

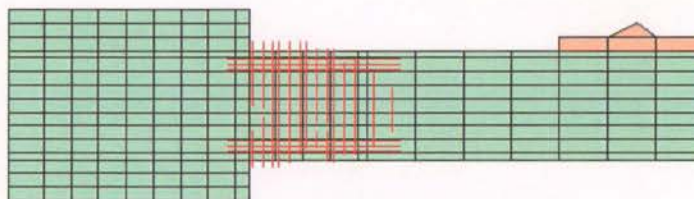


Figure 5.18-Analytical yield result (A2)

Figure 5.19 and Figure 5.20 compare the results of beams A1 and A2 for the numerical and experimental cases respectively. The differences between the numerical results seen in Figure



5.19 are very minor and could be due to the slightly different mesh geometry used. Figure 5.20 shows the significant difference between the experimental results of A1 and A2. These figures show that UC-win does not adequately capture the effect of different levels of transverse reinforcement.

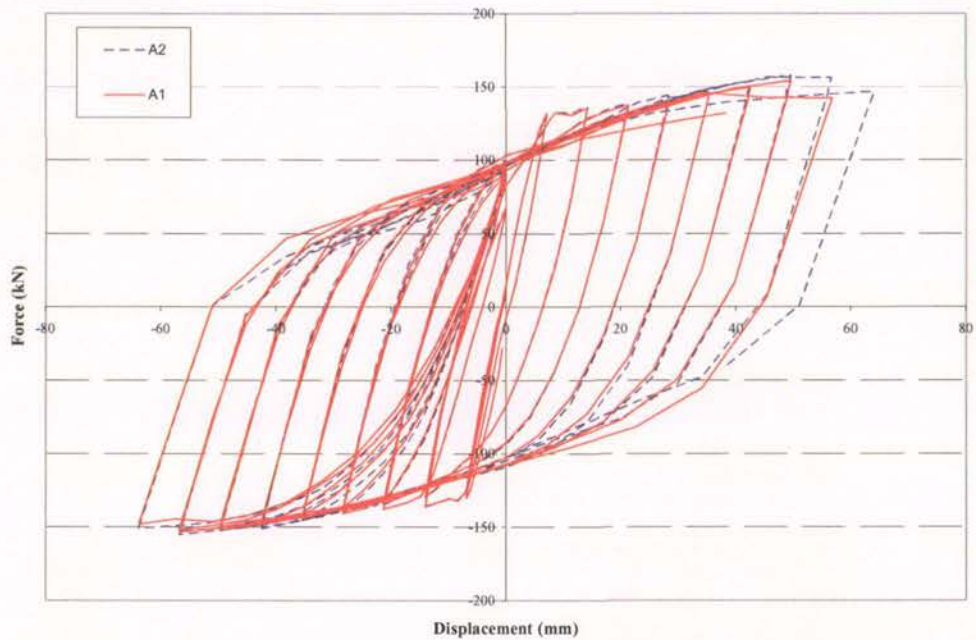


Figure 5.19-Numerical comparison for Tests A1 and A2

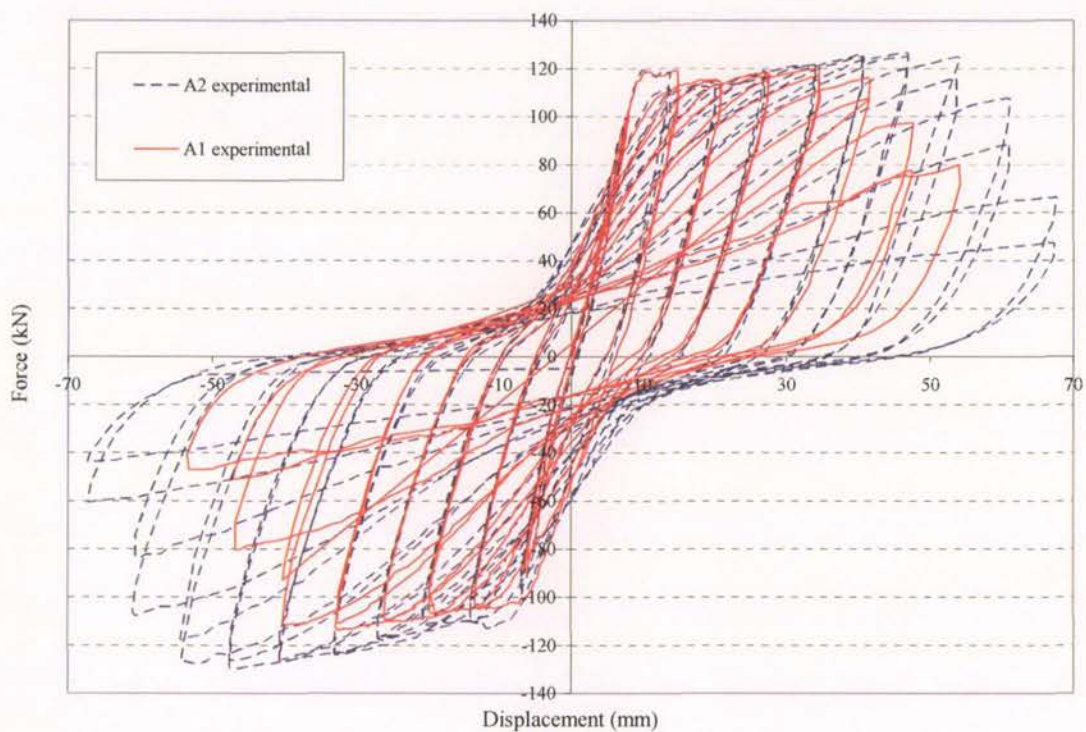


Figure 5.20-Experimental comparison for Tests A1 and A2

### 5.3.2. Unit B

Figure 5.21 shows the comparison between numerical and experimental results for Test B1. The absence of yield seen in the experiment is reflected in the numerical results as well. The strength degradation in the negative displacement direction was captured well by the analysis. In this case the degradation was due to crushing of concrete rather than excessive shear or reinforcement buckling and concrete crushing is adequately modelled in the analysis tool. The model also captures the behaviour in the positive displacement direction reasonably well. However the stiffness in the negative direction is not well represented. After viewing the numerical results of unit A it was not expected that the model will capture the shear-led strength degradation of the remaining tests well and this is confirmed in Figure 5.21.

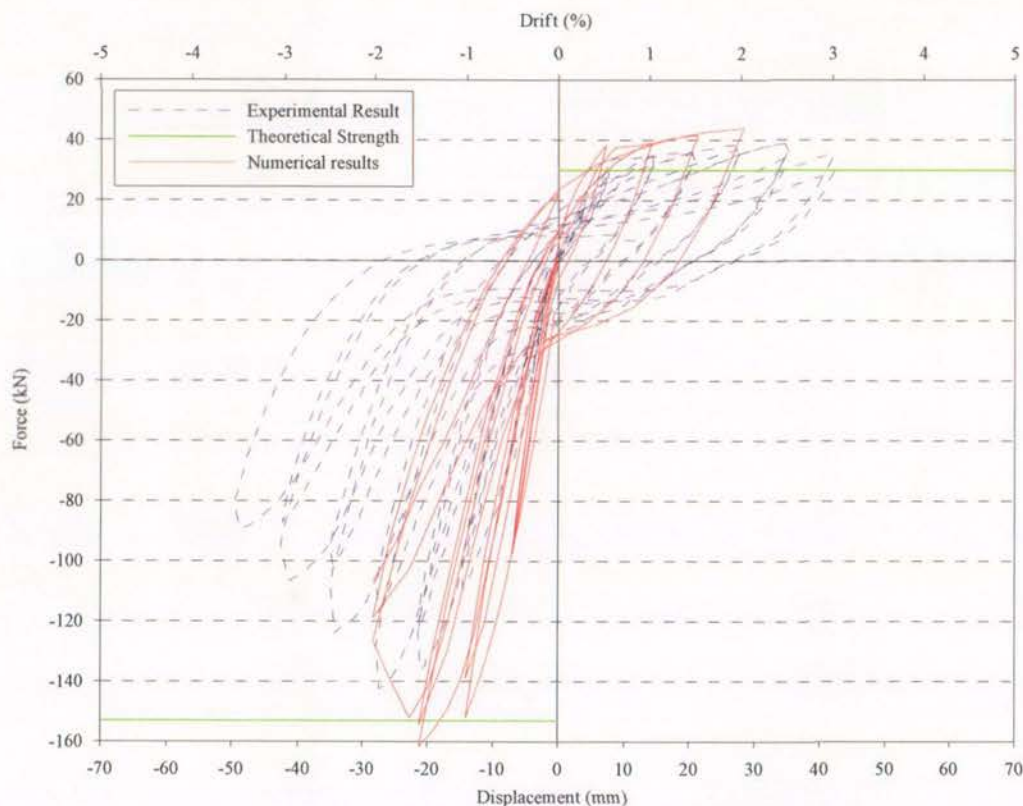


Figure 5.21-Numerical and experimental comparison (B1)

Figure 5.22 shows the failure and damaged regions for beam B1. As was the case in the experiment failure occurred in compression at the bottom of the beam. The absence of considerable damage at the top of the beam adjacent to the beam springing is also representative of the experiment.

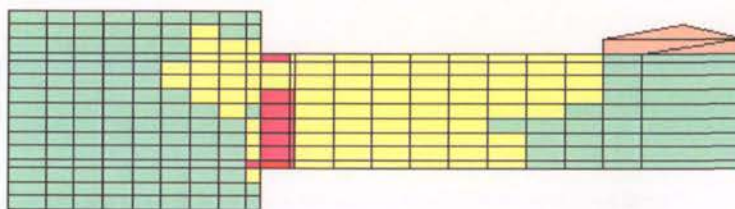


Figure 5.22-Failure and damage regions (Compression failure) (B1)

Figure 5.23 and Figure 5.24 show the crack pattern of the analysis and experiment at 2.0% drift, near the displacement that caused failure in the analysis. There is only a small amount of residual cracking at the bottom of the beam under downwards loading, similar to that seen in the test, while several flexural cracks and diagonal tension cracks open at the top of the beam.



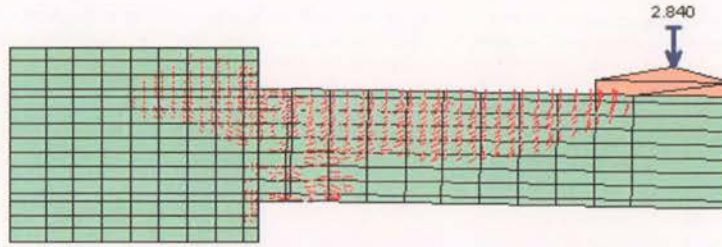


Figure 5.23-Analytical crack pattern (B1)

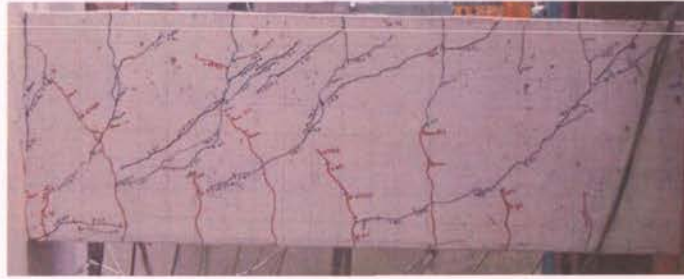


Figure 5.24-Experimental crack pattern (B1)

The stress result for B1 shown in Figure 5.25 has a large amount of compressive (blue) stress. This is due to the large neutral axis depth (from bottom) required to resist applied force as the concrete compressive strength is very low.

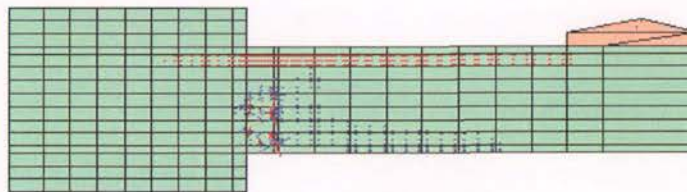


Figure 5.25-Analytical stress result (B1)

The analysis predicts a small amount of yielding in both the longitudinal and transverse reinforcement, as shown by Figure 5.26. While the yielding of the bottom reinforcement is expected, neither the experimental observations and results or the analytical force displacement curve (see Figure 5.21) indicate any yield of the top longitudinal reinforcement. The yield length in this case is between 420mm and 550mm.

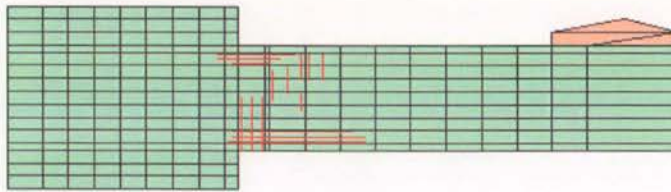


Figure 5.26-Analytical yield result (B1)

Similar issues with the analytical model are seen in the uni-directional case (beam B2) shown in Figure 5.27. Again the initial stiffness is overestimated and degradation of strength is not captured. The analysis stopped before the displacement history could be completed. The failure was compressive, located adjacent to the beam springing at the bottom of the beam. Although the analysis terminated when this localised element failure occurred, the experimental results show that the beam can sustain much greater displacement even after severe crushing of the concrete.

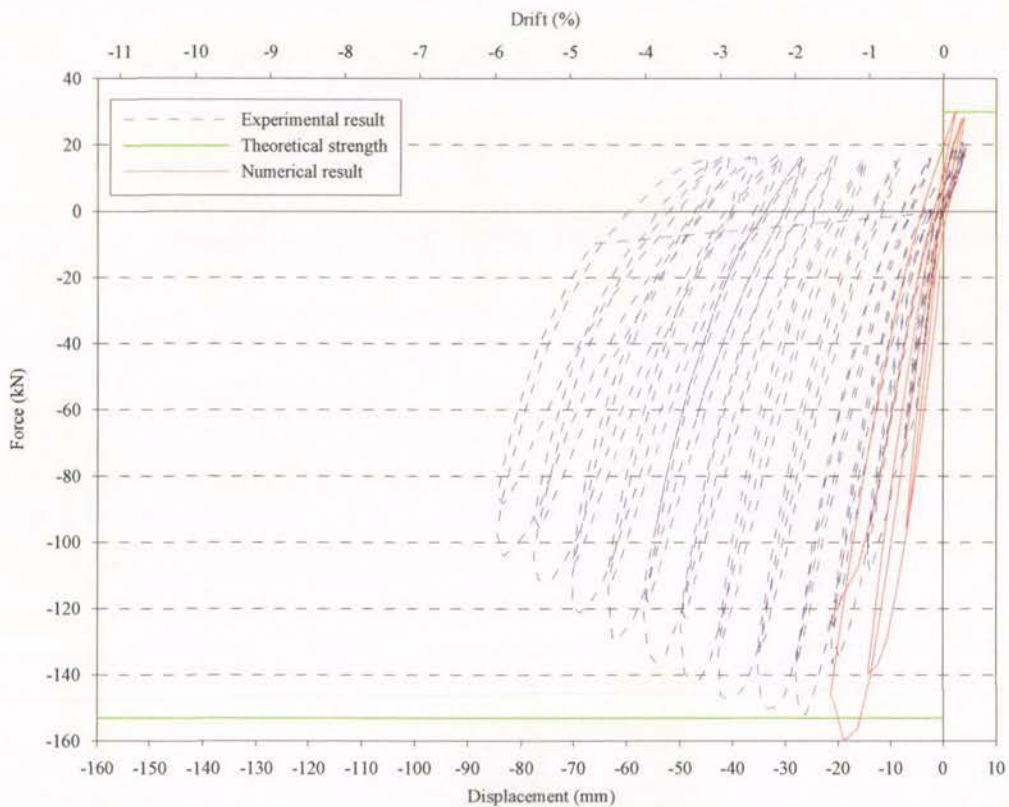


Figure 5.27-Numerical and experimental comparison (B2)

The failure and damage regions shown in Figure 5.28 reflect the uni-directional nature of Test B2. The significant damage is located at the bottom of the beam adjacent to the beam springing while only light damage is sustained at the top of the beam due to the low shear

force sustained during upwards displacement. The failure mode is compression at the bottom of the beam, as was the case in the experiment.

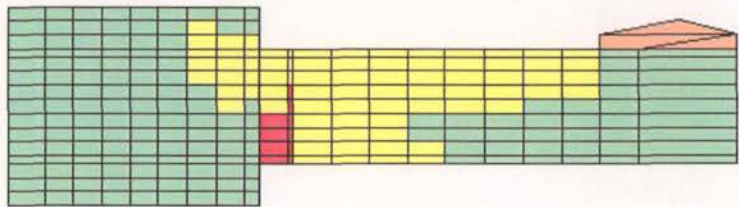


Figure 5.28-Failure and damage regions (Compression failure) (B2)

Figure 5.29 and Figure 5.30 show the crack patterns during the 2.0% drift cycles obtained from the analysis and experiment respectively. The two exhibit many similarities, significant cracking along the beam in the tension zone in the form of flexural and diagonal tension cracks while at the bottom of the beam the majority of the cracking is associated with crushing of concrete.

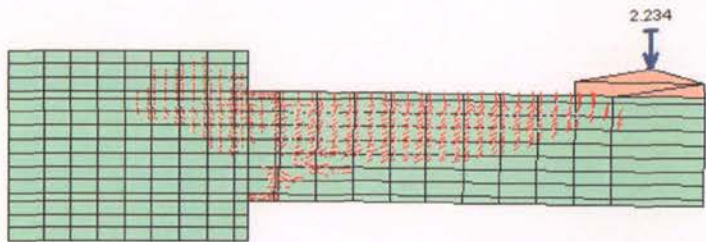


Figure 5.29-Analytical crack pattern (B2)

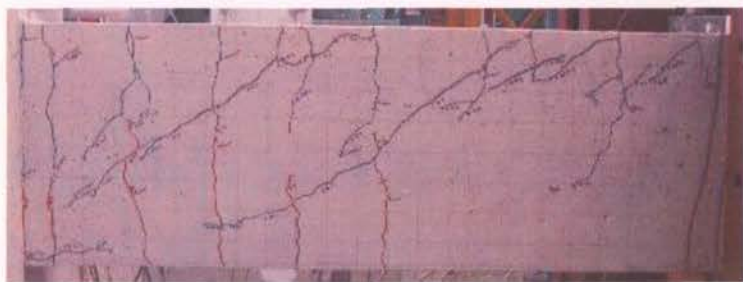


Figure 5.30-Experimental crack pattern (B2)



The stress distribution shown in Figure 5.31 is very similar to that of B1 (see Figure 5.25) with a large neutral axis depth.

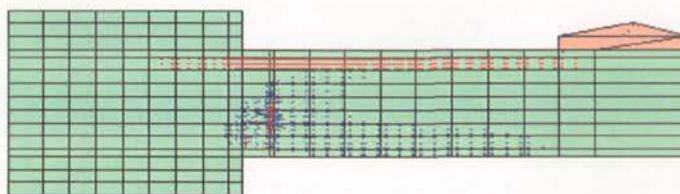


Figure 5.31-Analytical stress result (B2)

Figure 5.32 indicates that yielding of the bottom longitudinal reinforcement occurred near the beam springing in the analysis. This is surprising given that B2 was a uni-directional hinge test. It is possible that this yielding occurred in compression. There is less yielding of transverse reinforcement in this case than seen in beam B1, see Figure 5.26, despite the shear forces the two beams were subjected to being virtually the same. But the uni-directional beam B2 is likely to undergo less deterioration and concrete may contribute more to the shear capacity in this case. Moreover, the diagonal cracks seem flatter in B2 than in B1, which again suggests that the stress in transverse reinforcement is likely to be smaller in B2. The yield length in this case is between 150mm and 285mm in length.

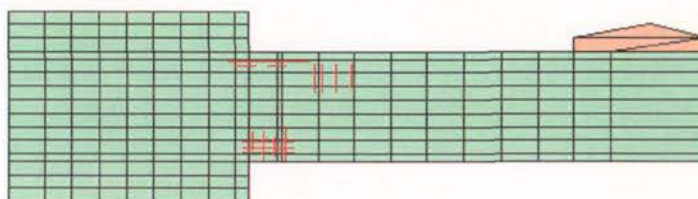


Figure 5.32-Analytical yield result (B2)

### 5.3.3. Unit C

The force displacement curve of Test C1 is shown in Figure 5.33. The model captures the loss of strength associated with crushing of the concrete although this occurs at an earlier displacement level. As in previous cases the model overestimates both the stiffness and load capacity.

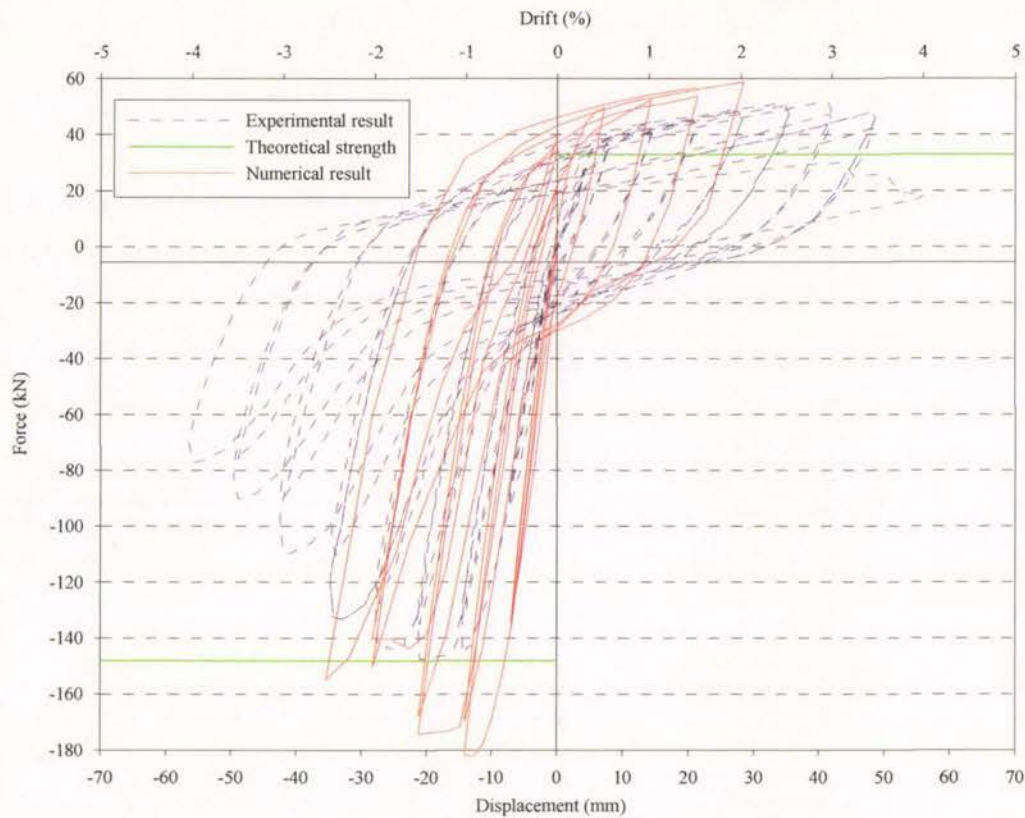


Figure 5.33-Numerical and experimental comparison (C1)

Figure 5.34 shows the damaged regions of C1. Because yield of the top longitudinal reinforcement occurred in beam C1 and the large flexural cracks (see Figure 5.36), it is surprising that there is not more damage shown at the top of the beam. The damage associated with the concrete crushing seen in the test is shown. However the failure mode for this beam was tension at the bottom of the beam. As in beams A1 and A2, the model does not consider the ability of the beam to function even after considerable cracks have opened in tension.



Figure 5.34-Failure and damage regions (Tension failure) (C1)

Figure 5.35 and Figure 5.36 display the analytical and experimental crack patterns at the same loading stage (i.e. 1.5% drift). The majority of the cracking is within the plastic hinge region while several flexural cracks are open at the bottom of the beam. When the load direction is reversed, more diagonal cracks would be expected to open and the bottom flexural cracks close.

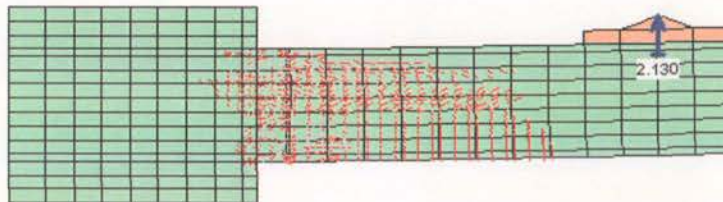


Figure 5.35-Analytical crack pattern (C1)

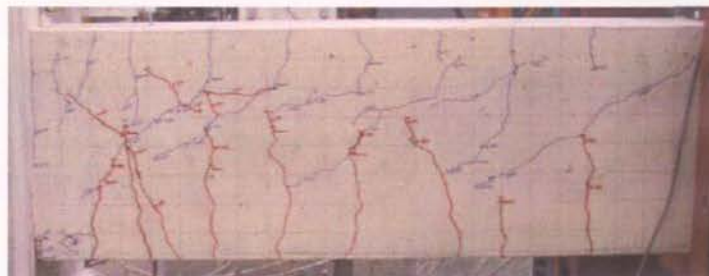


Figure 5.36-Experimental crack pattern (C1)

The stress distribution (1.5% drift) of C1 is shown by Figure 5.37. The tensile stresses in the third row of elements show that the second layer of reinforcement is in tension, thus the neutral axis lies somewhere between the two layers of top reinforcement.



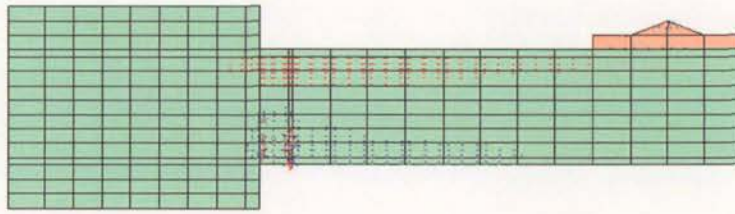


Figure 5.37-Analytical stress result (C1)

There were only moderate levels of yielding as shown in Figure 5.38. This is expected due to the concrete crushing limiting the progression of reinforcement yielding. The yield length shown here is between 400mm and 520mm in length.

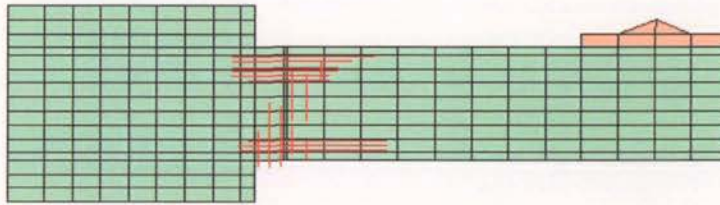


Figure 5.38-Analytical yield result (C1)

The comparison of the experimental and analytical force displacement curves of beam C2 shown in Figure 5.39 is similar to that of C1. The model captures the drop in strength due to concrete crushing but still overestimates the maximum force and initial stiffness. In this case the failure was in shear at the bottom of the beam as shown in Figure 5.40. As in the previous case, more damage is expected at the top of the beam than shown.

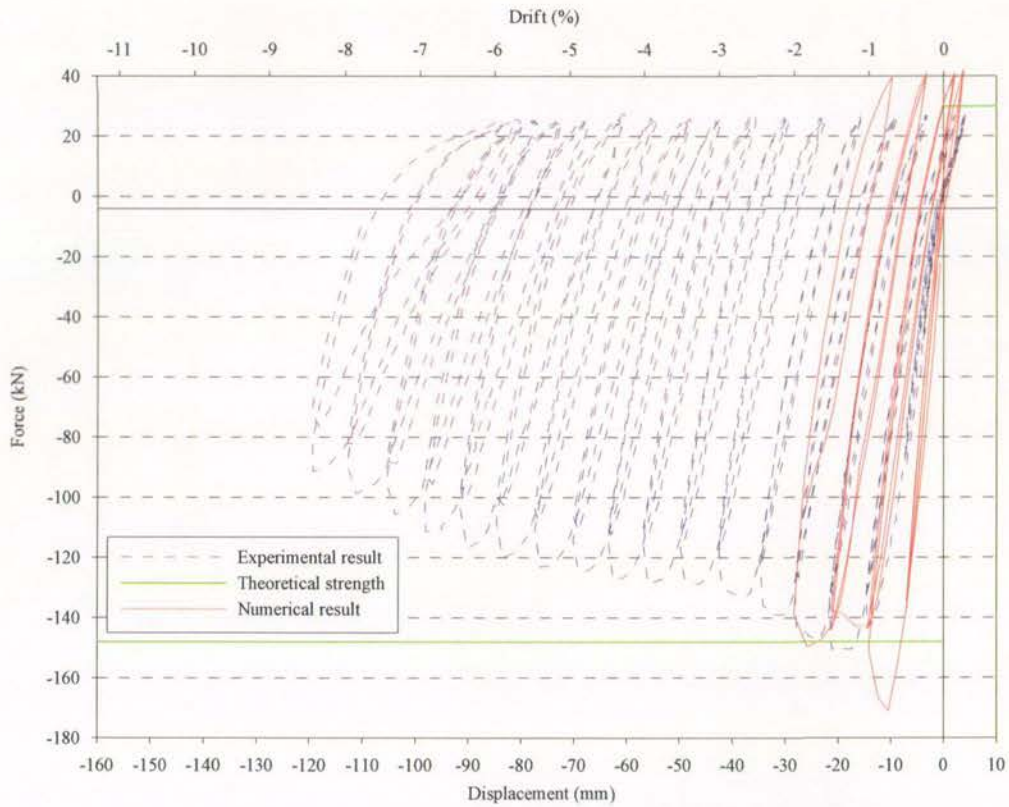


Figure 5.39-Numerical and experimental comparison (C2)



Figure 5.40-Failure and damage regions (Shear failure) (C2)

The analytical crack pattern shown in Figure 5.41 represents the experimental crack pattern of Figure 5.42 well. There are several diagonal tension cracks and flexural cracks along the length of the member in the tension zone while crushing of the concrete is seen at the bottom of the beam adjacent to the beam springing.

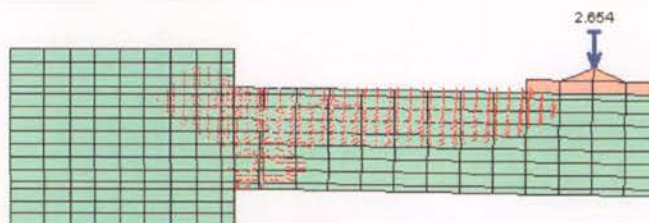


Figure 5.41-Analytical crack pattern (C2)



Figure 5.42-Experimental crack pattern (C2)

The stress distribution shown in Figure 5.43 is more significant than that of C1 due to the larger shear sustained in the downwards load direction.

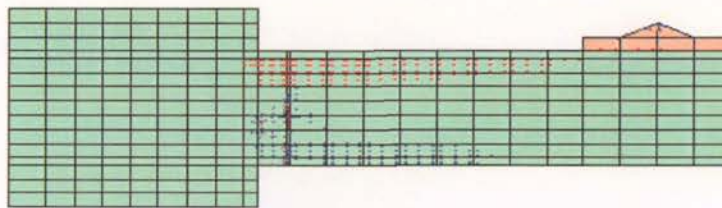


Figure 5.43-Analytical stress result (C2)

Figure 5.44 shows that the yield length of C2 is relatively short, between 180mm and 300mm in length. As in beam B2, the yielding of the bottom reinforcement is likely due to compression.

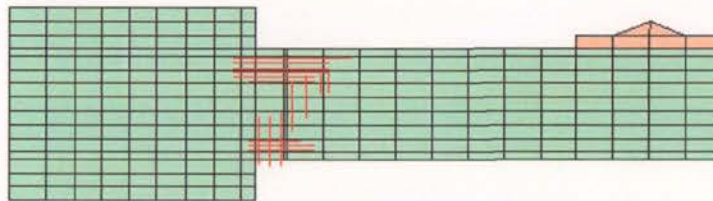


Figure 5.44-Analytical yield result (C2)



### 5.3.4. Unit D

The force displacement curves from analysis and experiment for beam D1 are shown in Figure 5.45. The differences between the two curves relate to the issues previously described for beam A1, see Figure 5.4. The analysis results for this beam does exhibit a slight pinching behaviour not seen in the previous six tests. This is due to the increased width of the section and reduction of the longitudinal steel content. This means that the concrete component of the beam behaviour is more significant and the pinched nature of the concrete stress strain curve (Dhaka and Mackawa, 2002) is modelled well by the program.

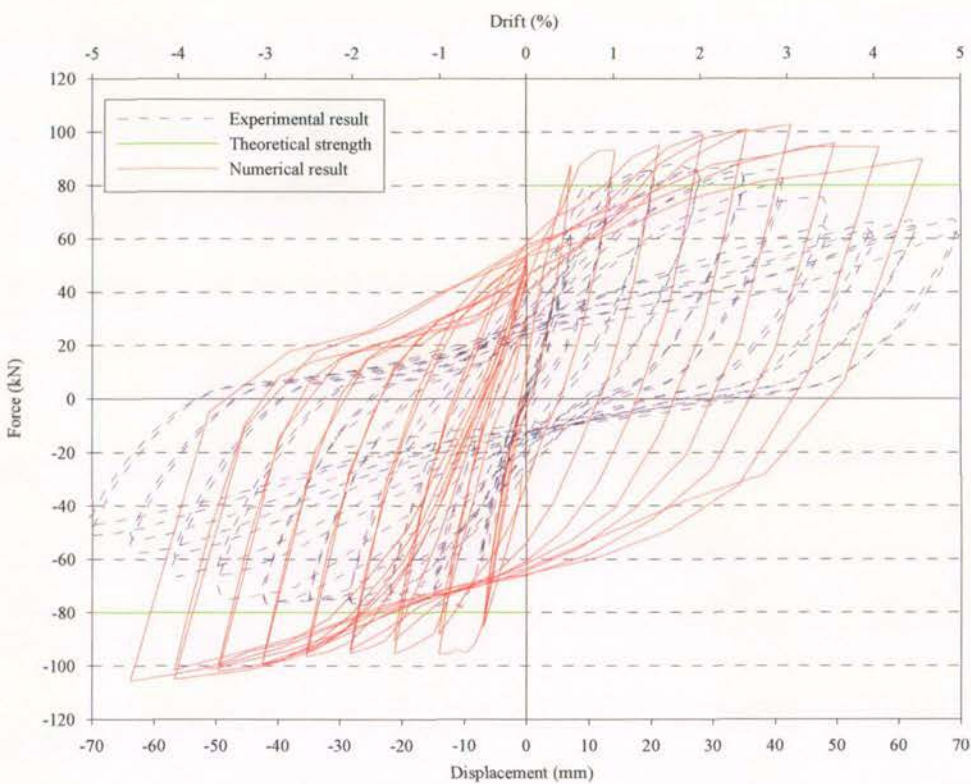


Figure 5.45-Numerical and experimental comparison (D1)

The significant damage shown in Figure 5.46 is distributed fairly evenly between the top and bottom of the beam as expected from a symmetrical section. The failure in this case was in tension at the top of the beam.

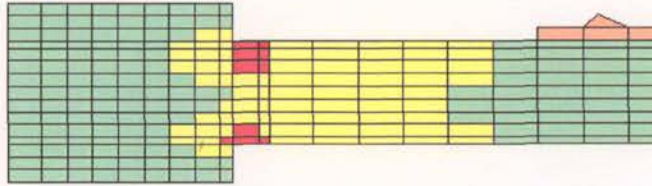


Figure 5.46-Failure and damage regions (Tension failure) (D1)

Figure 5.47 and Figure 5.48 show crack patterns at 3.0% drift obtained from the analysis and experiment. There is significant cracking within the hinge zone while along the length of the beam the cracking is mostly flexural until the cracks reach mid-depth where they become slightly inclined.

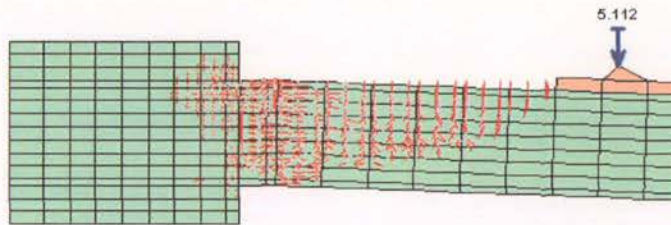


Figure 5.47-Analytical crack pattern (D1)

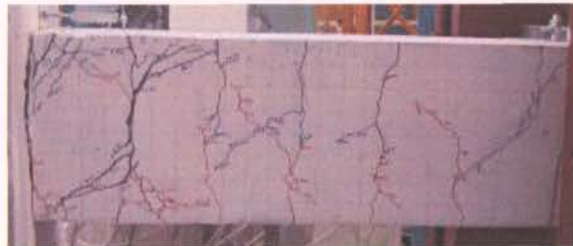


Figure 5.48-Experimental crack pattern (D1)

The stress distribution shown in Figure 5.49 is as expected with most of the stress located in the tension reinforcement and concrete compression zone. Because of the low shear force and increased section width of this beam the concrete compression zone is quite small compared with previous tests.

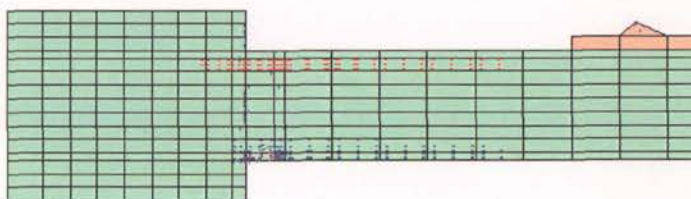


Figure 5.49-Analytical stress result (D1)



Figure 5.50 shows that the yield length is between 325mm and 500mm in length. The yield of the transverse reinforcement is understandable when looking at the large diagonal tension crack shown in Figure 5.48.

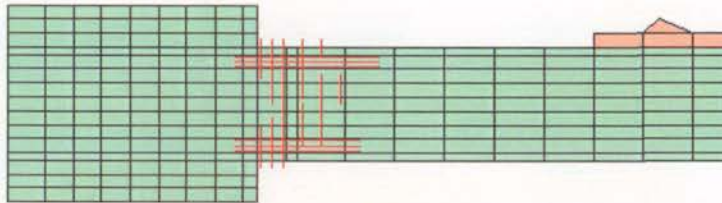


Figure 5.50-Analytical yield result (D1)

As expected based on the results of previous uni-directional cases, the level of deformation before failure of specimen D2 is underestimated by the numerical model (see Figure 5.51). The behaviour during unloading cycles on the way back to 75% of the theoretical load limit is unusual in that the load gets continually lower and a reduction in stiffness can be seen. This feature is observed in the experimental results during the large cycles only.

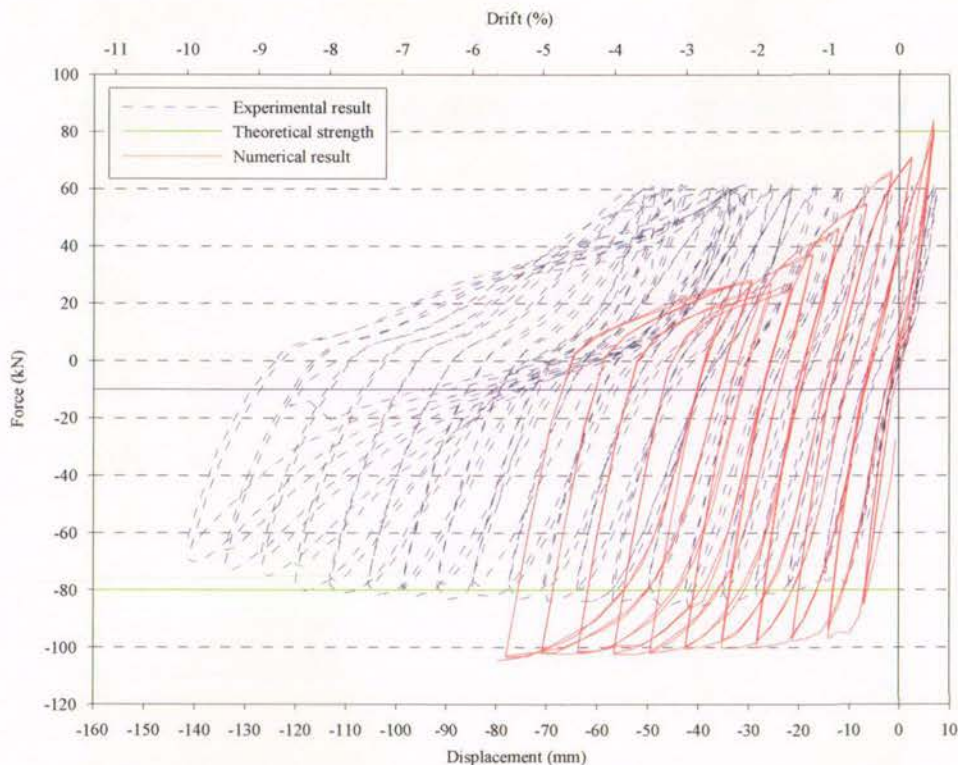


Figure 5.51-Numerical and experimental comparison (D2)



Because of the low shear stress in this beam and the relatively late occurrence of crushing and buckling the tensile failure of the analysis as shown in Figure 5.52 is expected based on the previous analytical cases. However more significant damage at the top of the beam would be expected around the failure region. The compressive damage at the bottom of the beam is represented in the analyses.

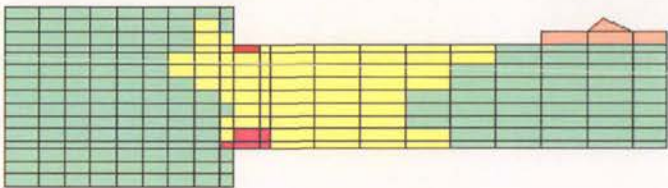


Figure 5.52-Failure and damage regions (Tension) (D2)

The analytical crack pattern of Figure 5.53 matches well with the experimental cracking of Figure 5.54, with mostly vertical flexural cracks. There is little cracking at the bottom of the beam due to the uni-directional nature of the test except for some crushing of concrete.

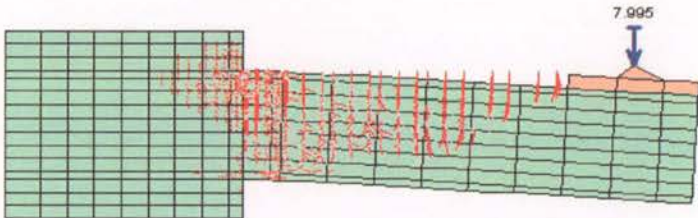


Figure 5.53-Analytical crack pattern (D2)

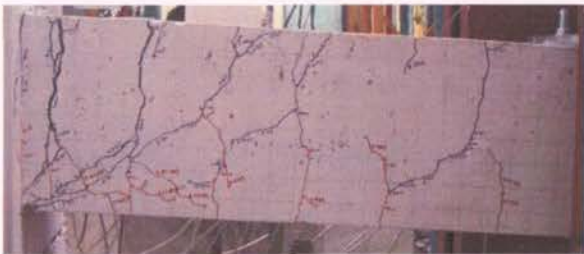


Figure 5.54-Experimental crack pattern (D2)

The stress distribution shown in Figure 5.55 is similar to that of D1, see Figure 5.49. When the direction is reversed, the distribution of stress will not be so extensive due to the limit on the force in the positive direction for the uni-directional test.

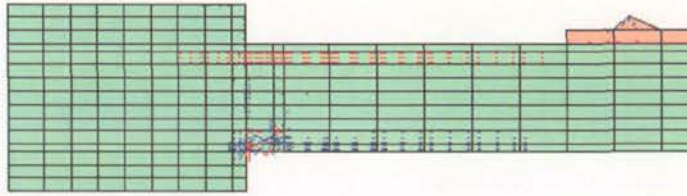


Figure 5.55-Analytical stress result (D2)

The yield length indicated by Figure 5.56 is between 325mm and 500mm as was the case in D1. However, the length of yielding in the bottom steel is reduced. There is only minor yielding of transverse reinforcing bars; this is anticipated as there are no major diagonal cracks to be seen in the experimental crack pattern shown in Figure 5.54.

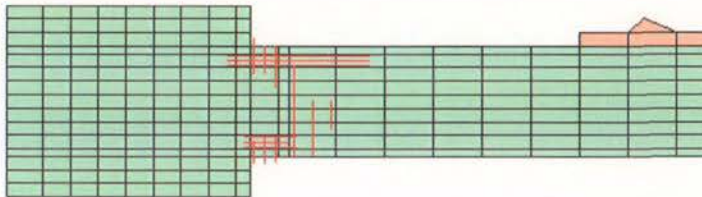


Figure 5.56-Analytical yield result (D2)

#### 5.4. ELONGATION

Figure 5.57 through Figure 5.62 show the elongation data obtained from the numerical analyses of Tests A1 through D2 respectively. The elongation was taken from the horizontal displacement results for the node at mid depth at the loading end of the beam.

Figure 5.57 shows that the numerical result of A1 matches qualitatively well with the experimental results. The key difference is a greater reduction in elongation as the beam displacement returns to zero. The difference is probably related to shear performance and aggregate movement in cracks preventing closure, which is not modelled in the analysis. The experimental elongation does not increase significantly during the last two drift levels. This is possibly due to the onset of buckling or instrument error, suggesting that the elongation could have reached greater levels than shown in Figure 5.57.

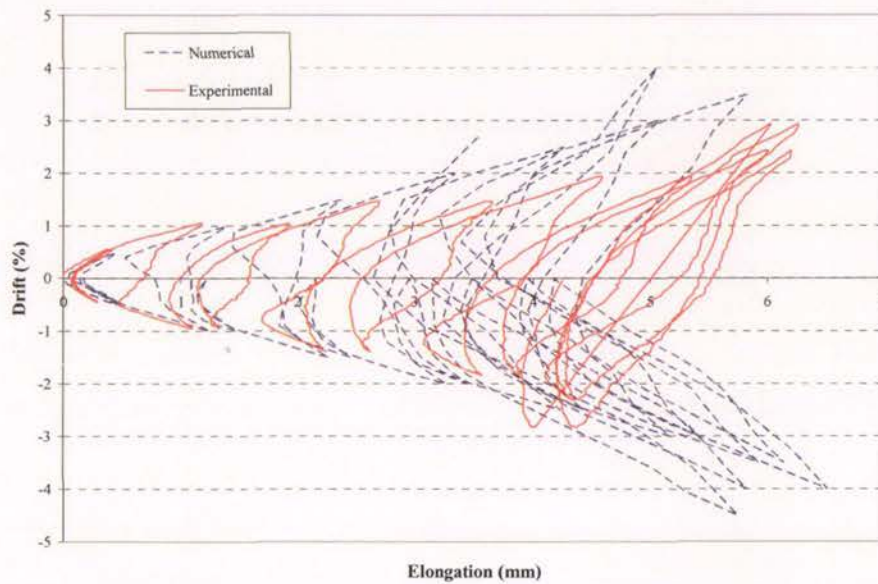


Figure 5.57-Comparison of elongation between the experiment result and the numerical model (A1)

The elongation of beam A2 is shown in Figure 5.58. The numerical result does not achieve the same level of elongation as found in the experiment. This is in contrast to expectation given the reasonable match between experiment and analysis for beam A1. As the stirrups are spaced closer in A2 than A1, the contribution of shear in the elongation is expected to decrease. The analysis has been found to capture the flexure related elongation reasonably well (Peng, 2005). Nevertheless, the larger difference between the experiment and analytical elongation as seen in this case (A2) is difficult to explain. Similar issues related to the gradient on the return to zero displacement as seen in A1 exist in this case (A2) as well.



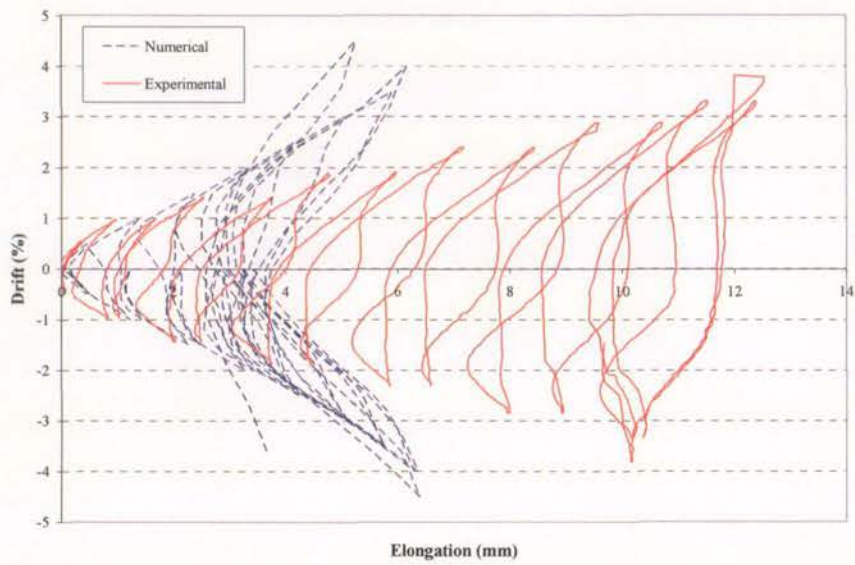


Figure 5.58- Comparison of elongation between the experiment result and the numerical model (A2)

The elongation of B1 seen in Figure 5.59 shows a good match between the experimental observation and the analytical prediction. The result is only shown over a short range of the total experimental data due to the localised failure stopping the analysis at a low drift level. Surprisingly the analysis even captures the negative elongation (i.e. shortening) in the negative drift cycles, although the mechanism behind this negative elongation cannot be explained.

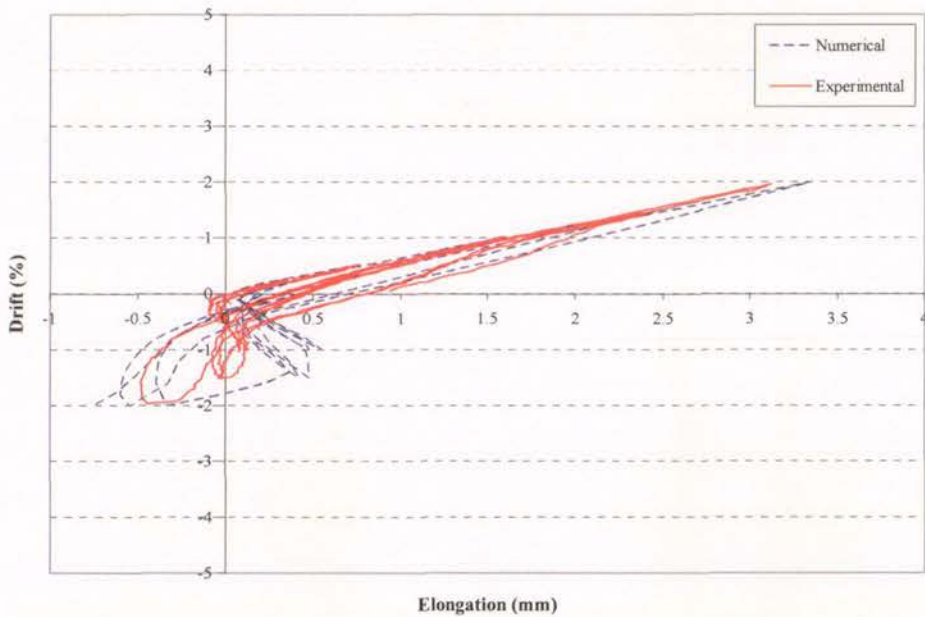


Figure 5.59- Comparison of elongation between the experiment result and the numerical model (B1)

The analytical elongation of beam B2 was very small ( $<0.5\text{mm}$ ) and so is not shown. This is somewhat expected as the reinforcement did not yield in this test and the numerical analysis is stopped by localised failure before extensive cracking could occur.

The elongation of beam C1 is shown in Figure 5.60. The analysis matches well with the experimental result in the first two displacement cycles but then underestimates the elongation as the drift level is increased. This is similar to the behaviour seen in beams A1 and A2.

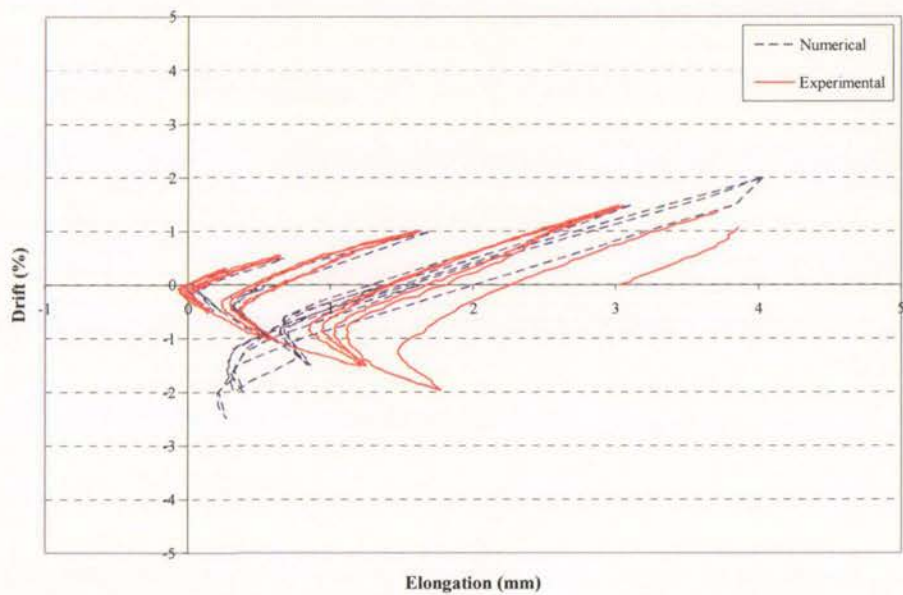


Figure 5.60- Comparison of elongation between the experiment result and the numerical model (C1)

The analytical elongation for beam C2 was very small ( $<0.5\text{mm}$ ) and so is not shown. The reason for such small amount of elongation is similar to B2, in this case only a small amount of yielding occurred in the reinforcing bars and early failure of the analysis occurred due to localised strains.

Figure 5.61 shows the elongation result of D1. The analysis fails to predict the elongation accurately in the higher displacement levels, similar to beam A2.

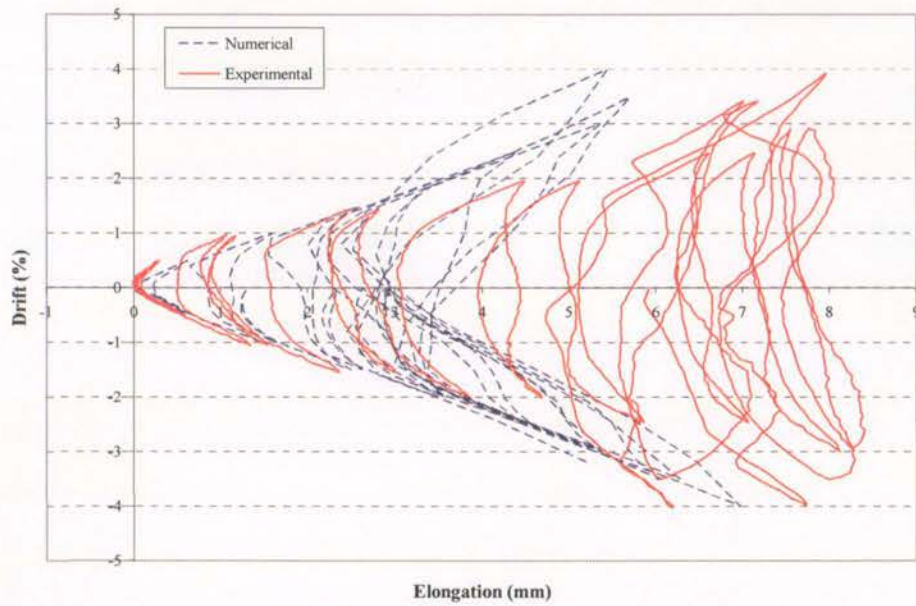


Figure 5.61- Comparison of elongation between the experiment result and the numerical model (D1)

The analytical prediction of D1 captures the elongation of uni-directional beam tests much better than B2 and C2. This is because there was significant yielding of longitudinal reinforcing bars in this test. As seen in previous tests, the reduction of elongation during the unloading is too steep. This difference gets accumulated during the repeated cycles, thereby resulting in a significant reduction of the residual elongation.

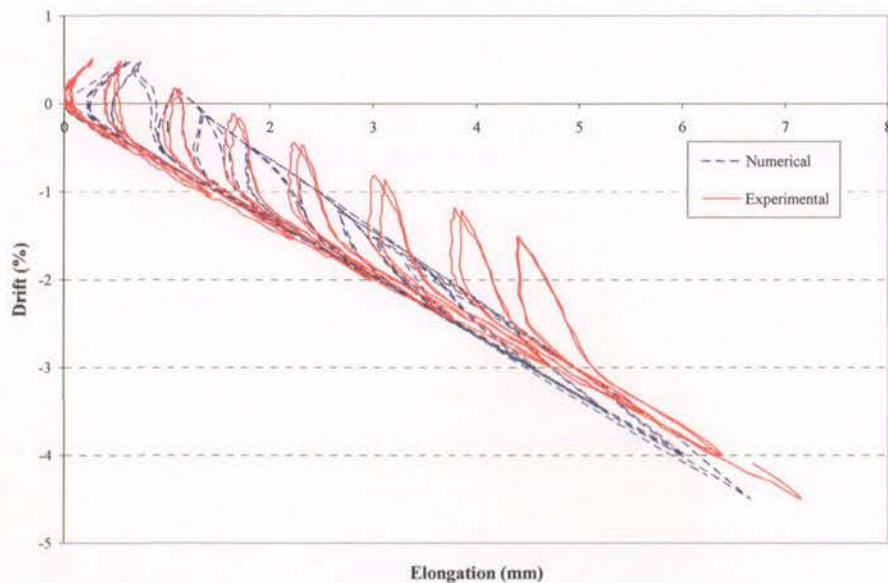


Figure 5.62- Comparison of elongation between the experiment result and the numerical model (D2)



## 5.5. FURTHER INVESTIGATION

To further explore the ability of the analysis program to capture the effect of different transverse reinforcement configurations a small parametric study was carried out. This study involved monotonic loading of cantilevered beams with length to depth ratios of 1, 2 and 4. Two different vertical reinforcement ratios were used, one with 2% shear steel and one with no vertical reinforcement. Two different load conditions were also used, one where the end of the beam was free to move in the horizontal direction and a second where the horizontal movement was prevented. The default failure criteria were used for this study.

Figure 5.63 shows the mesh used for the case where the length to depth ratio was equal to two. The cases of  $L/d=1$  and  $L/d=4$  simply halve or double the number of horizontal elements. A constant horizontal reinforcement ratio of one percent was used in all elements. The concrete compressive strength specified was 30 MPa and the steel yield stress specified was 350 MPa. An elastic plate with a specified elastic modulus of 500 MPa was used at the end of the beam to transfer the load. The displacement increments were applied at the central node at the end of the beam. To restrain the horizontal movement of the beam the nodes at the top and bottom of the elastic plate were fixed in the horizontal direction. The support conditions at the left hand end of the beam were modelled by fixing all the left hand nodes in both directions.

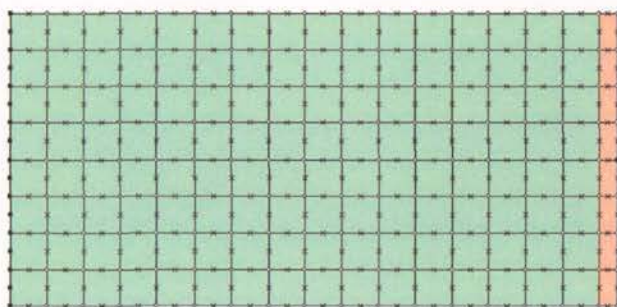


Figure 5.63-Mesh layout for length to depth ratio of 2

The results of each analysis are displayed in the form of force displacement curves taken from the node at which the displacement was applied. The general trends of changing each parameter are shown in Figure 5.64 through Figure 5.70.

Figure 5.64 shows the effect of increasing the length of the beam for the restrained horizontal displacement case. Increasing the length decreases the yield force and increases the displacement ductility of the beam. The pronounced peak of the force displacement curve is reduced as the length is increased. A similar trend can be observed in Figure 5.65 which shows the effect of increasing the length for the unrestrained horizontal displacement case.

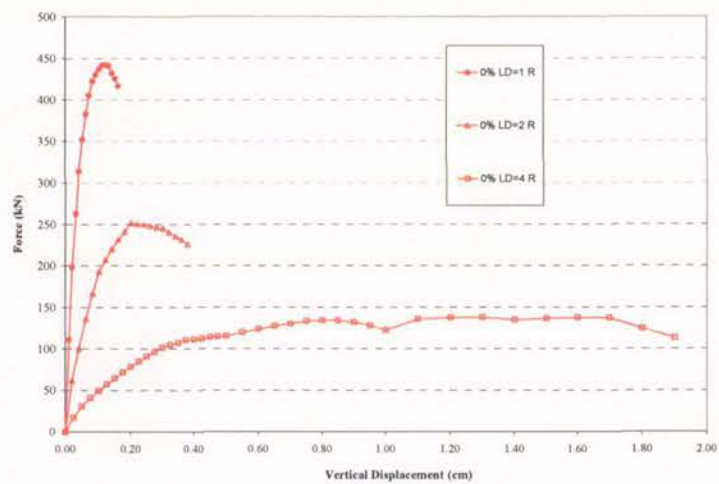


Figure 5.64-Effect of increasing length of restrained beam

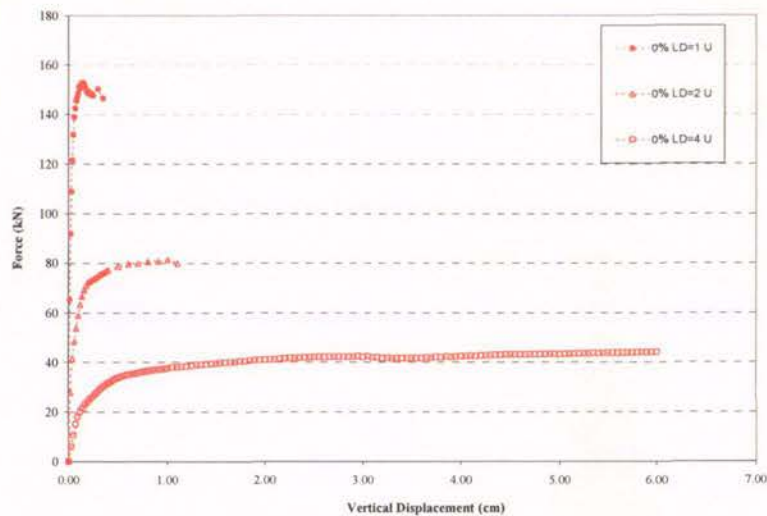


Figure 5.65-Effect of increasing length of unrestrained beam

The effect of changing the transverse reinforcement content for the restrained horizontal displacement case, when the length to depth ratio is unity, is shown in Figure 5.66. Increasing the transverse steel content simply increases the peak force sustained by the beam. This trend is reduced when the length to depth ratio is increased to two, as shown in Figure 5.67.

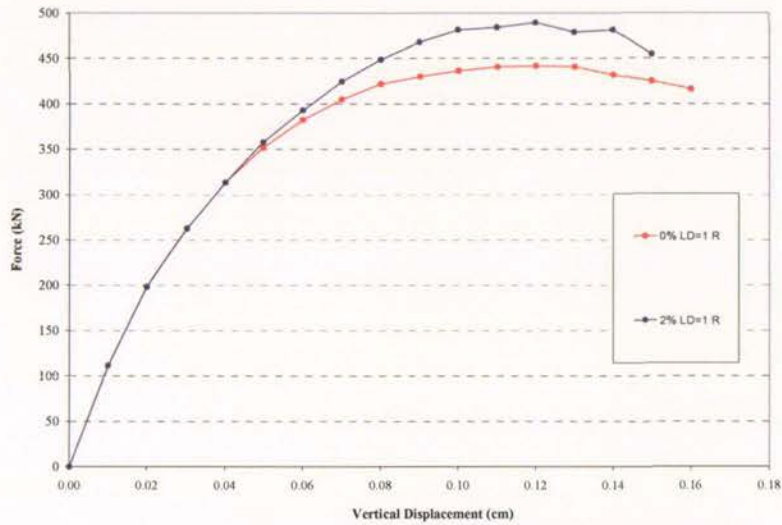


Figure 5.66-Effect of increasing transverse steel content for restrained beam,  $L/d=1$

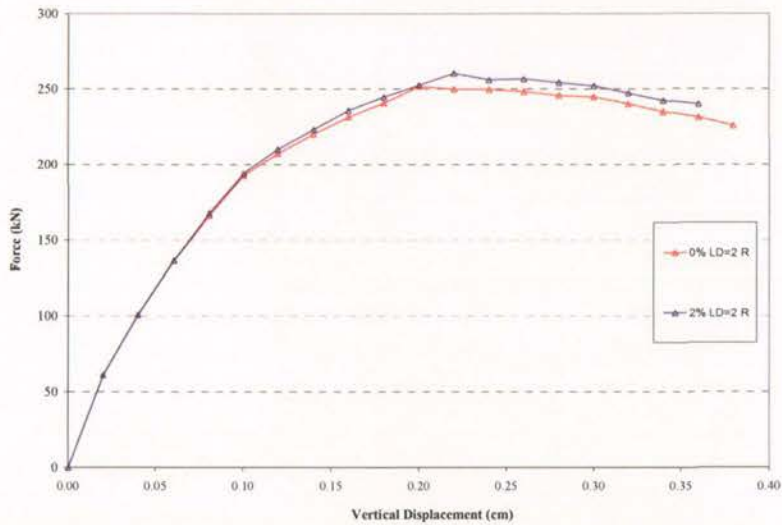


Figure 5.67-Effect of increasing transverse steel content for restrained beam,  $L/d=2$

Figure 5.68 illustrates the effect of restraining the horizontal displacement of a beam with a length to depth ratio of one. The restraint of the horizontal degree of freedom places the beam under pure shear rather than flexural type load. This is reflected in the displacement patterns shown in Figure 5.69. The unrestrained beam loses the distinct peak in the force displacement curve and can sustain higher displacement.



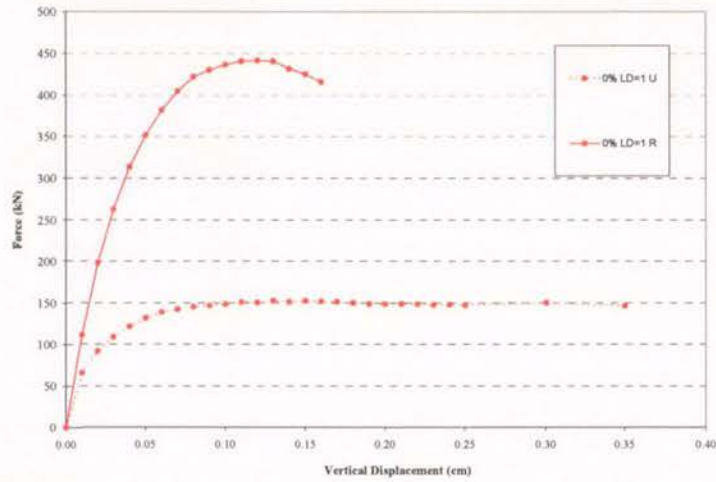


Figure 5.68-Effect of restraining horizontal degree of freedom

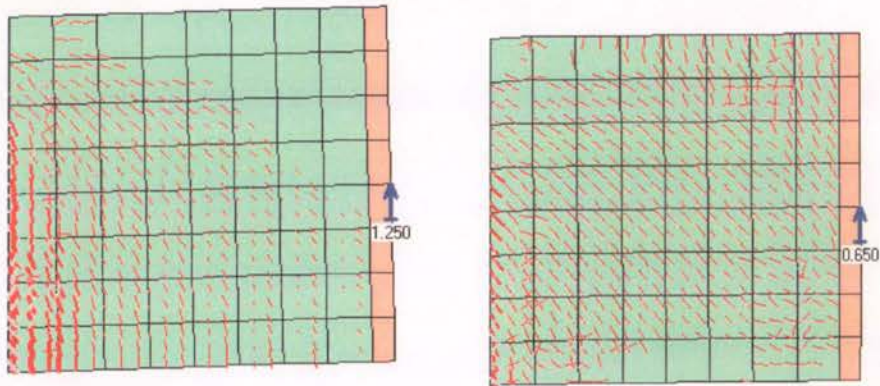


Figure 5.69-Deflection and crack pattern for  $L/d=1$  with a) Unrestrained horizontal displacement and b) Restrained horizontal displacement

Finally, Figure 5.70 shows the effect of increasing the transverse steel content when the beam is unrestrained in the horizontal direction. No change is observed in the peak force and only a minor change in the displacement sustained is observed.

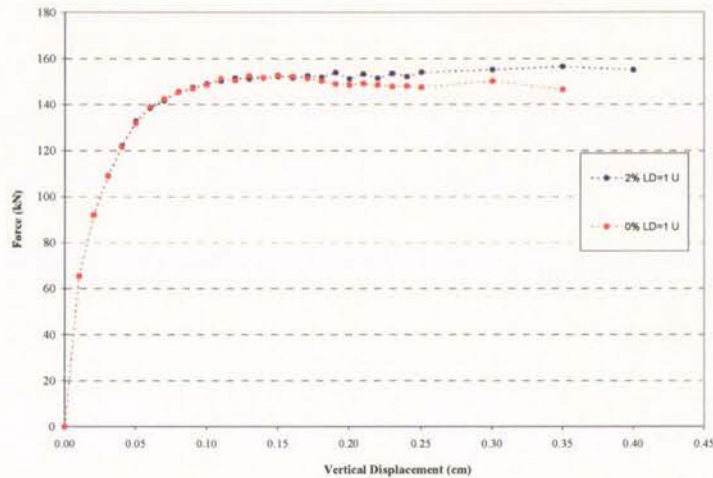


Figure 5.70-Effect of increasing transverse steel content of unrestrained beam

The general trend observed in this study is that additional transverse reinforcement only serves to slightly increase the shear strength of the beam; this is especially relevant when the beam is subjected to pure shear loading. This effect is reduced as the length of the beam is increased. No increase in the beam displacement capacity was observed when the transverse steel content was increased. For cases where the beam was subjected to shear and flexural loading the effect of adding shear steel was negligible.

The purpose of this investigation was to see if the analytical tool could be used to examine beam arrangements that have not covered by the experiments. Because UC-win is a non-linear finite element program based on element material properties it is more suitable for modelling the beam behaviour than other common finite element programs that model the overall member behaviour. The key requirement for the program is to capture the effect of changes to the transverse reinforcement as this is one of the key features that differentiates the different detailing categories in NZS 3101:2006.

There are several key areas where the analytical model fails to satisfactorily capture the experimental results. The most important are the issues that effect the calculation of appropriate material strain limits; namely the localised failures due to excessive strains, the absence of strength degradation due to buckling, and the absence of any difference in results when the transverse steel content is altered. The localised failure due to excessive strains within an element means that the displacement at which the strength degrades to below the failure criteria is not reached. Related to this is the absence of strength degradation due to buckling behaviour which was seen in most of the experiments. Without strength degradation

the maximum displacement sustained before the load drops below 80% of the theoretical strength cannot be established. This is of particular importance for members with nominally ductile detailing as wide stirrup spacing is common making the bars very susceptible to buckling.

Other issues include the overestimation of the beam strength. While this is not crucial for the setting of material strain limits, it does place serious doubts on the analytical results validity. The beam elongation appears to be reasonably well represented by the analysis at the peak drifts. However the residual elongation when the load is removed is significantly less than that seen in the experimental results. The initial stiffness is overestimated but that is not surprising due to the inherent slop in any experimental setup. This would not be expected to have significant effect on the determination of material strain limits.

The overall effect of these issues is that the analytical tool cannot be used to reliably predict limiting material strains for members with nominally ductile detailing.



## 6. DISCUSSION

This chapter further discusses points raised in Chapter 4. It includes the calculation of material strain limits based on the experimental results. Approximate plastic hinge lengths from the experiments are compared with those recommended in the concrete code (NZS 3101:2006). The shear behaviour of the beams is further discussed. The member stiffness in terms of initial, secant and tangential stiffness is derived from the experimental results. Finally, comments are made on the buckling of beam reinforcing bars observed during the tests.

### 6.1. MATERIAL STRAIN LIMITS

The major objective of this thesis is to review the existing material strain limits for nominally ductile beams. Comparisons can be made between the existing material strain limits and those obtained in the tests of eight beams. In order to compare the existing limits and experimental results they must first be transformed to a comparable measure, which in this case is a curvature.

As discussed in Chapter 2, the recommendations by Fenwick and Dhakal (2007 b) limit the strain to 0.004 in compression and 0.016 in tension for uni-directional plastic hinges. These limits are reduced to 60% for reversing plastic hinges. The allowable curvature is given by dividing by the distance from the neutral axis to the strain location of interest, as shown in Figure 6.1. The neutral axis depth is calculated using basic section analysis for each individual beam. Calculations illustrating this method are included in Appendix C.

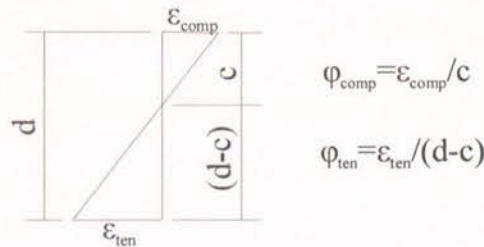


Figure 6.1-Calculating allowable curvature from strain limits

The curvature sustained in the beam tests is obtained from the maximum displacement of the beam at the load application point. The displacement used is the maximum displacement sustained before failure occurred (the criteria for failure is discussed in detail in Chapter 2).

The ultimate displacement ( $\Delta_{ult}$ ) is divided by the distance from the centroid of the plastic hinge to the load application point to give the ultimate rotation and this is transformed to a curvature by dividing by the effective plastic hinge length ( $l_p$ ). The effective plastic hinge length is defined by NZS 3101 as the smaller of half the beam depth or  $0.2M^*/V^*$  but need not be taken as less than one quarter of the beam depth. It is important to note that this length is only an approximation and is used to give an index of the curvatures. The process for calculating the curvature from the ultimate deflection is outlined in Figure 6.2. In each beam the effective plastic hinge length was 200mm ( $h/2$ ).

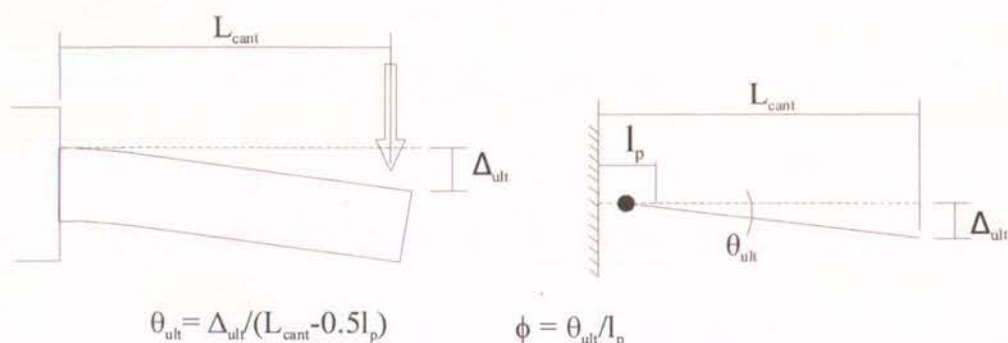


Figure 6.2-Obtaining experimental curvature

The experimental curvatures and the current design limits are presented in Table 6.1. The ratio of experimental curvature to allowable curvature is shown. For beams with unsymmetrical steel content, only the direction of maximum moment capacity is considered. In design the lower characteristic material properties are used. Thus the calculation of the neutral axis depth use the lower characteristic values rather than the measured values for  $f_y$  and  $f_c'$  when calculating the experimental curvatures and design limits. A second table (Table 6.2) is shown comparing the curvature limits considering the actual concrete strength and steel yield stress in the calculations.

For all beams the ratio of experimental ultimate curvature to the design limit is greater than unity. Because little experimental material was available at the time the limits were set they were set conservatively. This is not surprising as the values shown in Table 6.1 are much larger than unity. The ratio for the uni-directional beams is greater than the reversing tests in all cases, indicating an excessive conservatism with the uni-directional limits. The governing (i.e. lowest ratio) strain (i.e. compressive or tensile) varies between the beams. However, the

two units where the concrete compression governs (B and C) were the units with the lowest concrete strength and exhibited only limited or no yielding of the reinforcing bars.

It is evident that the ratio of ultimate curvature to design curvature is particularly high for the limiting concrete strain in uni-directional tests. For the worst uni-directional case (D2) a limiting compressive strain of 0.0225 gives a ratio of ultimate to design curvature of unity compared with the value of 0.004 currently used in NZS 3101:2006. Similarly, in all cases the ratio of ultimate to design curvature corresponding to the limiting steel strain is greater than 2.0. These values show that the values currently used in NZS 3101:2006 are overly conservative.

The displacement results shown in Table 6.1 indicate that the uni-directional plastic hinges are able to sustain in excess of twice the rotation sustained by the corresponding reversing plastic hinge. The ratio of uni-directional to reversing rotation ranges from 2.2 to 2.9 for the three beams tested in this project, compared with the conservative 2.0 currently used in NZS 3101:2006.



Table 6.1-Comparison of curvature limits and experimental curvatures using nominal material properties

Test	Experiment			Predicted	Design limits		Ratio ultimate/design	
	$\Delta_{ult}$ (mm)	$\theta_{ult}$ (rad)	$\phi_u$ (mm <sup>-1</sup> )	c (mm)	$\phi_{all,comp}$ (mm <sup>-1</sup> )	$\phi_{all,ten}$ (mm <sup>-1</sup> )	$\phi_u / \phi_{all,c}$	$\phi_u / \phi_{all,s}$
A1	42.6	0.0322	0.000161	58.3	$4.29 \times 10^{-5}$	$3.43 \times 10^{-5}$	3.75	4.70
A2	56.8	0.0430	0.000215	58.3	$4.29 \times 10^{-5}$	$3.43 \times 10^{-5}$	5.01	6.27
B1*	28.4	0.0215	0.000108	121.2	$2.06 \times 10^{-5}$	$4.37 \times 10^{-5}$	5.24	2.47
B2* <sup>+</sup>	63.9	0.0484	0.000242	121.2	$3.30 \times 10^{-5}$	$6.99 \times 10^{-5}$	7.33	3.46
C1	35.5	0.0269	0.000134	158.1	$1.58 \times 10^{-5}$	$5.21 \times 10^{-5}$	8.47	2.57
C2 <sup>+</sup>	78.1	0.0592	0.000296	158.1	$2.53 \times 10^{-5}$	$8.34 \times 10^{-5}$	11.7	3.55
D1	49.7	0.0377	0.000188	41.9	$5.97 \times 10^{-5}$	$3.25 \times 10^{-5}$	3.15	5.79
D2 <sup>+</sup>	142.0	0.108	0.000538	41.9	$9.55 \times 10^{-5}$	$5.19 \times 10^{-5}$	5.64	10.4

\* Denotes beams not meeting neutral axis limit due to low concrete strength.

+ Denotes uni-directional hinge tests.

Table 6.2-Comparison of curvature limits and experimental curvatures using measured material properties

Test	Experiment			Predicted	Design limits		Ratio ultimate/design	
	$\Delta_{ult}$ (mm)	$\theta_{ult}$ (rad)	$\phi_u$ (mm <sup>-1</sup> )		$\phi_{all,comp}$ (mm <sup>-1</sup> )	$\phi_{all,ten}$ (mm <sup>-1</sup> )	$\phi_u / \phi_{all,c}$	$\phi_u / \phi_{all,s}$
A1	42.6	0.0322	0.000161	53.0	$4.44 \times 10^{-5}$	$3.4 \times 10^{-5}$	3.63	4.73
A2	56.8	0.0430	0.000215	53.0	$4.44 \times 10^{-5}$	$3.4 \times 10^{-5}$	4.84	6.31
B1*	28.4	0.0215	0.000108	171.2	$1.36 \times 10^{-5}$	$6.03 \times 10^{-5}$	7.96	1.79
B2* <sup>+</sup>	63.9	0.0484	0.000242	171.2	$2.17 \times 10^{-5}$	$9.65 \times 10^{-5}$	11.14	2.51
C1	35.5	0.0269	0.000134	173.2	$1.26 \times 10^{-5}$	$6.59 \times 10^{-5}$	10.62	2.03
C2 <sup>+</sup>	78.1	0.0592	0.000296	173.2	$2.02 \times 10^{-5}$	$10.1 \times 10^{-5}$	14.67	2.81
D1	49.7	0.0377	0.000188	45.4	$5.21 \times 10^{-5}$	$3.31 \times 10^{-5}$	3.61	5.68
D2 <sup>+</sup>	142.0	0.108	0.000538	45.4	$8.33 \times 10^{-5}$	$5.3 \times 10^{-5}$	6.46	10.15

\* Denotes beams not meeting neutral axis limit due to low concrete strength.

+ Denotes uni-directional hinge tests.

The strains suggested by Fenwick and Dhakal (2007 b) for limited ductile and ductile plastic regions (see Chapter 2.2) uses a factor relating to nominal yield of the section. The nominal first yield condition is defined as (Priestly and Kowalsky, 2000):

$$\phi_y = \frac{2\varepsilon_y}{h}$$

Equation 11

where  $\varepsilon_y$  is the yield strain of the reinforcing bars and  $h$  is the beam height. The factor is found by dividing the experimental curvature by the curvature at nominal first yield and the  $K_y$  factor that ensures that the ultimate curvature does no change for yield strengths greater than 425MPa. A further reduction is made by dividing by a factor of 1.8 to convert design level earthquake to ultimate limit state, as described in Chapter 2. It would be desirable to maintain a uniform approach across all three hinge classifications. Table 6.3 shows the ultimate curvatures as a factor of nominal first yield and  $K_y$ . Only the lower characteristic material properties are used in these calculations.

Table 6.3-Ultimate curvature as a factor of nominal first yield

Test	$\phi_y \text{ (mm}^{-1}\text{)}$	$\phi_u/(1.8 \phi_y K_y)$
A1	$7.50 \times 10^{-6}$	11.9
A2	$7.50 \times 10^{-6}$	15.9
B1*	$1.25 \times 10^{-5}$	5.7
B2* <sup>+</sup>	$1.25 \times 10^{-5}$	12.7
C1	$7.50 \times 10^{-6}$	9.9
C2 <sup>+</sup>	$7.50 \times 10^{-6}$	21.9
D1	$1.25 \times 10^{-5}$	9.8
D2 <sup>+</sup>	$1.25 \times 10^{-5}$	28.1

There is significant difference in calculation difficulty between the two different methods of defining the curvature limits (i.e. multiple of first yield or limiting compressive or tensile strains). Deriving the allowable curvature from the strain limitation requires the relatively complex calculation of the neutral axis depth. The alternative is calculating a limiting curvature based on a multiple of the curvature at first yield which only require the simple calculation of  $\phi_y$  using Equation 11. Considering the latter approach is already used for ductile and limited ductile hinges, preference is given to this method when determining the limits for nominally ductile hinges.



## 6.2. PLASTIC HINGE LENGTHS

The length over which yielding occurs (i.e. the plastic hinge length) is an important parameter in the design of reinforced concrete structures. NZS 3101:2006 does not specify a recommended plastic hinge length. However, it does use a ductile detailing length which is the length over which additional seismic detailing must be provided (i.e. additional stirrups) and an effective hinge length which is used in the calculation of curvature demands and limits.

The ductile detailing length should extend past the plastic hinge region in order to provide a degree of safety should seismic actions exceed those estimated in design. For ductile and limited ductile members the ductile detailing length is specified as  $2.0h$  for reversing plastic hinges and uni-directional plastic hinges that form at the column face. The ductile detailing length for uni-directional plastic hinges which form in the beam span away from the column face is extended to  $4.0h$  as yielding can extend either side of the critical section. However this second hinge type is not subject to as extreme curvature demand as the former case and as such the detailing requirements are not as stringent. Currently the code does not specify a ductile detailing length for nominally ductile beams as they are not subject to the additional seismic design requirements.

The effective length ( $l_p$ ) specified is used to determine the curvature limits for classification of potential plastic regions. The effective hinge length is an approximation which assumes that all the plastic rotation occurs in this length with uniform curvature. Thus the length and calculated curvatures are only an index to the actual values. The effective hinge lengths used in the concrete code (NZS 3101:2006) is  $0.5d$  for reversing hinges and uni-directional hinges located at the column face. For uni-directional hinges in the beam span the effective length is  $1.0d$ .

The experimental hinge lengths from the eight beam tests were estimated by a combination of measured crack widths and readings of longitudinal potentiometers. A crack width greater than approximately  $0.1\text{mm}$  when the load is removed indicates that the longitudinal reinforcing bars have yielded at least to that point. Presented below are photos of each beam near the end of their test, the yellow marks indicate the last crack along the beam with a width greater than  $0.1\text{mm}$  with the load removed and the blue mark indicates the subsequent

crack which closes when the load is removed. These give an indication of the upper (blue) and lower (yellow) limits for the plastic hinge length based on the crack widths.

The strain in the longitudinal reinforcing bars can be approximated using the peak displacement measurements taken from the potentiometers attached to the longitudinal reinforcement. The potentiometer displacements are divided by their original length to give an average strain over that length. Accompanying the photos are plots of the average strain in each block of potentiometers plotted against the distance along each of the eight tested beams. Strains from the potentiometers attached to both the top and bottom reinforcing bars are shown. Strains in excess of  $\epsilon_y$  ( $\sim 0.2\%$ ) indicate that yield has occurred somewhere in that section of beam. It is important to note that these strains are only an approximation and only reliably give an upper bound to the hinge length. The strains in the longitudinal reinforcement will be overestimated in the first block of potentiometers due to the pullout at the beam springing increasing potentiometer displacement but not inducing strain in the steel.

Figure 6.3 shows the crack pattern and the limits to the plastic hinge length for beam A1. The intersecting diagonal tension cracks within the plastic hinge zone opened as wide as 7mm. The flexural crack indicated by the yellow lines opened to 1.5mm, while the next flexural crack (indicated by blue lines) closed when the load was removed. This indicates a hinge length of between 450mm and 600mm.

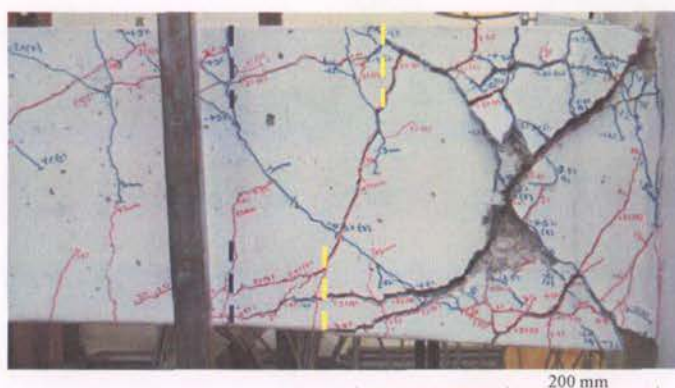


Figure 6.3-Crack widths and estimation of yielding length (A1)

Figure 6.4 plots the average strain obtained from the longitudinal potentiometers against the distance from the beam springing for beam A1. Strains in excess of 1.0% in the first two sections of the beam indicate definite yield in this area. A strain of approximately 0.25%



indicates that some small amount of yield has occurred in the third section, indicating that the plastic region extends to somewhere between 400mm and 700mm out from the springing. Combined with the Crack pattern of Figure 6.3, the plastic hinge length can be estimated to be 500mm.

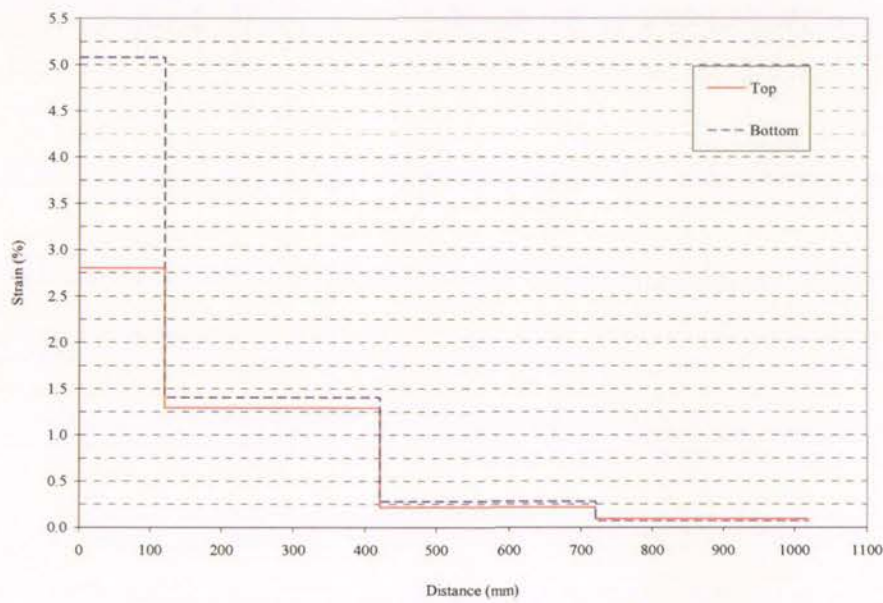


Figure 6.4-Strains obtained from longitudinal potentiometers (A1)

The flexural cracks indicated in yellow in Figure 6.5 (for beam A2) opened to 0.9mm at the top of the beam and 1.0mm at the bottom of the beam. Diagonal tension cracks formed to a width in excess of 7mm. The pattern indicates a plastic hinge length of approximately 350mm to 450mm.



Figure 6.5-Crack widths and estimation of yielding length (A2)



The approximate strain profile in beam A2 shown in Figure 6.6 indicates yielding of reinforcing bars occurred to between 400mm and 700mm from the beam springing. This is longer than the length indicated by the crack patterns. The length is also longer than that in beam A1.

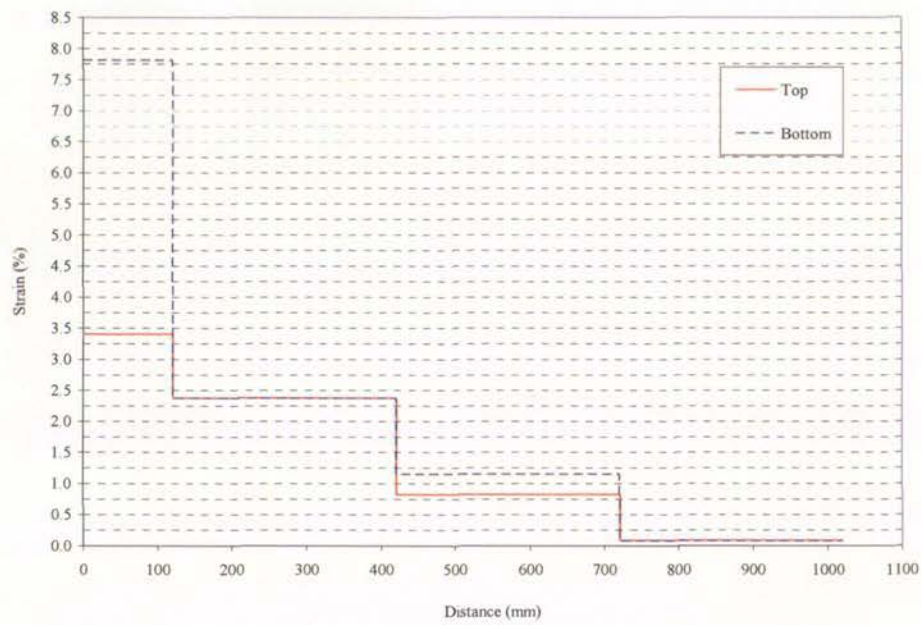


Figure 6.6-Strains obtained from longitudinal potentiometers (A2)

The few flexural cracks in the top of the beam all closed when the load was removed, as seen in Figure 6.7. This agrees with the force-displacement curve of beam B1 (Figure 4.29), which indicated that yielding of top reinforcing bars did not occur. A large flexural crack located approximately 180mm from the springing opened to 3.1mm during positive drift cycles while the next crack along the beam closed completely when the load was removed. These limits indicate a plastic hinge length of between 180mm and 320mm in the positive direction.

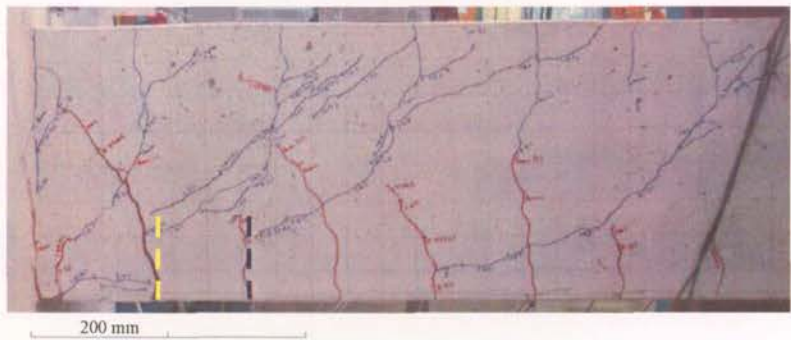


Figure 6.7-Crack widths and estimation of yielding length (B1)

Due to concrete crushing the longitudinal strains in the reinforcement, shown in Figure 6.8, are smaller than the previous cases. Yielding occurred in the positive direction with strains in excess of 0.5% in the bottom reinforcing bars up to 400mm from the beam springing. In the first section the top bars experienced a strain of approximately 1.0%, which is much larger than the yielding strain. This is possibly caused by the pullout and gap opening at the beam springing overestimating the strain in the bars within that section of beam. The strains indicate a plastic hinge length of about 400mm, significantly larger than that indicated by the crack pattern.

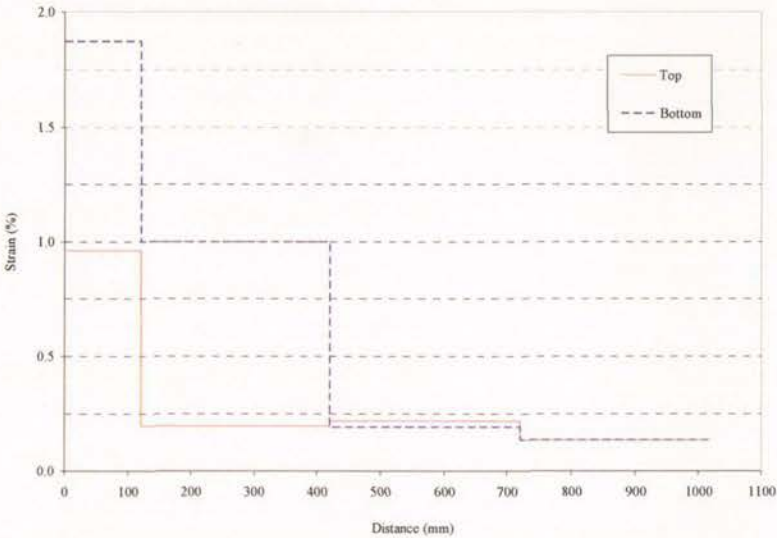


Figure 6.8-Strains obtained from longitudinal potentiometers (B1)

No yielding occurred in either direction in beam B2 and this is reflected in the crack pattern shown in Figure 6.9. The flexural cracks all closed completely when the load was removed except the crack at the springing. Diagonal tension cracks along the beam opened as wide as 4.0mm in later drift cycles.

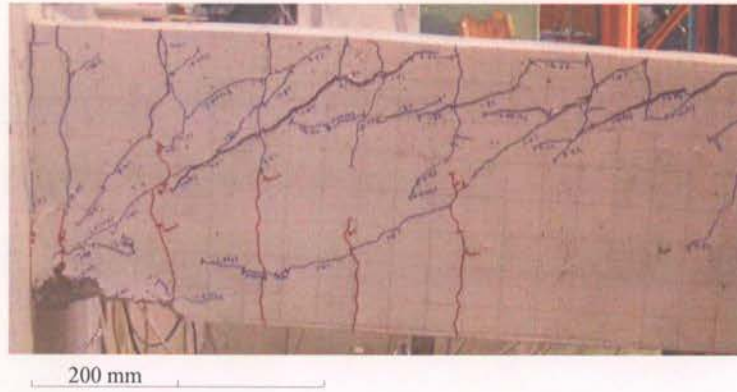


Figure 6.9-Crack width and estimation of yielding length (B2)

Due to unreliability of the potentiometer readings towards the end of the test for beam B2, Figure 6.10 shows the estimated strain profile at 3.0% drift. For this uni-directional hinge test the strains are not expected to exceed the yield strain anywhere in the beam. This is represented in the figure, with strains below 0.2% throughout except in the first section, where, as discussed earlier, the strains are inflated by the crack opening at the springing.

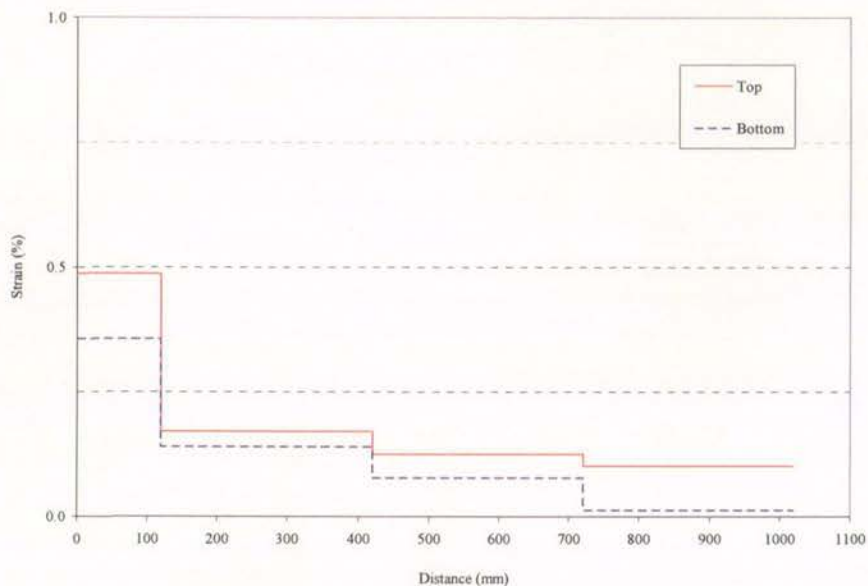


Figure 6.10-Strains obtained from longitudinal potentiometers (B2)

Figure 6.11 shows the physical condition of beam C1 at the end of the test. Cracks located approximately 300mm from the springing remained open to 0.7mm while the next flexural crack along the beam closed completely when the load was removed. These limits suggest the plastic hinge length is between 300mm and 400mm.



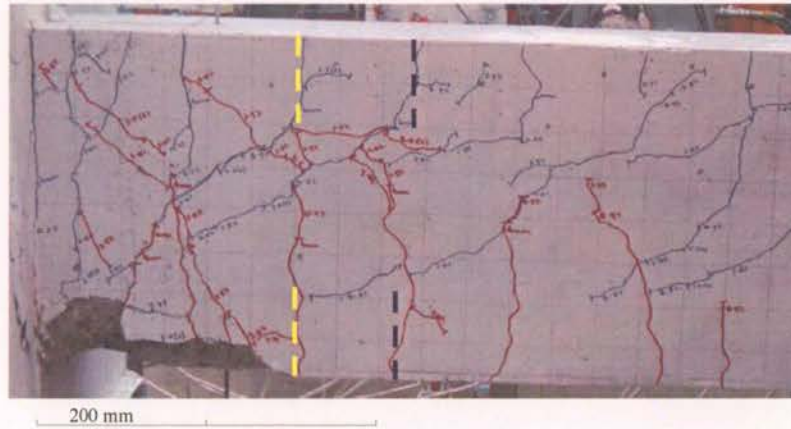


Figure 6.11-Crack width and estimation of yielding length (C1)

The strain profile for beam C1 seen in Figure 6.12 indicates yielding occurred over a longer length than the crack pattern seen above. The strains suggest a plastic hinge length of approximately 400mm in both directions of loading.

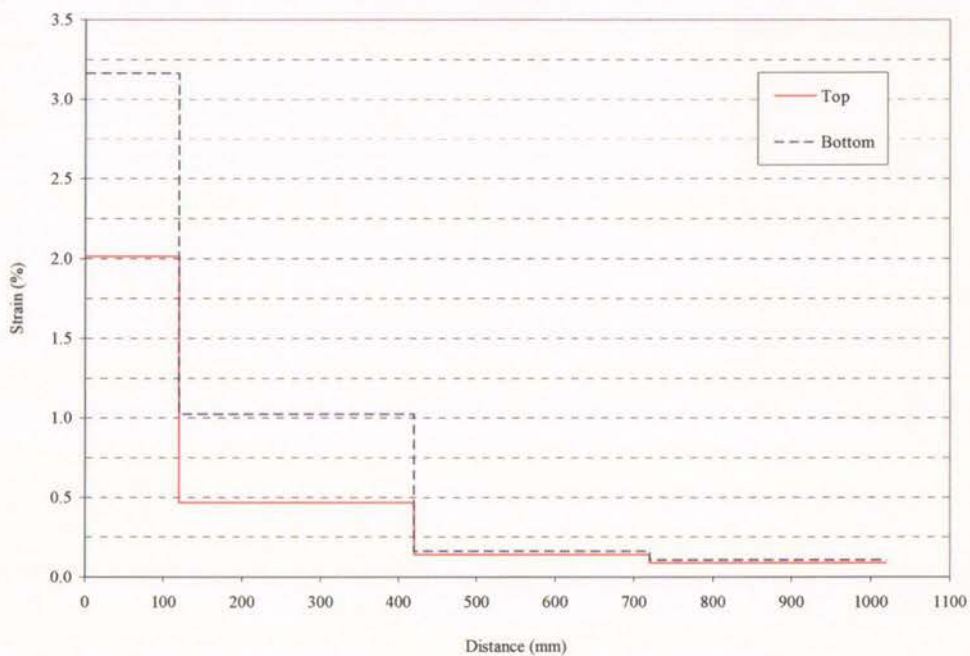


Figure 6.12-Strains obtained from longitudinal potentiometers (C1)

Figure 6.13 shows the crack pattern and bounds for the yielding length of beam C2. Because beam C2 was a uni-directional test, no significant flexural cracks opened in the bottom of the beam as seen in Figure 6.13. The last flexural crack along the beam which remained open when the load was removed was located approximately 320mm from the springing and the next crack that closed completely is located approximately 500mm from the springing.

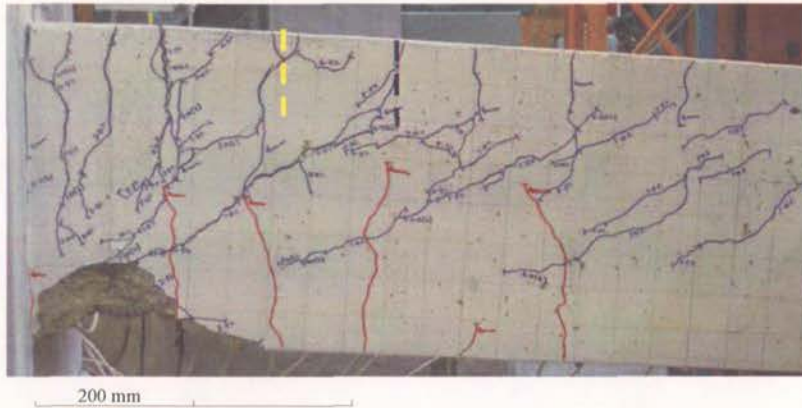


Figure 6.13-Crack width and estimation of yielding length (C2)

Figure 6.14 shows the strain profile for beam C2 at 1.5%. Problems with reliability of the potentiometer readings forced the use of a strain profile at a lower drift than desired. The strain profile agrees well with the crack widths (Figure 6.13) and force displacement relationship (Figure 4.56) indicating yielding of the top reinforcing bars but no yielding in the bottom reinforcing bars. Again the strains are overestimated in the first section of the beam due to bar pullout. The strain profile and crack widths indicate a yield length of approximately 400mm.

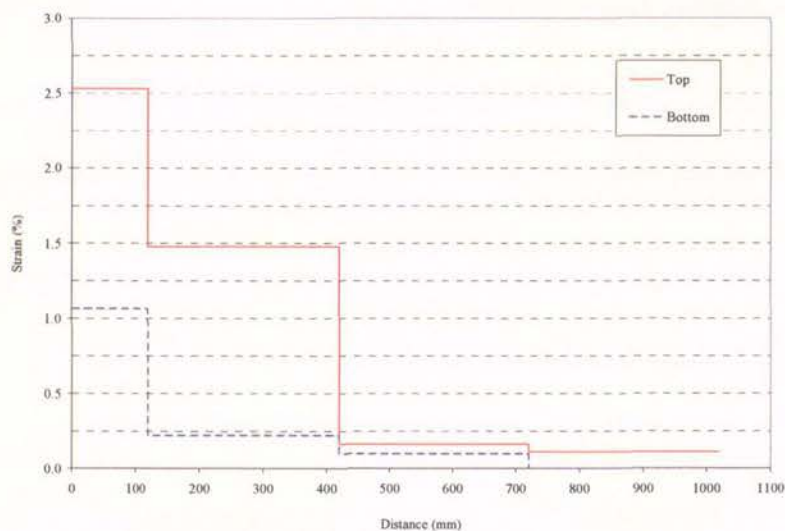


Figure 6.14-Strains obtained from longitudinal potentiometers (C2)

Figure 6.15 shows the physical condition of beam D1 near the end of the test. The only cracks which remained open when the load was removed were the crack at the springing and the crack located approximately 200mm out. The cracks at approximately 450mm from



springing (indicated in blue) closed upon load removal. There were several diagonal tension cracks which opened in excess of 3mm with in the hinge region.

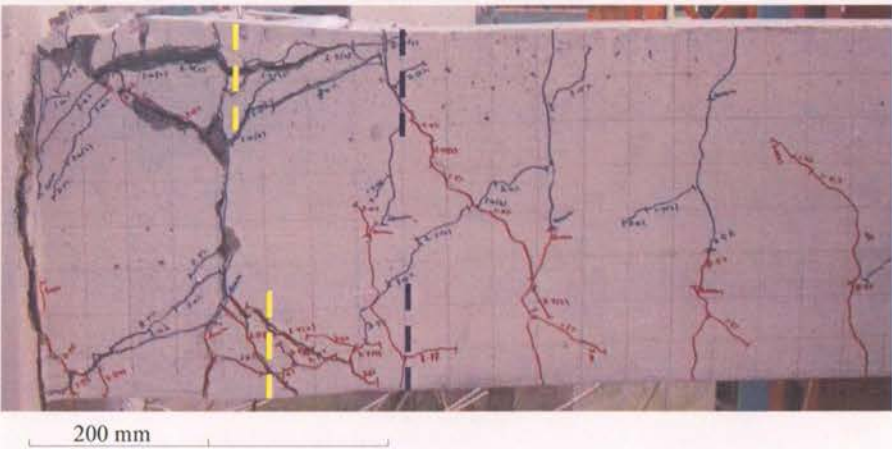


Figure 6.15-Crack widths and estimation of yielding length (D1)

Figure 6.16 shows the strain profile obtained from the potentiometers attached to the longitudinal reinforcement for beam D1. From the above crack pattern, higher strains are expected out to 300mm from the springing and this is reflected in Figure 6.16. The strains indicate that some yielding may have occurred in the third section. Combined with the crack pattern the plastic hinge length is estimated to be approximately 400mm in length, although the strain profile indicates a slightly larger value.

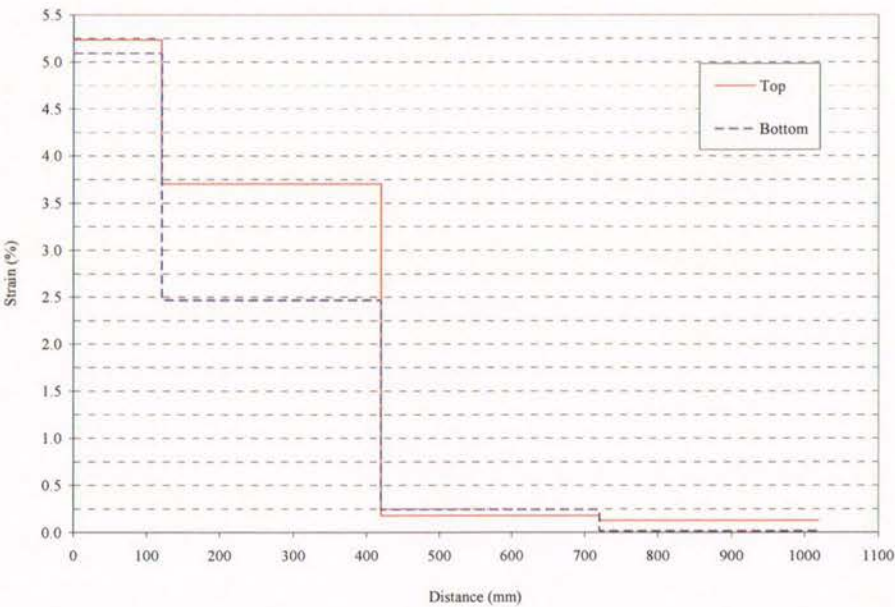


Figure 6.16-Strains obtained from longitudinal potentiometers (D1)



Figure 6.17 shows the physical condition of beam D2. In this uni-directional beam test no yielding occurred in the bottom reinforcing bars and significant yielding occurred in the top bars. The figure shows that a large flexural crack was located at 50mm from the springing. The last flexural crack that remained open when the load was removed was located 270mm from the springing. The diagonal tension cracks did not open significantly in this test.

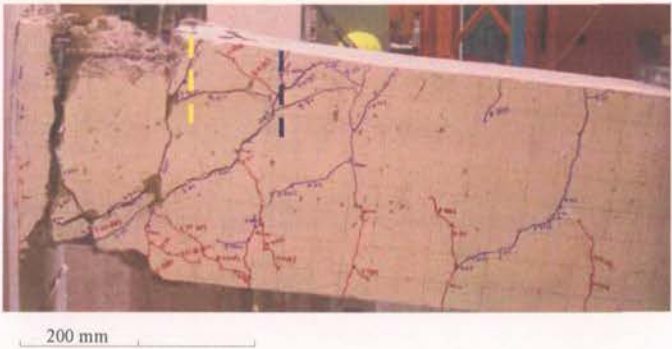


Figure 6.17-Crack widths and estimation of yielding length (D2)

The strain profile of beam D2 shown in Figure 6.18 reflects the trend shown by the crack pattern. Yielding has definitely occurred out to 400mm in the top reinforcing bars, after which the strains drop below 0.2%. The strains in the bottom reinforcing bars are low in all sections except for the first section which gives a strain of 0.5%, slightly in excess of yield strain. This is possibly due to the pullout at the beam springing causing overestimation of strains. Combined with the crack pattern the plastic hinge length is estimated to be around 400mm.

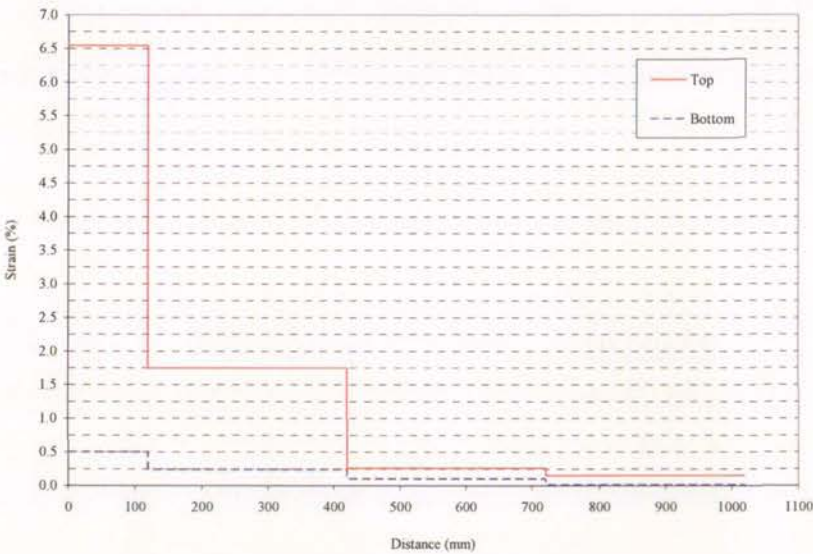


Figure 6.18-Strains obtained from longitudinal potentiometers (D2)

Using the above pieces of information an approximation to the yield length ( $L_{ph}$ ) can be made. Table 6.4 gives the approximate length over which the longitudinal reinforcement has yielded in each test. Also shown are the ductile detailing lengths ( $L_y$ ) and effective hinge lengths ( $l_p$ ) as prescribed by the concrete code (NZS 3101:2006). These plastic hinge lengths can also be compared to the yielding range obtained from the numerical analysis (Chapter 5). This is discussed in Chapter 6.3. The table shows that the length over which yielding occurred in the experiments was approximately equal to the beam depth (400mm). It is expected that the effective hinge length is substantially smaller than the experimental yield length due to the assumptions involved (i.e. uniform curvature). The ductile detailing length specified by NZS 3101:2006 is approximately twice the yielding length observed in the tests. This appears to be excessive; however, the beams tested are nominally ductile beams. It is likely that the greater inelastic actions sustained by ductile and limited ductile members will result in a greater yielding length. The results obtained from the numerical analysis tend to slightly overestimate the experimental yielding lengths.

Table 6.4-Comparison of experimental and code hinge lengths

Beam	Experimental $L_{ph}$	Numerical $L_{ph}$	$L_y$ (NZS 3101)	$l_p$ (NZS 3101)
A1	500mm	480-610mm	800mm	200mm
A2	450mm	440-610mm	800mm	200mm
B1	400mm	370-500mm	800mm	200mm
B2	No yielding	100-230mm	800mm	200mm
C1	400mm	350-470mm	800mm	200mm
C2	400mm	130-250mm	800mm	200mm
D1	400mm	275-450mm	800mm	200mm
D2	400mm	275-450mm	800mm	200mm

The effective hinge length in the concrete code approximates the plastic region as a length with uniform curvature that has the same rotation as the actual curvature profile. The strain profile indicated by the potentiometer readings is assumed triangular then a rectangular approximation of the same area can be made as shown in Figure 6.19. The level of uniform strain is taken as equal to the value of maximum strain in the triangular distributions. For the

majority of the tested beams such this approximated effective length is 250mm. This corresponds reasonably well with the approximation specified by the concrete code.

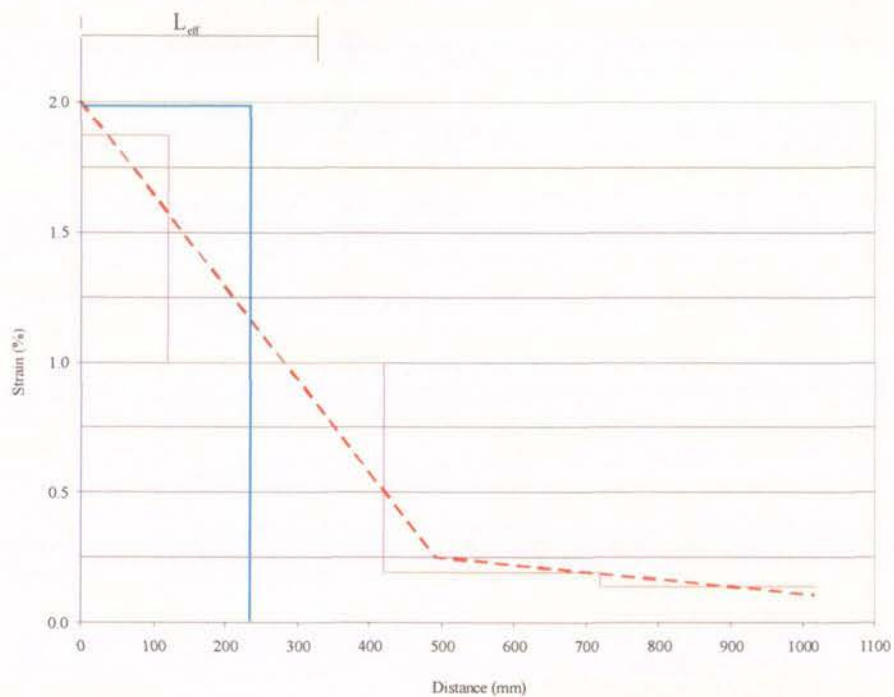


Figure 6.19-Triangular approximation of strain profile and corresponding effective hinge length



6.3. SHEAR BEHAVIOUR

All of the tested beams developed diagonal tension cracks during the tests, as discussed previously in Chapter 4. This section reviews the crack angles and attempts to correlate the crack angle to the distribution of transverse reinforcement. Table 6.5 shows the capacity of one stirrup set and the shear capacity of the transverse reinforcement calculated following NZS 3101:2006 where:

$$V_s = A_s f_y \frac{d}{s}$$

Equation 12

Where:  $V_s$  = Shear strength provided by transverse reinforcement (kN)  
 $A_s$  = Total area of one stirrup set (mm<sup>2</sup>)  
 $f_y$  =Stirrup yield stress (MPa)  
 $d$  =Stirrup diameter (mm)  
 $s$  =Stirrup spacing (mm)

The capacity of one stirrup set ( $V_1$ ) is also shown.

Table 6.5-Transverse reinforcement details

Beam	$f_y$ (MPa)	Diameter (mm)	Legs	Spacing (mm)	$V_s$ (kN)	$V_1$ (kN)
A1	445	10	2	175	140	70
A2	445	10	2	100	245	70
B	575	10	2	135	234	90
C	570	10	2	130	241	90
D	560	10	2	175	176	88

Table 6.6 shows the concrete contribution to the shear capacity calculated following NZS 3101 where

$$v_c = k_a k_d v_b$$

Equation 13

$$v_b = (0.07 + 10\rho)\sqrt{f'_c}$$

Equation 14

$$k_a = 0.895 \quad k_d = 1.0$$

$$V_c = v_c b_w d$$

Equation 15

In theses equations:  $v_c$  is the shear stress resisted by concrete,  $k_a$  is a reduction factor for maximum aggregate size,  $k_d$  is a reduction factor for member depth,  $\rho$  is the longitudinal

reinforcing ratio,  $b_w$  is the beam width,  $d$  is the effective depth,  $V_c$  is the shear force resisted by concrete and  $f'_c$  is the concrete compressive strength.

The concrete shear capacity is compared with the shear demand ( $V^*$ ) in Table 6.6. Note that the demand is approximately equal to or greater than  $V_c$  in all tests, thus some shear reinforcement is required. Note that due to inelastic response, the concrete shear capacity will degrade during the test within the plastic hinge regions.

Table 6.6-Concrete shear capacity

Beam	$f'_c$ (MPa)	$\rho$	$v_c$ (MPa)	$b_w$ (mm)	$V_c$ (kN)	$V^*$ (kN)
A	42	0.0168	1.38	250	121	120
B <sup>+</sup>	21	0.0168	0.97	250	85	140
B <sup>-</sup>	21	0.0038	0.45	250	39	40
C <sup>+</sup>	27	0.0280	1.63	250	143	145
C <sup>-</sup>	27	0.0046	0.54	250	47	50
D	26	0.0042	0.83	410	73	85

The following figures show crack patterns from each of the tested beams. Shown on the photos are the approximate location of the transverse reinforcement (black dotted line) and an approximation of the diagonal crack angle (red dotted line). This enables the number of stirrups crossed by each diagonal crack to be determined. The capacity of the stirrups crossing a crack can then be compared with the shear demand.

The crack pattern of beam A1 is shown in Figure 6.20. The two diagonal tension cracks outside of the plastic hinge region cross two stirrups. The angle of both of these cracks is approximately 40 degrees to the horizontal. Within the plastic hinge region where the shear capacity of the concrete is expected to have degraded most significantly the diagonal cracks only cross one stirrup. The inclined cracks within the hinge region have an angle of 55 degrees. The horizontal cracks extending from these diagonal cracks indicate that a shear failure has occurred and that the horizontal cracks have formed to allow a second stirrup to partially contribute to the shear strength. In this beam the maximum shear demand ( $V^*$ ) was 120kN and the capacity of one stirrup is 70kN.



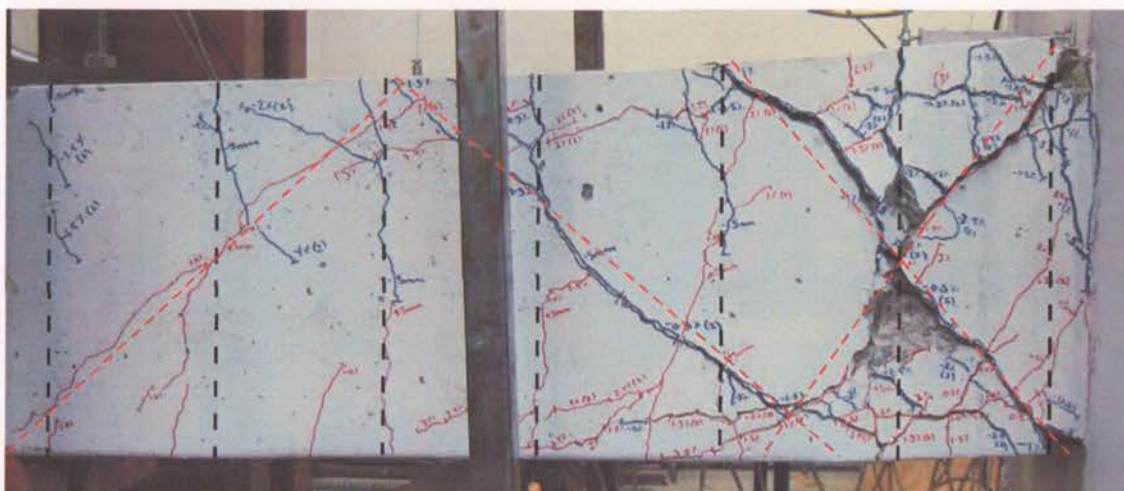


Figure 6.20-Diagonal tension cracks at 3.0% drift (A1)

Figure 6.21 shows an increased number of diagonal tension cracks in beam A2 compared with A1. Most of the cracks cross two sets of stirrups. One exception is the crack that started approximately 50mm from the springing at the top of the beam and propagated to approximately 500mm at the bottom of the beam at an angle of 40 degrees, crossing three stirrup sets. The angles of cracks range from 40 degrees to 60 degrees in this test. The capacity of one stirrup set is 70kN and the shear demand is 120kN.

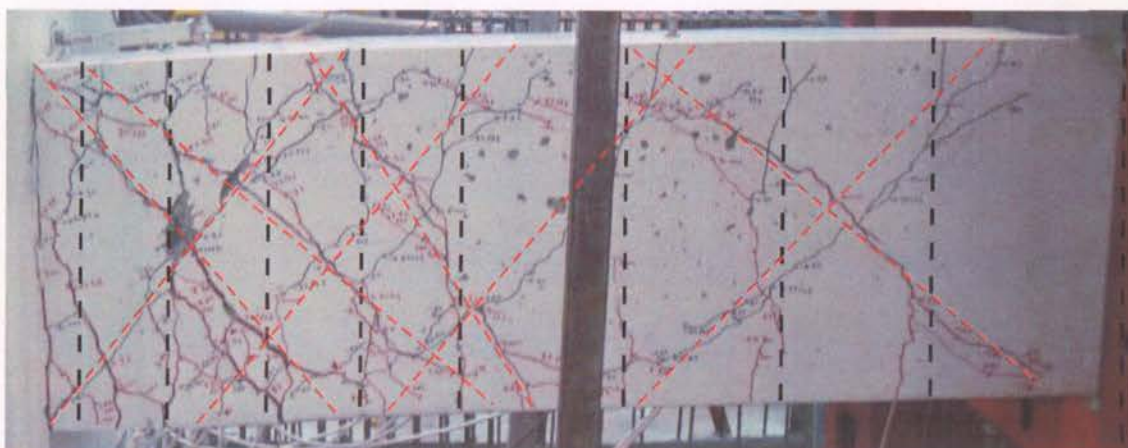


Figure 6.21-Diagonal tension cracks at 3.5% drift (A2)

Figure 6.22 shows the diagonal tension cracks for beam B1. The cracks outside the hinge region cross three to four stirrup sets while the two cracks in the hinge region cross two stirrups sets. As the concrete is likely to have a significant contribution to the shear strength in this relatively undamaged region, it can be said that the stirrups are elastic in this region. The yield result from the numerical analysis (see Figure 5.26) also indicates that the stirrups



are elastic in this region. The angle of crack varies from 55 degrees adjacent to the springing to 30 degrees in the middle of the beam. The shear demand in this beam was 140kN and the capacity of one stirrup is 90kN.

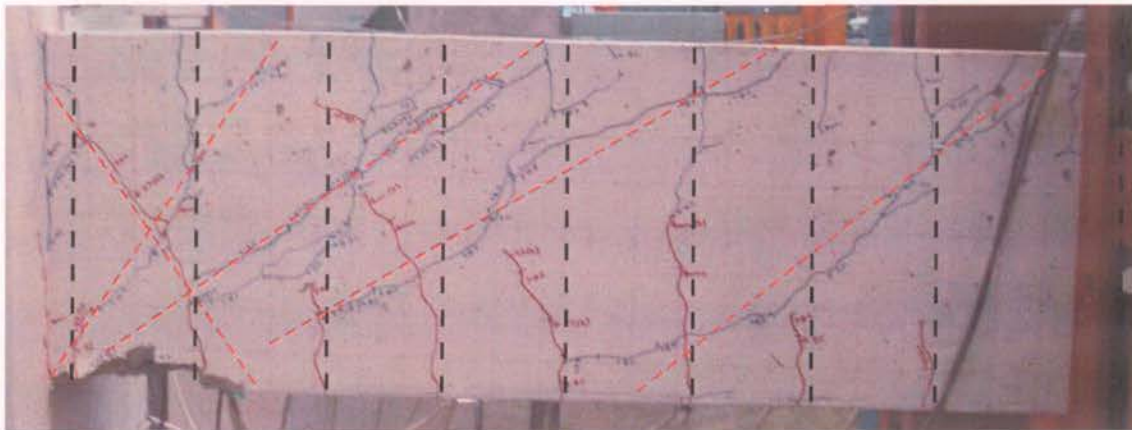


Figure 6.22-Diagonal tension cracks at 2.0% drift (B1)

Figure 6.23 shows that the angle of the diagonal cracks of the uni-directional test B2 is in many ways similar to B1 except for the absence of a diagonal crack adjacent to the springing in the positive drift direction.

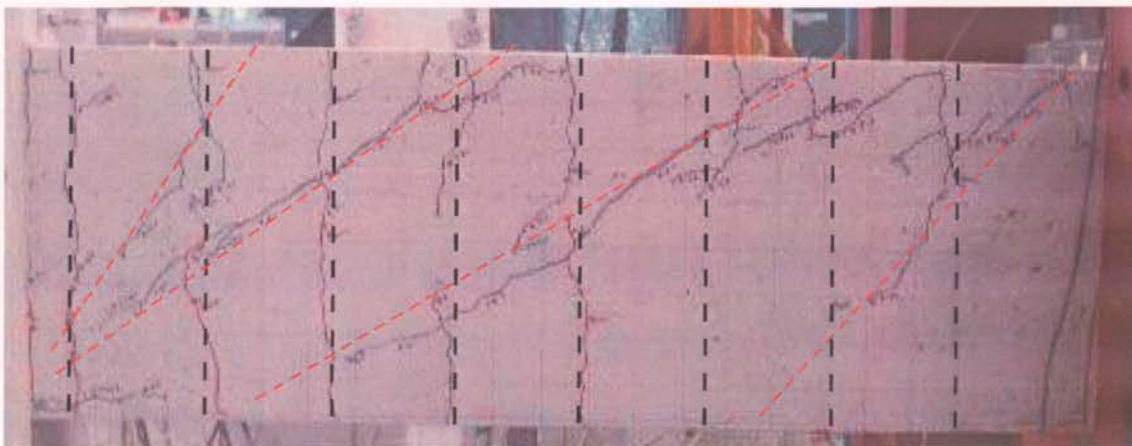


Figure 6.23-Diagonal tension cracks at 2.0% drift (B2)

Figure 6.24 shows that the diagonal tension cracks formed in beam C1 are very flat, ranging from 30 degrees to 35 degrees. There are no significant diagonal tension cracks in the positive direction as the shear demand is much smaller in this direction (50kN). A similar pattern is seen in Figure 6.25 for beam C2.

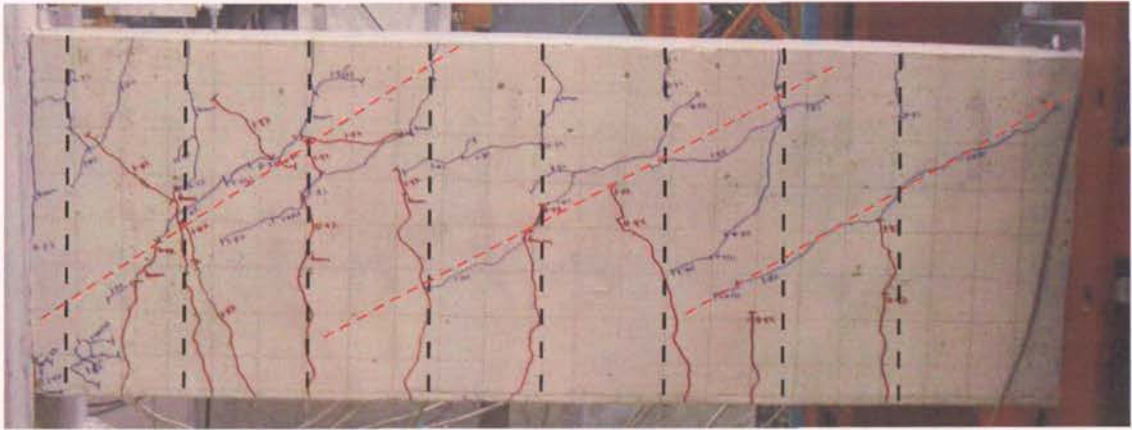


Figure 6.24-Diagonal tension cracks at 1.5% drift (C1)

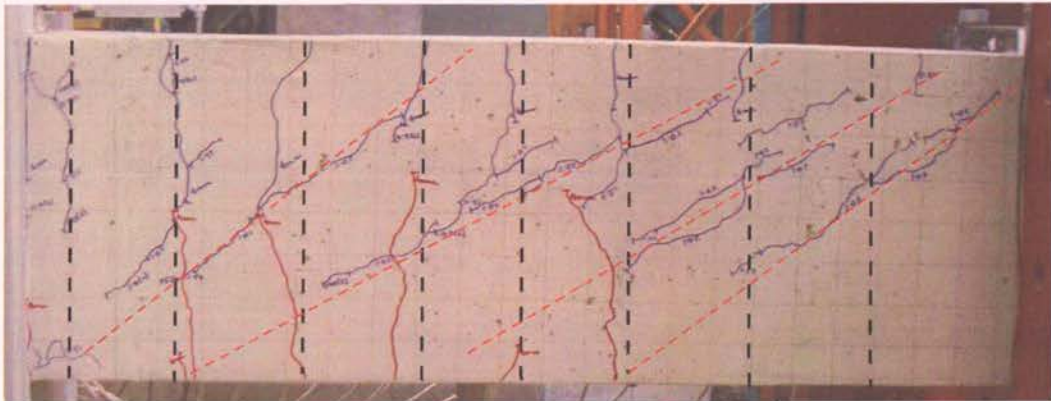


Figure 6.25-Diagonal tension cracks at 1.5% drift (C2)

Figure 6.26 shows the diagonal tension cracks for beam D1. This beam had an increased width (larger shear area) and reduced longitudinal steel content (less flexural capacity), therefore the shear stress sustained by the beam was much lower than in previous tests. The diagonal crack in the hinge region changes from 35 degrees to vertical, crossing one stirrup.

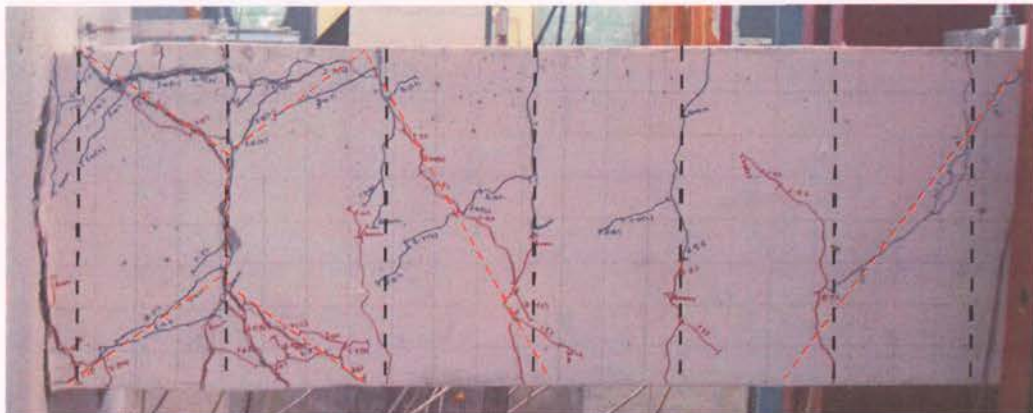


Figure 6.26-Diagonal tension cracks at 3.0% drift (D1)



The case of beam D2 is similar to that of D1 except that because of the uni-directional testing no diagonal cracks formed in the positive direction as seen in Figure 6.27. Again the cracks only crossed one stirrup set or partially crossed two. The angles from left to right are 45 degrees and 55 degrees, respectively.

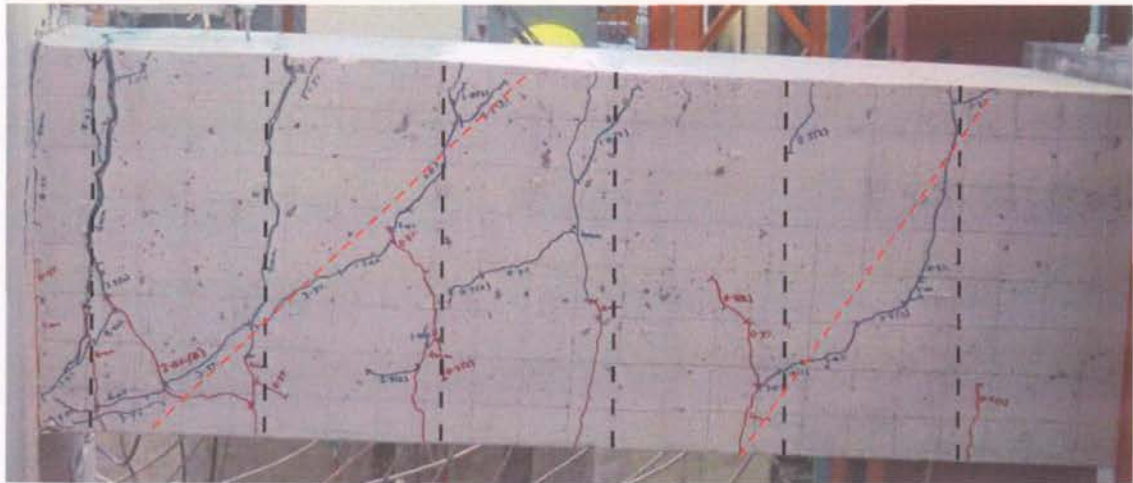


Figure 6.27-Diagonal tension cracks at 4.0% drift (D2)

The concept of shear carried by number of stirrups being equal to the shear demand holds true only in the heavily deteriorated plastic hinge regions of ductile or limited ductile members where the inelastic action is so severe that the concrete deteriorates and loses its contribution to the shear capacity. The shear deformation must also reach the critical level that induces yield of transverse reinforcement. But in hinges of nominally ductile beams the inelastic action is not very severe and the cracks can be flatter because they are able to balance the shear demand by a combination of concrete contribution and elastic force in the stirrups.



6.4. MEMBER STIFFNESS

The initial stiffness of a beam is difficult to measure due to slop in the system, cracking and the sensitive instrumentation required. However, an approximation to the stiffness can be made by taking a line from the origin to the point corresponding to 75% of the theoretical strength. This process is illustrated in Figure 6.28 and the resulting member stiffness's are shown in Table 6.7. A variation of up to 0.5kN/mm can be seen for symmetrical beams. It can be seen that the stiffness for beams B1 through C2 varied greatly with the direction of loading. This is due to the presence of different amounts of longitudinal reinforcement in the top and bottom of the beams. This is in agreement with Priestley (2003), who suggested that members yield at an approximately constant curvature and the stiffness is related to the longitudinal steel content.

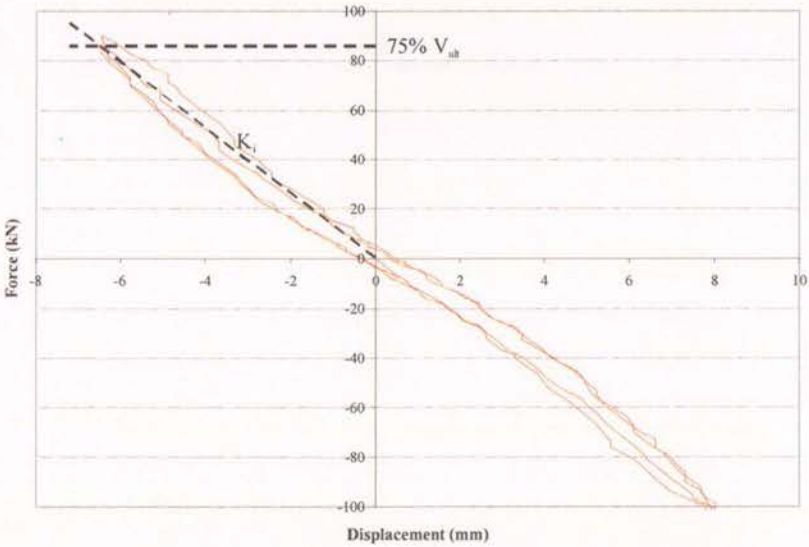


Figure 6.28-Calculating initial stiffness

Table 6.7-Initial Stiffness's

Beam	A1	A2	B1	B2	C1	C2	D1	D2
Downwards Stiffness (kN/mm)	12.9	13.0	9.5	9.7	12.0	11.4	8.1	7.7
Upwards Stiffness (kN/mm)	13.4	12.7	4.0	4.4	4.8	6.5	8.2	8.0

On subsequent cycles the stiffness decreases and can be quantified by using either a secant or tangential stiffness. The secant stiffness is found by connecting the origin and the point of peak displacement and force for any given cycle as illustrated in Figure 6.29.

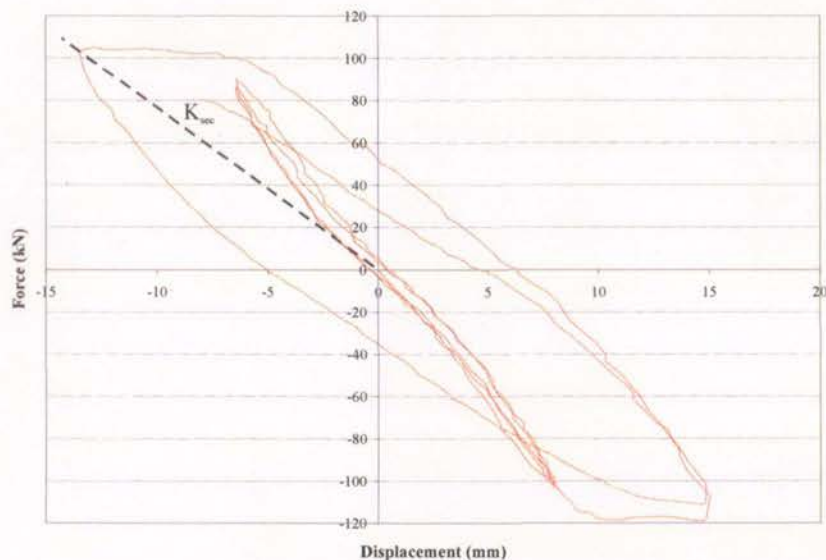


Figure 6.29-Calculating secant stiffness

Figure 6.30 shows the secant stiffness normalised by the initial stiffness plotted against the drift cycle for all beams. This gives an indication of the degradation of stiffness as the drift is increased. The intermediate division on the drift axis corresponds to the second cycle at the former drift level.

Beams A1, A2, D1, D2 and the positive displacement directions of beams B1 and C1 exhibited no or little reduction of stiffness on subsequent cycles at the same drift level, especially at the lower drift levels. For beams B2, C2 and the negative displacement directions of beams B1 and C1 there is a reduction of secant stiffness on subsequent cycles at the same drift level. This is associated with crushing of concrete in the compression zone of the hinge region, resulting in degradation of the compression zone on each subsequent cycle. This indicates that the loading history is important parameter in the member secant stiffness for beams where crushing of the concrete occurs.

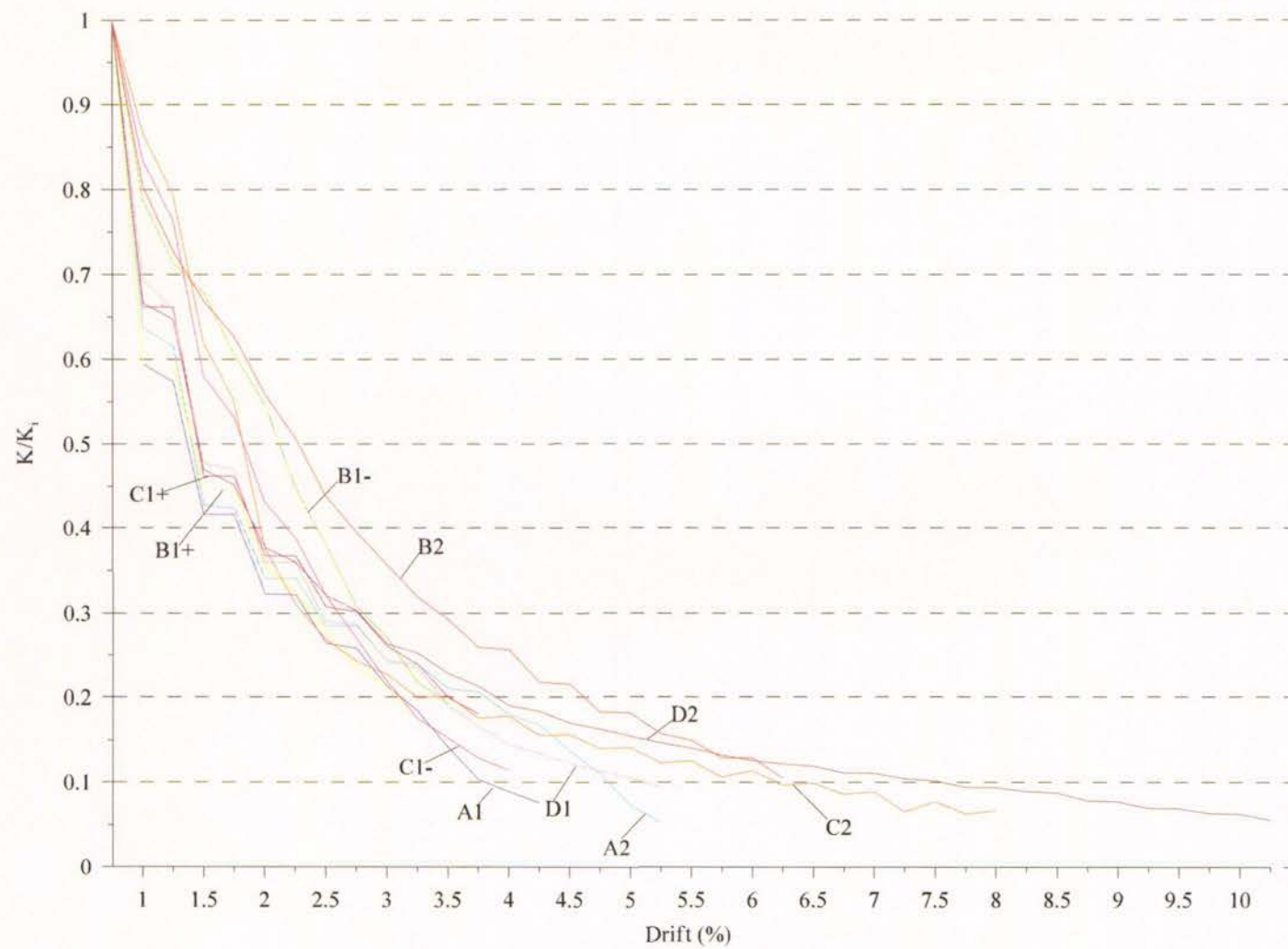


Figure 6.30-Normalised secant stiffness versus drift level



To a large extent the secant stiffness is predetermined by the drift level and the theoretical strength, up until strength degradation occurs. A second measure of the post yield stiffness is the tangent stiffness. For the purposes of this project the tangent stiffness will be defined as the slope of a line connecting a point at 75% of the theoretical strength and the point where shear pinching is no longer evident. This is illustrated in Figure 6.31.

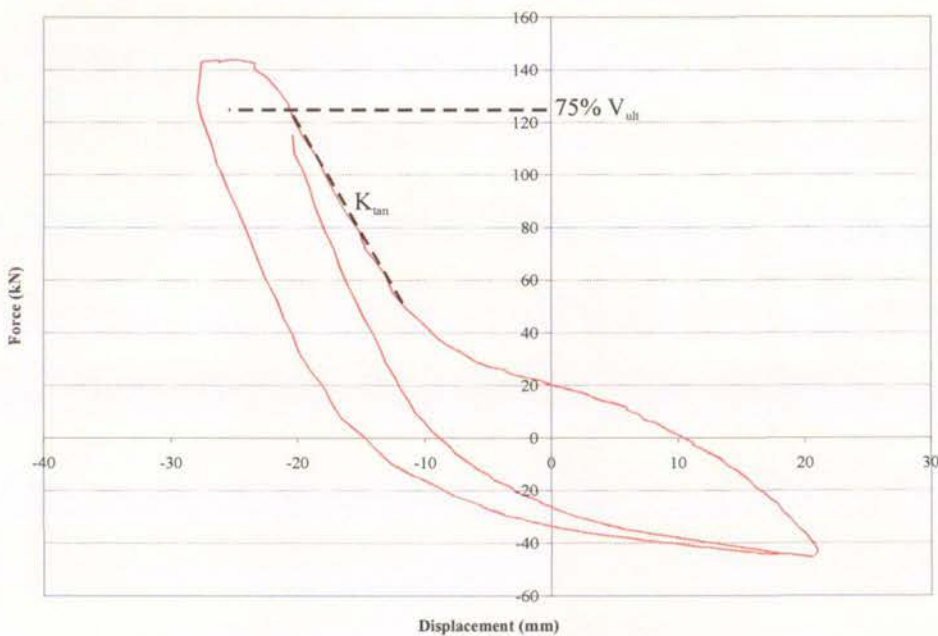


Figure 6.31-Calculating tangential stiffness

Figure 6.32 plots the normalised tangent stiffness against the drift level. It shows that the tangent stiffness does not degrade as rapidly as the secant stiffness; this is especially true for the uni-directional hinge tests. For the reversing hinges there is an obvious path dependency for the tangent stiffness as there are very few cases where the stiffness remains constant on subsequent cycles at the same drift level. However, if the typical hysteresis loop is considered, it would be expected that this path dependency would decrease on the third or fourth cycle at the same drift level, provided significant degradation did not occur.

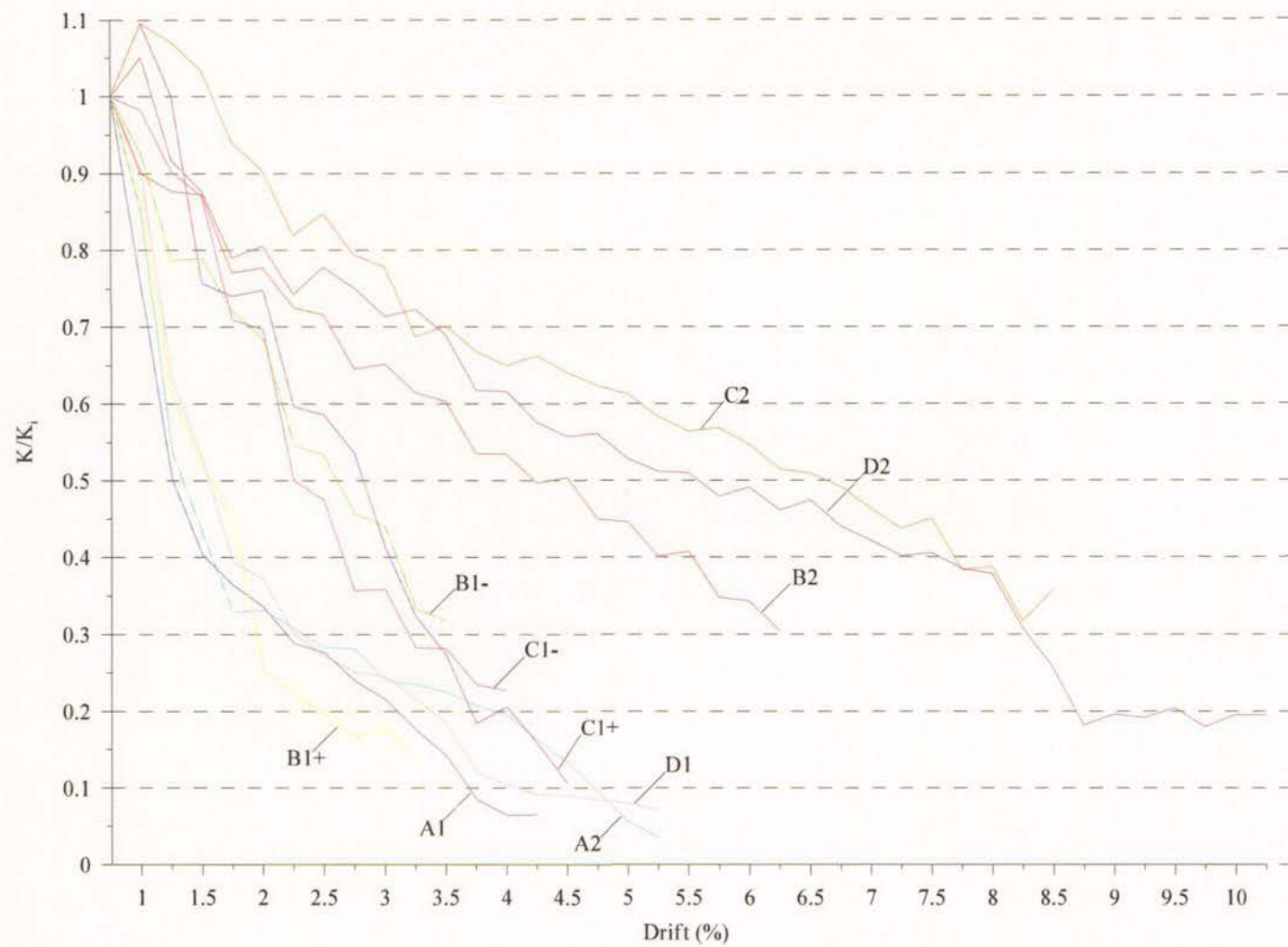


Figure 6.32-Normalised tangent stiffness versus drift level

While the beam failure used to determine the material strain limits was based on strength degradation, stiffness also has a bearing on structural integrity and can be used to define failure. If a limit of 20% of the initial stiffness is adopted to define failure, then comparisons can be made between the strength and stiffness criteria. Table 6.8 displays the drift level at which the secant stiffness drops below 20% of the initial stiffness, the drift at which failure occurred according to the strength criteria and the drift at which the tangential stiffness drops below 40% of the initial stiffness.

In Table 6.8 it can be seen that the uni-directional hinges can sustain much higher drifts than the reversing plastic hinges when using the strength and tangent stiffness criteria. However, there is very little variation in failure drift for the secant stiffness criteria. This is largely because the secant stiffness is predetermined by strength and loading protocol as discussed earlier. The tangent stiffness approach predicts failure at very low drift levels for beams A1, A2 and D1; yet these beams were the best performing reversing hinges. These inconsistencies suggest that it is inappropriate to set failure criteria based solely on tangent or secant stiffness. The two different stiffness values can be used to provide additional information on specimens whose failure is determined by strength degradation.

Table 6.8-Drifts at which failure occurred using strength, secant stiffness and tangent stiffness criteria

Beam	Strength failure	Secant Stiffness	Tangent Stiffness
A1	3.0%	3.0%	1.5%
A2	4.0%	4.0%	1.5%
B1	2.0%	3.5%	3.0%
B2	4.5%	4.5%	5.5%
C1	2.5%	3.0%	2.5%
C2	5.5%	3.5%	7.5%
D1	3.5%	3.5%	1.5%
D2	10.0%	4.0%	7.5%



## 6.5. BUCKLING BEHAVIOUR

As seen in Chapter 4, buckling of longitudinal reinforcing bars occurred in all of the beam tests. There were two main mechanisms of buckling. The first was observed in beams A1 and A2 where the longitudinal reinforcing bars displaced upwards across the spacing of two or more stirrup sets. Figure 6.33 shows an example of this mechanism. The second mechanism was seen in beams B1 and C1 where the longitudinal steel buckled between two adjacent stirrup sets. An example of this is shown in Figure 6.34. This was usually the outer two of the three reinforcing bars. Beams D1 and D2 exhibited both of these mechanisms, with the central bar buckling across two stirrup spacings and the corner bars buckled in the first mode.

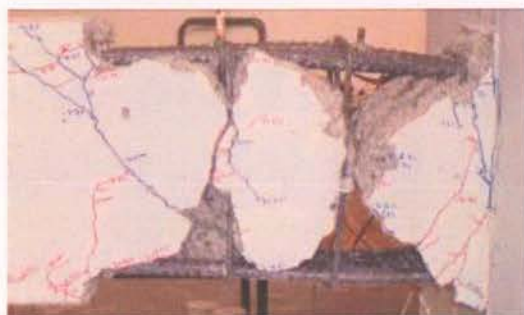


Figure 6.33-Buckling mechanism #1



Figure 6.34-Buckling mechanism #2

In all cases, the buckling of reinforcement coincided with the degradation of the beam strength and a reduction in beam stiffness in the force-displacement relationships. The factor governing the buckling mechanism is the restraint of the stirrups under axial load (corner bars) or flexural load (middle bars). Dhakal and Maekawa (2002) investigated a method for calculating the buckling mode of reinforcing bars. The method described finds the available stiffness from a stirrup and compares it to the stiffness required to restrain the longitudinal bars.

For bars restrained in the corner of stirrups, the longitudinal bars are trying to deform the vertical leg of the stirrup in axial tension. The available stiffness for this case is given by:

$$k_t = \frac{E_t A_t}{l_e} \times \frac{n_l}{n_b}$$

Equation 16

Where  $E_t$  is the elastic modulus,  $A_t$  the area of one leg,  $l_e$  the leg length being considered and  $n_l/n_b$  weights the stiffness for different combinations of bars and ties. Figure 6.35 shows the arrangement for beam A1. In this case  $n_l=2$  and  $n_b=3$ .

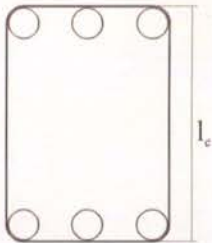


Figure 6.35-Layout of reinforcing for beam A1 to determine  $n_b$ ,  $n_l$  and  $l_e$

The stiffness required to restrain a longitudinal bar is given by:

$$k_n = k_{eq} \cdot \frac{\pi^4 EI}{s^3}$$

Equation 17

Where the elastic modulus ( $E$ ) and second moment of area ( $I$ ) are the values for one longitudinal bar,  $s$  is the spacing of the stirrups. By dividing  $k_t$  by  $k_n$  the equivalent stiffness factor  $k_{eq}$  is obtained. This is compared with values in Table 6.9, to determine the predicted buckling mode from the largest value of  $k_{eq}$  from the table that is smaller than  $k_t/k_n$ .

Table 6.9-Values of  $k_{eq}$  for stable buckling modes (Dhakal and Mackawa, 2002)

Buckling mode	1	2	3	4	5	6	7
$k_{eq}$	0.7500	0.1649	0.0976	0.0448	0.0084	0.0063	0.0037

Table 6.10 shows the parameters used in the calculation of the predicted buckling mode. The table also compares the results of the calculations with the buckling modes observed in the tests. Photos illustrating the buckling modes of each beam are included in Appendix D. For the unsymmetrical beams (Units B and C) calculations are carried out for both directions of loading.

Table 6.10-Results of buckling mode calculation

Beam	A1	A2	B-	B+	C-	C+	D
Tie diameter (mm)	10	10	10	10	10	10	10
Bar diameter (mm)	25	25	25	12	25	16	16
Spacing (mm)	175	100	135	135	130	130	175
$l_e$ (mm)	300	300	300	300	300	300	300
$n_b$	3	3	3	2	3	2	3
$n_l$	2	2	2	2	2	2	2
$k_t$ (N/mm)	34,907	34,907	34,907	52,360	34,907	52,360	34,907
$k_n$ (N/mm)	69,702	373,559	151,830	8,060	170,031	28,527	11,694
$k_t/k_n$	0.501	0.093	0.230	6.496	0.205	1.835	2.985
Predicted mode	2	4	2	1	2	1	1
Observed mode	3	4	N/A	1	N/A	1	1
Buckling Length (mm)	350	400	270	135	260	130	175

For the central bar of the top layer of reinforcing, the restraint is provided by the stirrup in bending. The clear span is considered to be from the inside to inside of the corner reinforcing bars, as illustrated in Figure 6.36. The end conditions of this analogous beam are assumed to be fixed-fixed. The stiffness provided by a stirrup in bending is calculated by:

$$k_t = \frac{192.EI}{l^3} \quad \text{Equation 18}$$

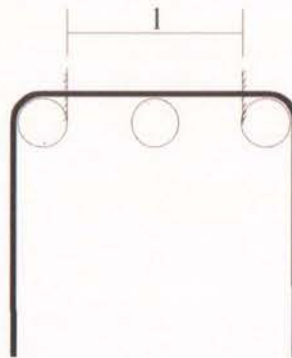


Figure 6.36-Assumed clear span for stirrup bending

The required stiffness is found as following the method described earlier by Dhakal and Maekawa. Beams D1 and D2 were the only beams that exhibited this buckling mechanism.



For these beams the clear span distance was 318mm. Calculation of the required stiffness ( $k_n$ ) for modes 3 and 4 return values of 1,141N/mm and 523N/mm, respectively. The available stiffness is found to be 586N/mm, meaning the buckling is predicted to occur in the 4th mode. This does not compare well with the buckling modes for the central bar in beams D1 and D2 where the buckling mode was the second mode.

Buckling is not considered in the horizontal direction. Buckling is not likely to occur in this direction as lateral load is not applied and the reduced leg length of the stirrups greatly increases the stiffness in this direction. Not considering lateral buckling due to load direction and reduced length of leg in the lateral direction. The second layer of top reinforcing bars used in unit C are not considered either. These bars are subjected to substantially lower strains than the top layer and are restrained by the surrounding concrete.

A further contributing factor is the yielding of longitudinal reinforcing bars on previous loading cycles in the opposite direction. Yielding of the bar in previous cycles significantly reduces the bars resistance to buckling. For uni-directional beams, this can lead to the principal tensile reinforcement buckling during the elastic half cycle before the principal compressive reinforcement. This was the order in which buckling occurred in beam D2.

Once the reinforcing bars buckled they were subjected to repeated straightening and bending on subsequent cycles. This creates issues with failure due to low cycle fatigue. This is especially important for cases where buckling occurred in the first mode. As such, reinforcing bars fractured in tension due to low cycle fatigue in beams B1, B2, C1, D1 and D2. These were the beams in which the buckling occurred in the first mode.

## 6.6. ELONGATION

Elongation of the beam occurred in every test. The magnitude of the elongation varied between each test. This section summarises the elongation observed in the tests. It also discusses some of the parameters influencing the magnitude of the elongation.

Fenwick and Megget (1993) showed that a beam detailed to comply with NZS 3101 elongated two to five percent of the beam depth under reversed cyclic loading. For reversing hinges the elongation is due to the flexural rotation and the unrecoverable compression reinforcement extension such that:

$$\text{Elongation} = e + \sum \frac{\theta(d - d')}{2} \quad \text{Equation 19}$$

where  $e$  = the elongation of the compression reinforcement

$d$  = beam depth

$\theta$  = beam rotation

$d'$  = cover depth

In unidirectional plastic hinges the strain in the compression reinforcement is negligible and if it is assumed to be zero then the elongation is found from:

$$\text{Elongation} = \sum \frac{\theta(d - d')}{2} \quad \text{Equation 20}$$

They showed that the contribution of the extension of the compression reinforcement ( $e$ ) can be three times the contribution from the flexural rotation, making the reversing hinge case more critical. Table 6.11 displays the maximum elongation obtained from each beam as well as the maximum elongation from the numerical analysis of each beam. Plots of elongation against drift are given in previous chapters for the experimental results (Chapter 4) and numerical results (Chapter 5). The maximum drift applied in each experiment or analysis are shown in the table to allow comparisons between the elongations which are drift dependent.

The values in the table show that the magnitude of the elongation varies between 0.5% and 3.6% of the beam depth. This is slightly lower than that observed by Fenwick and Megget (1993). This is due to the nominally ductile detailing of the experimental work of this project which sustains lower rotation compared with the ductile type detailing used by Fenwick and Megget. It is also clear that the elongation is significantly lower in the uni-directional beam tests than the reverse cyclic tests, even in the unit D where the uni-directional test (D2) sustained substantially more displacement than the equivalent reversing test (D1).

The maximum elongation values for the experimental results shown in Table 6.11 are significantly larger than the elongation obtained from the numerical analysis. The key reason for this is the localised failure due to excessive strains stopping the analysis before the full displacement history could be applied, reducing the sustained rotation and elongation. Within the range of the numerical data the results of the numerical and experimental maximum elongation matched reasonably well (see Chapter 5). However, the residual elongation is not well modelled by the analysis program. The elongation decreases much more rapidly in the numerical model than the experiment as the displacement returns to zero. Note that the residual case is not relevant for the uni-directional hinge tests.

Peng (2005) found that axial force has a major influence. Under large compressive force the elongation is reduced significantly while tensile axial force increases elongation. An increase in concrete compressive strength only slightly increased the elongation. Increasing the longitudinal bar yield stress or increasing the reinforcing ratio reduces elongation. These parameters are minimal compared with axial load. This agrees well with the results in Table 6.11, where the beams with increased steel content and lower concrete strength (Units B and C) exhibit less elongation than Units A and D. No comparisons are able to be made relating to axial load.



Table 6.11-Maximum elongation from experiment and numerical analysis

Beam	Maximum applied drift (%)	Maximum elongation (mm)	% $h_b$	Residual elongation (mm)	Maximum applied drift (%)	Maximum elongation (mm)	Residual elongation (mm)
A1	3.0	6.3	1.6%	5.5	4.0	6.5	4.4
A2	4.0	12.5	3.1%	11.8	4.0	6.2	3.9
B1	3.0	6.8	1.7%	3.5	2.0	3.3	0.7
B2	5.5	5.8	1.5%	N/A	N/A	<0.5	N/A
C1	3.0	7.2	1.8%	5.5	2.0	4.0	2.0
C2	7.0	1.9	0.5%	N/A	N/A	<0.5	N/A
D1	5.0	14.2	3.6%	11.4	4.0	5.7	3.7
D2	9.0	13.7	3.4%	N/A	4.5	6.7	N/A

## 7. DUTILE AND LIMITED DUCTILE PLASTIC REGIONS

The loading standard requires appropriate material strain limits to be set for all three classification of plastic region; ductile, limited ductile and nominally ductile. The experimental component of this project dealt with the gap in the literature for tests detailed as nominally ductile beams as identified by Fenwick and Dhakal (2007 b). The paper by Fenwick and Dhakal attempted to increase the confidence with which the material strain limits are set by expanding on the limited database of experiments used at the time of writing the code. However, this work was limited by time constraints to readily available literature. No information was obtained for limited ductile or nominally ductile beams. There was also a lack of tests relating to uni-directional plastic hinges.

This section of the thesis reviews the material strain limits proposed by Fenwick and Dhakal (2007 b) for NZS 3101:2006. Additional test results from the literature are added to the database of tests for determining material strain limits. From test results published in the literature and the experimental program work in this project, material strain limits are proposed for all forms of potential plastic region.

### 7.1 BEAMS

To gain information for beam plastic hinges Fenwick and Dhakal reviewed tests on 37 beams. Test results were taken from work by Fenwick and Fong (1979); Fenwick et al. (1981); Brown and Jirsa (1971); Scribner and Wight (1978); Popov et al. (1972). Of these 19 were classified as containing ductile detailing and 18 tests were discarded as they contained details not representative of current practice.

Figure 7.1 plots the ultimate curvatures sustained by each of the tests as multiples of the nominal curvature at first yield,  $\phi_y$ , and the factor  $K_y$ , which restricts the ultimate curvature for higher reinforcing grades, against the normalised shear stress. Thirteen additional tests including the beams tested as part of this project are included in Figure 7.1. The tests were taken from Fang et al. (1994); and Fang et al. (1993). Nominally ductile beams are plotted in

red, limited ductile beams in orange and ductile beams are plotted in green. The two nominally ductile, uni-directional tests carried out in this project are plotted in blue.

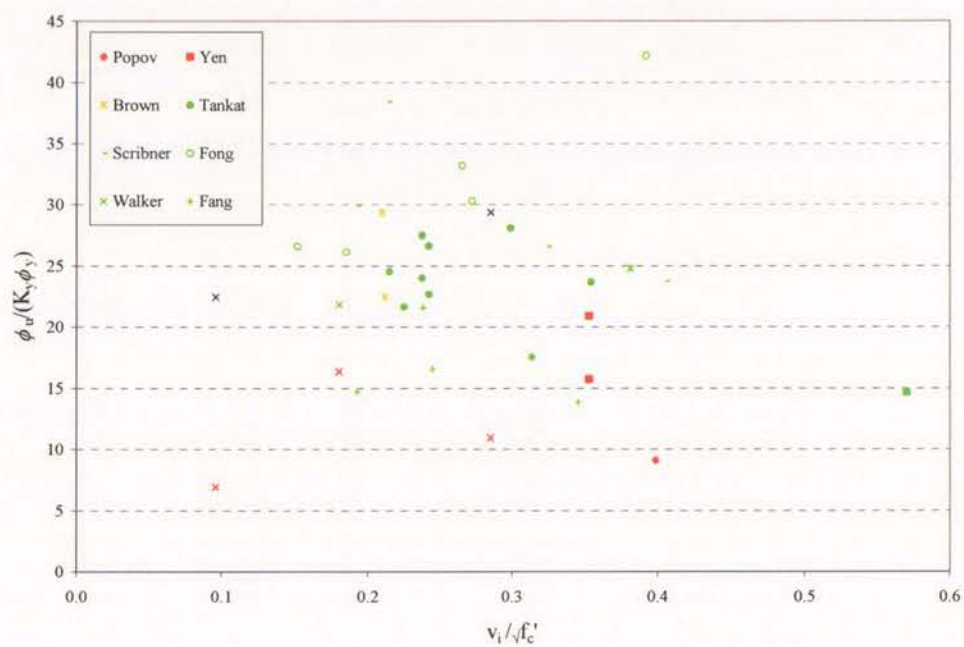


Figure 7.1-Ultimate curvatures sustained in beam tests versus normalised shear stress

## 7.2 COLUMNS

Limiting curvatures were calculated from column tests from work by Ang (1981); Soesianawati (1986); Gill (1971); and Tanaka (1990). Of these nine were classified as having ductile plastic regions, seven as limited ductile plastic regions and nine as nominally ductile plastic regions. The ultimate curvature, as a ratio of  $K_y$  and  $\phi_y$ , is plotted against the axial load ratio in Figure 7.2. No suitable additional tests for columns were obtained from the literature.



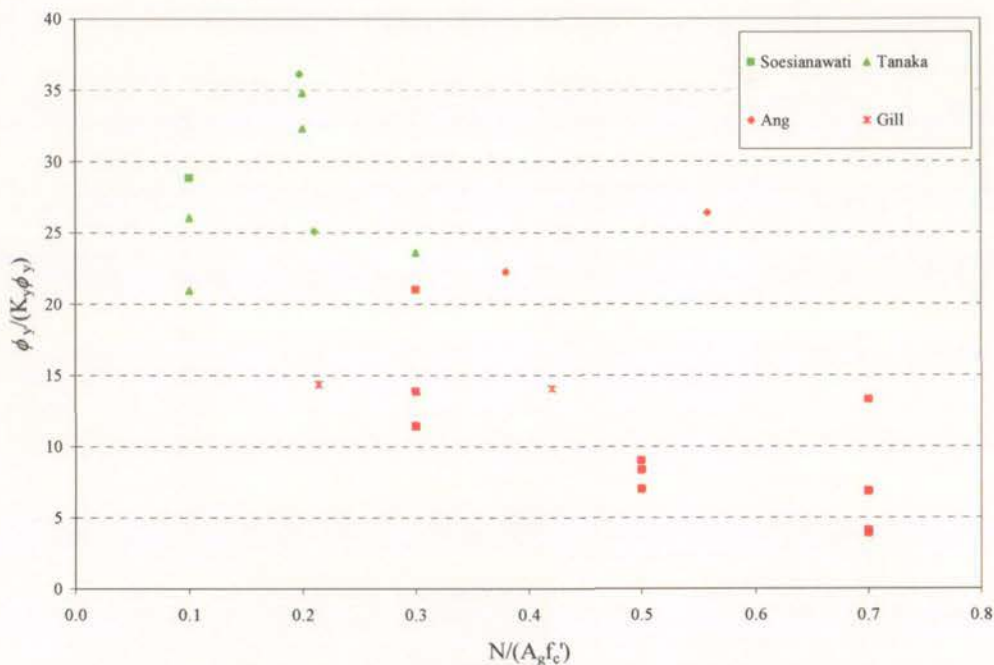


Figure 7.2-Ultimate curvatures sustained in column tests versus normalised axial stress

### 7.3 WALLS

Two different sets of wall tests were examined by Fenwick and Dhakal, namely thin singly reinforced walls and ductile walls with two layers of reinforcement. The singly reinforced walls were regarded as having limited ductility while the walls with two layers of reinforcing fell into the ductile category. Ultimate curvature values were determined from the results of 20 thin singly reinforced walls from work by Beattie (2003); Chiewanichakorn (1999); Whiteside (2000); McMenamin (1999) and Synge (1980) together with results of tests carried out at the University of Auckland, which have not been published in the literature.

Figure 7.3 plots the ultimate curvatures, as a ratio of  $K_y$  and  $\phi_y$ , against the factor  $(pf_y / f'_c + N / A_g f'_c)$  as an indication of the maximum compression force induced in the wall. Two additional tests are incorporated into the results from work by Salonikios (2001).

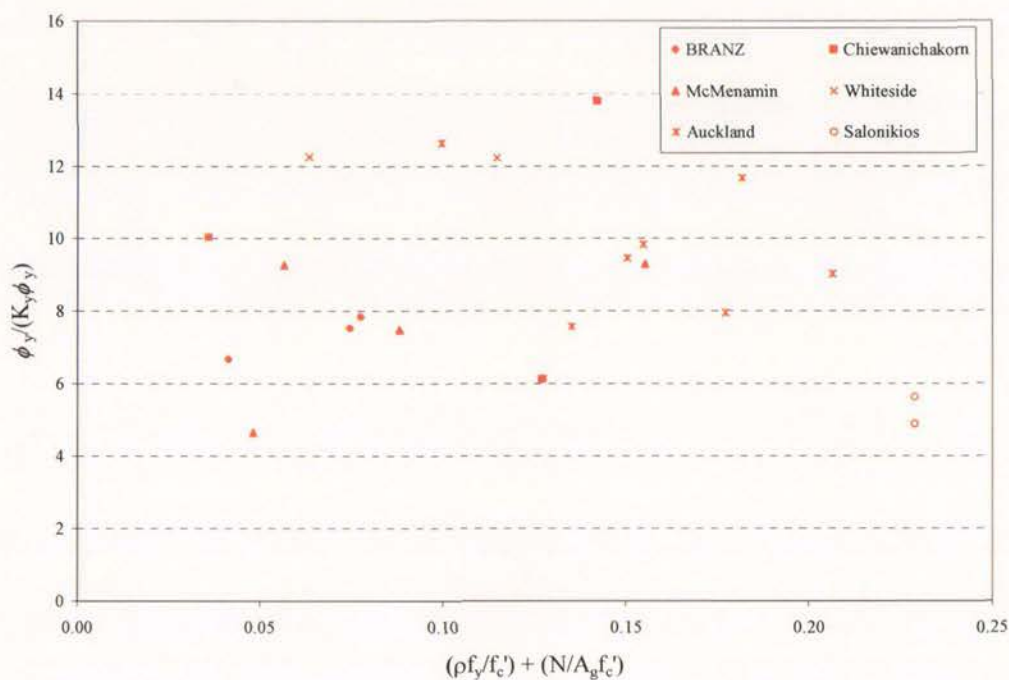


Figure 7.3-Ultimate curvatures sustained in singly reinforced walls versus normalised stress

Fenwick and Dhakal examined results of tests on seven doubly reinforced walls reported by Spurr (1984); Goodsir (1985) and Santhkumar (1974). One additional doubly reinforced wall was incorporated into the results from work by Greifenhagen and Lestuzzi (2005). The analysis of the curvatures from these ductile walls is included in Table 7.1.

It was found that the addition of a boundary element at each end of a wall should increase the axial strain level and hence the curvature that can be sustained. They suggest that on this basis the curvature limit for such walls could be expected to approach the corresponding limit for columns provided the boundary element resists the majority of the compression force in the wall and the boundary element satisfies the appropriate confinement requirements for columns.

#### 7.4 RECOMMENDATIONS FOR MATERIAL STRAIN LIMITS

Table 7.1 summarises the ultimate curvatures obtained from the tests examined. The curvatures are given in terms of  $K_y$  and  $\phi_y$ . The average values and standard deviations have been calculated which are used to give the lower characteristic values.

Table 7.1-Summary of ultimate curvatures from test results

	Beams		Columns		Walls		
	Nominally ductile	Ductile	Limited ductile	Ductile	Nominally Ductile	Limited Ductile	Ductile Doubly Reinforced
Average	13.3	24.8	19.5	29.2	7.5	9.2	20.8
Std. deviation	5.2	6.9	4.6	5.6	3.6	2.2	3.8
Lower Characteristic	4.7	13.5	11.9 <sub>y</sub>	20.0	1.6	5.6	14.6
Number of units	6	25	7	9	5	17	8

As no additional tests could be obtained for uni-directional beams with detailing corresponding to ductile or limited ductile plastic regions the increase in the curvature limit should remain at twice those for reversing hinges. As discussed in Chapter 6, this increase is reasonable for uni-directional hinges in beams detailed following the nominally ductile requirements.

The approach included in Table 7.1 gives the ultimate curvature for nominally ductile beams and walls in terms of  $K_y$  and  $\phi_y$ . This is inline with the approach recommended by Fenwick and Dhakal (2007) for limited ductile and ductile beams and walls, giving a uniform methodology for design regardless of plastic hinge classification. For nominally ductile beams and walls, Fenwick and Dhakal suggest an approach using maximum permissible tensile and compressive strains in the reinforcement and concrete, respectively. As discussed



in 6.1, based on the results of the experiments the current provisions of NZS 3101:2006 are conservative and may warrant revision with more data. Thus the limiting strains for uni-directional beams and walls are 0.004 in compression and 0.016 in the reinforcing bars as recommended by Fenwick and Dhakal (2007).

Table 7.2 gives the recommended values for the coefficient,  $K_d$  taken as appropriately rounded lower characteristic values from Table 7.1. No suitable tests for limited ductile beams were found thus the limit is placed approximately midway between the nominally ductile and ductile limits. As discussed above the limits are increased by a factor of two for uni-directional plastic regions.

Table 7.2-Recommended  $K_d$  values for determining curvature limits for reversing plastic regions

Beams			Columns		Walls		
Nominally Ductile	Limited Ductile	Ductile	Nominally & Limited Ductile	Ductile	Nominally ductile	Limited ductile *	Ductile**
4.5	9	13.5	12	20	1.5	5.5	14.5

\* limited ductile doubly reinforced and singly reinforced walls

\*\* two layers of reinforcement in each direction and confined as required by NZS 3101:2006

## 8. CONCLUSIONS AND RECOMMENDATIONS

### 8.1. CONCLUSIONS

The recent revisions to the New Zealand standards relating to earthquake loading and design of reinforced concrete structures (NZS 1170.5:2004 and NZS 3101:2006) require the use of expected material strains to determine the minimum level of detailing in potential plastic regions of reinforced concrete structures. For this provision to work effectively, appropriate material strain limits are required to classify different plastic regions as either ductile, limited ductile or nominally ductile.

Two papers by Fenwick and Dhakal (2007 a&b) were reviewed in which the authors proposed a revision to the limiting material strains currently included in the concrete code (NZS 3101:2006). New limits were proposed for limited ductile and ductile beams, columns and walls based on limited experimental results.

Tests were made on eight cantilevered beams detailed to meet the requirements for nominally ductile plastic regions in NZS 3101:2006. The purpose of these tests was to fill a gap in experimental work. Variations in parameters between the tests included yield stress, reinforcing ratio, stirrup spacing, beam width and loading protocol.

Measurements were taken from a series of potentiometers attached to the longitudinal reinforcing bars. This enabled the flexural and shear components of the total displacement to be calculated. The elongation of the beam was also obtained from these potentiometers.

The ultimate curvature sustained by the beams was found following the method described by Fenwick and Dhakal. The point which determined failure of the beams was the cycle during which the load capacity dropped below 80% of the theoretical strength. Comparisons were made with the curvature limits currently in the concrete structures standard and found the existing limits to be conservative.

An investigation was carried out to determine the suitability of an analytical program to increase the range of data available for determining the material strain limits. The program used was UC-win. The program was able to capture the elongation of the members well.

However key deficiencies were the accuracy of the theoretical strength, the absence of pinching behaviour due to shear, localised failure prematurely terminating the analysis and the lack of strength degradation caused by buckling of the reinforcing bars. There was no way of discerning an appropriate failure point that matched the experiments carried out, thus the tool was not able to be used further.

Plastic hinges lengths were estimated for each test based on crack widths, analytical predictions and approximate strains in the longitudinal reinforcing. The yielding length was found to be approximately 400mm for each beam.

Analysis of the buckling mechanisms of the reinforcing bars was discussed. Comparisons were made to the method of predicting the buckling mode proposed by Dhakal and Maekawa which was found to match well with the buckling mode of the corner bars. However, cases where the central bar buckled in a different mode to the corner bars was not able to be predicted accurately using a simple method.

Comparisons were made with the material strain limits proposed by Dhakal and Fenwick. Additional experimental tests were included for limited ductile and ductile members. An attempt was made to adopt a method for defining the nominally ductile limits in a similar manner to that proposed by Dhakal and Fenwick for limited ductile and ductile members. From the range of data available a summarised table of material strain limits were presented. It is intended for these limits to be suggested as an amendment to NZS 3101:2006.



## **8.2. RECOMMENDED FURTHER RESEARCH**

Although there is now a reasonable range of data for the setting of the material strain limits, an increased number of test results would increase the confidence with which these limits are set. In particular the degree of scatter of the nominally ductile beam tests could be obtained with several more tests detailed to the appropriate specifications.

The increase on deformation capacity of uni-directional beams has been conservatively set as twice the capacity of reversing plastic hinges. The tests carried out in this research indicate that this value could be increased. A series of tests examining the difference between reversing and uni-directional plastic hinges for all levels of detailing could increase the efficiency of this value.

Finally, the research found that the analytical tool used could not adequately capture the behaviour of the nominally ductile beams tested in this project. An improved tool capable of determining the failure of members of all levels of detailing would enable a comprehensive database of results to be established with relatively little effort.

## 9. REFERENCES

- Ang B.G, 1981, *Ductility of reinforced concrete bridge piers under seismic loading*, Dept. of Civil engineering, University of Canterbury, Report No. 81-3.
- Beattie G.J, 2003, *Design of slender precast concrete wall panels – experimental testing*, BRANZ, Draft study report.
- Bonacci J.F, 1994, *Bar Yield penetration in monotonically loaded anchorages*, Journal of Structural Engineering, Vol. 120, No. 3, pp 965-986.
- Brown R.H and Jirsa J.O, 1971, *Reinforced Concrete Beams Under Reversed Loading*, Journal of American Concrete Institute, Vol. 68, No. 5, pp380-390.
- Chiewanichakorn M, 1999, *Stability of thin precast concrete wall panels subjected to gravity and seismic forces*, ME Thesis, Dept. of Civil Engineering, University of Canterbury.
- Dhakal R.P and Maekawa K, 2002, *Reinforcement Stability and Fracture of Cover Concrete in Reinforced Concrete Members*, Journal of Structural Engineering, Vol. 128, No. 10, pp 1253-1262.
- Fang I.K, Yen S.T, Wang C.S and Hong K.L, 1993, *Cyclic Behaviour of Moderately Deep HSC Beams*, Journal of Structural Engineering, Vol. 119, No. 3, pp 2573-2591.
- Fang I.K, Wang C.S and Hong K.L, 1994, *Cyclic Behaviour of High Strength Concrete Short Beams with Lower Amount of Flexural Reinforcement*, ACI Structural Journal, Vol. 91, No. 1, pp 10-18.
- Fenwick R.C, and Fong A, 1979, *The Behaviour of Reinforced Concrete Beams under Cyclic Loading*, Bulletin of the New Zealand Society for Earthquake Engineering, Vol. 12, No. 2, pp. 158-167.

- Fenwick R.C, Tankat A.T and Thom C.W, 1981, *The Deformation of Reinforced Concrete Beams Subjected to Inelastic Cyclic Loading- Experimental Results*, University of Auckland, School of Engineering Report No. 268, p72.
- Fenwick R.C. and Davidson B, 1987, *Moment Redistribution in Seismic Resistant Concrete Frames*, Proceedings of the Pacific Conference for Earthquake Engineering, Wairakei, NZ, Vol 1, pp 95-106.
- Fenwick R.C and Megget L.M, 1993, *Elongation and Load Deflection Characteristics of Reinforced Concrete Members Containing Plastic Hinges*, Bulletin of the New Zealand Society for Earthquake Engineering, Vol. 26, No. 1, pp 28-41.
- Fenwick R.C, Dely R and Davidson B, 1999, *Ductility Demand for Uni-directional and Reversing Plastic Hinges in Ductile Moment Resisting Frames*, Bulletin of the New Zealand Society for Earthquake Engineering, Vol. 32, No. 1, pp 1-12.
- Fenwick R.C and Dhakal R.P, 2007a, *Material Strains and Relevance to Seismic Design*, SESOC Journal, Vol. 20, No. 1, pp 5-12.
- Fenwick R.C and Dhakal R.P, 2007b, *Material Strain Limits for Seismic Design of Concrete Structures*, SESOC Journal, Vol. 20, No. 1, pp 14-28.
- Gill W.D, 1971, *Ductility of rectangular reinforced concrete columns with axial load*, Dept. of Civil Engineering, University of Canterbury, Report No. 79-1.
- Goodsir W.J, 1985, *The design of coupled frame-wall structures for seismic actions*, PhD thesis, Dept. of Civil Engineering, University of Canterbury.
- Greifenhagen C. and Lestuzzi P, 2005, *Static Cyclic Tests on Lightly Reinforced Concrete Shear Walls*, Engineering Structures, Vol. 27, No. 11, pp1703-1712.



- Legeron F. and Paultre P, 2000, *Behaviour of high-strength concrete columns under cyclic flexure and constant axial load*, ACI Structural Journal, Vol 97, No. 4, pp 591-601.
- McMenamin A, 1999, *The performance of slender precast reinforced concrete cantilever walls with roof level lateral displacement restraint under simulated in-plane seismic loading*, ME Thesis, Dept. of Civil Engineering, University of Canterbury.
- Megget L.M and Fenwick R.C, 1989, *Seismic Behaviour of a Reinforced Concrete Portal Frame Sustaining Gravity Loads*, Bulletin of the New Zealand Society for Earthquake Engineering, Vol. 22, No. 1, pp 39-49.
- Okamura H and Maekawa K, 1991, *Nonlinear Analysis and Constitutive Models of Reinforced Concrete*, Gihodo Publications, Tokyo.
- Peng B, 2005, *Finite Element Modelling on Beam Elongation within the Plastic Hinge Zone*, University of Canterbury, Christchurch, NZ.
- Popov, E. P. Bertero, V. V. and Krawinkler, H, 1972, *Cyclic behaviour of three concrete flexural members with high shear*, Earthquake Engineering Research Center, University of California, Berkeley, Report No. EERC 72-5.
- Priestley M.J.N and Kowalsky M.J, 2000, *Direct Displacement Based Design of Concrete Buildings*, Bulletin of the New Zealand Society for Earthquake Engineering, Vol. 33, No. 4, pp 421-444.
- Priestley M.J.N, 2003, *Myths and fallacies in earthquake engineering, revisited*, The Ninth Mallet Milne Lecture, Pavia, Italy.
- Saatcioglu M, Alsiwat J and Ozcebe G, 1992, *Hysteretic behaviour of anchorage slip in RC members*, Journal of Structural Engineering, Vol. 118, No. 9, pp 2439-2458.

Santhkumar A.R, 1974, *Ductility of coupled shear walls*, PhD thesis, Dept. of Civil Engineering, University of Canterbury.

SANZ, *Concrete Structures Standard*, NZS3101:1995, Standards Association, Wellington, NZ.

SANZ, *Concrete Structures Standard*, NZS3101:2006, Standards Association, Wellington, NZ.

SANZ, *General Structural Design and Design Loadings for Buildings Standard*, NZS4203:1992, Standards Association, Wellington, NZ.

SANZ, *Structural Design Actions, Part 5: Earthquake Actions, New Zealand*, NZS1170.5:2004, Standards Association, Wellington, NZ.

SANZ, *Structural Steel Welding, Part 3: Welding of Reinforcing Steel*, Draft NZS 1554.3:2007, Standards Association, Wellington, NZ.

Salonikios T.N, 2001, *Shear Strength and Deformation Patterns of R/C Walls with Aspect Ratio 1.0 and 1.5 Designed to Eurocode 8*, Engineering Structures, Vol.24, No. 1, pp 39-49.

Scribner C.P and Wight J.K, 1978, *Delaying shear strength decay in reinforced concrete flexural members under large load reversals*, Dept. of Civil Engineering, University of Michigan, Report No. UMEE, 78R2.

Soesianawati M.T, 1986, *Limited ductility design of reinforced concrete columns*, Dept. of Civil Engineering, University of Canterbury, Report No. 86-10.

Spurr D.D, 1984, *Post-elastic behaviour of reinforced concrete frame wall components and assemblages subjected to simulated seismic loading*, PhD thesis, Dept. of Civil Engineering, University of Canterbury.

- Sritharan S, Priestley M.J.N and Seible F, 2000, *Nonlinear Finite Element Analyses of Concrete Bridge Joint Systems Subjected to Seismic Actions*, Finite Elements in Analysis and Design, Vol. 36, No. 3, pp 215-233.
- Synge A.J, 1980, *Ductility of squat shear walls*, Dept. of Civil Engineering, university of Canterbury, Report No. 80-8.
- Tanaka H, 1990, *Effect of lateral confining reinforcement on the ductile behaviour of reinforced concrete columns*, Dept. of Civil Engineering, University of Canterbury, Report No. 90-2.
- Whiteside M, 2000, *The performance of slender precast conventionally reinforced cantilever walls incorporating steel fibre reinforced concrete under seismic forces*, ME Thesis, Dept. of Civil Engineering, University of Canterbury.
- Zhao J and Sritharan S, 2007, *Modelling of Strain Penetration Effects in Fibre-Based Analysis of Reinforced Concrete Structures*, ACI Structural Journal, Vol. 104, No. 2, pp 133-141.



## 10.APPENDICES

### A. MATERIAL TESTING

#### A.1. Concrete cylinder tests

The results of concrete cylinder tests taken 7 and 28 days after casting are shown in Table A.1. Also shown are the results of cylinder tests carried out on the day of the respective beam test.

Table A.1-Full concrete cylinder test results

Unit	Test	7 Day (MPa)	28 Day (MPa)	Test Day (MPa)
A	1	29.4, 31.0, 28.0	39.4, 42.6, 39.8	39.1, 41.6, 43.9
	2			42.8, 42.3, 41.6
B	1	12.0, 12.8, 12.8	16.6, 15.6, 15.3	20.4, 20.8, 20.9
	2			21.9, 21.9, 21.5
C	1	20.8, 21.2, 20.8	29.1, 28.3, 28.6	27.5, 27.2, 27.4
	2			27.4, 27.5, 27.4
D	1	18.2, 17.5, 18.5	25.8, 25.3, 26.2	24.9, 25.4, 25.3
	2			25.7, 26.1, 26.1

## A.2. Steel testing

Shown below are stress-strain curves obtained from the tests on samples cut from the reinforcing steel for:

- Grade 300 reinforcing bars from Units A and C (Figure A.1)
- Grade 500 reinforcing bars from Units B and D (Figure A.2)
- Stirrup samples of all units (Figure A.3)

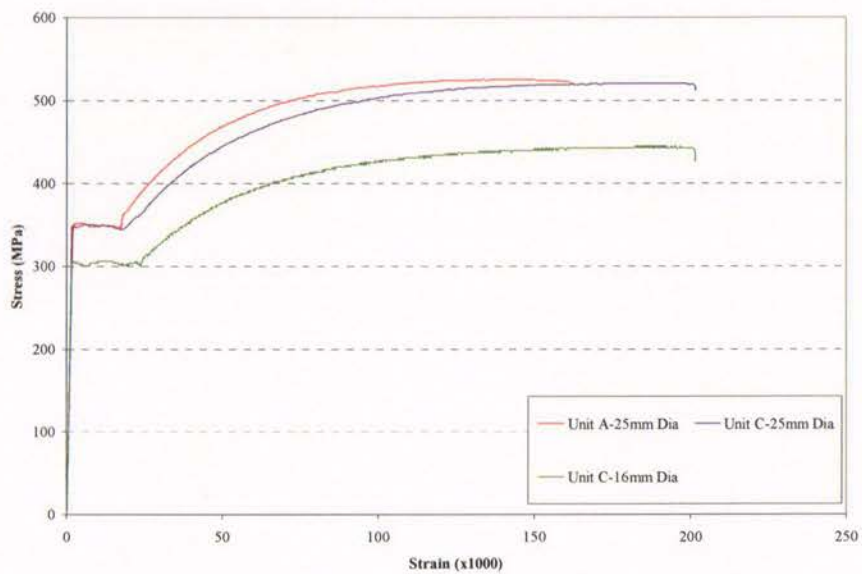


Figure A.1-Stress-strain curves from Grade 300 reinforcing bar samples

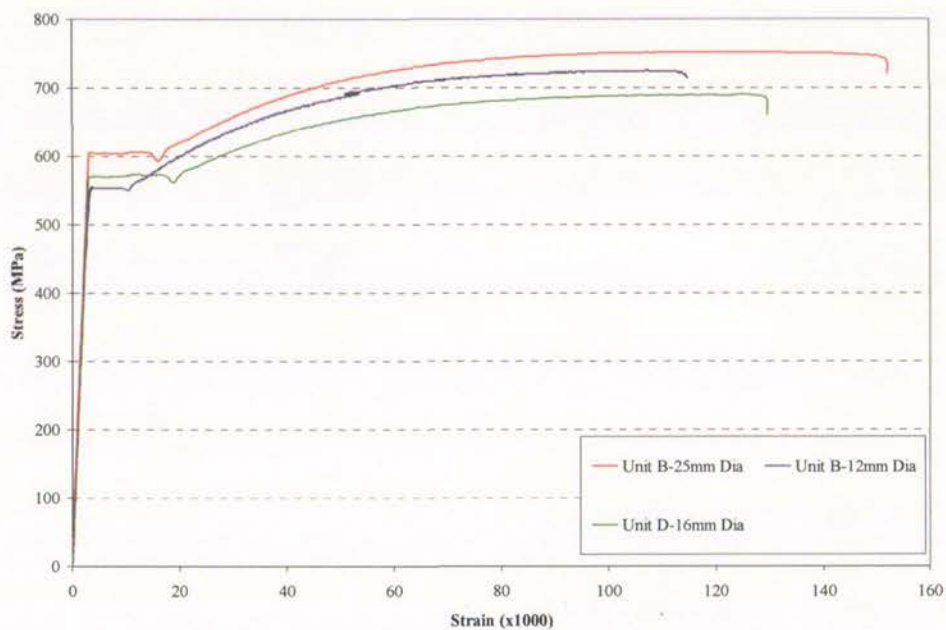


Figure A.2-Stress-strain curves from Grade 500 reinforcing bar samples

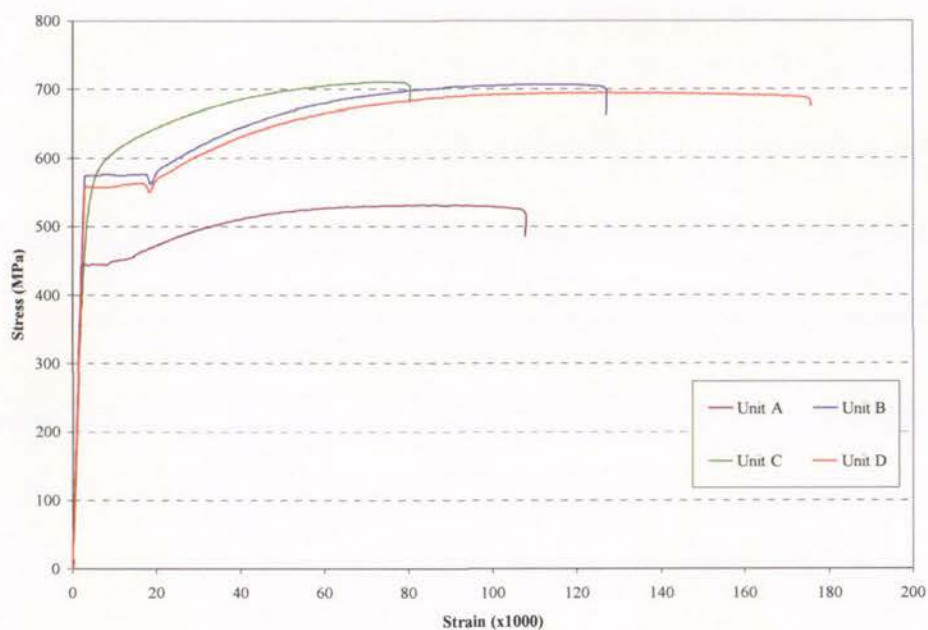


Figure A.3-Stress-strain curves from stirrup samples



Figure A.4 and Figure A.5 show the stress-strain curves obtained from tests carried out on sample pieces of Grade 500 reinforcing with studs and round bars welded to the samples replicating the conditions of test specimens. It is evident that there is little variation in the stress-strain curves between the welded and unwelded samples.

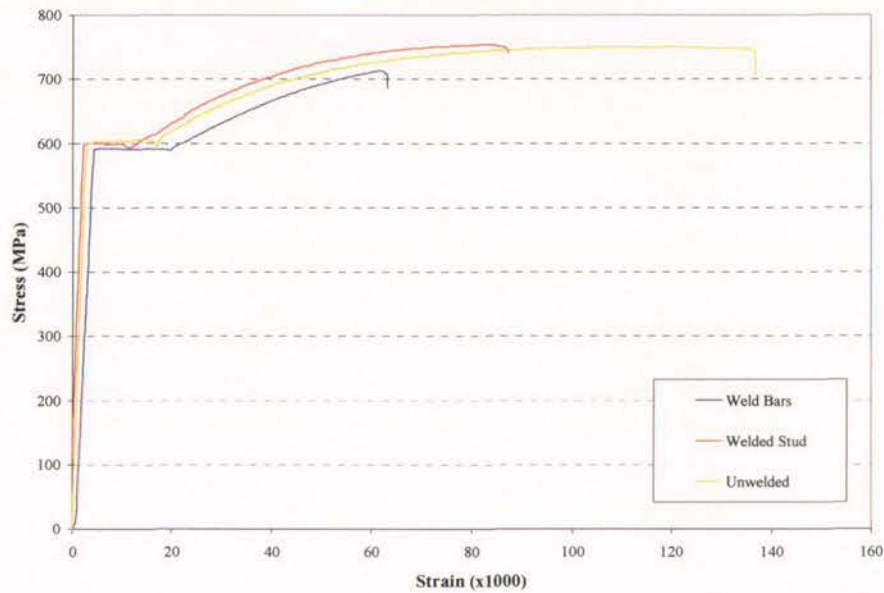


Figure A.4-Stress-strain curves of 25mm Grade 500 reinforcing bars with welds

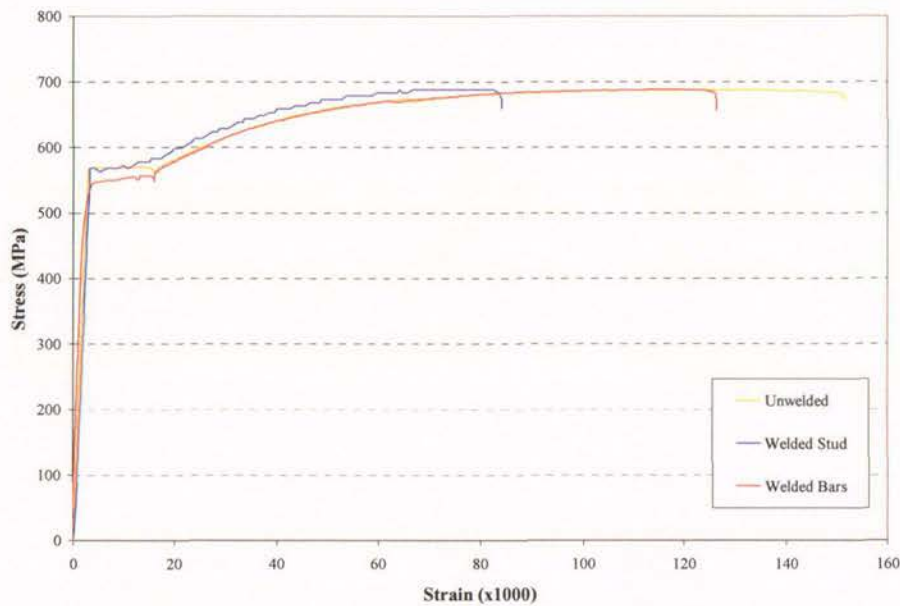


Figure A.5-Stress-strain curves of 12mm Grade 500 reinforcing bars with welds

Figure A.6 and Figure A.7 show photos of the welded reinforcing bar samples. The bars have all fractured approximately midway between the weld and the location of the restraint in the testing rig.

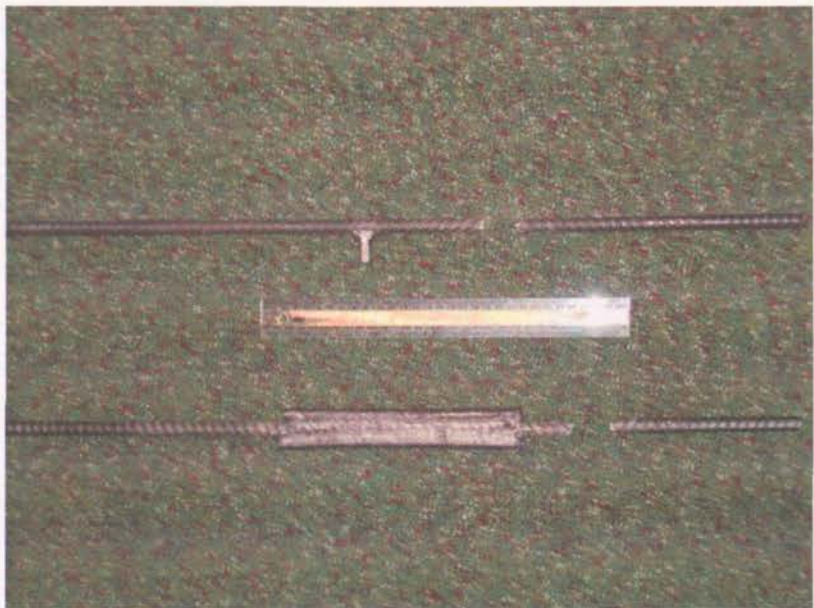


Figure A.6-Fractured steel sample of 12mm bar with stud and round bar welded to it



Figure A.7-Fractured steel sample of 25mm bar with stud and round bar welded to it

## B. FLEXURAL AND SHEAR DISPLACEMENT CALCULATIONS

The shear and flexural components of the total displacement can be calculated from the readings of the potentiometer grid attached to the longitudinal reinforcing bars as illustrated below in Figure B.1.

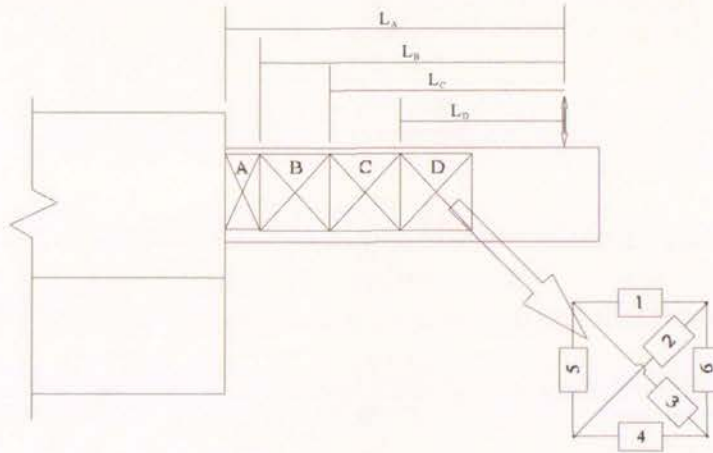


Figure B.1-Potentiometer layout for calculating shear and flexure displacement

$$\text{Shear Displacement (i)} = \frac{(G_{i2} + G_{i3})}{2 \cos \alpha_i}$$

$$\text{Total Shear Displacement} = \sum_{i=A}^D (\text{Shear Displacement (i)})$$

$$\text{Flexural Displacement (i)} = \frac{(G_{i1} - G_{i4})}{h} \ell_i$$

$$\text{Total Flexural Displacement} = \sum_{i=A}^D (\text{Flexural Displacement (i)})$$

Where:  $G_{ij}$  = Displacement reading from potentiometer at position j (i.e. 1, 2, 3, 4, 5 or 6) of block i (i.e. A, B, C or D).

$\alpha_i$  = The angle with the vertical of the diagonal potentiometers

$h$  = The original length of the vertical potentiometers

$\ell_j$  = Distance from start of potentiometer block j to the load application.

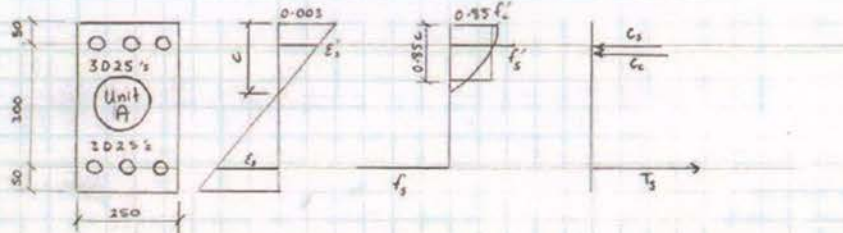


## C. SAMPLE NEUTRAL AXIS CALCULATIONS

### SAMPLE CALCULATION FOR NEUTRAL AXIS DEPTH

Section Info

$$f_y = 350 \text{ MPa} \quad f'_c = 41.0 \text{ MPa}$$



- We can assume bottom steel has yielded but not top steel
- For force equilibrium  $\Sigma F = T_s - C_s - C_c = 0$

$$T_s = A_s f_y = 3 \times \frac{\pi \times 25^2}{4} \times 350 = 515,418 \text{ N}$$

$$C_s = A'_s f'_s = A'_s \cdot E_s \cdot \epsilon'_s = A'_s \cdot E_s \cdot \frac{0.003}{c} \cdot (c - d')$$

$$C_c = 0.85 f'_c \cdot a \cdot b = 0.85 f'_c \cdot 0.85 c \cdot b$$

$$\Rightarrow 515,418 = 3 \times \frac{\pi \times 25^2}{4} \times 200,000 - 0.003 \cdot (c - d')/c + 0.85 \times 41.0 \cdot 250 \cdot 0.85 \cdot c$$

$$= 883,573 (c - d')/c + 7,406 \cdot c$$

$$\Rightarrow 515,418 \cdot c = 883,573 \cdot c - 883,573 \cdot d' + 7,406 \cdot c^2$$

$$0 = 7,406 \cdot c^2 + 368,155 \cdot c - 44,178,686$$

$$\Rightarrow c = \frac{-368,155 \pm \sqrt{368,155^2 + 4 \times 7,406 \times 44,178,686}}{2 \times 7,406}$$

$$= 56.3 \text{ mm} \quad \text{or} \quad -106.0 \text{ mm}$$

So internal forces are:

$$T_s = 515 \text{ kN}$$

$$C_s = 98.9 \text{ kN}$$

$$C_c = 417 \text{ kN}$$

$$\left. \begin{array}{l} T_s = 515 \text{ kN} \\ C_s = 98.9 \text{ kN} \\ C_c = 417 \text{ kN} \end{array} \right\} \Sigma F = 515 - 98.9 - 417$$

$$= -0.9 \text{ kN} \quad \checkmark \text{OK}$$

$$\text{Moment capacity} = T_s \cdot d - C_s \cdot d' - C_c \cdot \frac{a}{2}$$

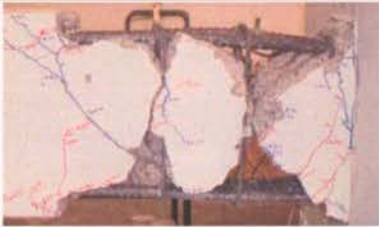

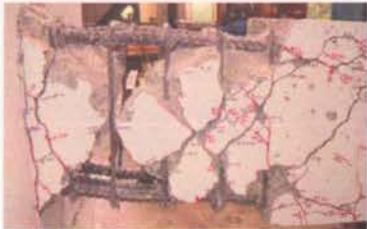

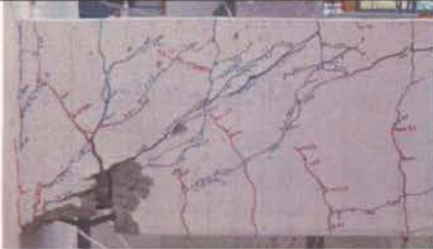

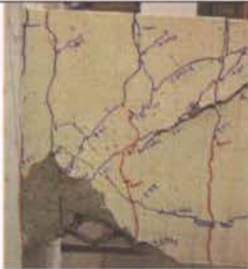

$$= 515 \cdot 350 - 98.9 \cdot 50 - 417 \cdot \frac{0.85 \cdot 56.3}{2}$$

$$= 165 \text{ kNm}$$

**D. BUCKLING CALCULATIONS AND PHOTOS**

Shown below in Table D.1 are photos of the buckling mode for each test as discussed in 6.5.

Table D.1-Photos of reinforcing bar buckling modes

Beam	Mode	Beam	Mode
A1		C1	
A2		C2	
B1		D1	
B2		D2	

## **E. DATA CD**

A CD is included on the back cover of the thesis which contains:

- Photos at each peak displacement for all tests
- Raw data from each test
- Spreadsheets used in calculating flexural and shear displacement components





TRANSONIC

CD-R

80mins 700mb 52x

COMPACT  
disc  
Recordable  
Multi Speed

- ☐ Audio
- ☐ CD-Rom
- ☐ Datafiles
- ☐ Backup
- ☐ Archive
- ☐ Mac
- ☐ PC

Title \_\_\_\_\_

Contents \_\_\_\_\_

Date \_\_\_\_\_